N° d'ordre:

THÈSE EN CO-TUTELLE

FRANCE - THAILANDE

PRÉSENTÉE A

L'UNIVERSITÉ BORDEAUX 1
ÉCOLE DOCTORALE DES SCIENCES CHIMIQUES

ET

KASETSART UNIVERSITY
GRADUATE SCHOOL KASETSART UNIVERSITY

par Chularat Wattanakit

POUR OBTENIR LE GRADE DE

DOCTEUR

SPÉCIALITÉ : Chimie – Physique

ELABORATION ET APPLICATION DE MATERIAUX POREUX : ETUDES THEORIQUES ET EXPÈRIMENTALES

« The Novel Synthesis of Microporous and Mesoporous Materials and their Applications for Hydrocarbon Transformation and Chiral Recognition »

Directeurs de thèse : Prof. Alexander Kuhn et Prof. Jumras Limtrakul

Soutenue le : 06.08.2013

Devant la commission d'examen formée de :

Assoc. Prof. SCHULTE, Albert	Associate Professor, Suranaree University of Technology	Rapporteur
Assoc. Prof. JONGSOMJIT, Bunjerd	Associate Professor, Chulalongkorn University	Rapporteur
Prof. KUHN, Alexander	Professor, Institut Polytechnique de Bordeaux	Directeur de thèse
Prof. LIMTRAKUL, Jumras	Professor, Kasetsart University	Directeur de thèse
Prof. BOPP, Philippe	Professor, Université de Bordeaux I	Examinateur (Président)
Dr. WARAKULWIT, Chompunuch	Kasetsart University	Examinateur

ABSTRACT

In the present work, the elaboration, characterisation and applications of different porous materials have been studied. Porous materials are divided into three categories depending on the porous cavity size, namely microporous materials (pore diameter < 2 nm), mesoporous materials (2 nm < pore diameter < 50 nm) and macroporous materials (pore diameter > 50 nm). The thesis work is organized in three major parts: the synthesis of hierarchical micro/mesoporous zeolites and their potential application for the petrochemical industry, the theoretical study of reaction mechanisms on microporous zeolite and the design of mesoporous metals with intrinsic chirality at their inner surface.

The hierarchical micro/mesoporous zeolite, composed of microporous and mesoporous features, has been prepared using carbon-silica (C/SiO_2) composites derived from a pyrolysis of hydrocarbon gas on silica gel. Our findings demonstrate that not only the presence of a high surface area and porosity, but also an improved efficiency of these materials for many petrochemical processes such as *n*-butene isomerization, *n*-hexadecane catalytic cracking and hydrocracking. The novel synthetic method is expected to be generalized for other types of zeolites, and is considered to be a promising method for creating hierarchical micro/mesoporous zeolites for potential catalytic applications, especially in the petrochemical industry.

In addition to the study of practical catalytic aspects, a theoretical approach has been used to investigate potential reaction mechanisms such as the selective isomerization of *1*-butene into isobutene. More specifically, the monomolecular skeletal isomerization of *1*-butene into isobutene on H-FER zeolite was theoretically studied by using the ONIOM approach. This process was found to involve the transformation of adsorbed *1*-butene through *2*-butoxide, isobutoxide, and *tert*-butyl cation intermediates. The rate-determining step is the conversion of isobutoxide into isobutene, in which the reaction has to proceed through the primary isobutyl cation transition state. The shape selectivity due to the “nano-confinement” effect of the zeolite framework strongly affects the

adsorption, the stability of alkoxide species and carbenium ion, as well as the skeletal isomerization mechanism of *1*-butene.

Moreover, the microporous and mesoporous zeolite, the generation of chiral mesoporous metal and its enantioselective recognition properties have been studied. Molecular imprinting (MI) is a major approach for generating materials with enantioselective properties. In this work, a chiral imprinted mesoporous platinum has been obtained by the electrochemical reduction of platinum salts in the simultaneous presence of a lyotropic liquid crystal phase and chiral template molecules. The resulting materials exhibit not only a dramatic increase in active surface area due to their mesoporosity, but also a significant discrimination between two enantiomers of a chiral probe, confirmed by both electrochemical and enantioselective adsorption experiments. Most importantly the porous platinum retains its chiral character even after removal of the chiral template molecule. Our findings could lead to the development of new materials, which are of potential interest for applications in areas such as chiral synthesis, sensors, separation, purification and drug development.

Keywords: Hierarchical micro/mesoprorous zeolite, skeletal isomerization, catalysts, nano-confinement, chiral mesoporous metal, lyotropic liquid crystal, electrodeposition, electroanalysis

RESUMÉ

Dans ce travail nous étudions l'élaboration, la caractérisation et les applications de différents matériaux poreux. L'étude est organisée en trois parties majeures: la synthèse de zéolithes micro/mesoporeux et leur application potentielle dans l'industrie pétrochimique, l'étude théorique de mécanismes réactionnels sur des zeolites microporeux, et le design de métaux mesoporeux avec une chiralité intrinsèque de leur surface interne. Ces matériaux poreux montrent des propriétés excellentes, notamment pour des applications potentielles en catalyse et comme interfaces chirales.

Mots clés: Zéolithes micro- et mesoporeux, catalyseurs, métaux mesoporeux chiraux, électroanalyse, calcul quantique.

ACKNOWLEDGEMENTS

First of all I would like to take this opportunity to thank all members of the jury for having accepted to evaluate my thesis and for their useful comments and suggestions, particularly, Prof. Albert Schulte and Prof. Bunjerd Jongsomjit for accepting the invitation as examiners (rapporteurs) in the jury.

I would like to express my deepest gratitude to my advisor, Prof. Alexander Kuhn, for his valuable advice, guidance, support and fruitful discussion not only during my stay in France but also after returning to Thailand. He has given me the opportunity to conduct research on an interesting part of this thesis. I appreciate all what he has done for me because he not only always helped me to find a way to reach my research goals, but he also encouraged me when I got in trouble with my experiments. His inspiration has motivated me to continue my career in the field of research.

I am also deeply grateful to Prof. Jumras Limtrakul, my advisor in Thailand for giving me the good opportunity to be his Ph.D. student and conduct a great research in his professional field. Additionally, he always provided me with good advise, support and was patient with me for all different aspects during these years.

I would like to thank the Thailand Research Fund (TRF) for the financial support from the Royal Golden Jubilee Ph.D. fellowship program, the French Government for giving me an opportunity to be a part of RGJ-Ph.D program and to spend more than one year of my research in France, the French Ministry of Research, CNRS, and ENSCBP for supporting the project in France. The National Science and Technology Development Agency (NSTDA Chair Professor), the National Nanotechnology Center (NANOTEC Center of Excellence), Kasetsart University Research and Development Institute (KURDI), the Commission on Higher Education, Ministry of Education (The “National Research University Project of Thailand (NRU)” and the “National Center of Excellence for Petroleum, Petrochemical and Advanced Materials (NCE-PPAM)”) are also acknowledged for their support.

My special, grateful thanks go to Prof. Vincent Rodriguez for introducing me to the fundamentals of secondary harmonic generation (SHG) technique and supporting my experiments, Prof. Philippe Anthony Bopp and Dr. Somkiat Nokbin for their supports, discussions and suggestions for computational simulations. My thanks are extended to Asst. Prof. Piboon Pantu and Dr. Chompunuch Warakulwit for their valuable recommendations and discussions for my thesis work in Thailand. Assoc. Prof. Metta Charoenpanich and Dr. Boonruen Sunpetch are also acknowledged here for their discussions, and the kind help with the catalysis experiments. I also gratefully thank Prof. Mizuki Tada, my supervisor during my stay in Japan (IMS). Although I spent only 6 months with her, she always gives me good advise, encouragement and good opportunities even after returning to Thailand.

I gratefully thank all my friends and colleagues at Nsysa and Kasetsart University for their kind help, in particular, Yémima Bon Saint Côme, Matthias Heim, Veronique Lapeyre, Aline Simon-Lalande, Dodzi Zigah, Aleksandar Karajic, Milica Sentic, Zahra Fattah, Salem Ben-Amor, Catherine Adam, María, Lisa Peyrard, Léa Messager, Chawanwit Kumsapaya, Ratsupa Thammaporn, Oranit Phuakkong, Saowapak Choomwattana and Sombat Ketrat.

Finally, I would like to thank my parents for encouraging me and supporting whatever I have done. I also thank everybody who was important to the successful realization of this thesis work, and apologize that I could not mention personally everybody one by one.

Chularat Wattanakit

August 6, 2013

CONTENTS

Chapter 1 SYNTHESIS OF HIERARCHICAL MICRO- AND MESOPOROUS ZEOLITE AND ITS APPLICATIONS IN PETROCHEMICAL INDUSTRY AS CATALYST FOR HYDROCARBON TRANSFORMATIONS

1. INTRODUCTION

Zeolites are microporous crystalline aluminosilicate materials with open 3D framework structures. Generally, their framework structure consists of SiO_4 and AlO_4 tetrahedra linked to each other via the interconnected oxygen atoms, leading to the formation of regular intra-crystalline cavities and channels. Such formations provide the generation of different zeolite structures with various kinds of pore dimensions. The common pore sizes of zeolites are on the molecular scale, which is less than 20 Å by IUPAC definition. Normally, they range from about 3 to 12 Å, which are called as "micropores". Micropores of zeolites are open to the outermost surface allowing transfer of matters between the intra-crystalline channels and the surrounding environment. Molecules with a critical diameter less than the pore size are preferentially adsorbed into the pores while larger molecules are excluded. Accordingly, zeolites have a shape selectivity that opens up a wide range of molecular sieving applications.

Besides the potential in molecular sieving applications, zeolites also exhibit the potential in catalysis including hydrocarbon transformation, which is a very important process, especially petrochemical industry. The presence of Al^{3+} ions in zeolites leads to the creation of a negatively charged zeolite framework. Therefore, the positive cations are attracted to reside in the zeolite structure in order to compensate negative charge of the framework and preserve overall charge neutrality. Because the cations are not covalently bonded to the zeolite structure, they can be easily exchanged by other cations via a simple ion exchange process. The nature of the exchanged cations including size and charge plays an important role on the zeolite reactivity. For example, when the cations are protons, the zeolite can act as the proton donor of Brønsted acid catalyst. However, the catalytic properties of reactions do not rely only on the Brønsted acid property, but also depend on the nature of the exchanged cations, which can be applied to catalyze for various reactions, from acid to base and redox catalysis, for example. Apart from the particular properties including uniform porosity, interconnected pore/channel system,

accessible pore volume, high adsorption capacity, ion-exchange ability and shape/size selectivity, zeolites also have a high thermal stability. Their stability varies over a large temperature range from about 700°C for low-silica zeolites to about 1300°C for completely siliceous zeolite providing a promising feature for catalysis. These properties made zeolites as important heterogeneous catalysts in petrochemical industries.

As far as the importance of heterogeneous catalysts is concerned, synthetic zeolites for which their properties can be effectively optimized for a certain catalytic application have been widely used as catalysts in petrochemical industries such as in catalytic cracking[1], isomerization[2], aromatization of hydrocarbons[3] and hydrocracking[4] processes. Among them, ZSM-5 is one of the most important catalysts in the petrochemical industries. For this reason, it is of our interest to study the catalytic activities of ZSM-5 zeolite.

ZSM-5 is a medium pore zeolite involving two types of 10 membered-ring pore structures, which are straight and zigzag channels. The cavity sizes of the straight and the zigzag channels are 0.56 × 0.54 nm and 0.51 × 0.55 nm, respectively, as shown in Figure 1.

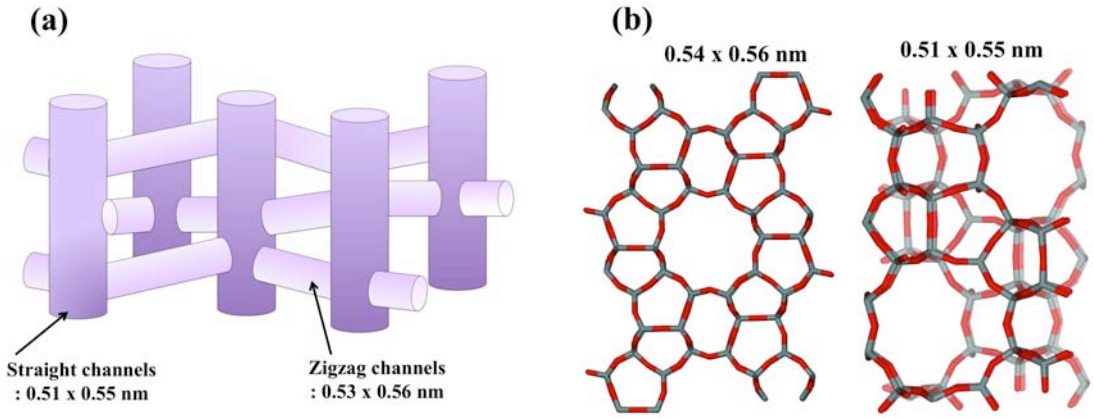

Figure 1. The illustrations of (a) ZSM-5 porous structure and (b) lattice structure of ZSM-5.

Although the micropores of zeolites provide a shape-selectivity, they sometimes limit the catalytic performance of zeolites. As diffusion of reactants and products in the micropores is slow, reactions encounter diffusion limitation. The pores of microporous zeolite become blocked when coke is formed during reaction process, resulting in the

deactivation of catalyst. For example, the conventional zeolites, such as ZSM-5, have been discovered to deactivate very quickly during the catalytic process due to yielding a carbon residue or coke inside the framework[5,6]. In addition to the mass transfer or diffusion limitation, micropores of zeolites can also show heat transfer limitation. Thus, in many cases, they decrease the catalytic performances in the terms of both activity and selectivity.

To improve the utilization of these materials, ZSM-5 zeolites with greater accessibility and shorter path length should be designed. Usually, two potential solutions have been explored: (i) synthesis of nanometer-sized zeolite crystals, (ii) addition of mesoporous cavities into some parts of zeolite framework.

(i) Synthesis of nanometer-sized zeolite crystals

As crystalline size of zeolites is typically large (more than 1 μm) so the first solution, which is able to minimize the diffusion limitation in zeolite framework, is the reduction of the crystalline diffusion path length by creating zeolites with extremely small crystals or nanocrystals. By this way, the external surface area is also significantly improved. Thus, zeolites with nanocrystals have typically exhibited good catalytic activity and adsorption capacity[7].

The preparation methods that are often used for preparation of nanocrystalline zeolites can be categorized into two major approaches. The first approach is based on the clear solution or gel synthesis methods. In this approach, the nanocrystals are synthesized from clear solutions or gels under condition that the nucleation process is preferable compared to the crystal growth[7-11]. As a result, zeolites are grown with small crystal size as colloids in the suspension. The crystal size is typically less than 100 nm and the particle size distribution is relatively narrow. Another approach is a confined-space synthesis. The nanocrystal zeolites are synthesized using inert matrix consisting of cavities or voids in which they provide steric hindered space for the zeolite crystal growth[12,13]. After removal of the matrix, nanocrystal zeolite is obtained. In this approach, the crystal size is directly related to the space of cavity or void of the inert matrix, thus the desired crystal size of zeolites can be controlled by the selection of matrix. So far, many types of matrix have been used in the confined space synthesis, for example, Jacobsen[14] prepared the nonosized ZSM-5 crystals using carbon black with two different pore diameters of 31.6 and 45.6 nm. They obtained nanocrystalline zeolite with the

corresponding crystal sizes in the ranges of 22-30 and 37-45 nm depending on the diameters of pore size of matrix.

(ii) Addition of mesoporous cavities into some parts of zeolite framework.

The generation of larger transport pores with improved diffusional properties can be obtained by creating larger pores or mesopores (diameter ranging from 2 to 50 nm by IUPAC definition) in addition to the micropores[15-17]. The addition of mesopores into zeolite framework introduces a concept of hierarchical dual micro- and mesoporous zeolites. The mesopores that interconnect to the micropores permit faster diffusion of guest molecules into zeolite framework solving the diffusional problem. Furthermore, the presence of mesopores enhances the catalytic activity of reactions, which involves large or bulky reactant, transition state and product. Particularly, it is also possible to create nanocrystalline zeolite containing mesopores[18], this synergy yields novel catalysts with high catalytic performance[19].

The methods used for synthesis of hierarchical dual micro- and mesoporous zeolites can be categorized into two major approaches which are based on nontemplating[16,20] and templating[12,17,20-23] approaches[4,11,14-17]. For the nontemplating approach, hierarchical mesoporous zeolites are obtained by postsynthesis modifications, such as the extraction by either metal atoms (demetalation) or silicon atoms (desilication) with acidic or basic solutions[16,20,24], for example. This approach can be considered as a top-down approach. However, such approach cannot commonly be used for all types of zeolites, only some types of zeolites can be successfully prepared. For example, the desilication method is suitable for zeolites having the moderate Si/Al ratio (Si/Al=25-50 for ZSM-5)[25]. Only low mesoporosity are obtained when the zeolites having the initially low Si/Al are used, whereas the zeolite structure can be destroyed when the frameworks having the initially high Si/Al are performed. Moreover, the pore size is difficult to be controlled by this route[17]. It has been reported that the mesopores obtained from such atom extraction do not always link to each other in order to form a connected network[26]. Thus, this nontemplating approach is obviously inefficient in reaching the improvement of transport limitation of zeolites.

As for the templating approach, the hierarchical zeolites can be obtained via both direct- and indirect template methods[17]. In the direct template methods, zeolite crystals grow around the template (mesopore template) and the hierarchical zeolites are observed

after the removable of such template. Generally, two types of template, namely, soft and hard template can be used. Polymers[27,28], surfactants[29], and resorcinol-formaldehyde aerogel[30] are categorized as soft templates while polymer beads[31] and carbon materials[12,32] are considered as hard templates. Mesoporous shape and size of the prepared zeolites is reflected from the shape and size of the template (mesopore-directing template), so that the selection of template is the key factors of this method. It has been reported that the hard templates have high confinement ability derived from their rigid structure compared to the soft templates[33]. In the case of indirect templating methods, hierarchical zeolites is transformed from (amorphous) mesostructured materials or obtained from zeolitization of diatomaceous earth or incorporation of zeolite nanocrystals into an existing mesostructured phase[34]. This templating approach can be considered as a bottom-up approach. Because the hierarchical zeolites with high purity are often obtained by the direct templating method so this method is attractive for synthesis of hierarchical zeolites.

Among hard templates utilized in the preparation of hierarchical dual micro- and mesoporous zeolites, carbon materials − including carbon black particles[14], multiwall carbon nanotubes[32] and carbon nanofibers[35] − have attracted a great interest due to their high removal ability during calcination of zeolite. In addition, they can be obtained via a simple and cheap ways. Carbon materials can be used for synthesis not only mesoporous zeolites but also nanocrystal zeolite depending on the synthetic condition. The confined space of porous carbons[20] or the inter-voids of carbon blacks[14] can be used for the generations of the nanosized crystals of zeolites. In order to obtain the crystallization of a zeolite only in the pores or voids of carbon materials, the amount of zeolite precursor should be equal to or less than the pore or void volume of the carbon template. In contrast, mesoporous zeolites are obtained by encapsulation of carbon materials into the zeolite crystals during synthesis; thus, it is required the high amount of zeolite precursor in order to grow around the carbon template. After removal of the embedded carbon template, porous zeolites are obtained[12]. Moreover, it is possible that the combined system of mesoporous zeolites and nanocrystal zeolite is obtained by using carbon material as templates[17].

Recently, Kustova and coworkers[36] have successfully prepared a hierarchical zeolite using a silica-carbon composites. The composites are obtained from decomposition of sucrose impregnated in a form of solution to silica gel[36]. The obtained

carbon deposits and silica gel act as mesopore-directing agent and silica source for the zeolite synthesis, respectively. Thus, it can be considered that such silica-carbon composites act as bifunctional materials for the zeolite synthesis. The hierarchical zeolite is obtained after zeolite crystallization and combustion of the carbon residues. This method is simple and inexpensive, however, it yields zeolite product with a low mesoporosity. This might be due to a poor dispersion of the sugar solution during impregnation process. In order to extend the idea for preparing hierarchical zeolites with such simple and inexpensive method, it is required to find a solution to obtain carbon materials with good dispersion in silica gels.

In this part of thesis work, we proposed an alternative way using low-cost and abundant carbonaceous gas as carbon source for *in-situ* generation of mesopore-directing agent. The silica-carbon composites (C/SiO_2) were obtained by its pyrolysis over silica gel under an inert atmosphere. Molecules of the gas used are rather small thus they are able to diffuse through voids of silica gel and silica gel bed. Due to such good diffusion, one can expect that this strategy will provide the silica-carbon composites with good carbon dispersion. To the best of our knowledge, this synthesis strategy has not previously been employed for preparation of hierarchical zeolites. We found that this straightforward method leads the formation of a hierarchical zeolite with a high mesoporosity. In addition, we also investigated the role of experimental parameters, which are very important to the zeolite synthesis in controlling crystallinity and mesoporosity of zeolite. These parameters are type and amount of carbonaceous gas used for silica-carbon composite preparation, Si/Al ratio and concentration of zeolite precursors. We found that these parameters play important role on morphology and property of the obtained zeolites.

In order to compare the catalytic efficiency of the hierarchical zeolite and the conventional one, the catalytic performances of the synthesized hierarchical zeolite were explored in three different important petrochemical reactions, including the skeletal isomerization of *1*-butene, cracking of *n*-hexane and *3*-methylpentane, and hydrocracking of hexadecane.

The skeletal isomerization of linear butenes is a key process in the petroleum refining to produce isobutene, an important intermediate that can be used for synthesis of many useful chemicals including gasoline additives, *e.g.*, methyl *tert*-butyl ether (MTBE) and ethyl *tert*-butyl ether (ETBE), polyisobutylene (PIB) and methacrylate[37-39]. Thus, it is

one of the most interesting topics from both academic and industrial points of view. Many medium pore zeolites including FER[40-42], ZSM-23[43], ZSM-22[44] and ZSM-5[45] exhibit potential in catalyzing this reaction. Mechanism of this reaction on these zeolites is varied depending on the type of zeolite. In FER system, the reaction occurs via a monomolecular pathway due to their small pore size, leading to a high selectivity of isobutene product[46,47]. For ZSM-5 system, because of their medium pore size the isomerization takes place on acidic sites via a bimolecular mechanism in which the reaction mechanism involves many elementary steps including (i) oligomerization (ii) isomerization and (iii) cracking[48]. By this mechanism, large intermediates and products may be included in the reaction. For example, at beginning of reaction, C8 surface species may take place and decompose to C5 and C3 or isomers of C4. Then, some C3 molecules that still adsorb onto the active sites may dimerize to hexenes or further oligomerize to C12 species and then crack to pentenes, hexenes and heptenes[45]. For this reason, ZSM-5 catalyst is easily to be deactivated. In this study, we investigated the catalytic behavior of our synthesized hierarchical ZSM-5 on the isomerization of *1*-butene. Although ZSM-5 typically yields lower selectivity for isobutene production than that of FER zeolite at a comparable acidity, ZSM-5 shows better stability than FER[49,50]. We demonstrate here that the hierarchical ZSM-5 has better catalytic performance for the reactions than that of the conventional ZSM-5. The hierarchical ZSM-5 zeolite improves the diffusion limitation problems of large molecular weight products and solves the catalyst deactivation occurred by pore blocking.

Generally, catalytic cracking is a main reaction performed in petroleum refining industry. Long-chain hydrocarbons are broken down into smaller molecules as existed in the production of gasoline fuel and liquefied petroleum gas (LPG) from crude oil distillation fraction[51]. In this thesis, the catalytic performance of catalytic cracking of *n*-hexane and *3*-methylpentane over synthesized hierarchical ZSM-5 as catalysts were also explored. The cracking reactions of *n*-hexane revealed that there is no limit in the diffusion during the cracking of *n*-hexane for both conventional and hierarchical ZSM-5 catalysts, since *n*-hexane molecule is rather small compared to pore opening and cavities of ZSM-5, while the presence of mesopores in zeolite structure plays important role on the catalytic performance of the catalyst for cracking of larger molecule.

Finally, we show that the presence of mesopores in zeolite structure does not only influence on catalysis of proton-type zeolite but also on catalysis of hybrid materials

containing zeolite such as metal-zeolite bifunctional catalysts. Bifunctional catalysts containing both Brønsted acid and Lewis acid sites, which are derived from proton-exchanged zeolite and metallic sites, respectively. This kind of catalyst exhibits high potential in many chemical reactions, especially “hydrocracking”. In such process, large hydrocarbon molecules can be broken down into smaller molecules under a high hydrogen pressure atmosphere. Thus, it can be used to treat oil residues and yield the middle distillation fractions products such as diesel and gasoline. As the demand for diesel and gasoline increases every year, the hydrocracking is one of the most important reactions performed in petroleum refining industry[52]. Due to high hydrogen pressure atmosphere condition, other reactions such as hydrosulfurization, hydrodemetallization and hydroisomerization may simultaneously take place. The hydroisomerization is the most important competitive reaction of hydrocracking. The mechanism of hydrocracking composes of many elementary steps including isomerization, cracking, hydrogenation and dehydrogenation. Isomerization and cracking processes preferentially occur on acid sites or Brønsted site via carbocation chemistry, whereas hydrogenation and dehydrogenation reactions require Lewis acid sites. Therefore, bifuntional catalysts containing both Brønsted acid and Lewis acid sites are necessary for the hydrocracking of alkanes. The dispersion of Brønsted acid and Lewis acid sites in bifunctional catalysts is a key factor on catalytic activity and selectivity for this reaction. It should be noted that a rapid molecular transfer of intermediates from the hydrogenation site (metallic site) to the Brønsted acid site is required in order to avoid other undesirable reactions. This aspect could be achieved by using hierarchical zeolites as starting materials for creating hierarchical metal-zeolite bifunctional catalyst. Here we show an improved catalytic performance for *n*-hexadecane hydrocracking by using the hierarchical Pt/HZSM-5 catalyst compared to the conventional one. This is due to an enhanced accessibility of molecules into the active site and dispersion of metal inside the micro/mesoporous zeolite network.

The aims of this chapter are summarized below:

Synthesis of a hierarchical micro- and mesoporous zeolite

- To develop a new, simple and practical synthesis methods of a hierarchical micro- and mesoporous zeolite based on *in-situ* generation of mesopore-structure template by a pyrolysis of the carbonaceous gases
- To study the effects of important parameters of crystallization processes on zeolite crystal morphology and mesoporous formation such as concentrations of precursors, the amount and nature of mesopore-directing agent and Si/Al ratio
- To improve the dispersion of metal nanoparticles on hierarchical micro- and mesoporous bifunctional zeolite by introducing the metal nanoparticles onto proton-exchanged zeolite in order to use these catalysts for reaction studies that require the existence of bifunctional catalytic sites such as hydrocracking

The catalytic study of a hierarchical micro- and mesoporous zeolite

- To study the catalytic performances of the synthesized hierarchical micro- and mesoporous zeolite for interesting hydrocarbon transformation reactions (such as isomerization, cracking and hydrocracking)
- To compare the catalytic efficiency of a hierarchical micro- and mesoporous zeolite and a conventional microporous zeolite

2. EXPERIMENTS

2.1 Catalyst preparations

2.1.1 Synthesis of hierarchical micro- and mesoporous Na-ZSM-5 by use of the C/SiO_2 composites obtained by hydrocarbon gas decomposition

2.1.1.1 Preparation of bifunctional carbonized silica (C/SiO_2 composites) by hydrocarbon gas decomposition on silica

The carbon-silica (C/SiO_2) composites, which were used as bifunctional materials acting as silicon source and mesopore template for the hierarchical micro/mesoporous zeolite synthesis, was prepared by the pyrolysis of carbonaceous gas (acetylene or propane, C_xH_y) over silica gel surfaces. In the zeolite synthesis solution, this carbon material was functioned as a secondary structure-directing template (mesopore template) in which zeolite crystals were grown around its surfaces. After calcination in air, the carbon was oxidized to create pores and cavities inside zeolite crystals.

A brief description of the preparation method is as follows: An amount of silica gel, typically 5.0 g, (Merck, silica gel 100, particle size 0.063-0.200 mm and pore volume 1.0 ml/g) was introduced into the middle zone of a fixed-bed tubular reactor (diameter of tube = 1.9 cm). The setup diagram of this experiment is shown in Figure 2. Nitrogen gas (N_2) was flown into the reactor with a flow rate of 180 or 190 ml/min depending on the desired concentration of the reactant gas. Nitrogen gas easily displaced air and therefore it formed an inert atmosphere in the chamber. The reactor temperature was gradually increased under the flow of nitrogen gas from room temperature to 1123 K and held at that temperature for 15 minutes. Then a flow of either acetylene (C_2H_2, 99.9%, Praxair - Rayong, Thailand) or propane (C_3H_8, 99.5%, BOC Scientific - Chachoengsao, Thailand) diluted in N_2 gas (N_2, 99.999%, Praxair, Thailand) was passed through the reactor. The gas mixture concentration was 5 or 10 v/v% of acetylene or propane in N_2 with a total flow rate of 200 ml/min. After that for 60 to 120 minutes, the C_xH_y flow was stopped. The work tube is cooled down to room temperature under the nitrogen flow. The obtained C/SiO_2 composites were used as bifunctional materials for the zeolite syntheses. The silica part of the composites was used as a silica source of the zeolites. The carbon residue formed in the composites was used as a mesopore template. The amount of deposited carbon over silica gel was determined by Thermal Gravimetric Analysis (TGA).

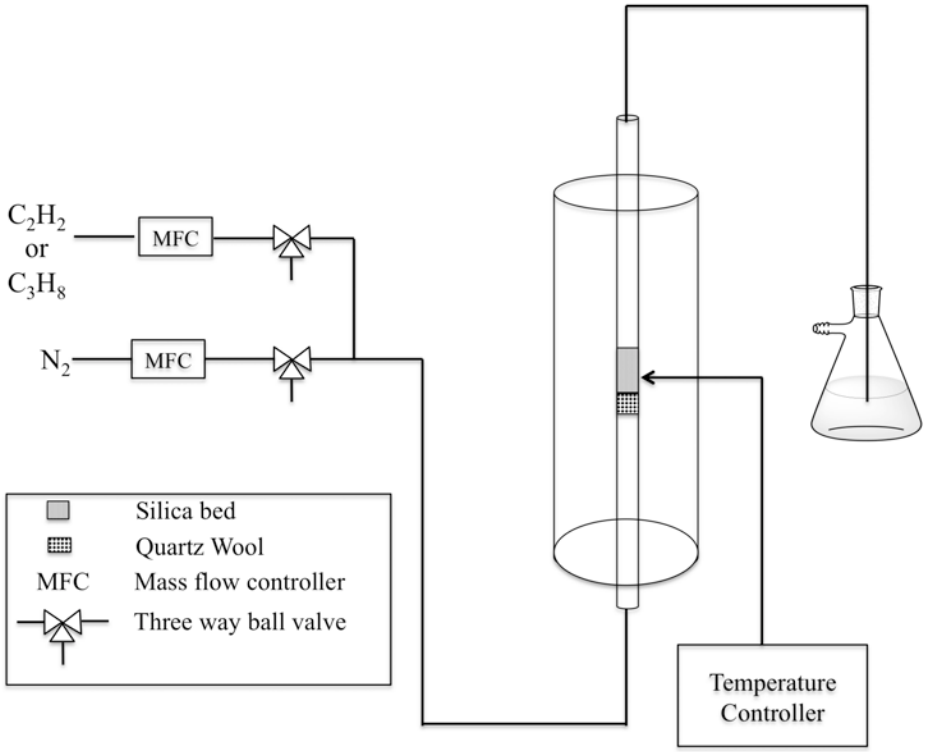

Figure 2. The setup diagram of a fixed-bed tubular reactor for preparation of bifunctional carbonized silica (C/SiO_2 composite).

2.1.1.2 Preparation of the hierarchical micro- and mesoporous Na-ZSM-5 by hydrothermal synthesis

The C/SiO_2 composites were used for the preparation of the hierarchical micro- and mesoporous Na-ZSM-5 zeolite in which the silica part was used as silica precursor for zeolite formation while a carbon residue was acted as mesopore template. The aluminium was added into the zeolitic framework by using $NaAlO_2$ (Riedel de Haën - Seelze, Germany) and the TPAOH (20 wt%, Fluka - Buchs, Switzerland) was used as a structure-directing agent for the ZSM-5 micropores. The molar composition of the synthetic gel was $1Al_2O_3 : 181SiO_2 : 36TPA_2O : 15Na_2O : 1029H_2O$. Typically, the aluminate solution is prepared by mixing 0.016 g of $NaAlO_2$ and 0.11 g of NaOH in 1.7 mL of deionised (DI) water. Then, the aluminate solution was added into 6.77 g of 20wt% of TPAOH in water under stirring condition. The mixture was stirred continuously until a clear solution was obtained. Then, the resulting C/SiO_2 composite (keep 1 g of SiO_2) was added into the mixture and stirred for 1 hour. The obtained

mixture was then transferred into a Teflon-lined stainless-steel autoclave for crystallization process at 453 K for 72 hours. After that, the autoclave was cooled down to room temperature and the resulting material was collected by filtration (using Whatman, No. 42 filter paper) and then the resulting material was rinsed with DI water until the pH of the filtrate was about 8. The obtained product was then dried at 383 K for 10 hours. Finally, the organic template and the carbon residues were removed by calcination in air at 823 K for 20 hours.

2.1.2 Preparation of the hierarchical micro- and mesoporous HZSM-5

In order to study the catalytic activity of the hierarchical micro- and mesoporous ZSM-5, the proton-exchanged zeolite were required and were generated from the initial Na^+ type zeolite obtained from previous step. Then the acidic form of zeolite can be utilized as catalysts in the catalytic studies of the isomerization and catalytic cracking reactions.

The Na^+ type ZSM-5 zeolites (Na-ZSM-5) were transformed to acidic ZSM-5 zeolite (HZSM-5) by ion-exchange with ammonium nitrate solution. Normally, 1 g of zeolite was placed into the cap-bottle in order to perform three consecutive ion-exchanges with 0.1 M ammonium nitrate (NH_4NO_3, 99.99+%, Aldrich) solution at 353 K for 2 hours. Then, the exchanged zeolites were rinsed by copious amounts of deionised water to remove excess solution, and let the cleaned zeolite samples dried overnight at 383 K. Finally, the resulting samples were calcined in air at 823 K for 6 hours in order to transform NH_4^+-ZSM-5 to HZSM-5. Prior to use all catalyst for reaction study, the HZSM-5 powder was crushed and seized to select the particle size in the range of 0.025 to 0.042 cm.

2.1.3 Preparation of the hierarchical micro/mesoporous bifunctional catalyst (the hierarchical micro/mesoporous Pt/HZSM-5)

In many catalytic reactions, especially hydrocracking, the bifunctional catalysts composing of metal sites and acid sites are necessarily used in the catalytic processes. Therefore, we also prepared bifunctional Pt/HZSM-5 by wet impregnation of the proton-exchanged zeolites with aqueous solution of tetraammine platinum (II) nitrate ($Pt(NH_3)_4(NO_3)_2$, 99.995%, Sigma-Aldrich, USA).

Typically, the 1 wt% of Pt loaded on HZSM-5 was prepared by adding the aqueous solution of ($Pt(NH_3)_4(NO_3)_2$) into 1 g of HZSM-5. The mixture was stirred for 24 hours at room temperature. Then the aqueous solvent was removed by freeze drying process. The resulting samples (Pt/HZSM-5) are calcined at 823 K for 6 hours. Prior to using of the Pt/HZSM-5 catalyst, the particle size in the range of 0.025 to 0.042 cm of the obtained sample powder was selected by crushing and seizing processes.

In order to get the metallic platinum inside Pt/HZSM-5, the sample was reduced in hydrogen atmosphere. The bifunctional catalyst was prepared according to the following steps. Basically, 0.3 g of prepared Pt/H-ZSM-5 was introduced into the middle zone of a fixed-bed tubular reactor (inner diameter of tube = 0.4 cm). Nitrogen gas (N_2) was flown into the reactor with a flow rate of 10 ml/min. The reactor temperature was gradually increased to 473 K under the nitrogen flow and held at this temperature for 15 minutes. Then, 5 % v/v of H_2 in N_2 is introduced though a catalyst at constant temperature of 473 K for 2 hours. Afterward, the work tube was cooled down to room temperature under the nitrogen flow. Finally, the obtained samples were ready to use as bifunctional catalysts for hydrocracking test.

2.2 To study the important parameters for the hierarchical micro/mesoporous Na-ZSM-5 synthesis

The important parameters for the formation of the hierarchical micro/mesoporous zeolite were systematically investigated. Types and amounts of carbon residue in carbonized silica (C/SiO_2 composites), Si/Al ratio, the concentration of synthesis solution and crystallization temperature were sensitive factors for the formation of the crystalline phase and zeolite morphologies. For examples, high temperature and long crystallization time were favorable to the growth of large crystal formation. Furthermore, the amount of mesopore template is also expected to influence on the crystallization process. In this work, the effects among these synthesis parameters on the formation of the hierarchical micro/mesoporous ZSM-5 were examined.

The molar ratio of ZSM-5 synthesis solution was represented as $a Al_2O_3 : b SiO_2 : 36\ TPA_2O : 15\ Na_2O : c H_2O$, where the ratio of b to a was varied in the range of 15-90 to investigate the effect of aluminium content on the hierarchical micro/mesoporous ZSM-5 formation and the value of c was varied in the range of 500 to 3500 to observe the effect

of the concentration of synthesis solution on zeolite morphologies. In addition, the type and amount of the mesopore template was varied by control the molar ratio of C/Si in the C/SiO_2 composites in the range of 0 to 3 in order to investigate the effect of the hard template on their morphology and mesoporosity.

2.3 Characterisations

During the preparation processes of zeolite, different characterisation techniques are involved. Thermal Gravimetric Analysis (TGA) is performed on PERKIN ELMER, TGA7 model in order to investigate the carbon contents in the C/SiO_2 composites. The structures of the synthesized zeolites were confirmed by an X-Ray Diffraction (XRD) measurement performed on a Rigaku TTRAX III, 18kW diffractometer using Cu K_α radiation. The measurement was operated at an accelerating voltage of 30 kV and a current of 40 mA. The diffraction patterns were collected at 2θ angles ranging from 5° to 50° with a scan speed and step size of 1.2 °/min and 0.02°, respectively. The Scherrer's equation was applied to calculate crystal sizes by using the most intense diffraction peaks at 8° (2θ), corresponding to 011 reflection plane[53,54]. The morphologies, crystal sizes and porous structures of the zeolite samples were investigated by scanning electron microscopy (SEM, JEOL-JSM 6301F) and transmission electron microscopy (TEM, JEOL JEM-2010 and JEM-2100). The textural properties (the specific surface area and porosity) of the prepared materials were determined using a N_2 adsorption/desorption measurements performed at 77 K on a Micromeritics ASAP 2010 instrument.

For the characterisation, the zeolite samples were degassed at 623 K in a vacuum for 20 hours before N_2 sorption measurements. The specific surface areas (S_{BET}) of the samples were calculated by the Brunauer–Emmett–Teller (BET) method (see Appendix A). The total pore volume (V_{tot}) was estimated by measuring the amount of adsorbed nitrogen at 0.97 P/P_0. The *t*-plot method was used to calculate the micropore volume (V_{micro}) (see Appendix A). The volumes of mesopore and macropore ($V_{meso+macro}$) were calculated from the difference between V_{tot} and V_{micro}[55]. The size distribution of the mesopores was obtained by applying a Barret–Jovner–Halenda (BJH) model[56] (see Appendix A).

As for the chemical analysis, Inductively Coupled Plasma Atomic Emission Spectrometer (ICP-AES), performing on Perkin Elmer (model PLASSMA 4000) was

used to investigate the Si/Al ratio in the zeolite framework. The 50 mg of prepared zeolite was digested by 1000 μL of HNO_3 and 500 μL of HF. Then, the solution was sonicated in an ultrasonic bath for 15 min. The solution was made up by DI water to make the solution with the total weight of 100g for ICP-AES measurement.

To indicate the nature of Al species in the zeolite framework, the solid state ^{27}Al magic-angle spinning (MAS) NMR spectroscopy (^{27}Al MAS NMR) technique was used. The signals were recorded at 78.20 MHz, using a Bruker Biospin (DPX-300, 300 MHz) spectrometer with a 2 μs pulse, 4 s delay time and 800 scans.

2.4 Catalytic activity studies

2.4.1 The catalytic study of the isomerization of *1*-butenes

The skeletal isomerization of linear butenes has been widely used to produce isobutene. The *n*-butene isomerization on zeolites has been paid attention in academic studies due to its behavior involving many reactions. For example, *n*-butene isomerization over ZSM-5 zeolite takes place via a bimolecular pathway, composing of (i) oligomerization (ii) isomerization and (iii) cracking. Therefore, the hierarchical micro/mesoporous ZSM-5 zeolite is expected to improve the catalytic performances of this reaction compared to conventional microporous zeolite.

Basically, the isomerization of *n*-butenes was carried out in a fixed-bed reactor at atmospheric pressure. The experimental setup is shown in Appendix B. The 2 v/v% of *1*-butene in Ar (C_4H_8, 2% in Ar, Praxair, Thailand) was used as reactant. The catalyst was packed into quartz tube (inner diameter of 4 mm). The packing of catalyst was divided into three zones. The bottom zone was packed by 0.025 g of quartz wool, the middle zone was occupied by the desirable amount of the proton-exchanged zeolite sample, and quartz chips covered the top zone. In the beginning step, the zeolite sample was pretreated by nitrogen gas with the total flow rate of 40 cm^3/min at 823 K for 1 hour. After that, the reactor was cooled down to the desirable reaction temperature and the 2 v/v% of *1*-butene in Ar was fed to the reactor with various flow rates. The products were analyzed by an online Agilent 6890N gas chromatography at different times on steam (TOS) equipped with a Flame Ionization Detector (FID) and a capillary column (GS-GasPro, 60 m × 0.32 mm ID). The condition of analysis by gas chromatography (GC) technique and exampled chromatogram are demonstrated in Appendix C.

2.4.2 The catalytic study of *n*-hexane cracking reaction and the competitive cracking reaction of *n*-hexane and *3*-methylpentane

In order to investigate the catalytic activity of cracking of small molecule (such as *n*-hexane), the experiments were carried out in a fixed-bed reactor. The 5 cm^3/min of N_2 was bubbled though *n*-hexane (*n*-C6) solution at 288 K. The *n*-hexane vapor in N_2 was then diluted with 20 cm^3/min of N_2 to make the reactant feed in the total flow rate of 25 cm^3/min. The reactant feed was introduced into 0.05 g of zeolite sample, which was diluted by 0.1 g of quartz chips (particle size of 0.025 to 0.042 cm) in order to enlarge a catalyst bed. The equipment setup is shown in Appendix D. The products were analyzed by an online Agilent 6890N gas chromatograph equipped with a Flame Ionization Detector (FID) and capillary column (GS-GasPro, 60 m × 0.32 mm ID). The exampled chromatogram is demonstrated in Appendix E.

The competitive reaction of *n*-hexane and *3*-methylpentane cracking can be used to investigate the constraint index, which relates to the pore size of zeolites. Typically, the catalytic cracking of *n*-hexane and *3*-methylpentane mixtures under the competitive reaction was carried out in a fixed-bed reactor. Before the reaction study, the 0.05 g of HZSM-5, diluted with 0.1 g of quartz chips (particle size of 0.025 to 0.042 cm), was *in-situ* activated in N_2 atmosphere with the total flow rate of 40 cm^3/min at 823 K for 1 hour. After that, the reactor was cooled down to the desirable reaction temperature under the flow of nitrogen gas. The 5 cm^3/min of N_2 was bubbled though mixtures of *n*-hexane (C_6H_{14}, Sigma-Aldrich, USA) and 3-methylpentane (C_6H_{14}, 99%, Sigma-Aldrich, USA) at 288 K in order to carry the reactant vapor (see Appendix F for the calculation of the desired concentration of reactant feed). At vapor-liquid equilibrium pressure, the reactant stream composes of 50 mol% of *3*-methylpentane and 50 mol% of *n*-hexane in N_2, which was used as carrier. To verify the concentration of feed, the mixture of *n*-hexane and 3-methylpentane in N_2 was checked by gas chromatography (GC) two times before switching into the reactor. Then, this feed was passed to the reactor at a given reaction temperature by diluent with 20 cm^3/min of N_2. The equipment setup is shown in Appendix D. The products were analyzed by an online Agilent 6890N gas chromatograph equipped with a Flame Ionization Detector (FID) and capillary column (GS-GasPro, 60 m × 0.32 mm ID) at the reaction time of 15 minutes.

2.4.3 The catalytic study of catalytic cracking and hydrocracking of *n*-hexadecane

The catalytic cracking and hydrocracking of *n*-hexadecane reactions on both the hierarchical micro/mesoporous ZSM-5 and the conventional one are studied because they involve large molecular weight molecules as reactant and this reaction is a useful process in a dewaxing procedure. In this study, both HZSM-5 (Brønsted acid catalyst) and Pt/HZSM-5 (bifunctional zeolite) were used as catalysts for catalytic cracking and hydrocracking, respectively. Because this reaction were studied in the slurry-phase in which the diffusion rate would be slow, the improving catalytic behavior of the hierarchical micro/mesoporous zeolite due to the shorten diffusion path length should be clearly observed compared with when the conventional microporous zeolite was used as catalyst.

As for the catalytic procedure, the catalytic cracking and hydrocracking of *n*-hexadecane were carried out in a stirred Parr batch autoclave in the slurry-phase. In the case of hydrocracking process, the Pt/HZSM-5 (1 wt% Pt) or bifuctional zeolite samples were use as the catalysts. Typically, a 0.3 g of catalyst and 10 ml of *n*-hexadecane ($C_{16}H_{34}$, 99%, Sigma-Aldrich, USA) were added to the batch autoclave. The vessel was pressurized to 10 bars with hydrogen gas. In the case of catalytic cracking of *n*-hexadecane, the HZSM-5 or proton-exchanged zeolite samples were used and the vessel was not pressurized with hydrogen. After that, the reactor was gradually heated to 553 K for 6 hours with continuous stirring. The reactor was then cooled down to room temperature. The catalysts were removed from reaction mixture by syringe filter and the products are analyzed by Agilent 7820A Gas Chromatograph (GC) equipped with a Flame Ionization Detector (FID) and a capillary column (DB-1, 100 m × 0.25 mm ID × 0.50 μm film thickness). The exampled chromatogram is demonstrated in Appendix G.

3. RESULTS AND DISCUSSIONS

3.1 Synthesis of the hierarchical micro/mesoporous Na-ZSM-5

In this study, the hierarchical ZSM-5 samples with dual meso- and microporosity were prepared by use of the C/SiO_2 composition obtained from a pyrolysis of carbonaceous gases in the presence of silica gel. The synthesis strategy is to create carbon template supported on a silica raw material that can be generally used as mesopore templates for synthesis any zeolites. The obtained zeolite crystals encapsulate the carbon particles. After calcinations to remove the organic template and the entrapped carbon particles, the micropores and mesoporous cavities inside zeolite crystals are created. The preparation process is illustrated in Scheme 1. Recently, Kustova and coworkers [36] used a carbohydrate (sugar) as a precursor for carbon template as mesopore-directing agent. Although, sugar solution can be conveniently impregnated into silica gel and carbonized at high temperature under inert atmosphere, the mesoporosity gain from sugar-derived carbon template is moderate (in a range of 0.04-0.1 cm^3/g). The reason of this behavior might be due to a poor dispersion of the sugar solution during the impregnation process. In order to organize carbon in finely dispersed form on silica surfaces, the use of hydrocarbon gases, as a precursor might simply be a direct answer. In this work, we demonstrate that by using *in-situ* carbon template generated from a pyrolysis of carbonaceous gases. The carbonized silica (C/SiO_2) composites play an important role as bifuntional materials in which the part of silica is used as silica source for zeolite formation and the part of carbon residue is performed as mesopore templates. As a result, the hierarchical micro/mesoporous ZSM-5 can be prepared.

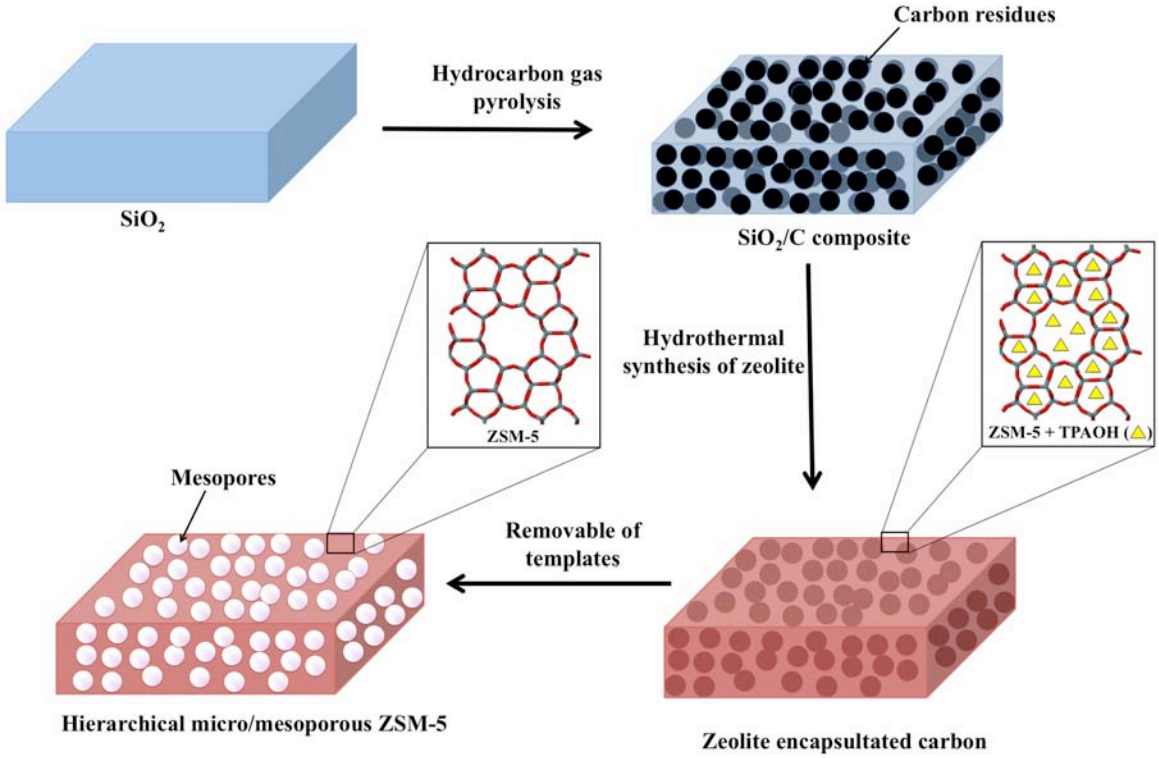

Scheme 1. Illustration of the preparation process of the hierarchical micro/mesoporous Na-ZSM-5.

3.1.1 Preparation of bifunctional carbon-silica composites (C/SiO_2)

Table 1 shows the carbon content in the C/SiO_2 composites (wt%) was measured by thermal gravimetric analysis (TGA). The amount of carbon deposits was found to vary with type and amount of the carbonaceous gases. The carbon content in the composites increases with increasing of the concentration of carbonaceous gases and the deposition time at the same flow rate. For example, by using 5 v/v% of C_2H_2, the carbon content in the composite is increased from 10 to 18 wt% by increasing the deposition time of 60 to 120 min. By using the deposition time of 120 min, the carbon content in the composite is increased from 18 to 29 wt% by increasing concentration of C_2H_2 in the gas mixture used for carbon deposition from 5 to 10 v/v%, respectively. Therefore, it can be suggested that the amount of deposited carbon can be simply controlled by varying the deposition time and the concentration of hydrocarbon gases.

Although C_2H_2 and C_3H_8 give the same trend in the amount of carbon residue, in which the carbon content is increased with increasing of the deposition time and the concentration of hydrocarbon gases, C_2H_2 yields a higher amount of carbon residue than

C_3H_8 under the same experimental conditions. For example, by using 10 v/v% of hydrocarbon gases and deposition time of 120 minutes, the carbon deposits in the cases of C_2H_2 and C_3H_8 are 29 and 22 wt%, respectively. Although C_3H_8 has a higher molar ratio of carbon atoms than C_2H_2, its thermal stability during the pyrolysis process is higher than that of C_2H_2 (ΔG_f° of propane and acetylene are 45.72 and 40.62 kcal/mol at 1,000 K, respectively[57,58]). Thus, at the temperature used for the preparation of the C/SiO_2 composites, the C_3H_8 could decompose with a less amount compared to C_2H_2, thus, yielding a less amount of the carbon residue in the C/SiO_2 composites.

Table 1. Carbon content in the C/SiO_2 composites (wt%) prepared by various experimental conditions.

Sample name	Conditions			Carbon content (wt%)
	Types of C_xH_y	Conc. of C_xH_y (v/v%)	Deposition time (minutes)	
SiO_2	-	-	-	-
5% C_2H_2-60 min-C/SiO_2	C_2H_2	5	60	10
5% C_2H_2-120 min-C/SiO_2	C_2H_2	5	120	18
10% C_2H_2-120 min-C/SiO_2	C_2H_2	10	120	29
5% C_3H_8-120 min-C/SiO_2	C_3H_8	5	120	11
10% C_3H_8-120 min-C/SiO_2	C_3H_8	10	120	22

The XRD pattern of the raw silica gel and a typical XRD pattern of the C/SiO_2 composites are shown in Figure 3. The XRD pattern of the raw silica gel shows a broad spectrum in the 2θ range of 20-30° indicating that silica gel is amorphous in nature. In the typical XRD pattern of the C/SiO_2 composite, no crystalline peak was also observed. Only, a broad spectrum in the 2θ range of about 20-30° was observed. This finding indicates that the carbon residue deposited on silica gel is amorphous.

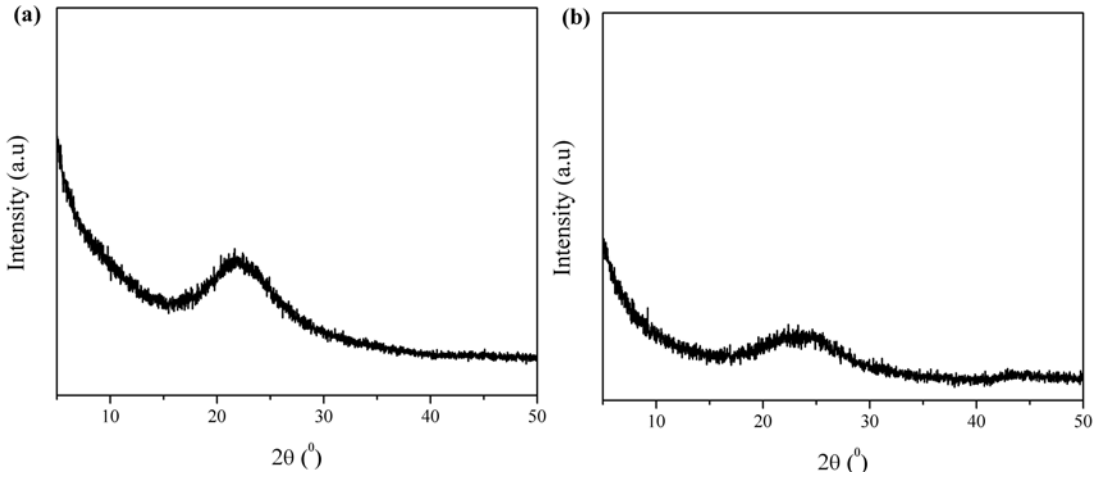

Figure 3. XRD pattern of (a) silica gel (SiO_2) and (b) carbonized silica (C/SiO_2) composite obtained by the carbon deposition of 10 v/v% C_2H_2 with deposition time of 120 minutes on silica gel.

Figure 4 shows the N_2 adsorption/desorption isotherms of the raw silica gel and the C/SiO_2 composites. The isotherms correspond to the type IV (described in IUPAC classification) [59]. This character is explained by the formation of monolayer followed by multi-layer corresponding to complete filling of the capillaries. It also exhibits the hysteresis loop, the lower branch representing the addition of gas into the adsorbent (adsorption branch) and the upper branch by progressive withdrawing (desorption branch). This character shows that the materials compose of mesoporous cavities, which are in the range of 2-50 nm (IUPAC definition). Table 2 shows the textural properties of the raw silica gel and the C/SiO_2 composites including mesopore volume (V_{meso}) and mesopore diameter (D_{BJH}) calculated by the difference of V_{tot} and V_{micro} (V_{tot}-V_{micro}) and BJH method, respectively. In part of this work, it was found that the micropore volume was almost zero for all samples. Therefore, the V_{meso} could be estimated directly from the total pore volume. It can be observed that when the deposition time or the concentration of hydrocarbon gases is increased resulting in an increase of the amount of carbon residue, the V_{meso} and D_{BJH} of the C/SiO_2 composites decrease in case that C_2H_2 is used. The V_{meso} of the C/SiO_2 composites decreases from 0.78 to 0.67 and 0.51 while the mesopore size (D_{BJH}) decreases from 9 to 8 and 7 with increasing of carbon contents in the C/SiO_2 composites from 10 to 18, and 29 wt%, respectively (see Table 2). This result indicates an increase of the carbon deposition in the mesopores of silica gel with increasing of carbon contents in the C/SiO_2 composites. In addition to the carbon

deposition in the mesopores of silica gel, we also suggest the carbon deposition on the outermost surface of silica gel particles. This suggestion is confirmed by an appearance of the black color of the C/SiO_2 composites and the SEM images of the C/SiO_2 composites. A typical SEM image of the C/SiO_2 composites is shown in Figure 5. The image shows silica gel particles, fully covered by carbon particles, obtained from the deposition of hydrocarbon gas.

Nevertheless, in case of C_3H_8, there is no significant change of V_{meso} and D_{BJH} of the C/SiO_2 composites when the deposition time and concentration are varied even though the amount of carbon residue alters. This finding indicates no carbon deposition in the mesopores of silica gel. Thus, the carbon deposition occurs preferentially on the outer surface of silica gel.

Table 2 Textural properties of the raw silica gel and the C/SiO_2 composites prepared by various experimental conditions.

C/SiO_2 composite	V_{meso}[a] (cm^3/g)	D_{BJH}[b] (nm)
SiO_2	1.00	11
5% C2H2-60 min-SiO_2/C	0.78	9
5% C_2H_2-120 min-SiO_2/C	0.67	8
10% C_2H_2-120 min-SiO_2/C	0.51	7
5% C_3H_8-120 min-SiO_2/C	0.83	11
10% C_3H_8-120 min-SiO_2/C	0.85	11

[a]V_{meso}: Mesopore volume calculated by V_{tot}-V_{micro}, The total pore volume, V_{tot}, was calculated at P/P_0 of 0.97, [b]D_{BJH}: Mesopore diameter calculated from the adsorption branch of nitrogen isotherms using BJH method.

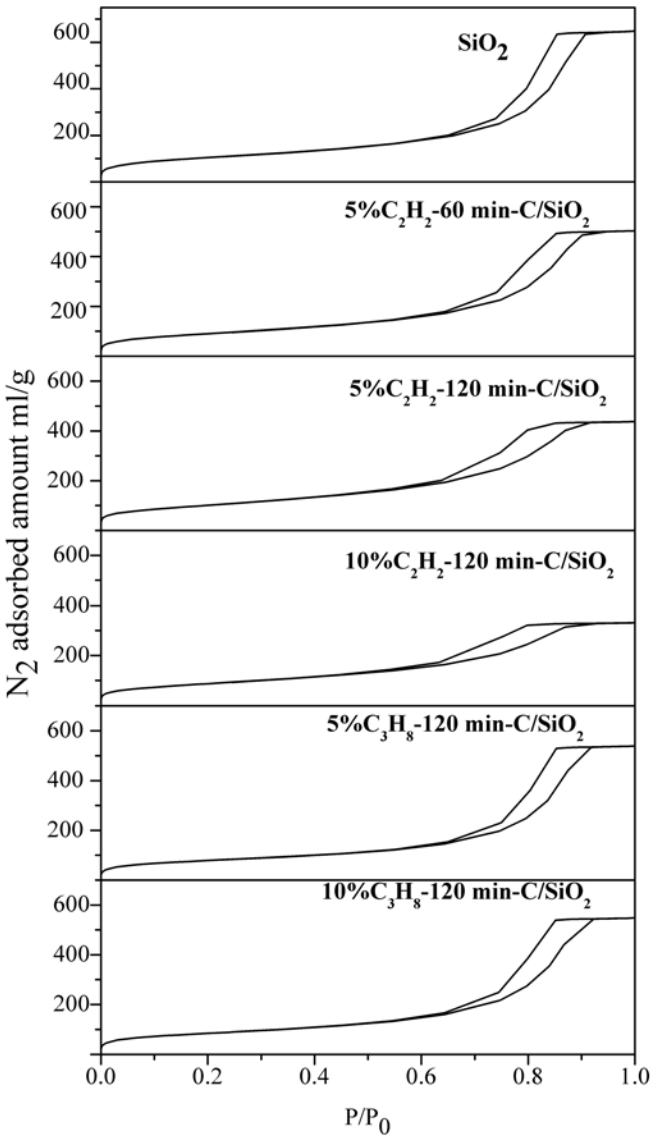

Figure 4. N_2 adsorption/desorption isotherms of the raw silica gel and the C/SiO_2 composites obtained by different carbon contents.

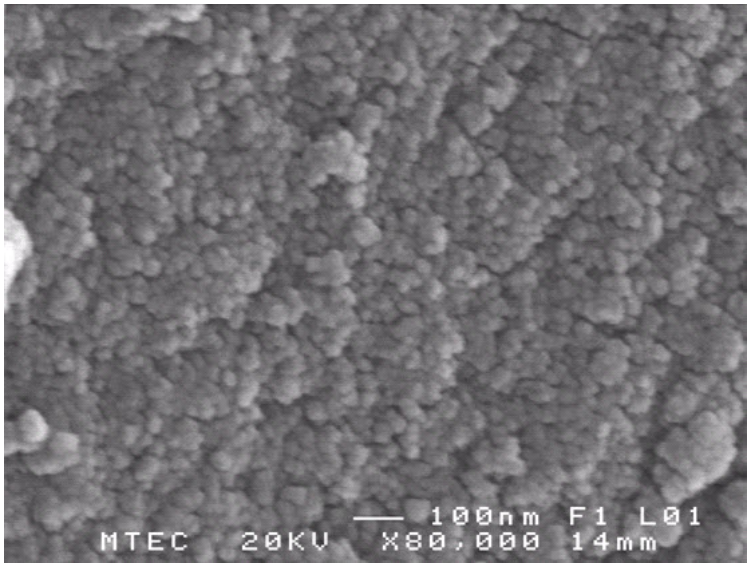

Figure 5. Typical SEM image of the C/SiO_2 composites. The image is of the sample obtained from the deposition of 10 v/v% C_2H_2 for 120 min.

3.1.2 Hierarchical micro- and mesoporous zeolite prepared from C/SiO_2 composites

3.1.2.1 Powder X-ray diffraction (XRD)

The X-ray diffraction (XRD) patterns of the raw silica gel, a reference zeolite (conventional microporous ZSM-5 or ALSI-PENTA Zeolithe GmbH (APZ)), and the hierarchical micro/mesoporous ZSM-5 samples are shown in Figure 6. A broad spectrum of the raw silica gel indicates that the silica source possesses an amorphous structure. However, after the crystallization of synthesis solution, the amorphous silica gel is transformed to a material with a crystalline phase. The XRD patterns of the hierarchical micro/mesoporous ZSM-5 samples are comparable to that of the reference ZSM-5 which shows high intensive peaks at 2θ of 7.94, 8.80, 23.10 and 23.98° reflecting to the crystalline planes of (011), (020), (051) and (033), respectively. The analyzed crystal structure corresponds to the characteristic of the MFI structure[60]. Furthermore, it was found that the diffraction peaks of the synthesized samples are sharp. The XRD pattern contains a very low background signal. The finding indicates that the samples were synthesized with high crystallinity.

The crystalline size of nanoparticles can be estimated from XRD peaks by applying Scherrer's equation, the average crystalline size can be calculated from the full-width at the half-maximum (fwhm) of the most intense diffraction peak by using the following equation.

$$D = \frac{K\lambda}{B_{1/2}\cos\theta}$$

Where D is the crystalline size, K is a numerical factor frequently referred to as the crystallite-shape factor (normally, this value is approximated as 0.9), λ is the wavelength of the X-rays, $B_{1/2}$ is the full-width at half-maximum of the XRD peak in radians, and θ is the Bragg angle.

Table 3. The average crystal size of the hierarchical micro/mesoporous ZSM-5 and conventional ZSM-5 according to Scherrer's equation.

Sample name	$B_{1/2}$[a] (°)	D_p[b] (nm)
5% C_2H_2-60 min-ZSM-5	0.50	17
10% C_2H_2-120 min-ZSM-5	0.63	13
5% C_3H_8-120 min-ZSM-5	0.50	17
10% C_3H_8-120 min-ZSM-5	0.50	17
Conventional ZSM-5	0.16	52

[a]$B_{1/2}$ is the full-width at half-maximum (fwhm) of the X-ray diffraction peak in radians and θ is the Bragg angle. [b]Dp is the crystalline size obtained from XRD pattern according to Scherrer's equation using a common peak at approximately 2θ=8°.

The calculated crystalline sizes are shown in Table 3. The average crystal sizes are approximately estimated in the range of 13-52 nm. It shows that the crystalline size of the hierarchical micro/mesoporous ZSM-5 obtained by use of the C/SiO_2 composites is significantly lower than that of conventional microporous ZSM-5. However, the difference in crystalline sizes of samples obtained by various carbon contents is not pronounced. It should also be noted that the crystal size differs from the particle size because the particles may be assembly of several crystals. Therefore, in order to investigate the actual particle size it is investigated by using electron microscopy technique.

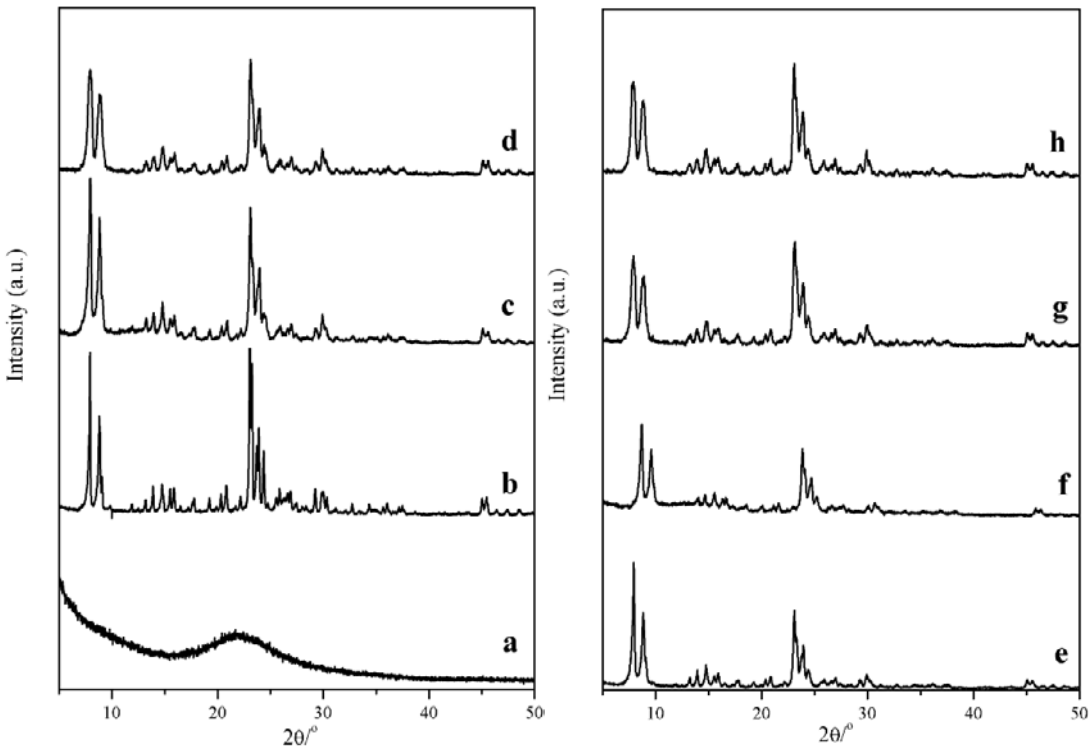

Figure 6. XRD patterns of (a) raw silica gel, (b) the reference zeolite sample (conventional ZSM-5, ALSI-PENTA Zeolithe GmbH (APZ)), (c) 0% carbon-ZSM-5, (d) 5% C_2H_2-60 min-ZSM-5, (e) 5% C_2H_2-120 min-ZSM-5, (f) 10% C_2H_2-120 min-ZSM-5, (g) 5% C_3H_8-120 min-ZSM-5, and (h) 10% C_3H_8-120 min-ZSM-5.

3.1.2.2 Scanning electron microscopy (SEM) and transmission electron microscopy (TEM)

The morphology and porous structure of the hierarchical micro/mesoporous ZSM-5 and the commercial ZSM-5 were observed by scanning electron microscopy (SEM) and transmission electron microscopy (TEM). The images are shown in Figures 7 and 8. The large crystal size of above 4 μm was observed for the conventional microporous zeolite (see Figure 7a). The crystal sizes of the hierarchical micro/mesoporous ZSM-5 samples are varied depending on the carbon contents in the C/SiO_2 composites used in the zeolite synthesis. In case of the sample obtained by use of SiO_2 without carbon residues (0% carbon-ZSM-5), the crystal morphology is in form of the well-faceted cubic crystals with the size distributed in the range of 150-400 nm (see Figure 7b). Because under the synthesis conditions, the concentration of the structure-directing agent (SDA) or tetrapropylammonium bromide (TPAOH) is high, thus it can be

suggested that a large amount of nuclei could be formed leading to the formation of small crystals. In case of the samples prepared by use of the C/SiO_2 composites with low carbon contents (e.g. 10 wt% and 11 wt% that C_2H_2 and C_3H_8 were used as carbon sources, respectively), the crystalline shape is nearly cubic crystal with the size of about 200-500 nm (see Figures 7c and 8a). For the hierarchical micro/mesoporous ZSM-5 samples that were prepared by use of the C/SiO_2 composites with high carbon contents such as 5% C_2H_2-120 min-ZSM-5, 10% C_2H_2-120 min-ZSM-5 and 10% C_3H_8-120 min-ZSM-5 which contain 18, 29 and 22 wt% of carbon, respectively, the large zeolite particles in the range of 500-900 nm were obtained as an aggregation of nanocrystals (see Figures 7d, 7e and 8b). The size of each nanocrystal was less than 50 nm. In order to prove the interaction among the nanocrystals, the TEM images were taken after a sonication of the synthesized samples. It was found that the aggregated structure was preserved, thus, these aggregates were considered as fully bound-nanocrystal aggregates. The formation of small nanocrystals obtained by use of the C/SiO_2 composites with high carbon contents could be explained by two reasons: the hindered crystal growth [14] and the promoted nuclei formation [61]. The first explanation is that the presence of high carbon content leads to hindering crystal growth and inhibiting the further nanocrystal growth, resulting in the formation of small crystal. In the second reason, the presence of high amount of carbon particles in synthesis solution results in giving a relatively high nuclei formation due to reducing of surface free energy of nuclei development; thus, the rate of nucleation respected to the growth rate is high, causing that the formation of small zeolite crystals is preferable [61].

The mesoporous structure was investigated by TEM. The bright area in TEM image of the zeolites is indicative of the porosity [62,63]. The mesoporous structure was not observed for the commercial ZSM-5 (see figure 8a). The mesoporosity was also not obtained for the zeolitic sample prepared by use of SiO_2 precursor without adding the carbon rasidues (see Figure 7b). However, the mesoporous structure was clearly observed for the samples obtained by use of the C/SiO_2 composites (see the bright spots inside particles in Figures 8c-e and Figure 9). Furthermore, it was observed that the amount of the bright spots in the TEM images corresponded well with the amount of carbon content in the C/SiO_2 composites, used for the zeolite synthesis. This result implies that an increase of the carbon content in the composites results in increasing of the mesopores in

the zeolite crystals. Therefore, the amount of mesoporous cavities can be simply controlled by variation of the carbon content in the C/SiO_2 composites.

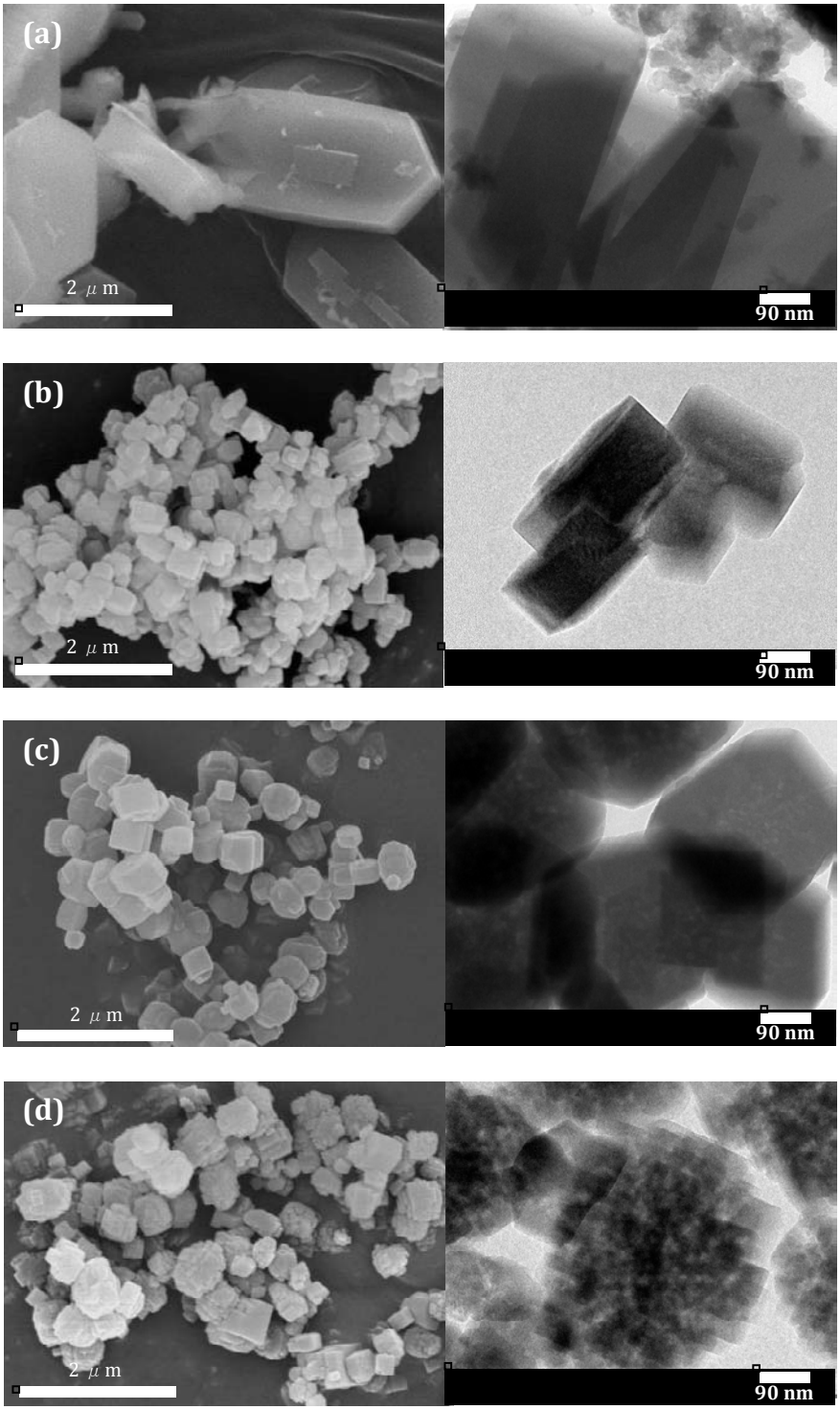

Figure 7. SEM (left hand side) and TEM (right hand side) images of (a) conventional microporous ZSM-5 (ALSI-PENTA Zeolithe GmbH (APZ)), (b) 0% carbon-ZSM-5, (c) 5% C_2H_2-60 min-ZSM-5 and (d) 5% C_2H_2-120 min-ZSM-5.

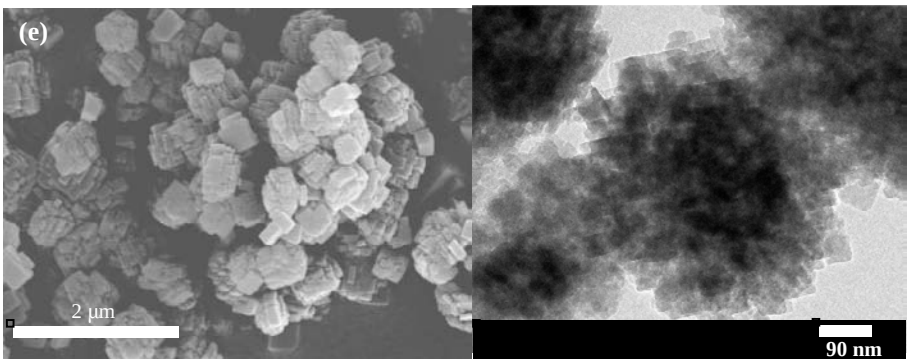

Figure 7 (Continued). SEM (left hand side) and TEM (right hand side) images of (e) 10%C_2H_2-120 min-ZSM-5.

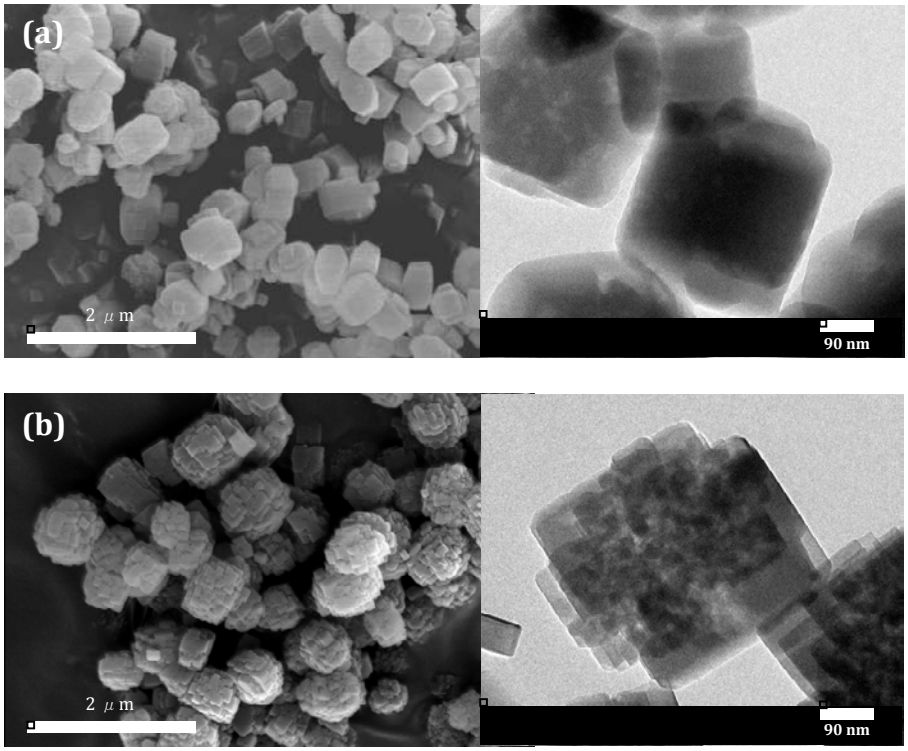

Figure 8. SEM (left hand side) and TEM (right hand side) images of (a) 5% C_3H_8-120 min-ZSM-5 and (b) 10% C_3H_8-120 min-ZSM-5.

3.1.2.3 Surface area and porosity characteristics

The N_2 adsorption/desorption isotherms of the samples are shown in Figure 9. For the isotherms of the conventional microporous ZSM-5, the adsorption at low relative pressure increases rapidly, and then, it is constant. The character of this sorption process is a type I isotherm with a long horizontal plateau [64] corresponding to the monolayer adsorption of the nitrogen molecules derived from small pore width of the micropores

preventing the multilayer adsorption. It can be concluded that the conventional microporous ZSM-5 is a pure microporous material. Furthermore, the micropore filling is also observed for all samples including the hierarchical micro/mesoporous ZSM-5 samples obtained by use of the C/SiO_2 composites indicating that all synthesized samples compose of the microporous feature, which is a key character for zeolites. Interestingly, the adsorption of nitrogen on the zeolites prepared by use of SiO_2 in the absence of carbon particles (0% carbon-ZSM-5 sample) increases precipitously at a high relative pressure ($P/P_0 > 0.9$) indicating the presence of large space voids or macropores as inter-voids generated among the small zeolite crystals (see Figure 7b). It is suggested that the small crystals are formed in this case because the synthesis is carried out under the condition with a high concentration of the SDA in which the nucleation process is facilitated. The N_2 adsorption/desorption isotherms of the prepared samples obtained by use of the C/SiO_2 composites (5% C_2H_2-60 min-ZSM-5, 5% C_2H_2-120 min-ZSM-5, 10% C_2H_2-120 min-ZSM-5, 5% C_3H_8-120 min-ZSM-5, and 10% C_3H_8-120 min-ZSM-5 samples) significantly differ from those of the sample prepared by use of SiO_2 in the absence of carbon residues (0% carbon-ZSM-5 sample) and the conventional microporous ZSM-5 sample. An increase of the nitrogen adsorption at the relative pressure in the range of 0.4-0.9 and the presence of hysteresis loop at the relative pressure in this range were clearly observed. These characters are derived from a capillary condensation in the mesopore voids of mesoporous materials [65]. The finding directly confirms that the synthesized zeolite samples obtained by use of the C/SiO_2 composites shows the mesoporous feature, particularly in cases of 10% C_2H_2-120 min-ZSM-5 and 10% C_3H_8-120 min-ZSM-5 where a large hysteresis loop exists in the isotherms. Additionally, a higher adsorption/desorption capacity and a larger hysteresis loop were observed with an increase of the carbon content in the C/SiO_2 composites used for the synthesis. Nevertheless, a significant hysteresis loop at high pressure ($P/P_0 > 0.9$) was not observed in the hierarchical micro/mesoporous ZSM-5 samples prepared by use of the C/SiO_2 composites indicating an absence of the macroporous cavities derived from the inter-void spaces. It is suggested that this is because the assembled zeolite particles in these cases are larger than those in the sample prepared by use of SiO_2 in the absence of carbon residues. As stated above, the microporous feature evidenced by the N_2 adsorption/desorption isotherms was also appeared in the case of the hierarchical micro/mesoporous ZSM-5 samples, thus, the zeolite samples synthesized by introducing the carbon particles composed of both mesoporous and microporous features.

The distribution of pores having size in the range of mesopores in the samples investigated by BJH method is shown in Figure 10. The distribution was calculated from the adsorption branch of the isotherm. The distribution of the samples synthesized by use of the C/SiO_2 composites including 5% C_2H_2-60 min-ZSM-5, 5% C_2H_2-120 min-ZSM-5, 10% C_2H_2-120 min-ZSM-5, 5% C_3H_8-120 min-ZSM-5 and 10% C_3H_8-120 min-ZSM-5 is significantly more broad compared to that of the zeolite sample obtained by use of SiO_2 in the absence of carbon particles (0% carbon-ZSM-5 sample) and the conventional microporous ZSM-5. The distribution of the samples prepared by use of the C/SiO_2 composites was various depending on the carbon content in the C/SiO_2 composites used in the synthesis. The 5% C_2H_2-60 min-ZSM-5 and 5% C_3H_8-120 min-ZSM-5 samples, which were prepared by use of the C/SiO_2 composite with a similar carbon content (≈10 wt%), exhibited a comparable distribution with the mesopore sizes in the range of 6-10 nm. Increase of the carbon content in the C/SiO_2 composites results in significant increasing of the amount of mesopores and broaden the size distribution of the mesopores. For examples, in case of 5% C_2H_2-120 min-ZSM-5, the mesopore sizes were in the ranges of 10-20 nm.

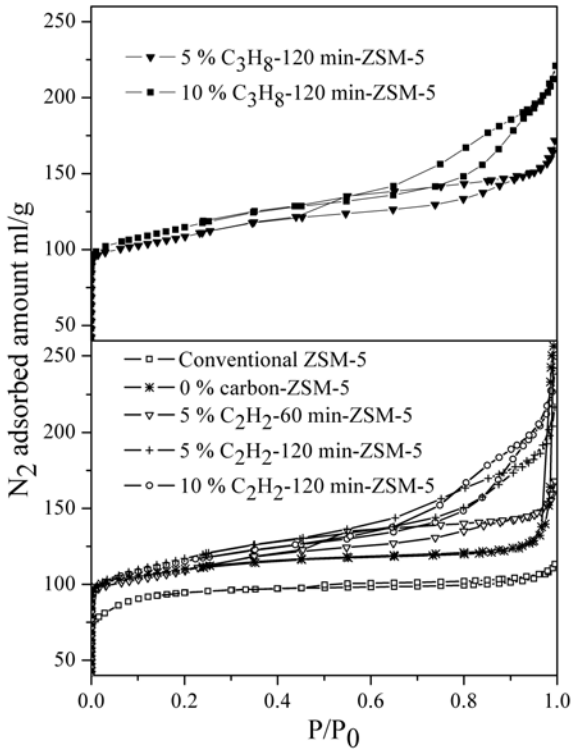

Figure 9. N_2 adsorption/desorption isotherms of the hierarchical micro/mesoporous ZSM-5 synthesized at various conditions and the conventional microporous ZSM-5.

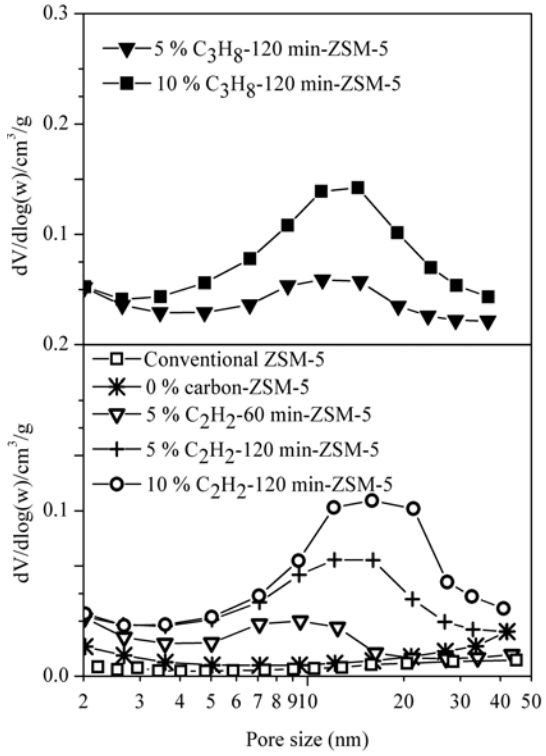

Figure 10. Size distribution of the mesopores of the synthesized zeolite samples calculated from the adsorption branch of the isotherm.

The specific surface area and porosity of the prepared zeolite samples are shown in Table 4. The micropores were formed by the presence of the tetrapropylammonium hydroxide (TPAOH) template, thus, the micropore volume should be depend on only the amount of TPAOH, not depend on the carbon content in the C/SiO_2 composite. As shown in Table 3, the micropore volume of the sample synthesized without carbon residues and the conventional microporous ZSM-5 is slightly higher than that of the samples obtained by use of the C/SiO_2 composites. The external surface areas of the 5% C_2H_2-60 min-ZSM-5, 5% C_2H_2-120 min-ZSM-5, 10% C_2H_2-120 min-ZSM-5, 5% C_3H_8-120 min-ZSM-5 and 10% C_3H_8-120 min-ZSM-5 samples are much higher than that of the conventional microporous ZSM-5, whereas the surface area of microporous cavities is slightly changed compared to the conventional one. Because the crystal size of the commercial ZSM-5 is very large (> 4 μm), the external surface is low. Furthermore, the ratio of the large pore volume (macropore and mesopore volume) to the small pore volume (micropore volume), $V_{meso+macro}/V_{micro}$, of the conventional microporous ZSM-5 is very low (0.14 cm^3/g) while the ratio of the synthesized samples is much higher. The $V_{meso+macro}/V_{micro}$ ratio of the synthesized sample obtained by use of the C/SiO_2 composites is higher than that of the conventional microporous ZSM-5 up to 14 times. An increase of the carbon content in the

C/SiO_2 composites results in a significant increase of the total pore volume. The mesopore volume is increased while the micropore volume is not significantly changed. It should be noted that the external surface area and the ratio of $V_{meso+macro}/V_{micro}$ of the sample prepared by use of SiO_2 without carbon residues (0% carbon-ZSM-5) are greater than those of the conventional zeolite. This is due to the presence of macroporous feature resulted from the interparticle void space. These observations indicate a successful introduction of the mesopores into the parts of microporous zeolite whereas the microporous feature is preserved. It is noteworthy that although the 0% carbon-ZSM-5 sample exhibits a larger external surface area compared to the conventional microporous ZSM-5, the preparation of this sample is not practical for the application in a large scale due to its small single particles requiring a high-speed centrifugation to separate them from the synthesis solution. Compared to the sample obtained by use of SiO_2 in the absence of carbon residues, the hierarchical micro/mesoporous ZMS-5 samples obtained by use of the C/SiO_2 composites not only increase the external surface area and mesopore volume up to 3 times but also improve the synthesis process in which the zeolite sample is easily collected after synthesis by a simple suction filtration. For these reasons, the synthesis method using the C/SiO_2 composites obtained from a pyrolysis of hydrocarbon gas is promising way for creating hierarchical micro/mesoporous zeolites.

Table 4. Surface area and porosity of the hierarchical micro/mesoporous ZSM-5 and the conventional ZSM-5 sample.

Sample	S_{BET}[a] (m^2/g)	S_{micro}[b] (m^2/g)	S_{ex} (m^2/g)	V_{tot}[c] (cm^3/g)	V_{micro}[d] (cm^3/g)	$V_{meso+macro}$[e] (cm^3/g)	$V_{meso+macro}/V_{micro}$ (cm^3/g)
0% carbon-ZSM-5	428	335	93	0.22	0.13	0.09[f]	0.69[f]
5% C_2H_2-60 min-ZSM-5	418	281	137	0.23	0.11	0.12	1.09
5% C_2H_2-120 min-ZSM-5	437	269	168	0.30	0.11	0.19	1.73
10% C_2H_2-120 min-ZSM-5	431	281	150	0.33	0.11	0.22	2.00
5% C_3H_8-120 min-ZSM-5	415	278	137	0.24	0.11	0.13	1.18
10% C_3H_8-120 min-ZSM-5	440	280	160	0.30	0.11	0.19	1.73
Conventional ZSM-5	343	321	22	0.16	0.14	0.02	0.14

[a]S_{BET}: obtained from the BET method (P/P_0=0.001-0.03). [b]S_{micro}: obtained from the *t*-plot method. [c]V_{tot}: calculated at P/P_0 of 0.97. [d]V_{micro}: calculated by the *t*-plot method. [e]$V_{meso+macro}$: calculated by V_{tot} - $V_{micro.}$ [f]the macropore volume resulted from the interparticle void space.

3.1.2.4 ^{27}Al MAS NMR

The environment around the aluminium atoms in the zeolite framework of the synthesized zeolite samples was investigated by ^{27}Al solid state MAS NMR. A typical spectrum is shown in Figure 11. The spectrum contains a strong peak at the chemical shift of about 55 ppm corresponding to the tetrahedrally coordinated aluminium atoms. Generally, the aluminium atoms with the octahedral coordination or the atoms in the external framework are observed at around 0 ppm. Such signal was not observed in this work. This result indicates that all aluminium atoms in the synthesized ZSM-5 were completely incorporated into the zeolite framework during the synthesis without the extra framework formation.

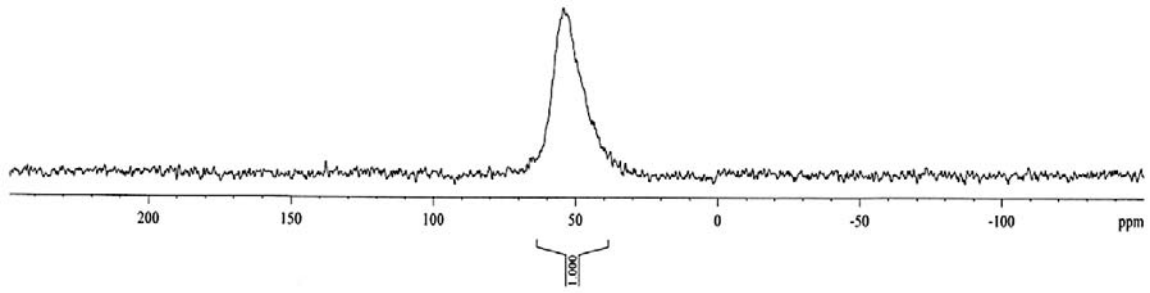

Figure 11. Typical ^{27}Al MAS NMR spectrum of the hierarchical micro/mesoporous ZSM-5. This spectrum is taken from 10% C_2H_2-120 min-ZSM-5 sample (29 wt% carbon, Si/Al = 83).

3.2. Effect of synthesis conditions on the morphologies and textural properties of the hierarchical micro/mesoporous ZSM-5

3.2.1 Effect of carbon content in the C/SiO_2 composites

The zeolite sample prepared with low carbon content shows the morphology of crystalline structure with nearly cubic shape (see Figure 7c). However, the morphology of the zeolite crystals changed to be assemblies of the small crystals when the C/SiO_2 composites with high carbon contents are used (see Figures 7d, 7e and 8b). This is because the presence of high carbon content leads to a hindered crystal growth of nanocrystals resulting in the formation assemblies of the small crystals. The external surface and mesoporosity of the samples shown in Table 4 are also altered with the

varying in the carbon content in the C/SiO_2 composites used for the zeolite synthesis whereas the microporosity of the samples is insignificantly changed for all samples. The micropore volume is in the range of 0.11-0.14 cm^3/g, while the total pore volume reflected from the mesopore and macropore volumes significantly increases with an increase of the carbon content in the C/SiO_2 composites. Therefore, the ratio of the mesopore and macropore volumes to the micropore volume ($V_{meso}+V_{macro}/V_{micro}$) is an important parameter that can be used to evaluate the porosity of the zeolite samples in study. It is noteworthy that the mesopore volume (V_{meso}) of the hierarchical micro/mesoporous ZSM-5 samples prepared by use of the C/SiO_2 composites is noticeable component respected to the macropore volume (V_{macro}) because of the hysteresis loop of the prepared zeolites giving in Type IV isotherms without the hysteresis loop at high relative pressure ($P/P_0 > 0.9$). Therefore, an increase of $V_{meso}+V_{macro}/V_{micro}$ should be derived from the improvement of the mesoporosity directly. The results show that this ratio dramatically increases when the carbon content in the C/SiO_2 composites increases. Furthermore, the mesoporosity of the synthesized samples prepared by use of the different C/SiO_2 composites shows the difference in BJH pore size distribution (see Figure 10). Both the mesoporous pore distribution and mesopore size increase with an increase of the carbon content in the C/SiO_2 composites. Therefore, it is very convenient to alter the mesoporosity by controlling the carbon content in the C/SiO_2 composites used in the synthesis. In other words, the mesoporosity and morphology of zeolites strongly depend on the amount of carbon template, which can be directly controlled by varying deposition time and concentration of hydrocarbon gases used in the pyrolysis.

3.2.2 Effect of aluminum contents

Because the catalytic performance of zeolites strongly depends on their acidity, thus, in order to investigate the role of the acidity, reflected from the Si/Al ratio, on the morphology and textural properties of the prepared zeolites, the hierarchical micro/mesoporous ZSM-5 with different Si/Al ratios were prepared by use of the C/SiO_2 composites that compose of 10 and 18 wt% carbon. The XRD patterns of the samples are shown in Figure 12. All XRD patterns of the hierarchical micro/mesoporous ZSM-5 samples are comparable to that of the reference ZSM-5, corresponding to the MFI structure characteristic. The SEM and TEM images showing morphology of the

hierarchical micro/mesoporous ZSM-5 samples synthesized with various Si/Al ratios are shown in Figures 13 and 14. The change in the Si/Al ratio leads to an alteration in the morphology of zeolite crystals and their crystal size. The crystal size of the sample with a high Si/Al ratio of 83 obtained by use of the C/SiO_2 composite with 10 wt% carbon was around 200-500 nm whereas the crystal size of the sample synthesized with a lower Si/Al ratio of 29 and 16 exhibits to be smaller (see Figure 13). Similarly, in case of the C/SiO_2 composite with 18 wt% carbon, the crystal size exhibits to be smaller when the Si/Al ratio is decreased (Figure 14). The reason could be explained based on the fact that in the case of high-silica zeolites the presence of aluminum in the synthesized precursors decreases the crystal growth rate. As shown in the literatures, the crystal growth rate ($K_g = dL/dt_c$, where K_g is the growth rate constant, L is the size of crystals at the certain crystallization time t_c) of the NH_4-ZSM-5 synthesized at 180°C from the mixture of precursors with a gel composition of $4(TPA)_2O/60(NH_4)_2O/xAl_2O_3/90SiO_2/750H_2O$ decreased with an increase of aluminum content [66,67]. The growth rate of the ZSM-5 crystals decreased in the presence of aluminum because the aluminum could interact with the hydroxyl (OH^-) group, thus, the ability that the OH^- group forming the active silicate species decreased. As a result, the crystal growth process decreased. The results obtained from this work thus agree well with that reported in the literatures.

In addition, the mesoporosity of all samples synthesized with different Si/Al ratios was clearly observed from TEM images. Table 5 shows the porosity of the synthesized samples. It was found that the amount of mesoporosity dramatically increases with an increase of the Al content corresponding to that very small zeolite particles were observed (see Figures 14b and 14c). Therefore, in this experiment, we demonstrate that the hierarchical micro/mesoporous zeolite samples, which exhibit high porosity compared to the conventional microporous zeolite, could be successfully prepared with various Si/Al ratios by use of the C/SiO_2 composites obtained by a pyrolysis of carbonaceous gas on silica gel.

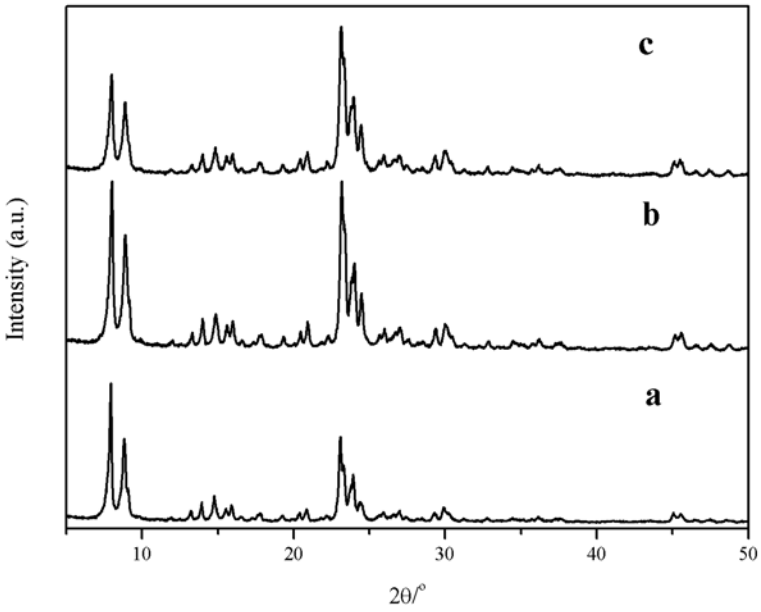

Figure 12. XRD patterns of the hierarchical micro/mesoporous ZSM-5 prepared by use of the C/SiO_2 composite with 18 wt% carbon content and with the Si/Al ratios of (a) 83, (b) 29 and (c) 16.

Table 5. Porosity of the hierarchical micro/mesoporous ZSM-5 (mZSM-5_X)*** samples synthesized by use of the C/SiO_2 composite with 18 wt% carbon content and with various Si/Al ratios and the conventional microporous ZSM-5.

Samples	Si/Al*	V_{tot} [a] (cm^3/g)	V_{micro} [b] (cm^3/g)	$V_{meso+macro}$ [c] (cm^3/g)	$V_{meso+macro}/V_{micro}$ (cm^3/g)
mZSM-5_83	83	0.30	0.11	0.19	1.73
mZSM-5_29	29	0.36	0.11	0.25	2.27
mZSM-5_16	16	0.52	0.12	0.40	3.33
Conventional ZSM-5	24**	0.16	0.14	0.02	0.14

[a]V_{tot}: at P/P_0 of 0.97. [b]V_{micro}: calculated by the *t*-plot method. [c]$V_{meso+macro}$: calculated by V_{tot} - $V_{micro.}$
*estimated by ICP-AES. **reported by producer. ***It should be noted that mZSM-5_X is denoted as the hierarchical mesoporous ZSM-5 obtained by use of the C/SiO_2 composite with 18 wt% carbon content and X refers to the Si/Al ratio, for example, mZSM-5_83 indicates the hierarchical mesoporous ZSM-5 with the Si/Al ratio of 83.

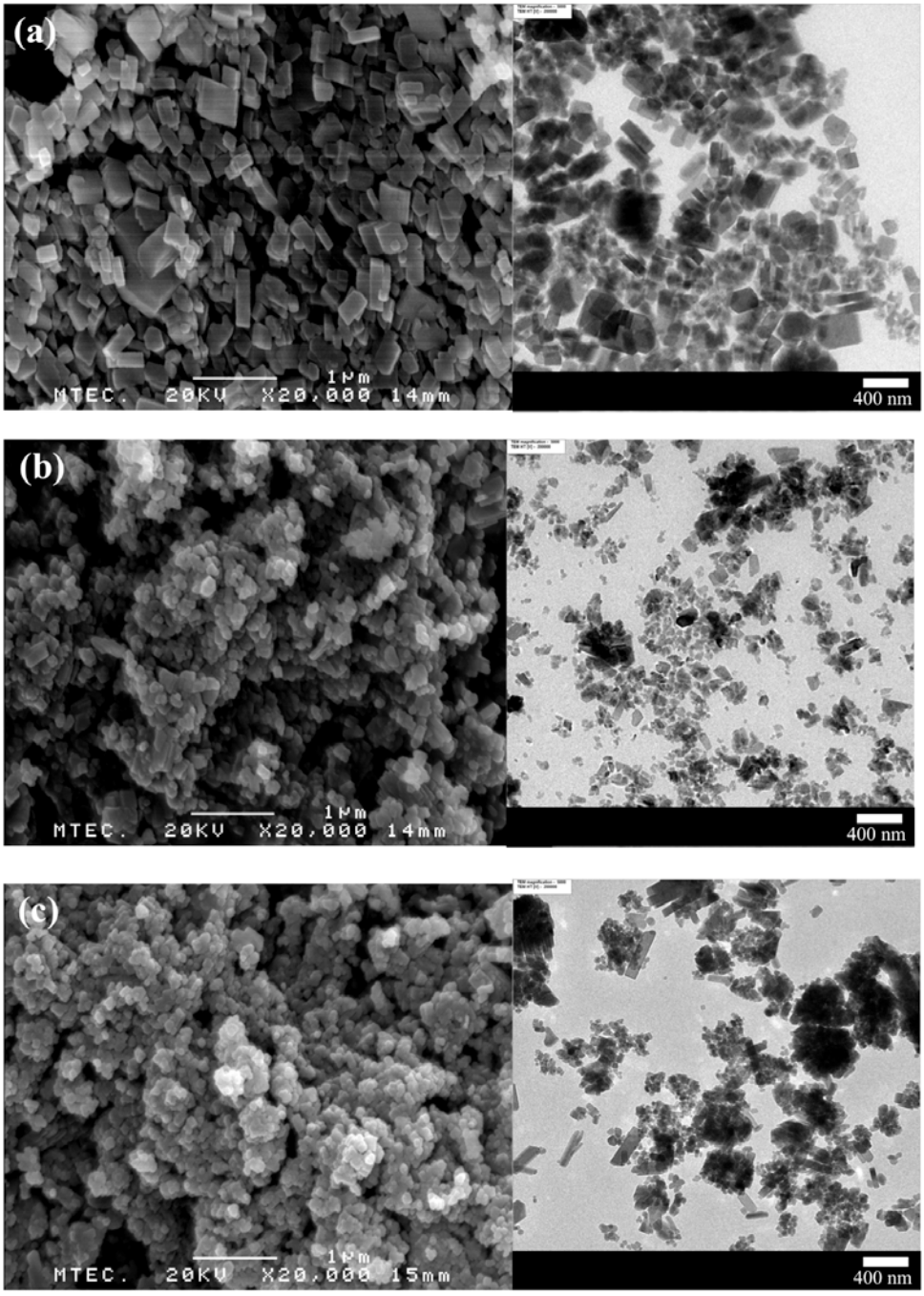

Figure 13. SEM and TEM images of the hierarchical micro/mesoporous ZSM-5 samples synthesized by use of the C/SiO_2 composite with 10 wt% carbon content and with the Si/Al ratios of (a) 83 (b) 29 and (c) 16.

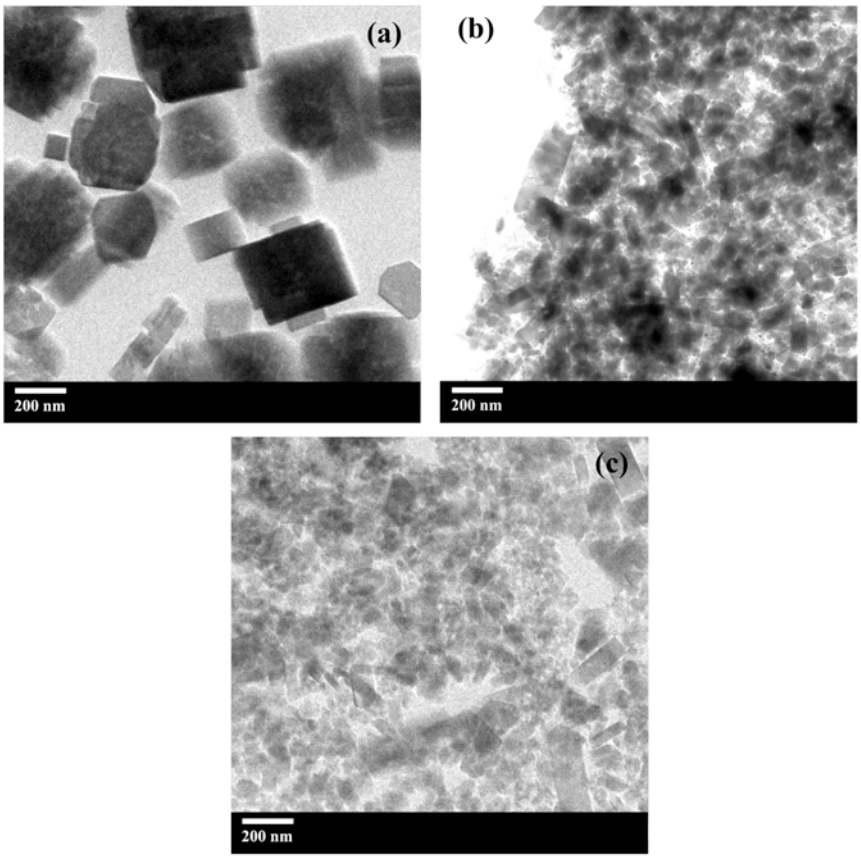

Figure 14. TEM images of the hierarchical micro/mesoporous ZSM-5 samples synthesized by use of the C/SiO_2 composite with 18 wt% carbon content and with the Si/Al ratios of (a) 83 (b) 29 and (c) 16.

3.2.3 Effect of concentration of zeolite precursors in the synthesis gel

The effect of concentration of the zeolite precursors in the synthesis gel with the composition of Al_2O_3 : $181SiO_2$: $36TPA_2O$: $15Na_2O$: yH_2O where Y was varied from 1029, 1816, 3026 and 4237 was investigated. The decrease of precursor concentration results in the reduction of nucleation rate. The SEM images (Figure 15) show the morphology of the zeolite crystals in the samples prepared with different precursor concentrations. The crystal size of the hierarchical micro/mesoporous ZSM-5 sample prepared at a low concentration was slightly larger than that of the sample prepared at a higher concentration. The crystal size of the sample obtained by using very high amount of water (y=4237) was about 1 μm whereas the crystal size of about 500 nm was found for the sample prepared by using the precursor gel with a lower water content (y=1029).

The specific surface area and porosity of zeolite samples prepared with different precursor concentrations are shown in Table 6. Although the decrease of precursor concentration results in a slight increase in the crystal size, the change of surface area and porosity with respect to an alteration of the crystal size is not obviously different in all samples synthesized with the varied water content in the synthesis gel.

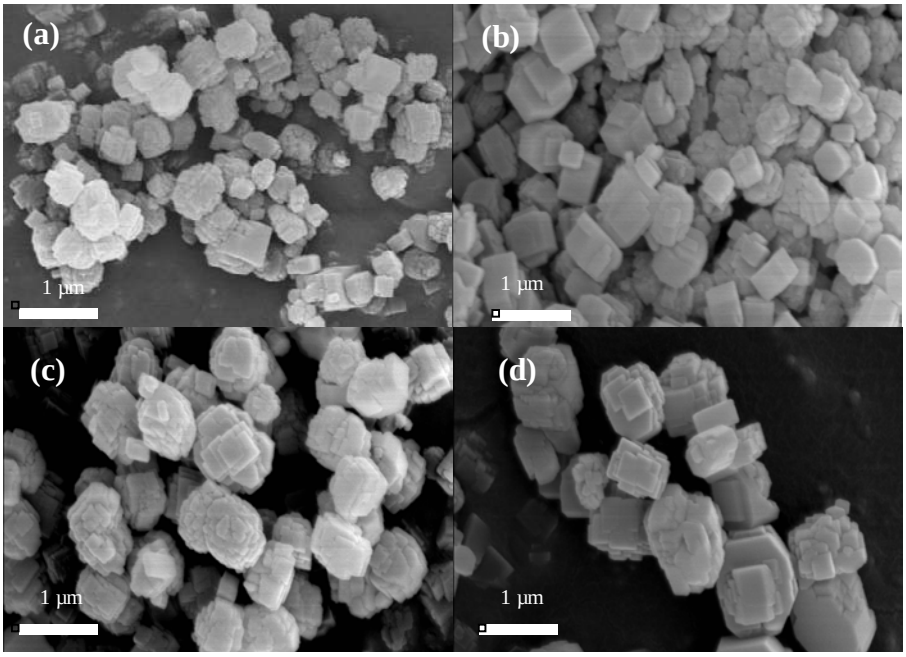

Figure 15. SEM images of the zeolite samples obtained by use of the C/SiO_2 composite with 18 wt% carbon content. The composition of the synthesis gel containing the zeolite precursors was Al_2O_3 : $181SiO_2$: $36TPA_2O$: $15Na_2O$: YH_2O where Y was (a) 1029, (b) 1816, (c) 3026 and (d) 4237.

Table 6. Surface area and porosity of the hierarchical micro- and mesoporous ZSM-5 samples (mZSM-5_Y)* synthesized by use of the C/SiO_2 composite with 18 wt% carbon content. The composition of the synthesis gel containing the zeolite precursors was Al_2O_3 : 181SiO_2 : 36TPA_2O : 15Na_2O : YH_2O where Y was 1029, 1816, 3026 and 4237.

Samples	Y	V_{tot}[a] (cm^3/g)	V_{micro}[b] (cm^3/g)	$V_{meso+macro}$[c] (cm^3/g)	$V_{meso+macro}/V_{micro}$ (cm^3/g)
mZSM-5_1029	1029	0.30	0.11	0.19	1.73
mZSM-5_1816	1816	0.29	0.11	0.18	1.64
mZSM-5_3026	3026	0.28	0.10	0.18	1.80
mZSM-5_4237	4237	0.29	0.11	0.18	1.64

[a]V_{tot}: at P/P_0 of 0.97. [b]V_{micro}: calculated by the *t*-plot method. [c]$V_{meso+macro}$: calculated by V_{tot} - V_{micro}.
***It should be noted that mZSM-5_Y is denoted for the hierarchical mesoporous ZSM-5 synthesized by use of the C/SiO_2 composite with 18 wt% carbon content and Y refers to the water content.

3.3 Preparation of the hierarchical micro/mesoporous bifunctional Pt/HZSM-5 catalyst (M/H-ZSM-5)

The bifuctional catalysts, composed of both the metallic sites and the Brønsted acid sites, are important for the hydrocracking process. Therefore, in this work, a bifunctional Pt/HZSM-5 catalyst was prepared by introducing the Pt nanoparticles into the hierarchical micro/mesoporous zeolite samples using wet impregnation of zeolite with a platinum salt solution, $Pt(NH_3)_4(NO_3)_2$. The dispersion of the Pt nanoparticles into both the hierarchical micro/mesoporous HZSM-5 zeolite and the conventional microporous HZSM-5 samples, synthesized with a similar Si/Al ratio, was observed by TEM images as shown in Figure 16. For the conventional Pt/HZSM-5 sample, most of the Pt nanoparticles located at the outer surface of zeolite crystals. The size of the nanoparticles was rather large. The size was about 25 nm. Compared to the particles in the case of the conventional Pt/HZSM-5, the Pt nanoparticles well dispersed over entire crystal of the hierarchical micro- and mesoporous zeolite. Interestingly, the size of the particles in the case of the hierarchical micro/mesoporous Pt/H-ZSM-5 samples, obtained by use of the C/SiO_2 composite with 18 wt% carbon content, was smaller (about 10 nm) compared with in the case of the conventional zeolite. This result confirms that the degree of metal dispersion can be enhanced by the introduction of mesoporous cavities into the zeolite

framework. Therefore, the catalytic performance of the prepared bifuctional catalyst prepared by using the mesoporous zeolite is expected to be greater compared to that of the catalyst prepared by using the conventional zeolite because of the better dispersion of the Pt particles. This behavior is expected because the dispersion of metal particles is one of the key factors prevailing the performance of the metal particles supported on zeolite catalysts [68].

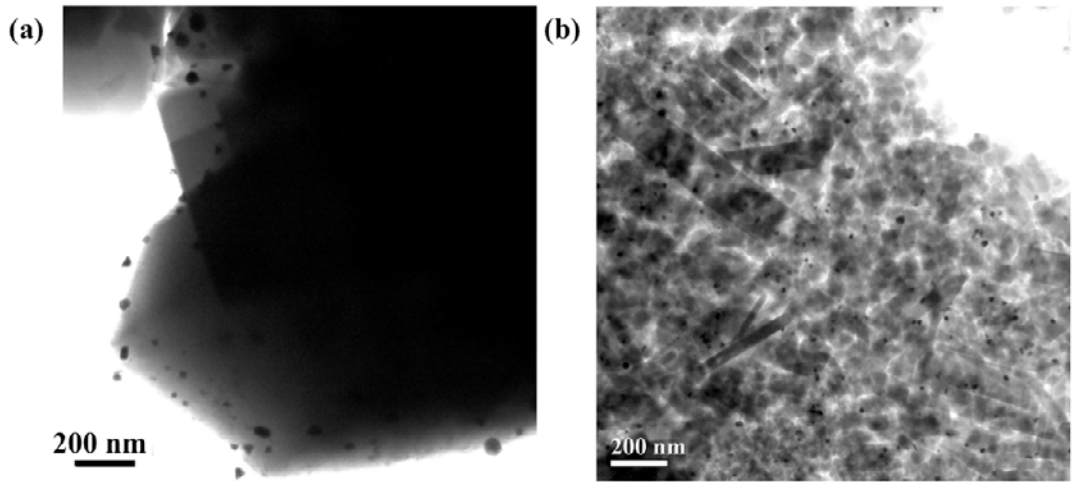

Figure 16. TEM images of (a) the conventional microporous Pt/HZSM-5 with the Si/Al ratio of 24 and (b) the hierarchical micro/mesoporous Pt/H-ZSM-5 prepared by use of the C/SiO_2 composite with 18 wt% carbon content and with the Si/Al ratio of 29.

3.4 Catalytic performances of the hierarchical micro/mesoporous zeolite

3.4.1 Catalytic study of the isomerization of *n*-butenes

The skeletal isomerization of *n*-butenes is a key process in the petroleum refining for production of isobutene. The medium pore zeolite is one kind of the most important catalysts used for this reaction. The medium pore zeolites which exhibit potential for this reaction are ferrierite (H-FER) [40-42], HZSM-23 [43], HZSM-22 [44] and HZSM-5 [45]. Among of them, H-FER has found to be a very selective catalyst for this reaction [47].

Although the selectivity of isobutene over the HZSM-5 catalyst is lower than that of the H-FER zeolite, the conversion obtained via this catalyst is higher. In addition, the stability of HZSM-5 catalyst is rather good [49,50]. There are many mechanisms proposed in

the literatures including the monomolecular, pseudomolecular and oligomerization-cracking mechanisms[45,69,70]. The oligomerization-cracking mechanism has been proposed as the dominant mechanism in zeolite such as HZSM-5 (see Scheme 2). The reaction mechanism on the HZSM-5 catalyst are composed of many elementary steps in which large intermediates and products are included due to the oligomerization[45]. By this mechanism, C8 surface species are obtained from the dimerization of butene at beginning of reaction. Then, they decompose to C5 and C3 or C4 isomers. After that, some C3 molecules that are occurred and adsorbed onto the active sites can immediately dimerize to C6 or further oligomerize to C12 species. Next, C12 species further crack to C5, C6 and C7[45]. This reaction mechanism could be remarkably facilitated by use of the hierarchical micro/mesoporous ZSM-5. This is because such catalyst can provide a larger accessibility into the active sites compared to the microporous zeolite. Therefore, *n*-butene isomerization reaction involving bulky molecules such as branched-chain products occurred in the oligomerization-cracking step was selected to study in order to gain a better understanding into the catalytic performance of the synthesized hierarchical micro/mesoporous HZSM-5 samples.

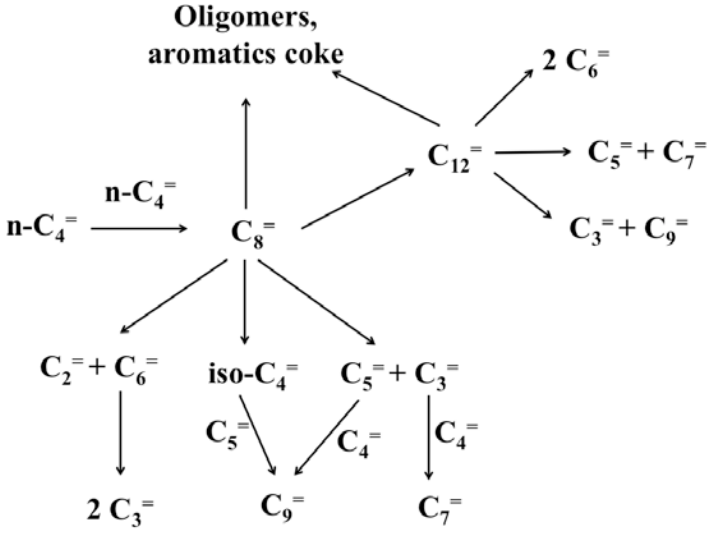

Scheme 2 Mechanism of *n*-butene isomerization over HZSM-5, reproduced from ref.[48].

Although *1*-butene was used as the initial reactant, both *1*-butene and *2*-butene can be considered as true reactants for the *n*-butene isomerization[71]. This is because *1*-butene are easily converted to *2*-butene over Brønsted zeolites via the double bond migration

process[72]. In addition, the conversion of both *1*-butene and 2-butene can be simultaneously reacted via the same mechanism. Therefore, the number of *1*-butene and *2*-butene molecules at equilibrium are considered as a real reactant[71]. The catalytic performance of the synthesized hierarchical micro/mesoporous HZSM-5 sample and the commercial ZSM-5 catalyst for the isomerization of *n*-butene was carried out at various reaction temperatures and times on stream (TOS).

The activity, product selectivity and distribution in product yield were investigated from the peak area in the chromatograms obtained from gas chromatography (GC) and calculated based on the mole percentage derived from the detected hydrocarbon signal, which is proportional to the number of carbon atoms[73]. The percentage of reactant conversion, product selectivity and yield are described by the following equations:

$$\text{Conversion} = \frac{(\text{Reactant})_{in} - (\text{Reactant})_{out}}{(\text{Reactant})_{in}} \times 100\ \%$$

$$\text{Yield} = \frac{(\text{Product})_{out}}{(\text{Reactant})_{in}} \times 100\ \%$$

$$\text{Selectivity} = \frac{(\text{Product})_{out}}{(\text{Reactant})_{in} - (\text{Reactant})_{out}} \times 100\ \%$$

Figure 17 shows the product distribution obtained from the *n*-butene conversion over the HZSM-5 catalysts at 240°C and the weight hourly space velocity (WHSV) of 1.8 h^{-1}. In all cases, the products are the hydrocarbon molecules composing of C3, C4, C5, C6 and C7. From the obtained product distribution, the results clearly show that the reaction on HZSM-5 catalyst is not very selective in the production of isobutene. Therefore, the monomolecular and pseudomolecular mechanism should be excluded while the oligomerization-cracking mechanism is suggested to be the predominant pathway. This result agrees well with that reported in the literatures [45].

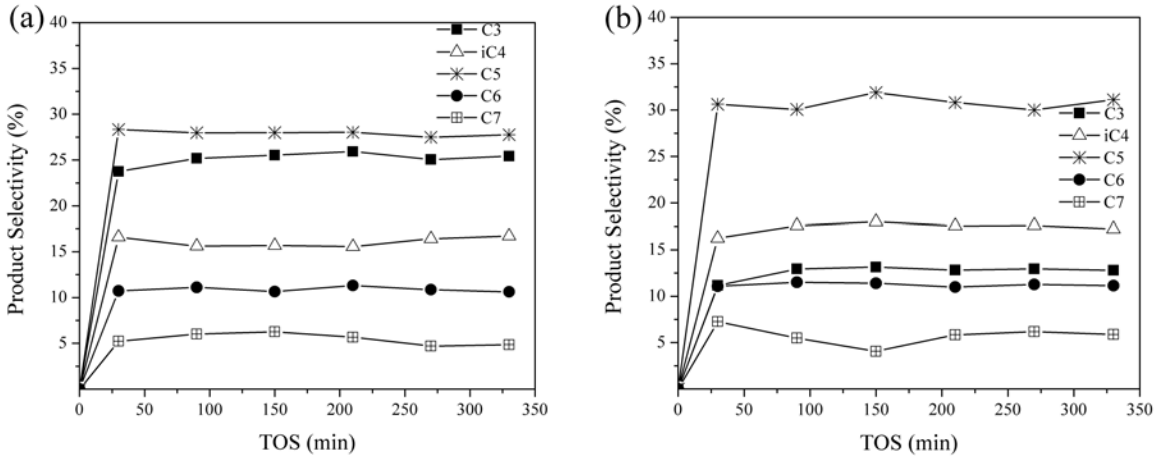

Figure 17. Distribution of products obtained from the *n*-butene conversion at 513 K and a weight hourly space velocity (WHSV) of 1.8 h^{-1} over (a) the conventional microporous HZSM-5 (Conventional HZSM-5_24) (b) the prepared hierarchical micro/mesoporous H-ZSM-5 obtained with the Si/Al ratio of 29 (mHZSM5_29). Conventional HZSM-5_X and mHZSM5_X denote for the conventional microporous HZSM-5 and the hierarchical micro/mesoporous HZSM-5 synthesized with the Si/Al ratio of X, respectively.

3.4.1.1 Effect of reaction conditions on n-butene isomerization

The effect of reaction temperature on the catalytic performance of the catalysts for the *n*-butene isomerization was also studied at the same WHSV (0.2 h^{-1}) and at temperature in the range of 493 to 573 K. It was found that an increase of temperature results in enhancing of the *n*-butene conversion over the synthesized hierarchical micro/mesoporous H-ZSM-5 samples (see Figure 18a). In addition, the product distribution at temperature ranging from 493 to 523 K is not significantly altered with the change in temperature (see Figure 18b). The $C_5^=$ products appears to be the main product. Interestingly, the amount of $C_5^=$ and propene are not comparable as it is expected for a bimolecular mechanism. The reason may be due to a further dimerization of propene to larger products such as hexenes and heptenes [45]. However, the product distribution at a high temperature of 573 K significantly changed. The propene selectivity increases with an increase of temperature while the products of $C_5^=$ and large molecules (> C6) become less resulting in a comparable amount of propene and $C_5^=$ products. This finding would be explained by a suppression of the further dimerization of propene at a high temperature.

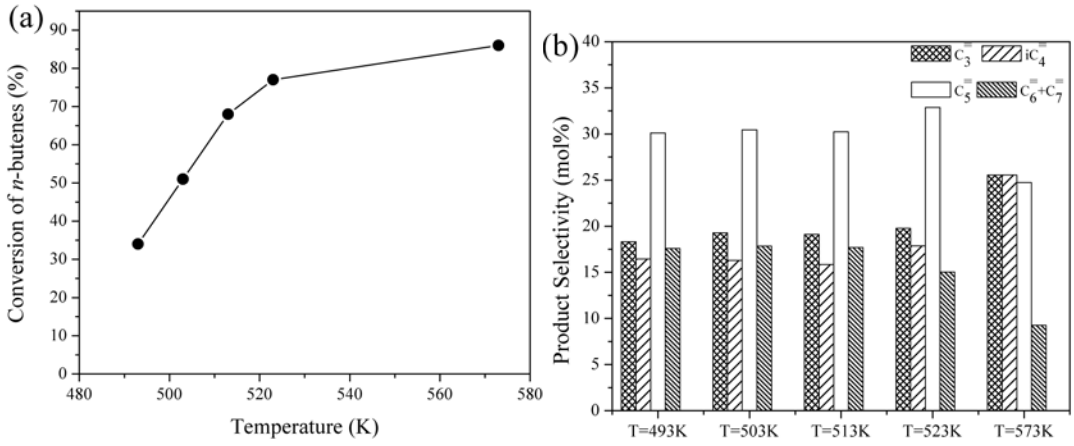

Figure 18. Effect of temperature on (a) *n*-butene conversion and (b) the product selectivity obtained in the case of the synthesized hierarchical micro/mesoporous HZSM-5 sample synthesized with the Si/Al ratio of 29 (mZSM-5_29). The WHSV was 0.2 h^{-1}. The pressure was 1 atm. The TOS was 30 min.

In addition, the role of the WHSV on the reaction over the hierarchical micro/mesoporous H-ZSM-5 was studied at 513 K. The *n*-butene conversion, product distribution and isobutene yield are plotted against the contact time (τ), which is derived by 1/WHSV and shown in Figure 19. The conversion of *n*-butenes increases with an increase of the contact time in the both cases, the hierarchical micro/mesoporous HZSM-5 and the conventional microporous HZSM-5 catalysts. Interestingly, at all contact times, the conversion of *n*-butenes on the hierarchical micro/mesoporous HZSM-5 sample is significantly higher than that on the conventional HZSM-5. For example, at contact time of 1.8 h, the butene conversions are 89% and 56% for the hierarchical zeolite and the conventional one, respectively (see Figure 19a). For the hierarchical micro/mesoporous HZSM-5, the amount of large molecule products such as $C_6^=$ and $C_7^=$ increases while the amount of small molecule products such as propene decreases with an increase of the contact time (see Figure 19b). The reason could be an increase of the further oligomerization process of olefin species at a higher contact time. In addition, the values of the initial reaction rate of isobutene formation over the hierarchical micro/mesoporous HZSM-5 and the conventional microporous HZSM-5 samples, estimated by the initial slopes of the tangent at time zero to the curves of isobutene formation versus time, are shown in Figure 19c. It can be seen that the initial rate of the isobutene formation over the

hierarchical micro/mesoporous HZSM-5 sample is 4 times higher than that of the reaction over the conventional catalyst.

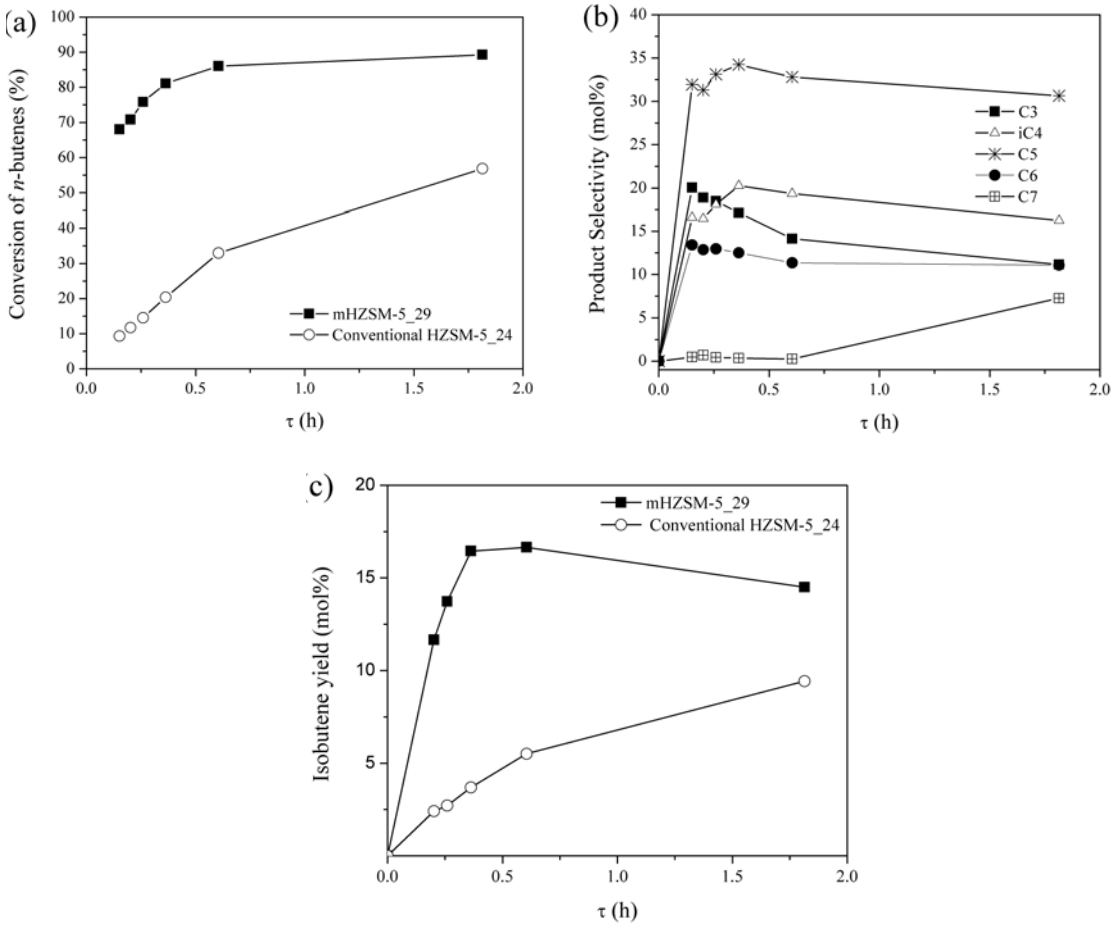

Figure 19. Effect of contact time, τ (τ=1/WHSV) on the *n*-butene conversion over (a) the hierarchical micro/mesoporous HZSM-5 obtained with the Si/Al ratio of 29 (mHZSM-5_29) and the conventional microporous HZSM-5 with the Si/Al ratio of 24 (Conventional HZSM-5_24), (b) the product distribution obtained in the case of the mHZSM-5_29 and (c) the isobutene yield obtained in the case of the mHZSM-5_29 and Conventional HZSM-5_24 zeolite samples. The reaction was performed at 513 K and 1 atm.

3.4.1.2 Catalytic performance of the hierarchical micro/mesoporous HZSM-5 for n-butene isomerization

To evaluate the catalytic performance of the synthesized hierarchical micro/mesoporous HZSM-5 and the conventional microporous HZSM-5 catalysts in the details, the conversion of *1*-butene was performed at 513 K with the WHSV of 1.8 h^{-1}. Because one of the drawbacks of the conventional microporous zeolites is the fast deactivation of the catalysts during a reaction process, the stability of the catalytic activity of the catalysts was investigated from the curve of the *n*-butene conversion as a function of the TOS (see Figure 20a). It is noteworthy that the conversion of *n*-butene on the hierarchical micro/mesoporous HZSM-5 samples is significantly higher than that of the reaction on the conventional microporous HZSM-5. Interestingly, the conversion of *n*-butenes on the synthesized micro/mesoporous HZSM-5 is up to 89%, whereas the conversion of *n*-butenes on the conventional HZSM-5 is less than 56 % even when the fresh catalyst is used (the reaction time about 30 min). In addition, the study of the stability in the activity of the catalysts shows that the conversion of *n*-butenes on the conventional microporous HZSM-5 sample decreases rapidly while that on the hierarchical micro/mesoporous HZSM-5 samples remains rather steady even after the TOS of 6 hours. This result indicates that the deactivation of catalyst is more retarded in the case of the hierarchical micro/mesoporous HZSM-5 compared to that in the case of the conventional zeolite, which composes of only microporous cavities. In order to evaluate the catalytic activity of the hierarchical micro/mesoporous HZSM-5 samples synthesized with different Si/Al ratios, the activity of the catalysts with the Si/Al ratios of 83 and 29 was studied. The results show that there is no significant difference in the catalytic performance of the hierarchical micro/mesoporous HZSM-5 samples prepared with different Si/Al ratios of 29 and 83.

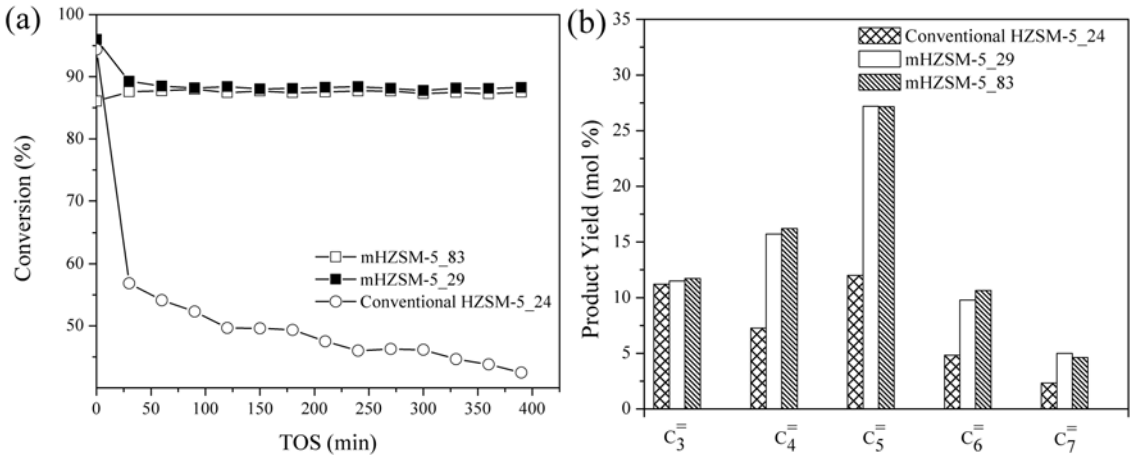

Figure 20. (a) Conversion of *n*-butenes at different times on stream (TOS) and (b) the product yield at the reaction time of 6 hours obtained over mHZSM-5_83, mHZSM-5_29 and Conventional HZSM-5_24. The reaction was performed at 513 K with the WHSV of 1.8 h^{-1}.

The evaluation of the amount of the product yield obtained on the hierarchical micro/mesoporous HZSM-5 and the conventional microporous HZSM-5 (Figure 20b) shows that the yield of isobutene is significantly higher in the case of the hierarchical micro/mesoporous HZSM-5. In addition, the yield is irrespective to the Si/Al ratio. The yield of C5-C7 products, obtained on the hierarchical micro/mesoporous HZSM-5, is visibly higher when it is compared to that obtained in the case of the conventional microporous HZSM-5, while the yield of propene does not considerably differ in the both cases. It should be noted that concentrations of the obtained $C_3^=$ and $C_5^=$ are comparable in the case of the conventional microporous HZSM-5, whereas the concentration of $C_3^=$ are almost three times lower than that of $C_5^=$ in the case of the hierarchical micro/mesoporous samples. This result is irrespective to the Si/Al ratio. This is suggested to be due to the introduction of the mesoporous cavities in the case of the hierarchical micro/mesoporous samples providing a larger void space for the further oligomerization.

The observations confirm that the introduction of mesoporous cavities into the part of microporous HZSM-5 results not only in an increase in the catalytic performance for the conversion of *n*-butenes but also in the retardation of the catalyst deactivation due to the small diffusion path length of the hierarchical micro/mesoporous could reduce the pore blocking, derived from the coke formation inside the porous structure. Thus, it diminishes the general drawbacks of the microporous materials [72].

3.4.2 Catalytic performance of the hierarchical micro/mesoporous HZSM-5 for cracking of *n*-hexane and *3*-methylpentane

The cracking of paraffin is one of the most important reactions in oil refinery process because it can be used to produce high value products from the refinery residues. The first cracking method had been achieved by thermal process. However, the thermal cracking requires high energy. Thus, the catalytic cracking has been developed instead of the thermal process. Moreover, as the catalytic cracking can be successfully achieved at a much lower temperature compared to the thermal process [74], the carbon dioxide emission from the process is lower. Zeolites are well-known solid acidic catalysts for catalytic cracking of alkanes [75]. Up to recently, there are two mechanisms proposed for paraffin cracking. These mechanisms are the classical or bimolecular mechanism (β-scission), which takes place via the carbenium ion intermediate and the nonclassical or monomolecular mechanism (protolytic cracking) processing through carbonium ions (see Scheme 3) [76].

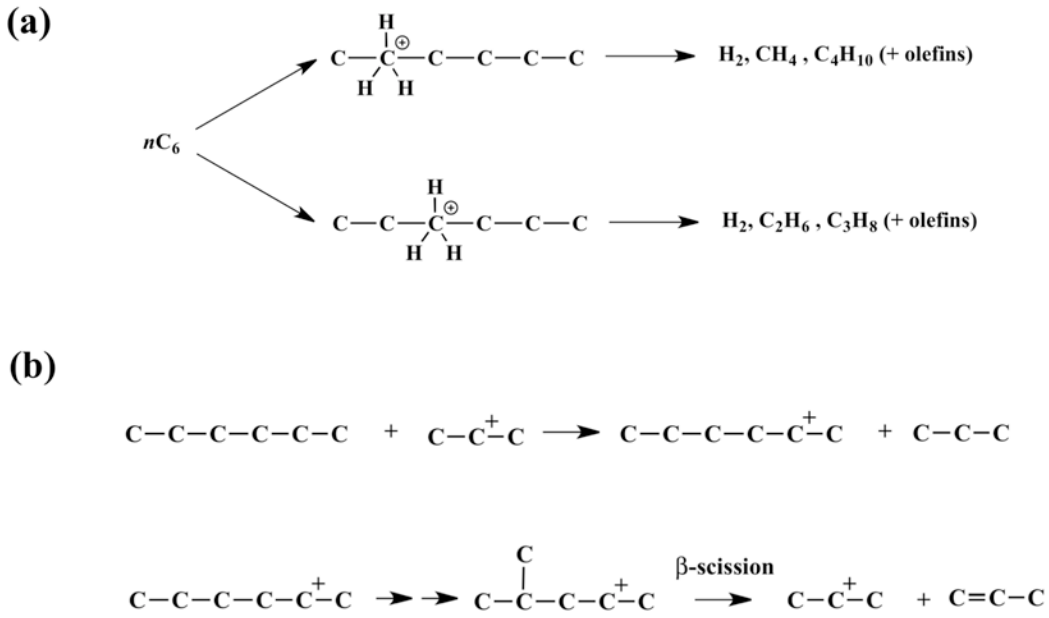

Scheme 3. Mechanism of *n*-hexane cracking via (a) the nonclassical or monomolecular mechanism (protolytic cracking) and (b) the classical or bimolecular mechanism (β-scission). Reproduced from [76] and [77].

In order to investigate the catalytic performance of the hierarchical micro/mesoporous HZSM-5 and the conventional microporous HZSM-5 for catalytic cracking of non-bulky molecules, the catalytic cracking of *n*-hexane was investigated at different temperatures by using a stream of *n*-hexane in nitrogen carrier gas as reactant. The conversion of *n*-hexane and product selectivity obtained at different temperatures are shown in Figures 21 and 22, respectively. The results reveal that an increase of the reaction temperature leads to an enhancement of the *n*-hexane conversion. The major cracked products obtained at a low reaction temperature of 573 K are C4. The amount of small molecules significantly increases with an increase of temperature. At temperature in the range of 573-673 K, methane is not observed as the by-product. However, the significant amount of C1 and C2 molecules is detected at a higher temperature of > 623 K. The main cracked product obtained at temperature of above 623 K is C3 for the both the hierarchical micro/mesoporous HZSM-5 and the conventional microporous HZSM-5 catalysts. The reason of the product distribution differences at various temperatures could be explained by different reaction mechanisms. Due to the existence of light alkane molecules such as methane and ethane at a high temperature, it can be suggested that the reaction mechanism takes place via the nonclassical pathway or protolytic cracking. These light alkane products could not be produced by the classical pathway or bimolecular mechanism in which the smallest cracked alkane product is propane or propene. This is because the β-scission process is very slow for the production of the small molecules such as methane and ethane, processing via the primary carbenium ions, which are high-energy species [78]. Thus, it is reasonable to exclude the bimolecular mechanism, occurred at high temperature. However, at a low temperature of 573 K, the bimolecular mechanism could be predominant. This suggestion is confirmed because the small alkane product is not detected, while the significant number of huge molecules (>C5) is significantly observed. Interestingly, a comparable amount of propane and propene is also investigated as well as the amount of C2 is equivalent to C4 at 673 K, indicating that the protolytic cracking of *n*-hexane is prevalent. However, at a higher temperature, the selectivity of propane decreases while the selectivities of methane, ethane and ethene increase. This reason could be explained by the further cracking of propane.

Concerning the catalytic performance for the *n*-hexane cracking, it was found that both catalytic activity and product selectivity of the hierarchical micro/mesoporous

HZSM-5 and the conventional microporous HZSM-5 insignificantly differed. Therefore, the catalytic performance of *n*-hexane cracking under the examined reaction conditions is not influenced by the presence of mesoporosity in the zeolite sample. In order to explain this finding, the kinetic diameter of *n*-hexane should be considered. The kinetic diameter reported by Maloncy et al. [79] of *n*-hexane is 4.3 Å. This value is smaller than the cavity of the conventional HZSM-5, composing of the pore opening of 5.6 x 5.4 Å along its b-axis for straight channels and 5.1 x 5.5 Å along its a-axis for sinusoidal channels [80]. In addition to the small kinetic diameter of *n*-hexane, in this case the reaction mechanism of hexane cracking predominantly proceeded via the protolytic monomolecular pathway [81], so that it is reasonable to suggest that the intermediates of this reaction are not large enough to contribute to the diffusion limitation inside the zeolite channels in which the mesoporosity should overcome.

In addition, the effect of the Si/Al ratio on *n*-hexane cracking was also investigated. The catalytic activity of the hierarchical micro/mesoporous HZSM-5 samples synthesized with the Si/Al ratio of 29 and 83 for the *n*-hexane catalytic cracking are shown in Figure 21. The results clearly show that the conversion of *n*-hexane cracking decreases with an increasing of the Si/Al ratio. This result is in good agreement with that reported in the literatures. It was found that the catalytic cracking strongly depends on amount of the acidic sites of zeolites [82]. Our results show that the introduction of mesoporosity does not improve the catalytic activity of *n*-hexane cracking on the HZSM-5 samples whereas the amount of acidic sites strongly influences on their activities.

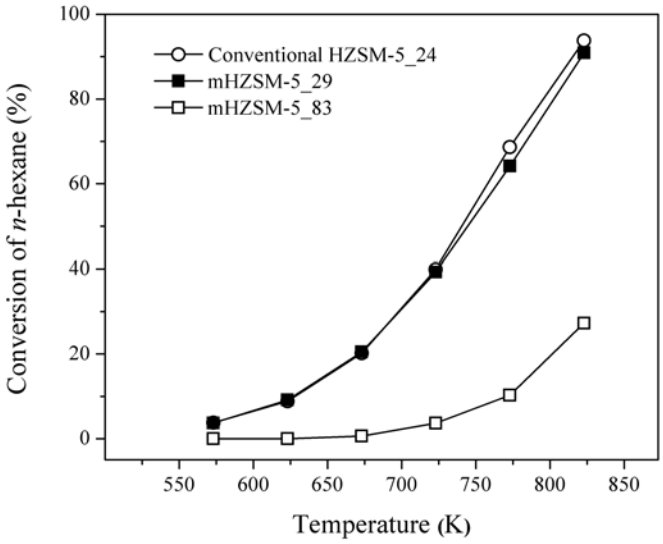

Figure 21. Effect of temperature on activity of *n*-hexane cracking over the hierarchical micro/mesoporous HZSM-5 samples prepared with the Si/Al ratios of 29 (mHZSM-5_29) and 83 (mHZSM-5_83) and the conventional microporous HZSM-5 (Conventional HZSM-5_24).

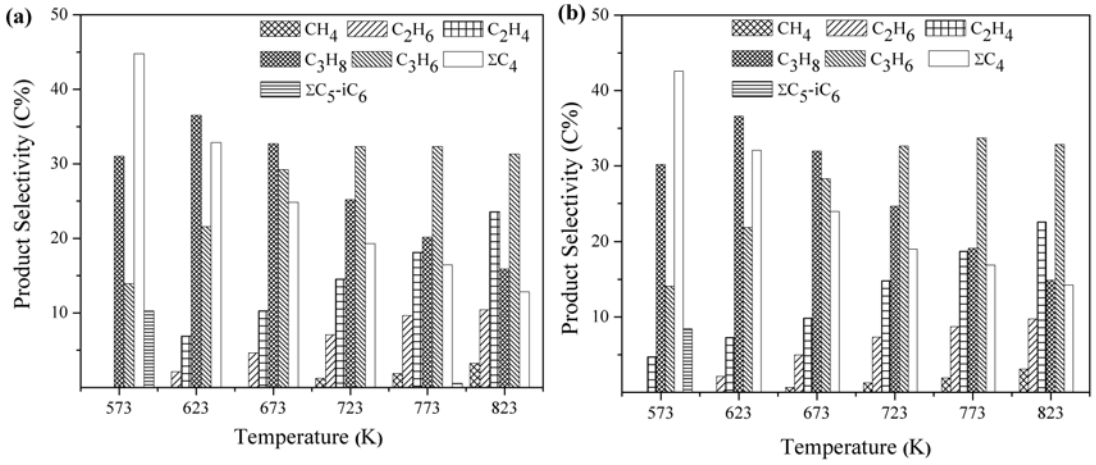

Figure 22. Effect of temperature on product selectivity of *n*-hexane cracking over (a) the conventional microporous HZSM-5 with the Si/Al ratios of 24 (Conventional HZSM-5_24) and (b) the hierarchical micro/mesoporous HZSM-5 obtained with the Si/Al ratios of 29 (mHZSM-5_29).

The constraint index (CI) was firstly described by Werner O. Haag and his colleagues in order to explain the shape selective catalytic behavior in zeolites [83]. This index is determined from the relative reaction rates of the cracking of *n*-hexane (*n*-C6)

and its isomer, *3*-methylpentane (3-MP) under competitive conditions. The CI is defined as the following equation.

$$\text{Constraint Index (CI)} = \frac{\log(1-X_{n-C_6})}{\log(1-X_{3-MP})}$$

Where $X_{n\text{-}C6}$ and $X_{3\text{-}MP}$ are the fractional conversion of *n*-hexane and *3*-methylpentane, respectively. The zeolites that are owing to a lower CI prefer to crack branched hydrocarbons compared to linear hydrocarbons as result of the absence of steric constraint from the zeolite wall. From the CI data of some zeolites taken from the literatures, it clearly shows that the CI value corresponds to porous cavities of the zeolite (see Table 1 in ref [84]). The zeolite with larger pores is owing to a lower CI value. Therefore, the examination of CI value can provide an insight into the structure of zeolites and the selectivity of the zeolites for the reactions. The CI values can be used to classify the zeolite materials into three groups. The zeolites with large pores (12-ring pores or the larger pores) give the CI value of <1. The zeolites with intermediate pores (e.g. 10-ring pores) give the CI value in the range of 1-12. The zeolites with small pores (8-ring pores or the smaller pores) give the CI value of > 12 [83,84]. Therefore, in this work, we also investigated the CI value of the synthesized hierarchical micro/mesoporous HZSM-5 prepared with the Si/Al ratio of 29 (mHZSM-5_29) compared to that of the conventional microporous HZSM-5 with the Si/Al ratio of 24 (Conventional HZSM-5_24). The CI values determined under competitive conditions of *n*-hexane and *3*-methylpantane cracking for the mHZSM-5_29 and the conventional microporous HZSM-5 are shown in Table 7. The CI values of the both zeolites decrease with an increase of the reaction temperature. This behavior could be explained by an alternation of the reaction mechanism from the bimolecular mechanism to the monomolecular one at a high temperature. Basically, the bimolecular mechanism requires a larger space for the reaction compared to the monomolecular mechanism so that the rate of *3*-methylpentane conversion is much slower compared to that of the *n*-hexane cracking at a lower temperature [85]. However, the rate of *3*-methylpentane cracking dramatically increases at a high temperature because the monomolecular or protolytic mechanism demanding less space for the reaction becomes predominant. Compared to the conventional microporous HZSM-5, the CI value of the hierarchical micro/mesoporous H-ZSM-5 is significantly

lower implying that the hierarchical micro/mesoporous HZSM-5 prefers to crack branched hydrocarbons compared to linear hydrocarbons. It should be noted that the difference in CI values (ΔCI) between the conventional and micro/mesoporous zeolites is greater at a low reaction temperature, while the ΔCI becomes lower at a higher reaction temperature. The reason of this result is that the hierarchical micro/mesoporous zeolite provides a large space for the reaction, which is important parameter for the bimolecular pathway, resulting in a better cracking of branched hydrocarbons compared to linear one at a low temperature. Therefore, it is reasonable to conclude that an investigation of the CI value is an alternative method that can be used to distinguish between the mesoporous zeolite and the conventional zeolite as their porous cavities are different.

Table 7. CI values of the hierarchical micro/mesoporous H-ZSM-5 synthesized with the Si/Al ratio of 29 (mHZSM5-29) and the conventional H-ZSM-5 with the Si/Al ratio of 24 (Conventional HZSM-5_24) at different reaction temperatures.

Temperature (K)	CI		ΔCI*
	Conventional HZSM-5_24	mHZSM-5_29	
673	6.5	2.1	4.4
823	4.0	1.7	2.3
873	2.8	1.5	1.3
923	2.5	1.2	1.3

ΔCI*: The different CI values of the conventional HZSM-5 with Si/Al = 24 (conventional HZSM-5_24) and the hierarchical micro/mesoporous HZSM-5 with Si/Al = 29 (mHZSM-5_29).

3.4.3 *Catalytic performance of the hierarchical micro/mesoporous HZSM-5 for cracking and hydrocracking of n-hexadecane*

In order to investigate the catalytic performance of the synthesized hierarchical micro/mesoporous zeolites for the reactions when the reactants are large molecules, the catalytic cracking and hydrocracking of *n*-hexadecane was investigated. As stated above, the catalytic cracking occurs on the Brønsted acid sites and produces both alkene and alkane products. In case of the hydrocracking process, large hydrocarbon molecules break down into smaller molecules in the presence of hydrogen atmosphere. Therefore, the

mechanism, product distribution and catalyst feature are different from those in the case of the catalytic cracking. The hydrocracking is successfully processed on bifunctional catalysts containing the metal sites and the Brønsted acid sites. The metal sites perform as the Lewis acid sites, which are the catalytic sites for the dehydrogenation, hydrogenation and dissociation of hydrogen molecules, while the Brønsted acid sites act as the catalytic sites for accelerating the isomerization and cracking reactions so that the hydroisomerization normally takes place as a competitive reaction of the hydrocracking. The products of the hydrocracking normally are saturated hydrocarbons. This is due to the presence of hydrogen that further promotes the hydrogenation reaction. Mechanisms of the hydrocracking and hydroisomerization are shown in Scheme 4.

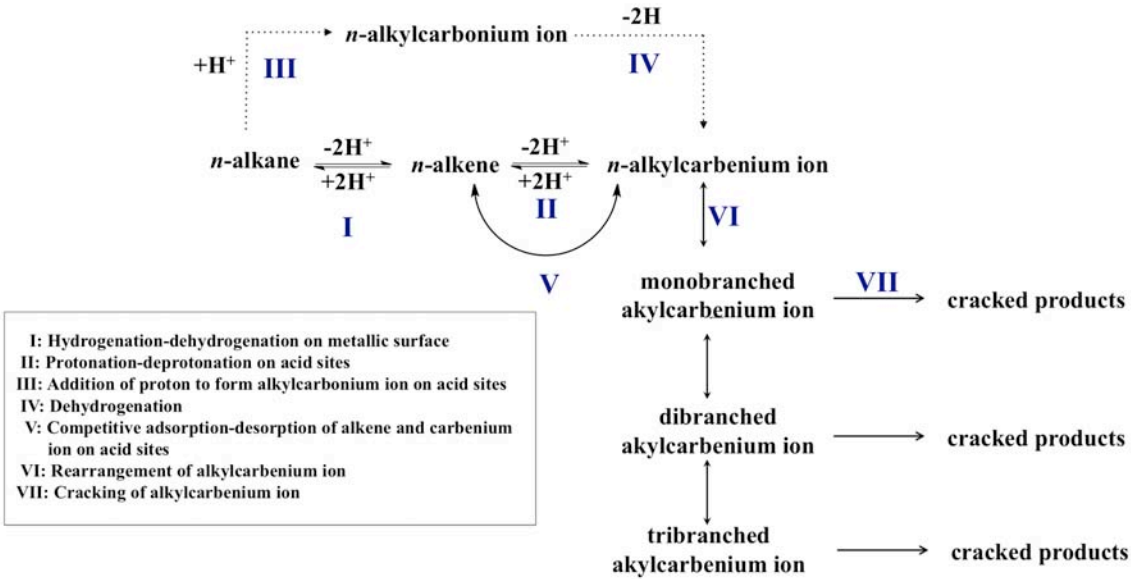

Scheme 4. Illustration of mechanism for hydrocracking occurred on bifunctional catalyst, reproduced from ref. [86].

In order to study the catalytic performance of the synthesized hierarchical micro/mesoporous zeolites for the reactions involving high molecular weight reactant, the catalytic cracking and hydrocracking of *n*-hexadecane were carried out in a slurry phase solution at 553 K. In this experiment, a typical H^+ type catalyst (HZSM-5), which is owing to the Brønsted acid sites, and a bifuctional catalyst (Pt/HZSM-5), composed of the metal sites and the Brønsted acid sites, were used for catalytic cracking and hydrocracking, respectively. The catalytic performances of the hierarchical micro/mesoporous ZSM-5 and the conventional ZSM-5 for the catalytic cracking and

hydrocracking of *n*-hexadecane are shown in Table 8. Because the reaction was performed at a moderate condition (medium temperature of 553 K and pressure of 10 barr), the main products were in the liquid phase. This result agreed well with that reported in the literature where a very low amount of gas products was observed for the both catalytic cracking and hydrocracking processes [87]. In addition, a low amount of C14 and C15 products was observed implying that methane and ethane could also form with an insignificant amount. Therefore, it is reasonable to suppose that the main products are in the liquid phase and the gas products can be neglected. The conversion of *n*-hexadecane to liquid products was observed for the both catalytic cracking and hydrocracking processes. In case of the catalytic cracking, the conversion of *n*-hexadecane to liquid products over the conventional HZSM-5 is very low (about 5.8%). Compared to the conventional microporous HZSM-5, the catalytic performance for *n*-hexadecane cracking of the hierarchical micro/mesoporous H-ZSM-5 is significantly better even when the zeolite with a high Si/Al ratio of 83 is used. The catalytic activity of the hierarchical micro/mesoporous zeolite for the cracking increases with an increase of the number of active sites or the Si/Al ratio. The conversion of *n*-hexadecane over the catalyst with the Si/Al ratio of 29 is higher than that occurs over the sample prepared with the Si/Al ratio of 83 by 3 orders of magnitude. This result confirms that the conversion rate of *n*-hexadecane cracking strongly depends on the acidity of zeolites [88,89].

The results clearly demonstrate that the introduction of the Pt nanoparticles into the hierarchical micro/mesoporous H-ZSM-5 samples extremely enhances the catalytic performance of the catalysts for the hydrocracking process. The conversion of *n*-hexadecane over a mesoporous catalyst (mPt/HZSM-5_29) is up to 98%, whereas that of the commercial one with the similar acidity is only 33%. This finding strongly confirms that the hierarchical micro/miesoporous H-ZSM-5 exhibits a better catalytic performance for the *n*-hexadecane hydrocracking. Because the product mixture in the C_4-C_{10} range is important for petroleum industry as it is largely in the gasoline boiling range so it is a benefit to categorize the cracked products into three groups, C_4-C_7, C_8-C_{10} , and C_{11}-C_{16}, respectively. The obtained product yields are shown in Table 8. The main products are in the C_4-C_7 range for all catalysts. The bifunctional catalyst prepared from the hierarchical micro/mesoporous zeolite shows a high yield of the mixture in the C_4-C_{10} range of up to 80%.

To gain a better understanding of the catalytic performance of the hierarchical micro/mesoporous zeolite for the *n*-hexadecane conversion, the molecular size and pore diameter of zeolite were considered. The kinetic diameter of *n*-hexadecane is 0.306 × 1.975 nm [90], whereas the pore opening of ZSM-5 zeolite is 0.56 x 0.54 nm along its b-axis for straight channels and 0.51 x 0.55 nm along its a-axis for sinusoidal channels [80]. Therefore, the moving of *n*-hexadecane molecules into the microporous channels is restricted by the molecular dimensions. When the mesoporous cavities are introduced into the parts of microporous zeolite, larger space for the reaction is provided. For this reason, the *n*-hexadecane molecules can diffuse easily into the zeolite active sites through the mesoporous structure. In addition, the dispersion of metal nanoclusters or nanoparticles supported on bifunctional catalysts also plays an important role on the catalytic performance of bifunctional catalysts. Because the Pt nanoparticles supported on the hierarchical micro/mesoporous HZSM-5 samples are smaller than those supported on the conventional one and their dispersions are better so the improved dispersion leads to a balance of the acidity active sites and hydrogenation/dehydrogenation sites in these bifunctional catalysts.

Table 8. Catalytic performance of the hierarchical micro/mesoporous ZSM-5 samples synthesized with the Si/Al of 29 and 83 and the conventional microporous ZSM-5 for *n*-hexadecane cracking and hydrocracking.

Entry	Catalyst	Wt % of Pt	Conversion (%)	Product Yield (%)		
				C_4-C_7	C_8-C_{10}	C_{11}-C_{16}^*
1	Conventional HZSM-5_24	-	5.8	2.0	1.6	2.1
2	mHZSM-5_29	-	45.6	19.6	12.4	13.6
3	mHZSM-5_83	-	15.2	6.4	4.5	4.3
4	Conventional Pt/HZSM-5_24	1.0	33.4	19.2	8.0	6.2
5	mPt/HZSM-5_29	1.0	98.2	51.6	27.8	19.2

C_{11}-C_{16}^* : C_{16} is the isomerization product for which *n*-hexadecane is not included. Conventional HZSM-5_24: Conventional HZSM-5 with Si/Al ratio of 24, mHZSM-5_29 and mHZSM-5_83: the hierarchical micro/mesoporous HZSM-5 samples with Si/Al ratio of 29 and 83, respectively, Conventional Pt/HZSM-5_24: Conventional Pt/HZSM-5 with Si/Al ratio of 24 and mPt/HZSM-5_29: the hierarchical micro/mesoporous Pt/HZSM-5 with Si/Al ratio of 29.

In conclusion, the hierarchical micro/mesoporous ZSM-5 synthesized by use of the C/SiO_2 composites, which are obtained from a pyrolysis of carbonaceous gases in the presence of silica gel, shows not only an improvement in the surface area and porosity due to the mesoporous feature but also an enhancement of the catalytic performance for the reactions involving the presence of huge molecules compared with the conventional zeolite in the both cases of the Brønsted and bifunctional catalysts. In addition, the dispersion of Pt nanoparticles, which is a key effect for catalytic performance of the bifuctional catalyst, is significantly improved in the presence of mesoporous feature. This finding demonstrates that our developed synthesis procedure for the preparation of the hierarchical mico/mesoporous zeolites, which are obtained by use of a pyrolysis of carbonaceous gases to produce carbon residues as the mesoporous templates, and the obtained catalysts can be considered as promising method and material for the potential applications, especially in petrochemical industry.

4. CONCLUSIONS

The hierarchical micro/mesoporous ZSM-5 zeolites were successfully prepared by using the C/SiO_2 composites obtained by pyrolysis of carbonaceous gases in the presence of silica gel. The C/SiO_2 composites act as a bifunctional material in which carbon residue and SiO_2 part function as a mesoporous template and a silica source for the zeolite synthesis, respectively. The results from XRD patterns confirm that the structures of all synthesized samples corresponding to MFI framework. In addition, TEM images and N_2 adsorption/desorption isotherms show that the using of C/SiO_2 composite results in a significant increase of mesoporosity. The mesoporosity of zeolite can be easily controlled by varying the carbon contents in the C/SiO_2 composites. Increasing the carbon content in such composite results in a significant increase of surface area and total pore volume, which reflect to a rise of the mesopore volume whereas the micropore volume of the samples is not significantly altered.

The morphology, particle size and mesopore volume also strongly depend on Si/Al ratios. A decrease in Si/Al ratio causes to reduction of crystal size, resulting in an increase of mesopore volume. In addition, the bifunctional zeolite, composing of H^+ site as acidic site and Pt nanoparticles as metal sites, has been successfully prepared by wet impregnation of $Pt(NH_3)_4(NO_3)_2$ solution on H^+ type zeolite and followed by freeze-drying to remove solvent. The hierarchical micro/mesoporous Pt/HZSM-5 improves the degree of metal nanoparticle dispersion on zeolite support, which plays an important role for bifunctional catalyst design. It was found the high dispersion of small Pt nanoparticles throughout the mesoporous network over hierarchical micro/mesoporous zeolite, while the larger Pt particles are located on the outermost surface for microporous zeolite.

The catalytic performances of both hierarchical micro/mesoporous ZSM-5 and conventional one were investigated on three different reactions, including the *n*-butene isomerization, *n*-hexane and *3*-methylpentane cracking and *n*-hexadecane catalytic cracking/hydrocracking. The catalytic performance of *n*-hexane cracking over hierarchical micro/mesoporous ZSM-5 is not significantly improved compared to conventional microporous ZSM-5 under the present condition because the diffusion of *n*-hexane inside microporous ZMS-5 is not restricted by zeolite wall. However, the catalytic performances of reactions, involving the big molecules as reactants (*n*-hexadecane hydrocracking) and intermediates or products (isomerization of *1*-butene), on hierarchical micro/mesoporous zeolite dramatically enhance. Compared to conventional microporous

ZSM-5, the hierarchical micro/mesoporous ZSM-5 is not only increase their catalytic activities in such reactions but also retard the deactivation of catalyst.

Our findings confirm the high efficiency of a hierarchical dual micro/mesoporous zeolite catalyst obtained based on an embedded nanocarbon cluster synthesis. This controllable and efficient synthetic method is expected to be generalised for other types of zeolites, it is considered to be a promising method for creating hierarchical micro/mesoporous zeolites. This type of catalyst is considered to be a promising material for the potential applications, especially in petrochemical industry.

Chapter 2 A QUANTUM CHEMICAL ANALYSIS OF STRUCTURES AND REACTION MECHANISMS OF SKELETAL ISOMERIZATION OF *1*-BUTENE ON FERRIERITE ZEOLITE

1. INTRODUCTION

Zeolites have been emerged as one of the most industrially important catalysts due to their fascinating properties such as separation, ion exchange and catalysis[91,92]. A large number of major industrial processes have been paid attention to their acid-base properties in order to catalyze the reactions in production lines for the desired high-cost products. Among major industrial reactions, the “skeletal isomerization of linear butenes” is one of them.

The skeletal isomerization of linear butenes to isobutene[93] has been considered as one of the most important reactions in petrochemical industrial processes, especially for the preparation of isobutene, which is used as the alkene precursor in the productions of gasoline additives such as methyl *tert*-butyl ether (MTBE), ethyl *tert*-butyl ether (ETBE)), polyisobutylene (PIB) and methacrylate[37,38,94,95].

Among various types of zeolites, the zeolites composing of medium pore diameters in the range of 4 to 5.5 Å such as FER[40-42], ZSM-23[43], ZSM-22[44] and ZSM-5[45], have been reported as good candidate catalysts for this reaction. As far as the product selectivity is concerned, ferrierite (H-FER) has been found to be the most selective catalyst for the skeletal isomerization of *n*-butenes[47], due to their specific pore dimension which is suitable for the monomolecular reaction. Thus, ferrierite zeolite was selected as the catalyst in this study.

On the focus of the skeletal isomerization mechanisms of linear butene to isobutene, three possible reaction pathways are proposed. These are (i) the monomolecular mechanism, (ii) the bimolecular mechanism and (iii) pseudomonomolecular mechanism (autocatalytic process). For the monomolecular mechanism, one molecule of *1*-butene can be directly converted to isobutene[96-98]. The monomolecular mechanism takes place through methyl shift or a protonated methylcyclopropane of *n*-butyl species to produce primary carbenium species. For

bimolecular mechanism, all of elementary steps involve with the linear butene dimerization (D), isomerization and cracking of octenes[99]. As for the pseudomonomolecular mechanism, the process involves the formation of carbenium ions at the active sites, subsequently the reaction undergoes with complex mechanisms of these carbenium species before the production of isobutene and by-product[46,100]. Although these reaction mechanisms have been proposed, the monomolecular mechanism is the possible one in the production of highly selective isobutene. This pathway has been emerged in the specific zeolites with highly constraining pore dimension, *e.g.*, H-FER[101-103], whereas the bimolecular mechanism requires larger pore space than that of the monomolecular mechanism. Many reports suggested that isobutene was predominantly produced from the monomolecular mechanism, whereas the bimolecular pathway results in the formation of by-products[102,104-106]. In order to further confirm the possible mechanism, the data of reversible skeletal isomerization reaction in different zeolites available in the literature were considered. The high reversibility of *n*-butenes skeletal isomerization was observed over H-FER. This behavior is not expected for the bimolecular mechanism because the formation of by-products cannot gain the high selectivity of *n*-butenes from isobutene isomerization [107,108]. Therefore, it is reasonable to propose that the skeletal isomerization of *1*-butene over H-FER processes via monomolecular mechanism.

The skeletal isomerization of *1*-butene to isobutene is particularly interesting in both theoretical and experimental studies because it involves several important intermediates both carbenium ions and alkoxides in the reaction pathway. For example, it has been reported that when using heterogeneous acidic catalyst, *e.g.*, zeolites, the reaction proceeds via the covalent alkoxide intermediate species rather than the carbenium ion[109-116]. On the other hand, the mechanism in homogenous catalyst, *e.g.*, superacid catalyst (see refs.[117,118]), linear butyl-cation is directly converted to *tert*-butyl cation through primary butyl transition state. Even though many experimental [97,99,101,107,119-126] and theoretical[116,127-130] studies have intensively been investigated the skeletal isomerization of *1*-butene to isobutene reaction, unclear issues still remain whether that the carbenium ion exists as a transition state or a stable intermediate. Therefore, selected details from literature for the skeletal isomerization of *1*-butene to isobutene are concisely discussed here as follow.

For the experimental studies, the FT-IR[125] and NMR[97] revealed that the carbenium ions are not stable species in the zeolite framework excepted for some cyclic carbenium ions that can persist in acidic zeolites[126]. Solid-state NMR revealed that the protonation of alkene by Brønsted zeolite produced the surface alkoxyl species instead of free carbenium ion[131].

As for the theoretical point of view, the skeletal isomerization of *1*-butene over zeolite has been involved with several important carbenium ions and alkoxides in the reaction mechanism. For examples, Boronat and coworker[132] proposed the skeletal isomerization of *1*-butene of theta-1 via monomolecular mechanism and they found that *2*-butoxide, primary butoxide and protonated methylcyclopropane were observed as reaction intermediates and transition states. In addition, the geometry restrictions of zeolite framework are considered by the increasing of zeolite cluster size. Constraint effects result in destabilization of these species compared with the adsorbed alkene. Besides, the stabilities of the carbenium ions and alkoxide intermediates were carried out at different levels of theory. The *tert*-butyl carbenium ion was reported to be a transition state by Boronat and coworker[111-113], while the true *tert*-butyl cation intermediate can be observed only from the Hartree Fock calculation[113]. In 2010, the *tert*-butyl carbenium ion was reported as the true intermediate from experimental and theoretical studies by Rosenbach *et al.*[133]. The formation of the *tert*-butyl cation as an intermediate inside cavities of zeolite was observed during the reaction of the nucleophilic substitution of *tert*-butylchloride and bromide over NaY impregnated with NaCl or NaBr. Because the nucleophilic substitution of *tert*-butylhalide takes place via SN1 mechanism, which involves carbocations formation, the ion pair of the *tert*-butyl cation and zeolite framework could be formed. Consequently, the carbocation can be attacked by the halide over halide impregnated inside zeolite. This result confirms the existence of *tert*-butyl cation as intermediate species inside zeolite cavities. Moreover, in the same work, the calculations were also carried out by the ONIOM(MP2/6-31G(d,p):PBE1PBE/6-31G (d,p))//ONIOM(MP2/6-31G(d,p):MNDO) and PBE1PBE/6-31G(d,p)//ONIOM (MP2/ 6-31G(d,p):MNDO) approaches. They found the *tert*-butyl cation as an intermediate with the energy lies between 9.6 – 12.2 kcal/mol higher than the *tert*-butoxide species.

Alternatively, the protonation of isobutene in various zeolites [109,111,113,114,127,128,130,134] have also been theoretically reported in order to examined alkoxide stabilities[105, 107,109,110,123,124,126,130]. For example**,** Rozanska*et al.*[127] studied the

isobutene chemisorptions in chabazite (CHA), ZSM-22, and mordenite (MOR) zeolites using the periodic DFT calculation, they proposed two reaction mechanisms of isobutene protonation through the primary and tertiary carbocation-like transition states. The corresponding activation energies for primary carbocation-like transition states are 32.9(CHA), 21.5(TON) and 28.2 (MOR) kcal/mol, while the activation energies for tertiary carbocation-like transition states are 10.8 (CHA), 5.7 (TON) and 7.2 (MOR) kcal/mol. As a result, on one hand, the reaction of the chemisorption of isobutene was favored to occur via the tertiary carbocation-like transition state rather than the primary carbocation-like transition states. They also reported that the energies of the tertiary carbocation and *tert*-butoxide intermediates were very close to that of the corresponding transition state, indicating the existence of reactive species and the possibility of finding carbocation intermediate in the reaction coordinate. On the other hand, the *pri*-butoxide is the intermediate species for the protonation of isobutene via the primary carbocation-like transition states. The *pri*-butoxide was more stable than their corresponding transition state structures by about 28-30 kcal/mol. Boronat *et al.*[114] reported that they found the free *tert*-butyl carbenium ion as a true reaction intermediate depending on the locations of the basic oxygen of the zeolite that the cation are bound.

Using the hybrid MP2:DFT calculations[130],when the dispersion effects of the zeolites framework were taken into account, the reaction energies (including the zero-point vibrational energy, ZPVE) with respect to the isolated isobutene molecule and H-FER zeolite system were reported to be -17.7, -9.6, -6.4 and -15.1 kcal/mol for the π-complex, the *tert*-butoxide, the *tert*-butyl carbenium ion and the isobutoxide, respectively, suggesting that the *tert*-butyl carbenium ion is not stable intermediate compared with *tert*-butoxide. Subsequently, Tuma and co-worker[134] theoretically studied the stabilities of isobutene, *tert*-butyl carbenium ion, *tert*-butoxide and isobutoxide using hybrid MP2:PBE method. They reported that the *tert*-butyl carbenium ion was higher in energy than isobutene, *tert*-butoxide and isobutoxide by 14.4, 5.7 and 12.2 kcal/mol, respectively. Likewise, the activation barriers of the *tert*-butyl carbenium ion transformations to isobutene, *tert*-butoxide and isobutoxide were also reported to be 3.3, 7.5 and 14.6 kcal/mol, respectively.

Although there are many literatures observed the reaction energies of intermediates and transition states, which related to skeletal isomerization of *1*-butene, it is still unclear to explain the effect of zeolite framework on the complete mechanism of

this reaction as well as the stabilities of reaction intermediates (alkoxide species), particularly the stability of *tert*-butyl carbenium ion which is not possible to directly detect by the experimental method. Thus, the goals of this chapter are:

- Exploring the complete monomolecular mechanism of skeletal isomerization of *1*-butene over ferrierite zeolite by means of a full quantum calculation using the ONIOM(MP2:M08-HX) approach.
- Investigating the effect of the extended zeolite framework on the stabilities of related intermediates, transition state and other complexes in the reaction mechanism.
- Examining the existence of *tert*-butyl carbenium in the system.

2. METHODOLOGY

It has been reported that the most active and selective catalysts for the skeletal isomerization of *n*-butenes are the medium pore zeolites, *e.g.*, ZSM-23[120], ferrierite[99,119,122,135,136] and MCM-22[121] in which the reactions process occurs via the monomolecular pathway. The medium pore zeolites with specific pore diameters can even suppress the dimerization or oligomerization reactions which are competitive reaction with the monomolecular skeletal isomerization of *n*-butenes[122]. In this study, ferrierite (H-FER) was selected as a catalyst due to the fact that it has been reported to be the most selective zeolite among the medium pore zeolites.

As a ferrierite model, a 37T (T refers to tetrahedral center) quantum cluster consisting of 136 atoms ($Si_{37}O_{49}H_{50}$) (Figure 23) was used since this is large enough to fully cover the catalytic pore, which behaves like "nanoreactor" in the ferrierite zeolite. The 37T model represents a two-dimensional pore system consisting of a 10-ring (4.2 Å × 5.4 Å) channel intersected by an 8-ring (3.5 Å × 4.8 Å) channel[137] (See Figure 23), thus the model can reveal the confinement effects of zeolite which plays a significant role in the predictions of reaction energies[138-145].

At the active site of the 37T model, a silicon atom at the T(2) position was replaced by an aluminum atom[115] and, in order to neutralize the system, an H atom was added to one of the neighbor oxygen atoms in the most energetically favorable position. From the literature, it was reported that the O(7) is the most suitable position rather than the O(1) position[146,147]. The additional H atom at the O(7) position results in the generation of a Brønsted acid site in the ferrierite zeolite (H-FER), as illustrated in Figure 23b. We note here that the O(7) and O(1) crystallographic positions are conventionally written as "O1" and "O2" in all Figures and Tables throughout this chapter. Moreover, in the models employed, the dangling bonds of surface oxygen atoms are terminated by H atom at the distance 1.47 Å from the Si, yielding Si-H bonds, aligned along the corresponding Si-O bonds of the structure.

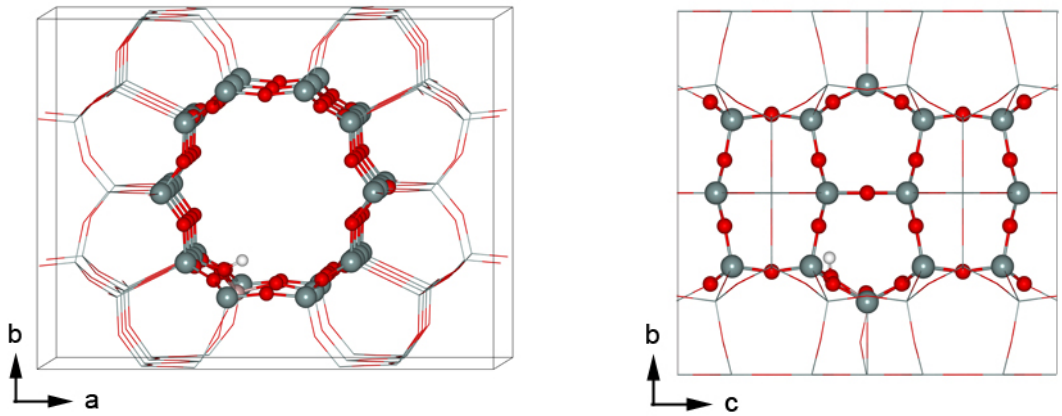

(a) (b)

Figure 23. The unit cell of ferrierite (H-FER); (a) the representation of the 10 member ring of the selected 37T model. (b) the cluster representation along the c direction of the ferrierite unit cell. Bond and stick model, excluding the terminating hydrogen atoms.

To account for the framework effect on the local geometry, especially for the van der Waals interactions, which play a significant role in the hydrocarbon interaction with the zeolite[143], the calculations were carried out by means of the ONIOM2 method (see Appendix H for more details). Structure optimizations were carried out using the Gaussian 03 program[148], which incorporates the Minnesota Density Functionals by Zhao and Truhlar[149]. The 5T quantum cluster, where the Brønsted acid site is located, is assigned to be the inner layer, and the extended 37T quantum cluster is the outer layer (Figure 24b). Only the adsorbed molecule and the 5T cluster at the active region ($AlSi_4O_4H$) of the zeolites were allowed to fully relax whereas the rest was kept fixed with the crystallographic structure. The 5T inner layer and adsorbed molecule were treated with the sophisticated MP2 method and the M08-HX functional was applied for the 37T outer layer to account for the framework effect on the local geometry. Beside the electrostatic interaction, the van der Waals interactions also play a significant role in the hydrocarbon interaction with the zeolite. The 6-31G(d,p) basis set was used for all atom types.

In order to study the mechanism and stability of intermediates and transition states with- and without framework effect, optimizations of 5T clusters were also carried out (Figure 24a). All results clarify the significance of the zeolite framework effects on the

reaction mechanisms compared to that of the 37T model and the available results in the literature. Finally, to improve the reaction and activation energies, single point calculations with the 6-311+G(2df,2p) basis set were performed for all models.

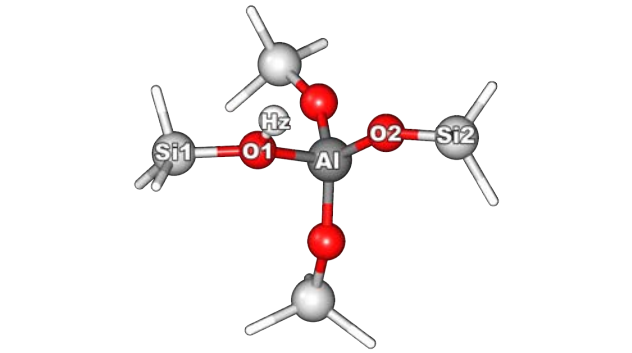

(a)

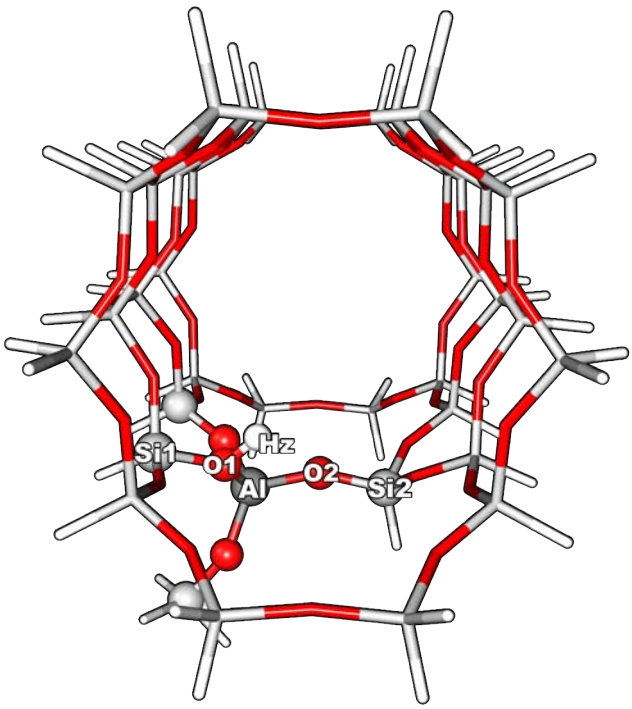

(b)

Figure 24. Models used in this study (a) 5T quantum model and (b) 5T/37T ONIOM2 model.

3. RESULTS AND DISCUSSIONS

3.1 Validation method

In order to establish the accuracy of method used, the adsorption energies of species adsorbed on H-FER were investigated at different levels of theory. Experimental adsorption energies for alkenes adsorbed on acidic zeolite are not available in the literatures because of the facile isomerization and oligomerization of alkenes on the zeolite surface. Therefore, in order to compare adsorption energies from the calculations, obtained with different methods, with data from experiments, the *n*-butane adsorption energies were investigated, as shown in Table 9.

In this work, four different DFT functionals, i.e., B3LYP, M06-L, M06-2X and M08-HX were examined. It results that the B3LYP method shows an underestimation of the adsorption energies of *n*-butane/H-FER and *1*-butene/H-FER compared to the results obtained from the Minnesota Density Functional (M06-L, M06-2X and M08-HX). Using the ONIOM2(MP2:DFT) methods: the combination, at the MP2/6-31G(d,p):B3LYP/6-31G(d,p) level of theory, of the ONIOM scheme still underestimates compared to experimental data. This is because the B3LYP functional (outer layer) does not represent the effect of the zeolite framework properly. When the ONIOM scheme was used together with the MP2 method and the Minnesota Density Functionals, the adsorption energies of *n*-butane were in good agreement with the experimental data especially for the combination of MP2 and M08-HX. Consequently, the ONIOM2(MP2:M08-HX) was selected to be the method utilized in this study.

In order to overcome the basis set error, the adsorption energies were also investigated by single point calculation with a larger basis set at the ONIOM(MP2/6-311+G(2df,2p):M08HX/6-311+G(2df,2p))//ONIOM(MP2/6-31G(d,p):M08HX/6-31G (d,p)) level of theory. All reaction energies as well as the activation energies in this chapter are reported at this level. The adsorption energy of *n*-butane is -15.4 kcal/mol, which is very close to the experimental value of -15.1 kcal/mol. The adsorption energies of *1*-butene in H-FER with different methods behave in a similar fashion as the butane adsorption.

Table 9. The adsorption energies of *n*-butane and 1-butene on H-FER obtained at different levels of theory, compared to experimental data.

Methods	Adsorption Energies (kcal/mol)	
	n-butane/ H-FER	1-butene/ H-FER
DFT		
Optimization		
B3LYP/6-31G(d,p)	-0.9	-5.6
M06-L/6-31G(d,p)	-19.3	-21.4
M06-2X/6-31G(d,p)	-17.8	-21.4
M08-HX/6-31G(d,p)	-16.6	-19.4
ONIOM2		
Optimization		
MP2/6-31G(d,p):B3LYP/6-31G(d,p)	-4.5	-
MP2/6-31G(d,p):M06-L/6-31G(d,p)	-18.2	-
MP2/6-31G(d,p):M06-2X/6-31G(d,p)	-16.4	-
MP2/6-31G(d,p):M08HX/6-31G(d,p)	-15.2	-18.0
Single Point Calculations		
MP2/6-311+G(2df,2p):M08HX/6-31G(d,p)// MP2/6-31G(d,p):M08HX/6-31G(d,p)	-16.2	-19.1
MP2/6-311+G(2df,2p):M08HX/6-311+G(2df,2p)// MP2/6-31G(d,p):M08HX/6-31G(d,p)	-15.4	-18.0
Experiment	-14.1[a] -15.1[b]	-

[a]Eder, F.; Lercher, J. A. *J. Phys. Chem. B***1997**, *101*, 1273-1278.
[b]Yoda, E.; Kondo, J. N.; Domen, K. *J. Phys. Chem. B***2005**, *109*, 1464-1472.

3.2 Adsorption of *1*-butene and isobutene on H-FER

Table 10 and Figure 25 show selected geometric parameters of *1*-butene and isobutene adsorption complexes in the 37T H-FER. Both *1*-butene and isobutene, as reactant and product, interact with the Brønsted acid site of the zeolite via π-interaction between acidic proton (Hz) and the C=C double bond of the butene molecules. This π-interaction changes the structures of the zeolite and butane insignificantly. The adsorbed molecules are located in the 10T straight channel of the H-FER, acting as a nanoreactor. For the *1*-butene adsorption, the O1-Hz distance of the acidic zeolite elongates from 0.97 to 1.00Å and the corresponding O1-Al-O2 angle is slightly increased by 2.3° (from90.8° to 93.1°), while the Al-O1-Si1 angle decreases by 2.6°. The proton of the Brønsted acid site is situated closer to the C1 position of the *1*-butene molecule (C1···Hz = 2.11 Å) than to the C2 position (C2···Hz = 2.24 Å) because the terminal carbon is less steric. The protonation occurs at the C1 position while the C2 interacts with the adjacent oxygen of the zeolite framework. The C1=C2 double bond distance does not change significantly compared to the isolated molecules due to a weak π-interaction. The weakening of the C=C double bond leads to the protonation of the *1*-butene and the subsequent formation of intermediates.

The isobutene adsorption complex has the same analogue as in the *1*-butene complex. The adsorption of isobutene induces the elongation of the acidic bond (O1-Hz) and of the C1=C2 double bond from 0.97 to 0.99 Å and from 1.34 to 1.35 Å, respectively. However, the C2-Hz bond distance of isobutene is longer than that of *1*-butene due to a steric effect on the carbon atom (C2). Since there is more steric hindrance on the C2 atom of isobutene, the π-interaction is very asymmetric. The C2···Hz and C3···Hz distances are 2.67 and 2.18 Å, respectively.

The calculated adsorption energies, at the basis set levels of 6-311+G(2df,2p), are -18.0 and -14.8 kcal/mol for *1*-butene and isobutene on H-FER, respectively. The experimental adsorption energies for alkenes on H^+-type zeolites are not available due to the facile isomerization and oligomerization reactions on the zeolite surface. Hence, the comparison is made with the values available in the literature such as the heat of adsorption of *n*-butane in H-FER. This value is for *n*-butane in ferrierite zeolite -14.1kcal/mol[150] or -15.1kcal/mol[151]. It is expected that the adsorption energy of *1*-butene should be stronger than that of *n*-butane, therefore, the calculated result of -18.0 kcal/mol appears to be reasonable. For comparison, it was reported that the adsorption energies of

1-butene over different zeolites are in the range of -6.1 to -18.2 kcal/mol depending on the methods, models, and choice of relaxation utilized in the calculations[111-113,115,152,153]. The adsorption energies for small cluster models were reported for different cluster sizes, for examples -6.1[111], -6.87[113], -7.4[152] kcal/mol for the 3T cluster, -6.85 kcal/mol for the 5T cluster[113], -6.42 kcal/mol for the 11T cluster[113], and -8.24 kcal/mol for the 27T cluster[113]. In addition, electron correlation shows a significant influence on the adsorption energies, comparable to the electrostatic interaction provided by the periodic HF calculation [-10.3 kcal/mol (3T, MP2/6-31G(d)//B3P86/6-31G(d)) vs -6.19 kcal/mol(periodic HF)][111]. When the framework effects were taken into account, improvements of the adsorption energies were reported[115,153]. The adsorption energy of *1*-butene in H-FER zeolite at the O(1) position of the active site using hybrid QM/MM method is reported to be -18.2 kcal/mol[115]. The different zeolite topologies strongly correlate with the confinement effect as shown in the calculated adsorption energies of *1*-butene over H-MOR and H-FAU[153]. It was found that calculations using ONIOM(MP2/6-31G(d,p) :UFF//B3LYP/6-31G(d,p):UFF) provide the adsorption energies of -17.4 and -12.5 kcal/mol for *1*-butene over H-MOR and H-FAU, respectively. This suggests a strong confinement effect in the stabilization of hydrocarbon in the smaller pore size zeolite such as MOR, resulting in the smaller adsorption energy (more negative).

For the adsorption of isobutene, the energy is evaluated to be -14.8 kcal/mol, which is more than that of *1*-butene by 3.2 kcal/mol, due to steric repulsion between the bulky isobutene molecule and the zeolite framework. These energies were reported from theoretical work in the range 1.89 to -17.7 kcal/mol, depending on the method and cluster size[109,111,113-115,127-130,152,154,155]. Using the small QM cluster approaches results in underestimated values, for examples, the adsorption energies of isobutene were reported to be -6.8[152], -7.07[113] for 3T and 5T, respectively. It was reported that the experimental adsorption energies of isobutane in a H-ZSM-5[156] and H-TON[157], medium pore zeolites, were -11.9 and -11.3 kcal/mol, respectively. Because the porous cavity of H-FER (4.2 × 5.4 Å) is smaller than that of H-ZSM-5 (5.1 × 5.5 Å), the steric repulsion between the isobutene and the zeolite walls could be more pronounced in H-FER. Therefore, our computed adsorption energy of isobutene of -14.8 kcal/mol appears to be reasonable.

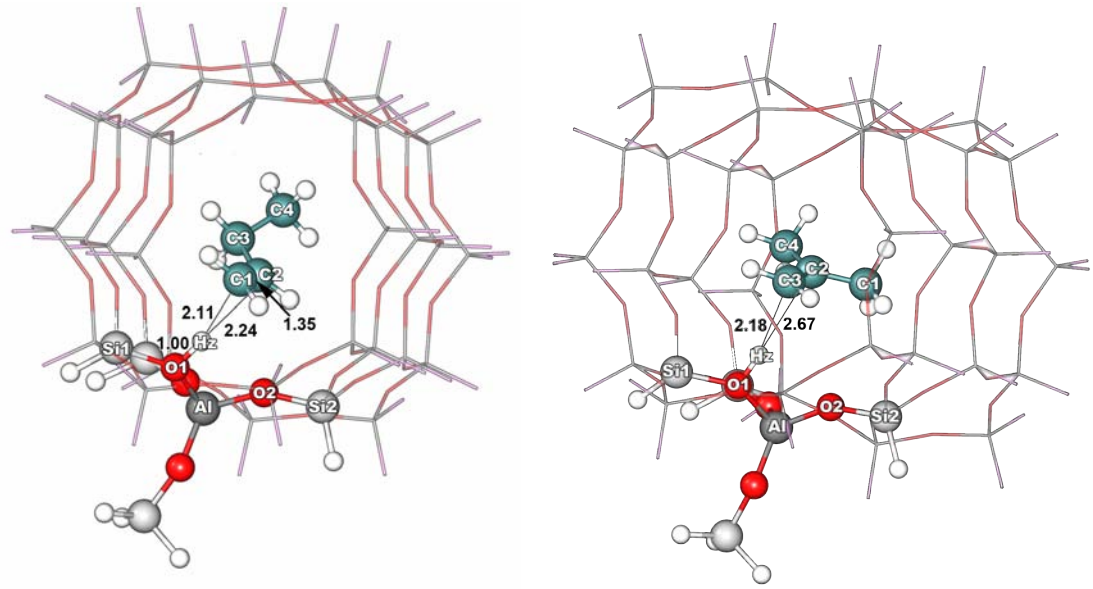

(a) (b)

Figure 25. Selected geometric parameters of the adsorption complexes on 37T H-FER obtained at the ONIOM(MP2/6-31G(d,p):M08HX/6-31G(d,p)) level of theory: (a) *1*-butene (reactant, **I**) and (b) isobutene (product, **IX**).

Table 10. Selected geometric parameters and calculated adsorption energies (kcal/mol) for the H-FER zeolite and the adsorbed π-complexes.

Parameters	H-FER	*1*-butene / H-FER	Isobutene / H-FER
Distances/Å			
O1-Hz	0.97	1.00	0.99
C1-Hz	-	2.11	-
C2-Hz	-	2.24	2.67
C3-Hz	-	-	2.18
C1-C2	-	1.34	1.35
Al-Hz	2.32	2.36	2.35
Al-O1	1.88	1.86	1.87
Al-O2	1.68	1.67	1.67
Si1-O1	1.67	1.67	1.67
Si1-O2	1.59	1.58	1.58
Angles/°			
O1-Al-O2	90.8	93.1	92.6
Al-O1-Si1	139.6	137.0	135.7
Al-O2-Si2	148.4	152.3	151.9
Energy/ kcal mol^{-1}			
$E_{ads}{}^{a}$(37T)	-	-18.0	-14.8
$E_{ads}{}^{b}$(37T)	-	-18.0	-14.8

[a] $E_{ads} = E_{olefin/\ H\text{-}FER} - E_{olefin} - E_{H\text{-}FER}$; obtained by 5T/37T ONIOM (MP2/6-31g(d,p):M08HX/6-31g (d,p))
[b] $E_{ads} = E_{olefin/\ H\text{-}FER} - E_{olefin} - E_{H\text{-}FER}$ obtained by 5T/37T ONIOM (MP2/6-311+G(2df,2p):M08HX/6-311+G(2df,2p)// MP2/6-31G(d,p):M08HX/6-31G(d,p))

3.3 Monomolecular pathway of skeletal isomerization of *1*-butene over H-FER

It was proposed that the skeletal isomerization of *1*-butene occurs via a monomolecular mechanism in which only one *1*-butene molecule is being converted to an isobutene molecule. Although some experiments suggested that the monomolecular mechanism involved the formation of a thermodynamically unstable primary carbenium ion as intermediate[46,119,158], this work and other theoretical studies[111,112,115,129] confirmed that the primary alkoxide exists as a stable species on the potential energy surface (PES) (see detail in the section 3.4). In addition, the experimental data confirm that isobutene is predominantly produced from the monomolecular mechanism, whereas the bimolecular pathway results in the formation of by-product[102,104-106]. Therefore, it is reasonable to suppose that the skeletal isomerization of *1*-butene takes place through a monomolecular mechanism over H-FER.

The proposed mechanism for the skeletal isomerization of *1*-butene over 37T H-FER is shown in Scheme 5, it consists of four elementary steps, which are described as follows: (i) protonation of adsorbed *1*-butene (I) on acidic site to provide the *2*-butoxide intermediate (III) via a transition state (II), (ii) transformation of the *2*-butoxide intermediate through a cyclic transition state (IV) into isobutoxide intermediate (V) (primary alkoxide), (iii) the formation of *tert*-butyl cation (VII) from the isobutoxide intermediate via 1,2 hydride shift transition state (VI), and (iv) the deprotonation of *tert*-butyl cation (VIII), leading to the formation of adsorbed isobutene (IX) over zeolite.

The complete reaction energy profile, the optimized structures of the intermediates and the transition states are shown in Figures 26, 27 and 28, respectively. The selected geometric parameters of the intermediates and transition states are also presented in Tables 11 and 12, respectively. Since the activation energy is mainly related to the true transition state structures, all transition-state structures are confirmed by frequency calculations for which the vibration movements at the transition states corresponding to the imaginary frequency are shown in Figure 29.

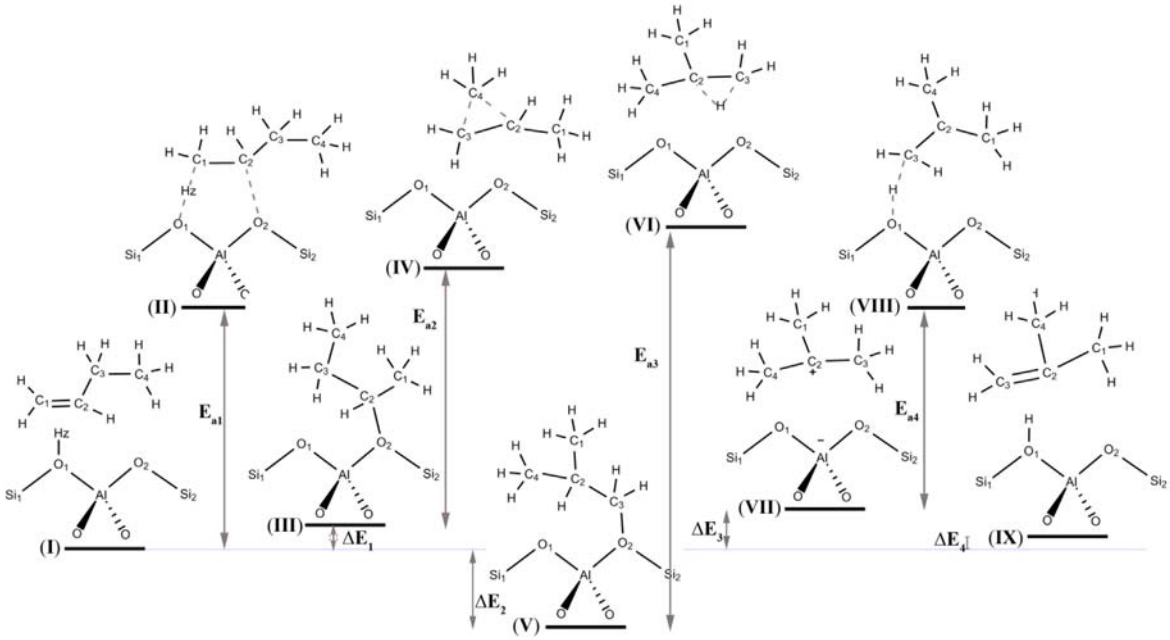

Scheme 5. The proposed monomolecular pathway for the skeletal isomerization of *1*-butene to isobutene over 37T H-FER.

For the skeletal isomerization mechanisms of *1*-butene to isobutene over 37T H-FER, it starts with the protonation of the adsorbed *1*-butene (**I**) to generate the *2*-butoxide (**III**) as intermediate via transition state (**II**). The protonation usually occurs through a concerted mechanism by which the hydrogen of the Brønsted acid site protonates the primary carbon atom (C1) of the double bond and, at the same time, the positively charged C2 interacts with the neighboring basic oxygen of the zeolite framework to form the covalent alkoxide species. The acidic proton is preferably protonated to the C1 atom of the *1*-butene since it is less steric and its transition state, a secondary carbenium ion, is more stable than the primary carbenium, which occurs via the protonation at the C2 atom. At the transition state (TS1 in Figure 28a), the proton of the active site is situated close to the carbon (C1) of the *1*-butene rather than to the framework oxygen (C1···Hz = 1.19 Å and O1···Hz = 1.72 Å), indicating that the proton transfer step is more advanced. The C2···O2 distance before forming an alkoxide species is about 2.79 Å, indicating that there is no covalent bond between the protonated butene and the zeolite framework. In addition, the Mulliken population analysis for the organic fragment shows a positive charge of +0.819*e*, the largest part of which is located on the C2 position with contribution of +0.186*e*, confirming that the transition state is a secondary butyl

carbenium ion. The activation energy (E_{a1}) of this step is calculated to be 19.5 kcal/mol. At the end, a strong covalent bond between the C2 atom of the butene fragment and the O2 atom of the zeolite framework is formed, giving the 2-butoxide intermediate (**III**). The C2-O2 covalent bond distance is 1.56 Å and the 2-butoxide intermediate is destabilized by 3.0 kcal/mol compared to the initial *1*-butene adsorption complex.

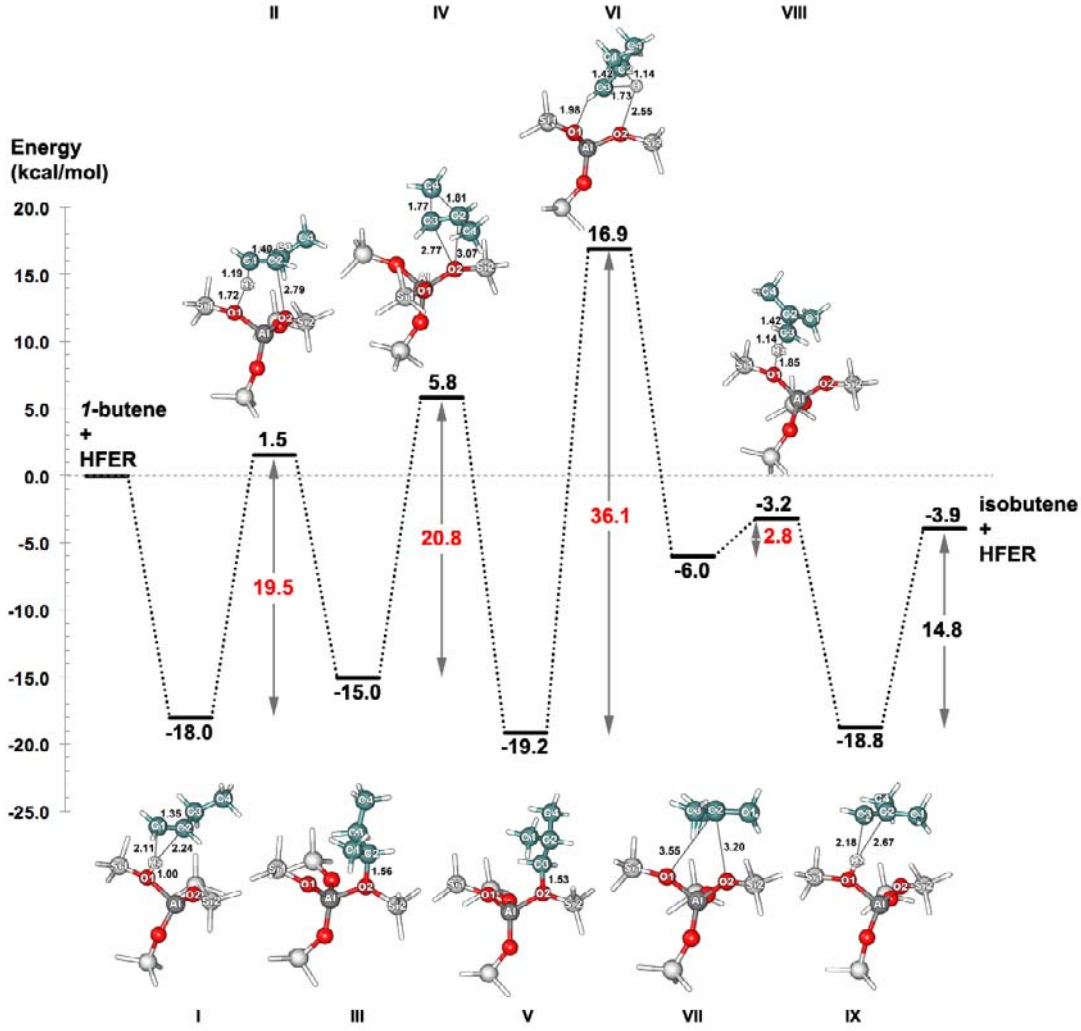

Figure 26. The reaction energy profile of the monomolecular mechanism of the *1*-butene skeletal isomerization over 37T H-FER zeolite model obtained at the ONIOM(MP2/6-311+G(2df,2p):M08-HX/6-311+G(2df,2p))//ONIOM (MP2/6-31G(d,p):M08-HX/6-31G(d,p)) level of theory. Geometrical parameters and energies are in Å and kcal/mol, respectively.

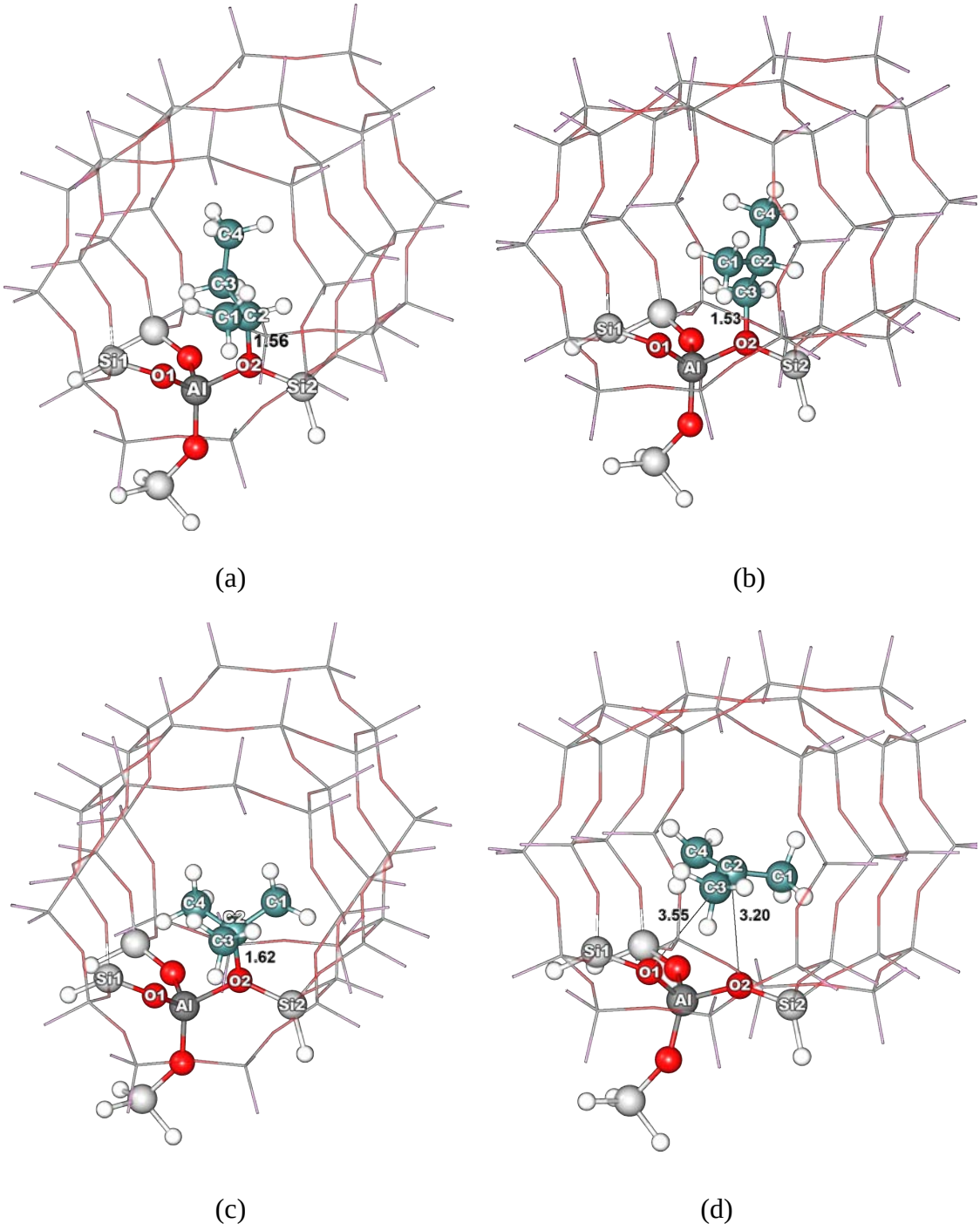

Figure 27. Selected geometric parameters (in Å) of intermediate structures (a) *2*-butoxide (III), (b) isobutoxide (V), (c) *tert*-butoxide (VII') and (d) *tert*-butyl cation (VII) over the 37T H-FER model.

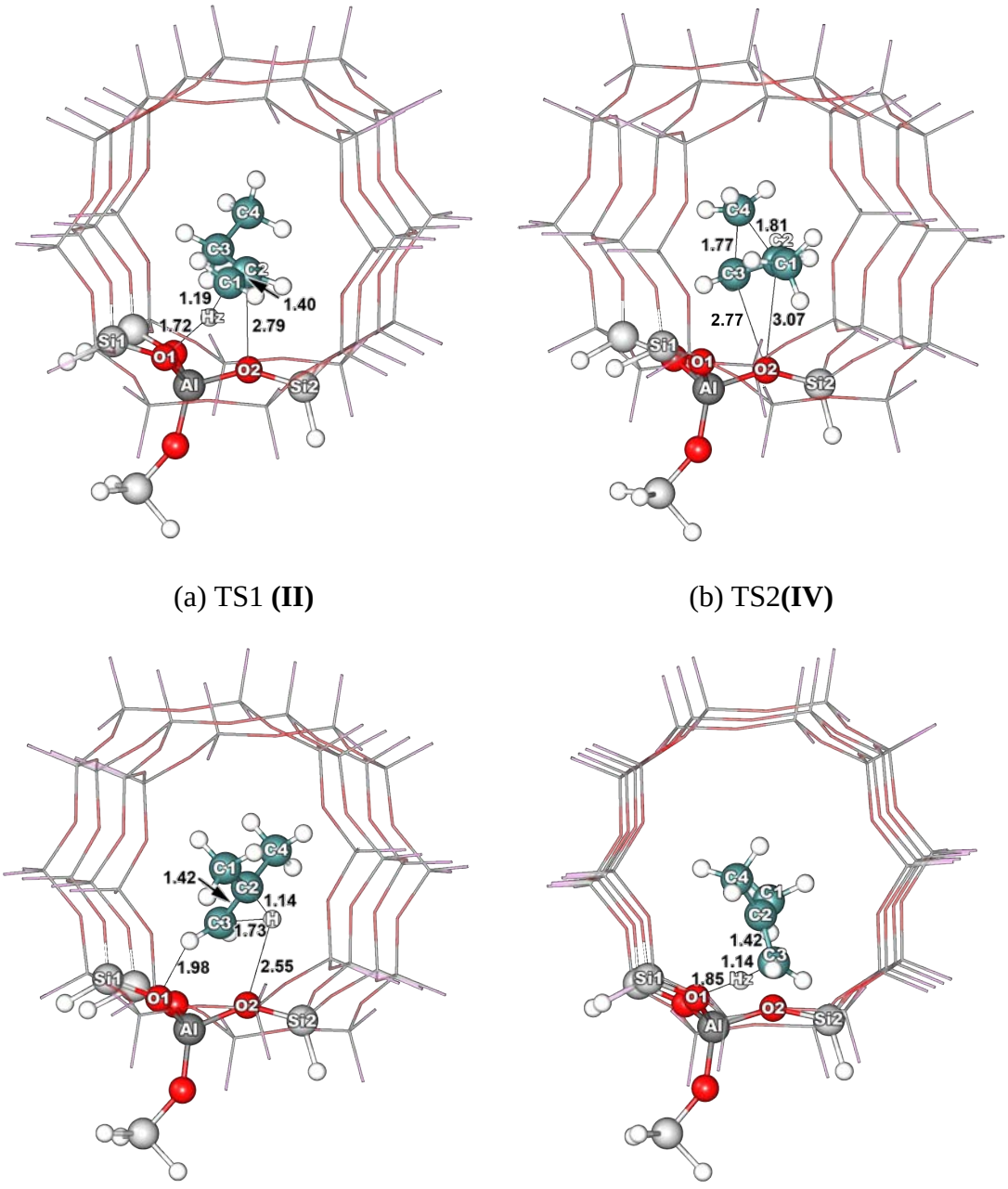

(a) TS1 **(II)**

(b) TS2**(IV)**

(c) TS3 **(VI)**

(d) TS4 **(VIII)**

Figure 28. Selected geometric parameters (in Å) of the transition states.

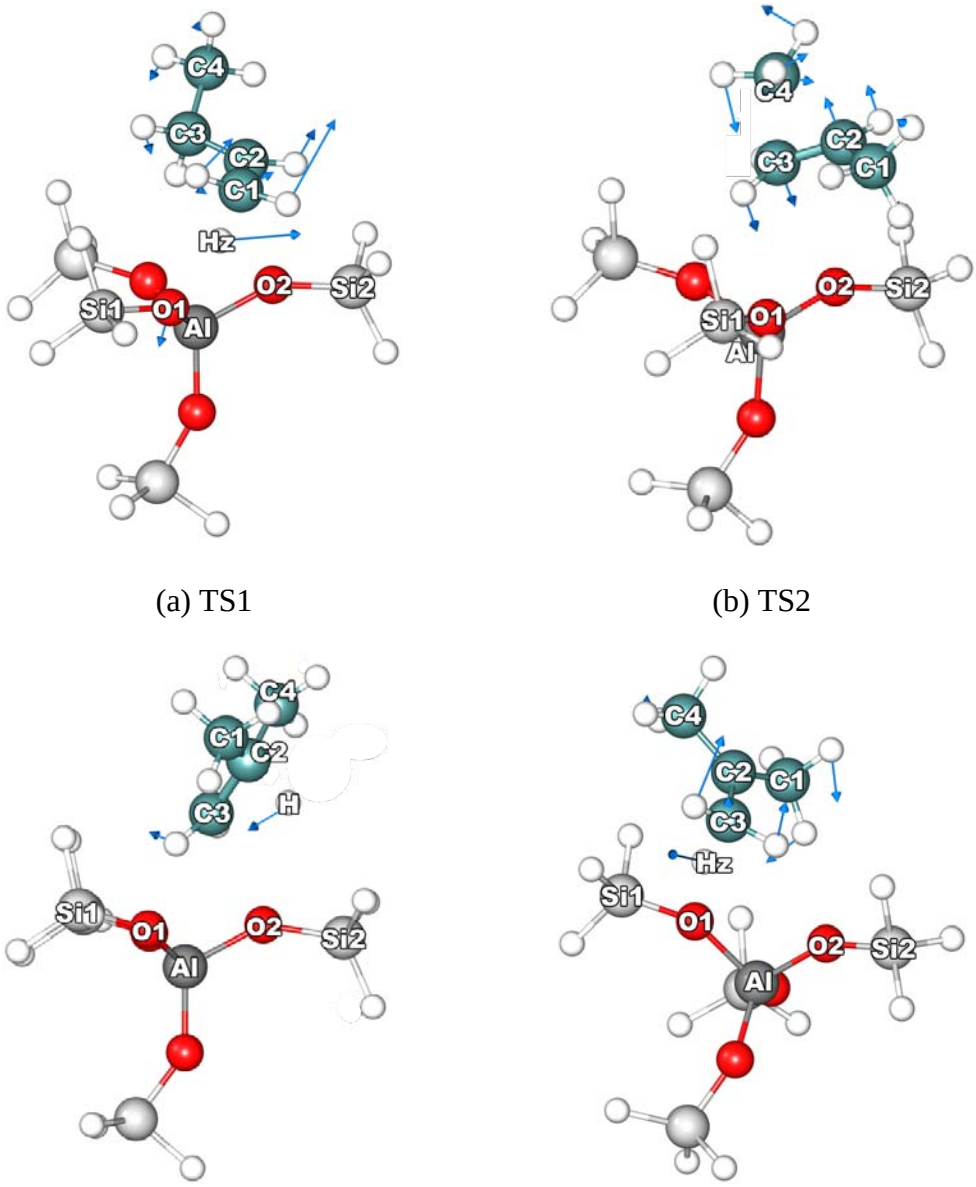

(a) TS1 (b) TS2

(c) TS3 (d) TS4

Figure 29. Vibrational movements (displacements corresponding to the normal coordinate) corresponding to the imaginary frequency of the transition state structures.

Table 11. Selected geometric parameters and calculated energies (kcal/mol) for the intermediates (alkoxide and cation species in the H-FER zeolite) calculated at the ONIOM(MP2/6-311+G(2df,2p):M08-HX/6-311+G(2df,2p))//ONIOM (MP2/6-31G(d,p):M08-HX/ 6-31G(d,p)) level of theory (at the O2 position in the 37T).

Parameters	*2*-butoxide **(III)**	isobutoxide **(V)**	*tert*-butyl cation **(VII)**
Distances/Å			
C-O	1.56	1.53	3.20
Al-O1	1.70	1.70	1.73
Al-O2	1.86	1.85	1.71
Si1-O1	1.58	1.59	1.58
Si2-O2	1.69	1.69	1.57
Angles/°			
C-O2-Al	118.3	107.7	102.7
O1-Al-O2	94.9	96.5	98.8
Al-O1-Si1	145.2	141.7	142.3
Al-O2-Si2	132.7	135.1	146.7
Relative energies, E_{rel}/ kcal mol^{-1}			
E_{rel} (37T)[a]	3.0	-1.2	12.0

[a] $E_{rel} = E_{intermediate} - E_{1\text{-butene adsorption comple}}$;

Relative energies, E_{rel}/kcal mol^{-1} (with respect to *1*-butene adsorption over H-FER)

Table 12. Selected geometric parameters and calculated energies (kcal/mol) for the transition states in the H-FER calculated at the ONIOM(MP2/6-311+G(2df,2p) :M08-HX/6-311+G(2df,2p))//ONIOM(MP2/6-31G(d,p):M08-HX/6-31G(d,p)) level of theory.

Parameters	TS1 (**II**)	TS2 (**IV**)	TS3 (**VI**)	TS4 (**VIII**)
Distances/Å				
O1-Hz	1.72	-	-	1.85
C1-Hz	1.19	-	-	2.67
C2-Hz/C2-H	1.78	-	1.14	1.87
C3-Hz/C3-H	2.65	-	1.73	1.14
C1-C2	1.40	1.49	1.52	1.47
C2-C3	1.46	1.38	1.42	1.42
C2-C4	2.50	1.81	1.52	1.47
C3-C4	1.54	1.77	2.50	2.52
C2-O1	-	-	-	3.18
C2-O2	2.79	3.07	3.26	-
C3-O2	-	2.77	2.40	-
Al-O1	1.75	1.72	1.73	1.75
Al-O2	1.71	1.70	1.74	1.70
Si1-O1	1.60	1.57	1.58	1.58
Si2-O2	1.58	1.57	1.60	1.57
Angles/°				
O1-Al-O2	97.0	100.6	98.8	97.8
Al-O1-Si1	138.9	143.8	146.0	139.3
Al-O2-Si2	148.1	148.2	142.2	149.7
Activation Energy/ kcal mol^{-1}				
E_a (37T)[a]	19.5	20.8	36.1	2.8

[a] $E_a = E_{transition\ state} - E_{intermediate}$

Activation Energies in kcal mol^{-1} (relative to the corresponding intermediate species)

As for the second step, the *2*-butoxide intermediate is converted into the isobutoxide intermediate via a cyclic transition state (**IV)** to yield isobutoxide **(V)**. At the transition state (**IV**), the C2-O2 covalent bond of 2-butoxide is cleaved. The methyl group, connected to the C3 carbon atom, moves toward the C2 atom. Such methyl group locates almost halfway in the direction between its position in the 2-butoxide and in the isobutoxide species (see Figure29b). The corresponding bond distances C4···C2, C4···C3 and C2···C3 are 1.81, 1.77 and 1.38 Å, respectively, and the C···O bond (C3-O2) corresponding to the formation of isobutoxide is 2.77 Å. It is noteworthy that the partial charge of the cyclopropyl cation transitions state is +0.913e and the largest positive charge is located on the C3 position as obtained by Mulliken population analysis. The calculated activation energy for this step (E_{a2}) is predicted to be 20.8 kcal/mol. The transition state (**IV**) is converted to isobutoxide (**V**) by breaking the C4-C3 bond and forming a new C4-C2 bond. The C3-O2 bond distance between isobutoxide and the zeolite framework is 1.53Å, which is slightly shorter than the C3-O2 bond distance of the *2*-butoxide by 0.03 Å. The isobutoxide intermediate is found to be lower in energy than that of the *2*-butoxide by 4.2 kcal/mol.

The breaking of the C3-O2 strong covalent bond results in the formation of the *tert*-butyl cation **(VII)** through a highly unstable primary isobutyl cation transition state (**VI**), for which the optimized transition-state structure is illustrated in Figure 28c. This step requires a high activation energy of 36.1 kcal/mol. The terminal C3 position of the highly unstable isobutyl cation transition state shows the largest positive charge and the partial charge of the butyl fragment is +0.853e. This result indicates that the primary isobutyl cation can be formed. Because the C2-H bond distance is 1.14 Å, whereas the C3-H bond distance is 1.73 Å at the transition state, it is reasonable to suppose that the hydride shift from the C2 to C3 position is still in an early stage. The vibrational analysis for this transition state yield only one imaginary frequency corresponding to the movement of the H atom from the C2 to C3 atom (Figure 29c). It strongly confirms that this species is a transition state but not an intermediate. In addition, there is a large distance between the H and O2 atom (2.55 Å) on the zeolite framework. Therefore, the proton should not be directly transferred back to the zeolite but should be shifted to the positively charged primary carbon to from either a tertiary butyl cation or tertiary butoxide. Although the *tert*-butyl cation and *tert*-butoxide in a zeolite cavities have not yet been found in experimental studies, many theoretical studies reported that they could

be presented as reactive intermediates[134]. In this study, the *tert*-butyl cation was observed as a reaction intermediate. The *tert*-butyl cation exists due to the steric hindrance between the bulky structure of the *tert*-butyl species and the local structure at the active site in which the closest bond distance between the tertiary C2 carbon atom and the O2 oxygen of the zeolite framework is 3.20 Å (as shown in Figure 27d). The structure of the *tert*-butyl cation is almost planar with all equivalent C-C bond lengths of 1.45 Å in good agreement with the literature (1.45 Å[134]). This intermediate is stabilized in the zeolite pore by the electrostatic interactions and the hydrogen bonds between the cation methyl group and the zeolite oxygen atoms. There are more than three possible hydrogen bonds between the *tert*-butyl cation and the zeolite framework with O-H distances below 2.5 Å (Figure 30). According to the Mulliken population analysis, the positive charge on the *tert*-butyl cation is about +0.89e and the C2 position carries most of this positive charge, +0.31e, confirming the tertiary carbocation species. This intermediate is more stable than the primary cation transition state (**VII**) by 22.9 kcal/mol, but it is less stable than isobutoxide and 2-butoxide by 13.2 and 9.0 kcal/mol, respectively. In this system, *tert*-butoxide was found with an energy higher by 4.6 kcal/mol compared to the *tert*-butyl cation. The *tert*-butyl species cannot easily gain access to the oxygen of the zeolite framework due to the high steric hindrance among the three methyl groups on the intermediate and the wall of the zeolite. Therefore, it is reasonable to consider the *tert*-butyl cation as a reaction intermediate.

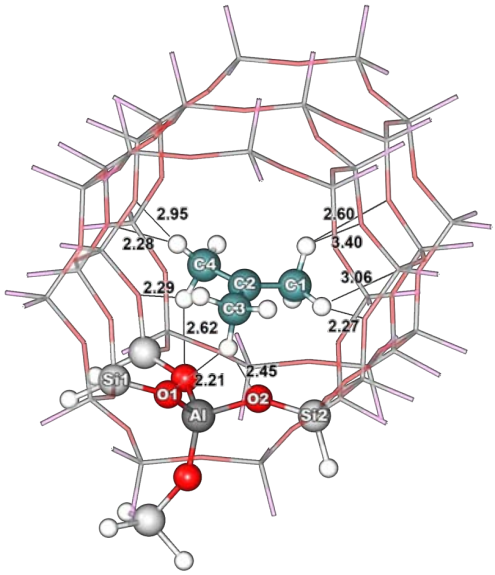

Figure 30. Illustrations of the hydrogen bonds among the cation methyl group and the zeolite oxygen of a *tert*-butyl cation stabilized in the zeolite cavity.

As for the last step, the *tert*-butyl carbenium ion is rapidly deprotonated to the zeolite through a tertiary carbocation-like transition state (**VIII**), resulting in the formations of an adsorbed isobutene complex (**IX**) over the Brønsted acid site. This step requires an activation energy (E_{a4}) of 2.8 kcal/mol, and the exothermic reaction of this step is observed with the energy of 12.8 kcal/mol. Our results agree well with the ones obtained from hybid MP2:DFT calculation in the H-FER system, where the activation energy is 3.3 kcal/mol and reaction energy is -14.4 kcal/mol[134].

With respect to the isobutene adsorption, the conversion of the *tert*-butyl cabenium ion into isobutene is one of two possible reverse reaction pathways of the isobutene protonation[127]. Two corresponding reaction pathways can occur, via either primary or tertiary carbocation-like transition states, depending on the carbon position of the isobutene where the proton is attracted to, leading to the production of the isobutoxide and tertiary alkoxide intermediates (*tert*-butyl cation), respectively. Rozanska and coworkers[127] calculated the activation energies of the isobutene protonation to be around 27.7-30.5 and 0.5-6.5 kcal/mol for the primary and tertiary transition states, respectively. They also reported that the isobutoxide is more stable than the tertiary species in zeolite pores due to the smaller steric constraint. Therefore, the reverse reaction of the protonation of isobutene (step IV in this study) can occur much more easily through a *tert*-butyl intermediate than through isobutoxide as expected from the low activation energies. This supports our proposed monomolecular mechanism for the skeletal isomerization of *1*-butene to isobutene through the *tert*-butyl carbenium ion.

From the energy profile of the monomolecular mechanism of the *1*-butene skeletal isomerization, the first two steps are facile and reversible, which is in keeping with the low activation barriers of 1.5 and 5.8 kcal/mol compared to the isolated *1*-butene and H-FER for the first step and second step, respectively. Similar relative energies are found for the three reaction intermediates (*1*-butene π -adsorption complex, *2*-butoxide and isobutoxide). This clearly shows that the conversion of isobutoxide to the *tert*-butyl cation intermediate via a 1,2-hydride shift transition state (**VI**) is the rate-determining step, with the corresponding activation energies of 36.1 kcal/mol. This step requires high activation energy to remove the strong covalent bond between the isobutoxide and the zeolite surface and to form the unstable primary isobutyl cation transition state. In order to compare the results with experimental data, the calculated apparent activation energy of the rate determining step was obtained from the relative stability of the transition state

compared with the isolated *1*-butene and zeolite. It was found to be 16.9 kcal/mol, which agrees well with the experimental value reported from a study of the monomolecular mechanism skeletal isomerization of *1*-butene to isobutene, for which the apparent activation energy for the rate of isobutene production is ~14 kcal/mol [102].

3.4 The effects of the zeolite framework on the stabilities of alkoxide species and the *tert*-butyl cation over H-FER

The effects of the zeolite framework on the relative stabilities of the reactive species in the monomolecular skeletal isomerization reaction mechanism of *1*-butene were demonstrated using 5T and 37T as models, thus excluding and including zeolite framework effects. In the 5T model, the adsorption complexes as well as the transition states and the intermediate species were treated at the MP2/6-31G(d,p) level of theory and the corresponding reaction energies were calculated at the MP2/6-311+G(2df,2p)//MP2/6-31G(d,p) level of theory.

Figure 31 and Table 13 show the optimized geometric parameters for *1*-butene and isobutene adsorbed over the 5T cluster active site. The adsorption energies of *1*-butene and isobutene were calculated to be -10.3 and -10.7 kcal/mol, respectively. Excluding the zeolite framework in the 5T model leads to an underestimation of the adsorption energies compared to those of the 37T model. Even though isobutene is bulkier than the *1*-butene isomer, the adsorption energy of isobutene is similar to that of the *1*-butene complex, indicating that the 5T model cannot correctly represent the shape selectivity of a medium pore zeolite.

As for the stabilities of the alkoxide and cation species, Figure 32 and Table 14 present selected geometries of the isobutoxide, *2*-butoxide, *tert*-butoxide, and *tert*-butyl cations. All these alkoxide species occur from a positively charged carbon atom of organic fragment, covalent forming a C-O bond with the basic oxygen atom of the framework. For the 5T model, the covalent C-O bond of *2*-butoxide, isobutoxide, and *tert*-butoxide are 1.52, 1.49 and 1.56 Å, respectively. Alkoxide species induce a decreasing of the Si-O-Al angle of zeolite structure for *2*-butoxide, isobutoxide, and *tert*-butoxide by 9.8°, 6.7° and 15.6°, respectively, resulting in the energies of intermediated species, which are in the order of *tert*-butoxide > *2*-butoxide > isobutoxide. For the

37Tcluster, the order of stabilities of the intermediated species is isobuoxide > *2*-butoxide >> *tert*-carbenium ion >*tert*-butoxide.

In order to compare the effects of different zeolite framework, the relative energies with respect to the *1*-butene adsorption complex were computed for both the 5T and 37T systems. The relative energy of isobutoxide adsorption is lower than that of *1*-butene complex by 3.7 and 1.2 kcal/mol for 5T and 37T, respectively. For *2*-butoxide, a similar trend can be observed for the relative energies. With respect to *1*-butene adsorption, they are -1.1 and 3.0 kcal/mol for 5T and 37T, respectively. The relative energy of *tert*-alkoxide is lower than that of the *1*-butene adsorption complex by -0.2 kcal/mol for 5T, but it is higher by 16.6 kcal/mol for 37T. The largest differences between 5T and 37T are the existence of *tert*-butyl carbenium cation in the 37T system, while this species cannot be observed as reaction intermediate for 5T model. This might be explained by the fact that when the extended zeolite framework is taken into account the steric hindrance at the active site is increased, resulting that the *tert*-alkoxide in 37T system is not stable. This circumstance leads to the existence of the *tert*-butyl carbenium cation as true intermediate instead of *tert*-alkoxide. The relative energy of such species is higher than that of the *1*-butene adsorption complex by 12 kcal/mol.

To summarize, the different stabilities of alkoxides for both models suggests that the confinement effect of the zeolite framework plays an important role on the stability of the alkoxide intermediates. The less steric hindrance is felt by the alkoxide intermediate, while the cation intermediate will be in the circumstance of high steric hindrance. As a result, among the alkoxide species, the isobutoxide is the lowest in energy while the *tert*-butoxide is the highest one.

From the literature, the relative energies of alkoxide intermediate were reported to be sensitive to the models, methods and relaxation criteria. For example, on one hand, the energies of alkoxide intermediate are reported in the order of *tert*-butoxide > isobutoxide >*2*-butoxide[111,115,152]. The relative energies of isobutoxide and the *tert*-butoxide, respectively, are higher than that of the *2*-butoxide by 0.7 kcal/mol[152], 2.0 kcal/mol[111], 2.6 kcal/mol[115] and 5.2 kcal/mol[152], 22.5 kcal/mol[115], 49.5 kcal/mol[111]. On the other hand, the isobutoxide was reported to be the stable intermediate[112,116] for which the relative energies are lower than those of the *2*-butoxide and the *tert*-butoxide, respectively, by 9.6 kcal/mol[112,116] and 22.5 kcal/mol[112], resulting in the energy in the order of *tert*-butoxide > *sec*-butoxide > isobutoxide.

Besides, the stability of the *tert*-butoxide, the *tert*-butyl carbenium ion, and the isobutoxide were also investigated with respect to the adsorption of isobutene on FER zeolite. Tuma and Sauer[130] reported that the reaction energy related to the isolated isobutene and the H-FER zeolite for the *tert*-butoxide, the *tert*-butyl carbenium ion, and the isobutoxide were -9.6, -6.4 and -15.1 kcal/mol. The *tert*-butyl carbenium ion was predicted to be a transient species in the zeolite system. Subsequently, however, the *tert*-butyl carbenium ion has been reported as a true intermediate by Rosenbach *et al.*[133] and Tuma *et al.*[134]. Rosenbach *et al.*[133] reported that the stabilities of the *tert*-butyl carbenium ion and *tert*-butoxide, calculated at the PBE1PBE/6-31G(d,p)//MP2:MINDO level of theory, are stable intermediates in the FAU zeolite. The *tert*-butyl cation is higher in energy than the *tert*-butoxide by 10.5 kcal/mol. Tuma *et al.*[134] investigated the stabilities of isobutene, the *tert*-butyl carbenium ion, *tert*-butoxide, and isobutoxide in ferrierite. The *tert*-butyl carbenium ion is reported to be a true intermediate, higher in energy than isobutene, *tert*-butoxide, and isobutoxide by 14.4, 5.7 and 12.2 kcal/mol, respectively.

Our results for 37T are in good agreement with the reports by Rosenbach *et al.*[133] and Tuma *et al.*[134]. The *tert*-butyl carbenium ion is a true intermediate in the system, while the *tert*-butyl carbenium ion is higher in energy than isobutene, *tert*-butoxide, and isobutoxide by 12.8, 4.6 and 13.2 kcal/mol. Finally, the *tert*-butyl cation is stabilized in the pore of the 37T H-FER zeolite as a truly stable intermediate rather than a transition state. This is due to the small pore size of the ferrierite, which is correctly represented by the extended framework in the 37T model, while it is omitted in 5T model.

Table 13. Selected geometric parameters and calculated adsorption energies (kcal/mol) for the 5T H-FER zeolite and the adsorbed π-complexes, obtained from the MP2/6-311+G(2df,2p)//MP2/6-31G(d,p) level of theory.

Parameters	H-FER	*1*-butene / H-FER **(I)**	Isobutene / H-FER **(IX)**
Distances/Å			
O1-Hz	0.97	0.98	0.98
C1-Hz	-	2.34	-
C2-Hz	-	2.26	2.48
C3-Hz	-	-	2.13
C=C	-	1.34	1.35
Al-Hz	2.27	2.33	2.34
Al-O1	1.90	1.88	1.87
Al-O2	1.69	1.69	1.69
Si1-O1	1.70	1.70	1.69
Si1-O2	1.62	1.61	1.62
Angles/°			
O1-Al-O2	88.6	91.4	90.8
Al-O1-Si1	142.5	141.3	141.9
Al-O2-Si2	144.3	147.0	145.8
Adsorption Energy/ kcal mol^{-1}			
E_{ads} [a]	-	-10.3	-10.7

[a] $E_{ads} = E_{olefin/\ H\text{-}FER} - E_{olefin} - E_{H\text{-}FER}$

Table 14. Selected geometric parameters and calculated energies (kcal/mol) for alkoxide species in the 5T H-FER zeolite obtained from optimization calculations at the MP2/6-31g(d,p) level of theory level of theory.

Parameters	*2*-butoxide(**III**)	isobutoxide(**V**)	*tert*-butoxide(**VII'**)
Distances/Å			
C-O	1.52	1.49	1.56
Al-O1	1.70	1.70	1.71
Al-O2	1.88	1.88	1.91
Si1-O1	1.61	1.62	1.61
Si2-O2	1.72	1.71	1.73
Angles/°			
C-O2-Al	119.2	109.2	118.5
O1-Al-O2	94.6	96.4	96.3
Al-O1-Si1	146.0	141.9	146.3
Al-O2-Si2	134.5	137.6	128.7
Relative energies, E_{rel}/ kcal mol^{-}			
E_{rel}[a]	-1.1	-3.7	-0.2

[a] $E_{rel} = E_{intermediate} - E_{1\text{-butene adsorption complex}}$
Relative energies, E_{rel}/ kcal mol^{-1} (with respect to *1*-butene adsorption over H-FER)

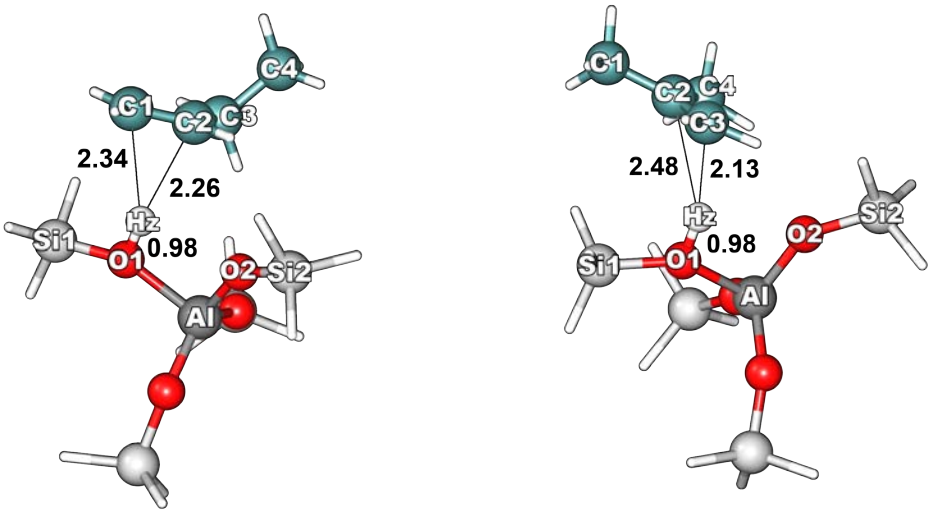

(a) (b)

Figure 31. The optimized structure of the adsorption complexes over 5T H-FER obtained from the MP2/6-31g(d,p) level of theory: (a) *1*-butene (reactant, **I**) and (b) isobutene (product, **IX**). Geometrical parameters are in Å.

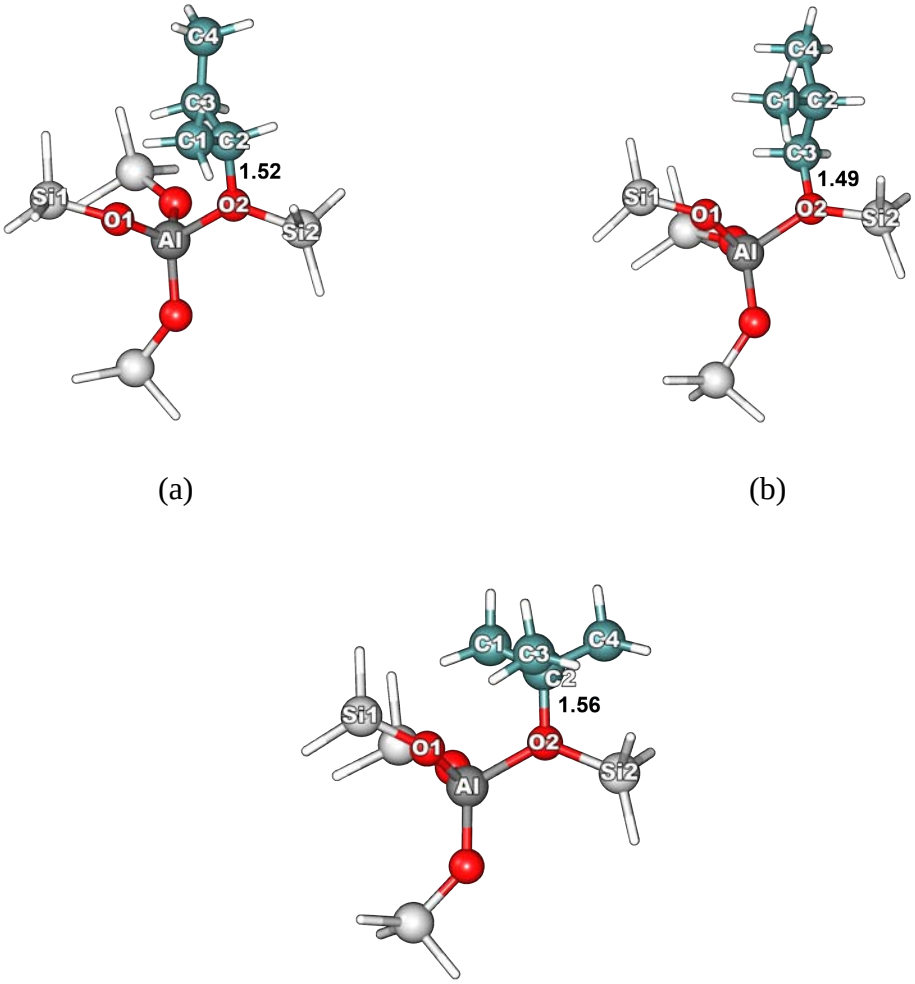

Figure 32. Optimized structure of (a) *2*-butoxide (**III**), (b) isobutoxide (**V**) and (c) *tert*-butoxide (**VII**) over the 5T H-FER model by from optimization calculations at the MP2/6-31g(d,p) level of theory. Geometrical parameters are in Å.

3.5 The effect of the zeolite framework on the monomolecular skeletal isomerization of *1*-butene

In this part of the work, the monomolecular mechanism of the *1*-butene skeletal isomerization is discussed in relation with effects of the zeolite framework. The proposed mechanism in 5T, neglecting the zeolite framework, is shown in Scheme 6. Figure 33 shows the complete reaction energy profiles for 5T model. Selected geometric parameters for the optimized structures of the transition states are shown in Table 15 and Figure 34.

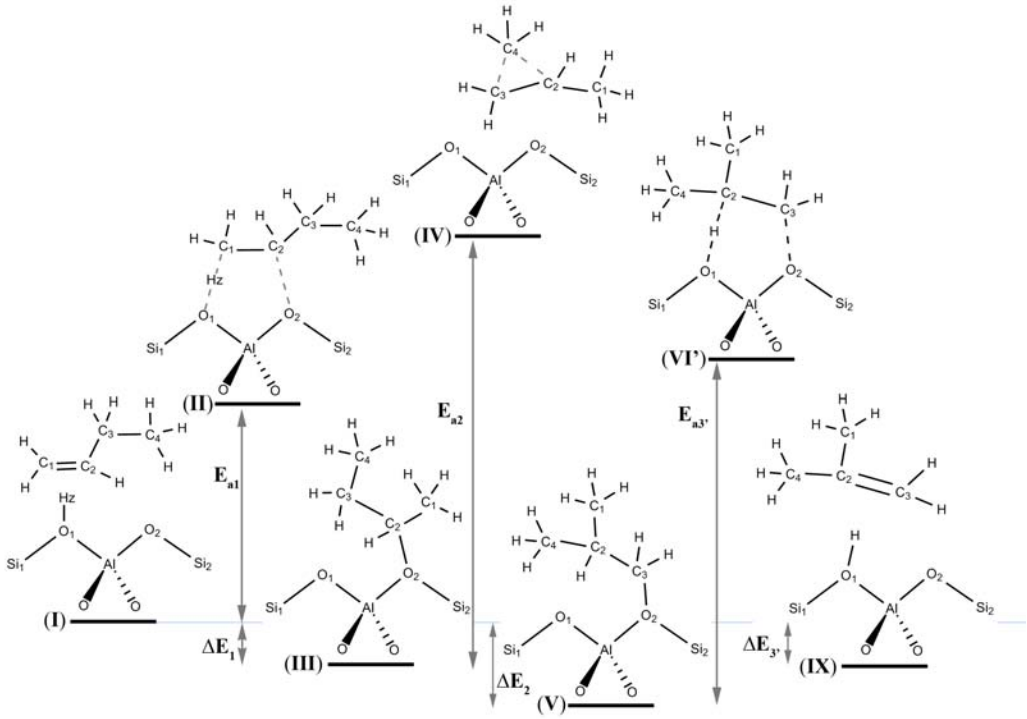

Scheme 6. Monomolecular mechanism for the skeletal isomerization of *1*-butene to isobutene using the 5T model.

As far as this mechanism is concerned, the first two steps are similar to those in the 37T model. Even though the structures of adsorption, transition state and intermediate complexes for both models are quite similar, the interaction energies are different due to the effects of the zeolite framework. The activation energies for the 5T model (27.2 and 37.8 kcal/mol for the protonation and branching step, respectively) are higher than those of the 37T systems (19.5 and 20.8 kcal/mol, respectively). This can be explained by the nature of the transition state structures that are typically more ionic than the

corresponding intermediates. As in the 37T model, the transition state structures undergo stronger stabilizing interactions by the zeolite framework compared to the intermediates. This was disregarded in the 5T model.

The differences between the 5T and 37T models begin at the third step of the mechanism in which the transformation of isobutoxide to isobutene occurs via two completely different pathways. In the 5T model, the isobutoxide intermediate can directly decompose to form the isobutene adsorption complex via transition state (**VI**). The alkoxide bond of isobutoxide species is dissociated and, simultaneously, a proton on the C2 tertiary carbon atom is transferred back to the zeolite O1 oxygen atom. In this step, both the O1 and O2 atoms of the zeoite participate. The negative charge on the O2 atom stabilizes the positive charge on the C3 atom, whereas the O1 atom abstracts a hydrogen atom from the C2 of the butyl transition state. The activation energy required for this step is 37.2 kcal/mol, which is less than that of the previous steps. As a result, the rate-determining step for the 5T model is the branching step in which *2*-butoxide transforms to isobutoxide with a required activation energy of 37.8 kcal/mol. Our results from the 5T model are in good agreement with the mechanism proposed by Boronat *et al.*[132], in which a small model was employed.

In contrast, the different mechanisms seen in the 37T model occur due to the restriction of the zeolite framework that prohibits the direct deprotonation of isobutoxide to isobutene. Hence, two consecutive steps are required for the transformation of isobutoxide to isobutene. The C3-O2 covalent bond of isobutoxide is dissociated, leading to the formation of a primary isobutyl carbenium ion transition state, which is stabilized by the interactions with the zeolite framework. At this transition state, the hydrogen atom (Hz) cannot be transferred to the oxygen atom of the zeolite framework due to the large distance between the hydrogen atoms on the C2 tertiary carbon atom and the O atom of zeolite framework so that the direct transfer of the hydrogen back to framework is prohibited. The hydrogen atom is, instead, transferred to the positively charged C3 carbon to form a tertiary butyl carbenium ion as a reactive intermediate. This intermediate is then rapidly decomposed to form isobutene. The rate-determining step is obtained from the formation of *tert*-butyl cation from isobutoxide via 1,2 hydride shift transition state and the activation energy is calculated to be 36.1 kcal/mol.

In conclusion, it is clearly demonstrated that the zeolite framework has a very strong influences on the structures and stabilities of reactive intermediates and transition

states, resulting in different mechanisms and different rate-determining steps in different zeolite models.

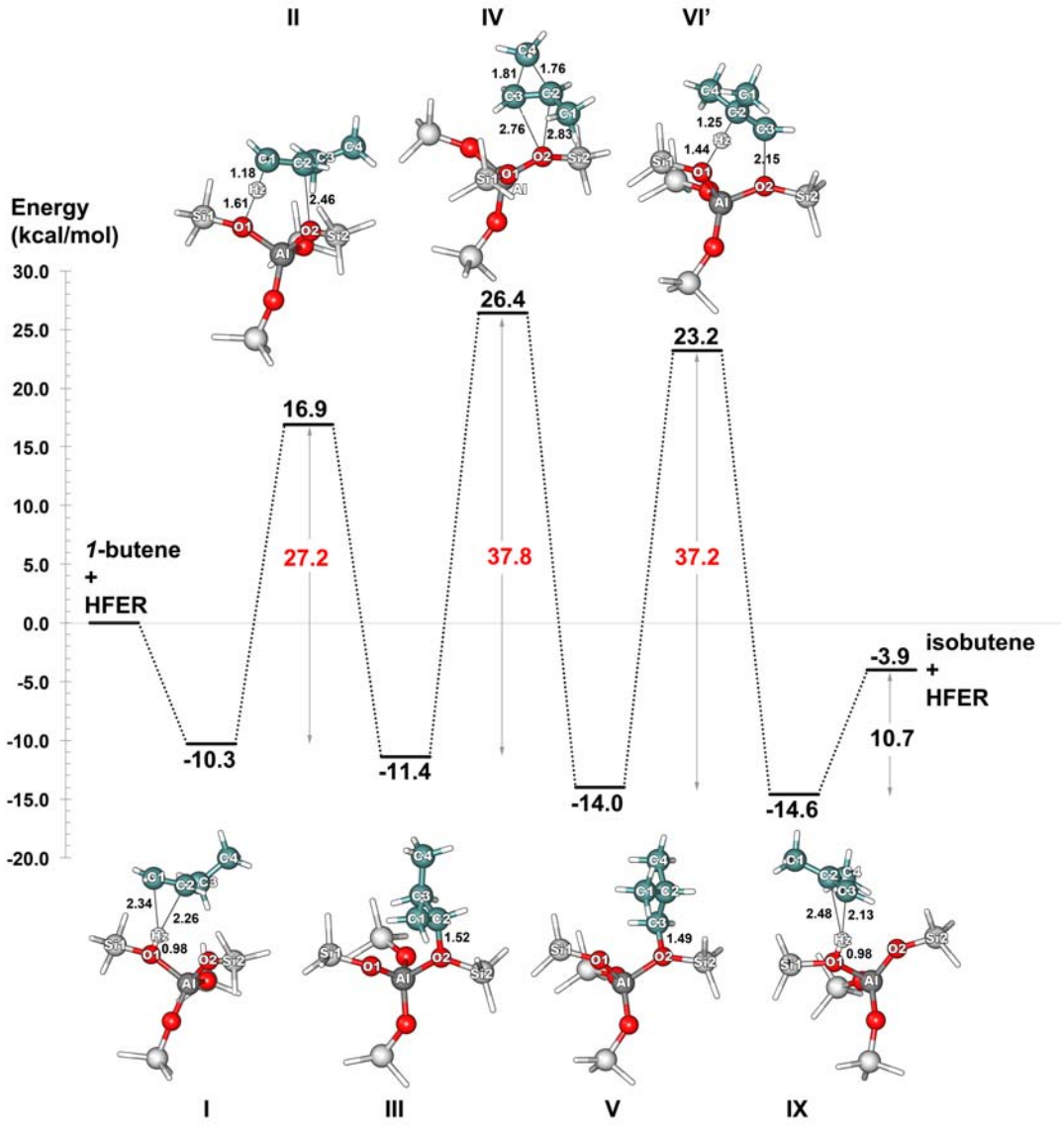

Figure 33. The reaction energy profile of the *1*-butene skeletal isomerization determined for the 5T H-FER zeolite model by optimization calculations at the MP2/6-31g(d,p) level of theory. Geometrical parameters and energies are in Å and kcal/mol, respectively.

Table 15. Selected geometric parameters and calculated energies (kcal/mol) for the transition states in the 5T H-FER model.

Parameters	TS1	TS2	TS3
Distances/Å			
O1-Hz	1.61	-	1.44
C1-Hz	1.18	-	2.20
C2-Hz/C2-H	1.93	-	1.25
C3-Hz/C3-H	2.78	-	1.93
C1-C2	1.41	1.49	1.52
C2-C3	1.46	1.39	1.40
C2-C4	2.50	1.76	1.53
C3-C4	1.53	1.81	2.48
C2-O2	2.46	2.83	2.96
C3-O2	3.06	2.76	2.15
Al-O1	1.76	1.74	1.78
Al-O2	1.73	1.72	1.74
Si1-O1	1.63	1.60	1.65
Si2-O2	1.62	1.60	1.63
Angles/°			
O1-Al-O2	96.6	99.5	94.2
Al-O1-Si1	140.4	143.6	139.3
Al-O2-Si2	144.3	147.8	145.5
Activation Energy/ kcal mol-1 (relative energies of intermediate species)			
E_a[a]	27.2	37.8	37.2

[a] $E_a = E_{\text{transition state}} - E_{intermediate}$

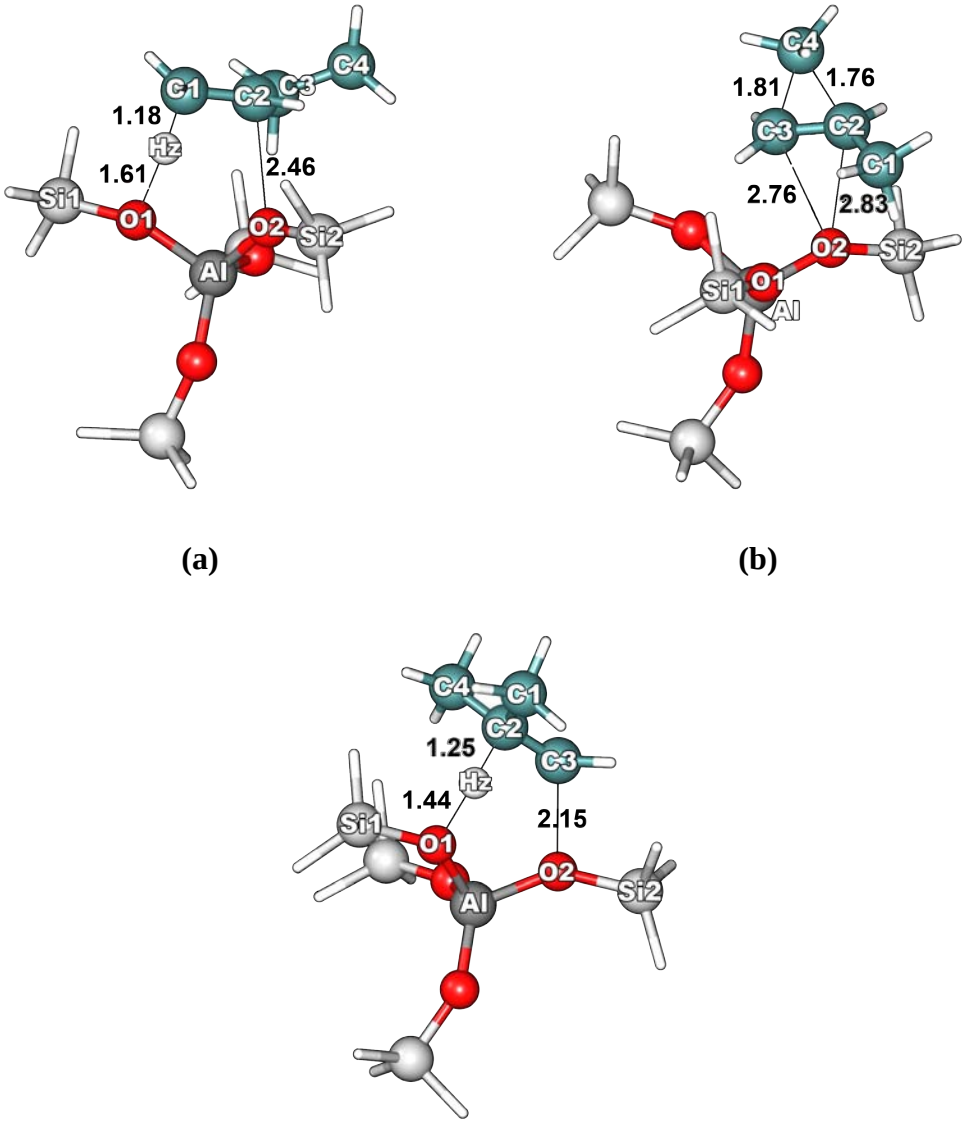

Figure 34. The optimized structures for the transition states (a) TS1 (**II**), (b) TS2 (**IV**) and (c) TS3 (**VI**) over the 5T H-FER model at the MP2/6-31g(d,p) level of theory. Geometrical parameters are in Å.

4. CONCLUSIONS

In this chapter, the complete monomolecular reaction mechanism for the skeletal isomerization of *1*-butene over H-FER was investigated by means of quantum mechanical calculations. The models and methods utilized here are well validated. The so-called 5T and 37T zeolite clusters were selected as models for the ferrierite zeolite in order to examine the influence of the zeolite framework. All calculations using the 37T H-FER model were performed at the ONIOM (MP2/6-311+G(2df,2p):M08-HX/6-311+G(2df,2p))//ONIOM(MP2/6-31G(d,p):M08-HX/6-31G(d,p)) level of theory, while the ones for the 5T H-FER models were carried out at the MP2/6-311+G(2df,2p)//MP2/6-31G(d,p) level. With 37T, the adsorption energies of *1*-butene and the isobutene complexes were calculated to be -18.0 and -14.8 kcal/mol, respectively. The zeolite framework differentiates between butene isomers, the lower adsorption energy of the isobutene complex, compared to *1*-butene, is observed due to the unfavorable steric hindrance of the branched isomer in the H-FER porous cavities. This cannot clearly see in 5T model in which the adsorption energies of *1*-butene and isobutene are -10.3 and -10.7 kcal/mol, respectively.

Monomolecular reaction has been proposed for the skeletal isomerization of *1*-butene[114]. However, two different mechanisms were found in the 5T and 37T models. In the 37T cluster, the monomolecular reaction mechanism proceeds through four transition state structures, namely the protonation of *1*-butene TS1(**II**), a cyclic transition state TS2(**IV**), the conversion of isobutoxide to a *tert*-butyl cation through the 1,2 hydride shift transition state (**VI**), and the deprotonation of the *tert*-butyl cation (**VIII**), with the corresponding intermediates; *2*-butoxide, isobutoxide and *tert*-butyl carbenium ion. The rate-determining step is found to be the decomposition of the surface isobutoxide intermediate through the highly unstable primary isobutyl carbenium ion transition state by an intramolecular 1,2-hydride shift with an activation energy of 36.1 kcal/mol, resulting in the formation of a *tert*-butyl cation as reactive intermediate. In contrast, the mechanism in the 5T model consisted of three transition state structures and three alkoxide species. The main difference in mechanisms between the 5T model and the 37T is that the isobutoxide (**V**) intermediate can be directly decomposed to form the isobutene adsorption complex. Moreover, the rate-determing step for the 5T model is the branching step in which *2*-butoxide transforms to isobutoxide with a required activation energy of 37.8 kcal/mol.

The confinement effect on the stabilities of the reaction intermediates as well as the transition states are also discussed. All alkoxide species find their origin in the positively charged carbon atom of the organic fragment, which covalently forms a C-O bond with the oxygen atom of the framework. The effects of the zeolite framework, in 37T model, show a major impact on the stabilization of the transition states, whereas bulkier alkoxide intermediate are destabilized, such that the stability of reaction intermediates is in the order of isobutoxide > *sec*-butoxide >> *tert*-butyl cation > *tert*-butoxide.

Attempts have been made in the literature in order to answer whether the question the *tert*-butyl cation in the reaction mechanism is a transition state structure or a true intermediate species. This investigation, using a medium-pore size ferrierite zeolite (H-FER), represented by 37T model, provides that the finding of *tert*-butyl carbenium cation as a true intermediate, which is in good agreement with the experimental and theoretical studies reported by Rosenbach *et al.*[133]. Our findings are also in agreement with the theoretical study, with sophisticated method, by Tuma *et al.*[134] This species cannot, however, be found when the effects of zeolite framework are neglected, i.e. in the 5T model.

Finally, this study indicates that the shape selectivity due to the "nano-confinement" effect of the zeolite framework strongly effects not only on the adsorption, the stabilities of reaction intermediates and the transition states, but also the mechanism of skeletal isomerization of *1*-butene in H-FER.

Chapter 3 ENANTIOSELECTIVE RECOGNITION AT METALLIC MESOPOROUS SURFACES

1. INTRODUCTION

Chirality refers to the property of an object that is not identical to its mirror image. In other words, the chiral molecule is a molecule that is not superimposable on its mirror image. The chiral molecule and its mirror images are called enantiomeric pair. Generally, the two enantiomeric compounds have identical physicochemical properties in an isotopic system, whereas they have dramatically different effects in the biological activity in an anisotropic environment[159]. Various biological molecules and medicines are currently used in the form of chiral structures in which one enantiomer might exhibit the desired pharmacologic effect, whereas the one is in the best case inactive or could be even toxic. It is therefore obvious that the studies related to the fabrication, the development and the application of chiral interface materials dramatically increased in recent years.

There are various methods that have been used to fabricate chiral surfaces, such as generating an intrinsically chiral surface on a crystal, the adsorption of molecules on a surface, polymeric chiral interfaces based on surface-grafting and molecular imprinting[160-164]. Although chiral surfaces have been successfully obtained by many different approaches, the most popular one is based on molecular imprinting with chiral molecules as templates[160-163]. This approach allows designing chiral materials having specific recognition properties, corresponding to the template structure[165,166]. Particularly, the molecular imprinting technique has been widely used to elaborate chiral surfaces on soft materials such as polymers[167]. However, molecularly imprinted polymers (MIPs) often suffers from some disadvantages, such as difficult template removal, poor mass transfer, low binding constants, slow binding kinetics and high flexibility of the polymer, which results in the destruction of the chiral structure of the cavity after removable of the template[168,169].

An alternative way of designing materials with a chiral interface is the generation of chirality on metallic surfaces[170]. Chiral metal surfaces have been studied over the past decade, and were mainly obtained by one of the following approaches[171]. (I) the chiral

surface can be fabricated on the metal surface by cutting a bulk metal along a low symmetry plane, resulting in the formation of the metal surface with a high Miller index and the absence of mirror symmetry[172,173]. Although the face-centered cubic (fcc) structure of many transition metals such as Cu, Ni, Pt, etc are achiral, the two enantiomers of chiral metal surface can be formed by cutting a bulk metal along a low symmetry plane. For example, the structures of (643) and ($\overline{6}\overline{4}3$) of Pt and Cu are enantiomeric pairs[174]. (II) chiral metal interfaces have been created by the molecular adsorption on crystalline surfaces[170,175]. The molecular adsorption approach is categorized into different ways such as achiral molecules adsorbed on achiral surfaces, chiral molecules adsorbed on achiral surfaces and chiral molecules adsorbed on chiral surfaces. An achiral molecule adsorbed on an achiral surface is able to generate a chiral surface because the symmetry of the adsorption system of adsorbate and substrate is reduced compared to that of an isolated system. For example, two enantiomers of chiral surfaces have been observed via the loss of mirror symmetry due to the adsorption of 4-[trans-2-(pyrid-4-yl-vinyl)]benzoic acid (PVBA) on the substrate (see Figure 1.3 in ref [170]). In the case of the adsorption of chiral molecules on achiral surfaces, chiral surfaces could be successfully designed when the structure and conformation of chiral molecules are retained after adsorption on achiral surface. The limitation of the molecular adsorption on the achiral substrate for designing the chiral surfaces is that the adsorbed chiral molecule can desorb, resulting in weak or no surface chirality[176]. As stated above, an intrinsically chiral metal surface can be generated due to the presence of chiral kink sites or a high Miller index on certain surfaces like in the case of (643) and ($\overline{6}\overline{4}3$) enantiomorphic structures of Pt, however this approach is rather tedious and might be difficult to apply for real applications. Therefore, an imprinting approach is expected to be the alternative method that could be used to produce an intrinsically chiral metal surface, retaining its enantioselectivity even after removal of a chiral template.

There are a few studies that reported metal surfaces with a chiral character, based on the chiral imprinting approach. For instance, the electrodeposition of a copper oxide film in the presence of chiral tartrate ions produced a chiral surface film on an achiral gold surface. It has been shown that this material retained the chirality of the molecules and exhibited enantioselective electrochemical oxidation of tartrate enantiomers, but with a moderate selectivity[177]. In addition, the entrapment of chiral molecules in Pd, Au, Pt and Ag has been reported[178-180].

Although a few works have attempted to study the chirality at metal surfaces after removable of chiral template, enantioselective recognition is not pronounced or even inexistent in some cases[178,180]. One reason for low enantioselectivity might be that the enantioselective recognition has been studied on flat metal surfaces, which exhibit a relatively small surface area and therefore a small number of imprinted recognition sites. Therefore, the enantioselective recognition ability might be improved on porous surfaces.

Mesoporous materials have the pore cavities in the range of 2-50 nm (IUPAC definition)[181]. They play an important role for a wide range of potential applications, such as catalysis[182,183], electronic devices[184,185], chemical detection[186] and drug-delivery[187]. This is due to their outstanding features, such as a high surface area, high stability, well-defined and tunable pore size as well as a predefined organization[188]. Therefore, many mesoporous materials have been designed, including mesoporous carbon[189], mesoporous silica[190] and mesoporous metals[191]. Mesoporous metals remarkably improve the accessibility of guest molecules into of the metallic framework. Generally, mesoporous metals have been successfully prepared by two major approaches: (i) hard template approach, which is based on using mesoporous silica or carbon as the mesopore-template[191], (ii) soft template approach. The soft template approach has been widely used to prepare mesoporous metals because the structures of the mesoporous cavities are controlled in a straightforward way by the mesostructure of Lyotropic Liquid Crystals (LLC), which can be adjusted by the molecular structure of surfactant, concentration and temperature. An increase in surfactant concentration results in the changing the template structure from a micellar (L_I), micellar cubic (I_I), hexagonal (H_I), bicontinuous cubic (V_I), lamellar (L_α) to inverse micellar shape (L_2)[191].

The reduction of metal salts around the LLC mesostructure allows producing the mesoporous metals. The reduction rate is an important parameter to control the quality of the mesoporous structure in metals. Typically, mesoporous metals have been successfully achieved by two methods: electroless deposition and electrodepositon. In the electroless deposition process, the deposition rate depends on the nature of the reducing agent. The deposition rate is very high when sodium borohydride is used as reducing agent for preparation of mesoporous Ni, resulting in the formation of disordered mesoporous structure. Compared to sodium borohydride, the deposition rate with dimethylaminoborane is much lower, leading to the formation of an ordered-mesostructure[191,192]. In the case of electrodeposition, the deposition rate strongly depends

on the chosen potential. At high overpotentials, the deposition rate extremely increases, resulting in the formation of disordered mesostructures. Attard and coworkers have successfully prepared highly ordered mesoporous Pt by the electrodeposition approach using LLC as a porogen[193].

It is very interesting to combine the advantages of mesoporous metal structures with chiral features. The fabrication of mesoporous chiral metal surfaces has not, to our knowledge, been demonstrated previously, despite the two-fold advantage of an active surface area that can be two to three orders of magnitude higher compared to flat surfaces, and an easy access of the chiral target molecule to the recognition sites. In addition, the electrodeposition method is very useful to control the structure of mesoporous metals by choosing the right applied potentials. In this chapter, the designing of mesoporous chiral metal surfaces based on the imprinting method has been investigated by electrodeposition of metal around lyotropic liquid crystal (LLC) mesostructures in the presence of chiral templates.

There are many established techniques for enantioselective recognition analysis such as high-performance liquid chromatography (HPLC), gas chromatography (GC), capillary electrophoresis (CE), quartz crystal microbalance and electrochemical methods. In contemporary analytical techniques such as HPLC and GC with chiral stationary phase, these approaches have been achieved by the presence of chiral selectors, which form a complex with the analyte and this leads to the fact that the equilibrium constants of formation or dissociation of the enantiomers and the chiral selector are different[194]. The electrochemical method is an alternative technique, which is an important and powerful technique for enantioselective recognition studies, especially in the frame of electrochemical sensor design[195]. For example, chiral penicillamine modified gold nanoparticles immobilized on gold electrodes exhibit a different electrochemical behavior for enantioselective recognition of 3,4-dihydroxyphenylalanine (DOPA) when using cyclic voltammetry[196].

In addition to the different interactions of each enantiomer and the chiral selector, chiral molecules are optically active species, which have different responses with respect to left- and right-hand circularly polarized light. One of the optical techniques for chiral surface characterisation is secondary-harmonic generation (SHG) of chiral thin films on surfaces. Basically, the intensity of the generated secondary-harmonic light will be different for left- and right-hand circularly polarized excitation when chiral surfaces are

exposed to circularly-polarized light[197,198]. This technique can be an alternative way to confirm the chirality of a thin film on a surface.

In this work, the fabrication of chiral imprinted mesoporous platinum films has been studied by the electrodeposition of Pt salts in the presence of a LLC phase and chiral molecules. Due to the introduction of both, mesoporous features and specific chiral cavities, these novel materials are expected to exhibit not only a dramatic increase in active surface area due to their mesoporosity, but also might retain the chirality at the mesoporous surfaces even after template removal. The characterisation of chiral surfaces and enantioselective recognition was studied by many techniques such as electrochemistry, high-performance liquid chromatography (HPLC) and secondary-harmonic generation (SHG). In addition, we discuss the effect of important parameters, grow around the removable matrix, quantity of chiral molecules, mesoporosity and electrodeposition time for imprinting the chirality at the mesoporous surface. This work opens the door for the design of chiral surfaces on mesoporous metals and such nanostructured materials could lead to the development of novel materials for applications in areas like chiral synthesis, separation, purification, sensing and drug development.

2. EXPERIMENTAL METHODS

2.1 Preparation of chiral imprinted mesoporous platinum electrodes

According to the literature procedures for the preparation of mesoporous platinum films from a lyotropic liquid crystalline phase[199], mesoporous platinum films were prepared by an electrochemical reduction of platinum salts dissolved in a liquid crystalline phase at -0.1 V (Ag/AgCl(sat. KCl) as reference electrode) on gold-coated glass slides (0.25 cm^2). Such a mesoporous platinum film is called a non-imprinted mesoporous platinum film throughout this thesis. Typically, the plating mixtures were a ternary system composed of 42 wt% of the nonionic surfactant polyoxyethylene (10) cetyl ether (Brij® 56) (Sigma-Aldrich), 29 wt% of hexachloroplatinic acid (Sigma-Aldrich) and 29 wt% of milli-Q water.

In the case of chiral imprinted mesoporous platinum films, the liquid crystal plating mixtures were prepared as a quaternary system composed of 42 wt% of nonionic surfactant polyoxyethylene (10) cetyl ether (Brij® 56), 29 wt% of chloroplatinic acid, 29 wt% of milli-Q water and the desired amount of L-DOPA or D-DOPA (Sigma-Aldrich). The electrochemical reduction of platinum salts in the presence of surfactant and DOPA enantiomer was carried out at -0.1 V on gold-coated glass slides (0.25 cm^2). After the electrodeposition process, the prepared samples were rinsed with a large amount of water in order to remove the surfactant and the chiral template. In order to ensure that all chiral molecules were completely removed, all electrodes where checked by differential pulse voltammetry (DPV) in 50 mM HCl (J.T. Baker) for the electrochemical signal of eventually remaining DOPA. Only completely DOPA free electrodes were used for the subsequent experiments.

In order to compare the enantioselective recognition activity of chiral imprinted mesoporous platinum electrodes and chiral imprinted non-mesoporous platinum electrodes, a chiral imprinted non-mesoporous platinum film was prepared by electrodeposition at -0.1 V in an aqueous mixture of 60 mM chloroplatinic acid and L-DOPA (L-DOPA/Pt = 1/25) without adding surfactant.

2.2 Characterisation of chiral imprinted mesoporous platinum electrodes

In order to investigate the morphologies and porosities of chiral imprinted mesoporous platinum films, SEM and TEM experiments were carried out on a Hitachi TM-1000 tabletop microscope and a JEOL JEM-2010 TEM for SEM and TEM experiments, respectively. For TEM measurements, chiral imprinted mesoporous platinum films on Au-coated glass slides were exposed to an aqueous solution of 4 wt% KI and 1 wt% I_2 for 20 min in order to dissolve the underlying Au layer. The Pt film could then be easily removed from the electrode and floated on the water surface after slow immersion of the samples into DI water. The freestanding films were then transferred onto TEM grids.

The active surface area of platinum electrodes can be estimated from cyclic voltammetry in 0.5 M H_2SO_4. The electrochemical experiments were performed with a μ-Autolab Type III using Ag/AgCl (sat. KCl), a Pt mesh and the prepared mesoporous electrodes as reference, counter and working electrodes, respectively. The cyclic voltammograms were carried out by scanning the potential between -0.25 V and +1.25 V in 0.5 M H_2SO_4 at a scan rate of 100 mVs^{-1}.

2.3 Enantioselective recognition at chiral imprinted mesoporous platinum electrodes and characterisation of chiral mesoporous surfaces

In order to investigate the enantioselective recognition at chiral mesoporous platinum surfaces, two independent chiral recognition studies were carried out. The first experiment was based on an electrochemical method. It was performed with a μ-Autolab Type III using Ag/AgCl (sat. KCl), a Pt mesh and the prepared mesoporous electrodes as reference, counter and working electrodes, respectively, using differential pulse voltammetry (DPV). The parameters of the DPV used here were a pulse modulation of +50 mV in amplitude, a pulse duration of 50 ms and an interval time of 0.1 s.

In addition, the chiral imprinted mesoporous platinum film was characterized by secondary-harmonic generation. The beam of a Nd:YAG laser (1064 nm, 20 Hz) was used. Initially polarized out of the plane of incidence (s), the beam was passed through a combination of two wave plates (half-wave plate and quarter-wave plate) in order to change the polarization states from linear, elliptical to circular polarized by rotating a half-wave plate and fixing a quarter-wave plate (see Scheme 8). The p-polarized and s-

polarized SHG responses were measured as a function of the wave plate angle. In this experiment, both transmitted and reflected secondary harmonic responses were investigated. In the case of reflection mode measurements, a chiral imprinted mesoporous platinum film was deposited on Au-coated glass slide by using the electrodeposition of liquid crystal plating mixtures as mentioned above. In contrast, in transmission mode measurements a chiral imprinted mesoporous platinum film was coated on an ITO electrode, acting as transparent electrode, by using the liquid crystal plating mixture.

Furthermore, the enantioselective adsorption experiments of a racemic mixture of DL-DOPA on the chiral imprinted mesoporous platinum layers (0.25 cm^2) were studied by monitoring the composition of the supernatant solution by high-performance liquid chromatography (HPLC). In this experiment, the dry prepared electrodes were immersed into 100 μM of racemix mixture of DL-DOPA for different periods of time. The remaining supernatant solution was collected and analyzed by HPLC. The HPLC analysis was performed on a Merck L-6200A instrument with detection at 230 nm using an UV detector (Model L-4000A). The HPLC analytical assays were carried out on a 150 mm x 3 mm ID CHIRALPAK ZWIX (+) column (Chiral Technologies Europe). All analytes were performed at a flow rate of 0.5 mL/min, using a mixture of 50/50 (v/v) methanol/acetonitrile, 50 mM formic acid and 25 mM diethylamine as mobile phase. Prior to HPLC analysis of all samples, the remaining supernatant solution was evaporated to remove aqueous solvent, and redissolved in the mobile phase (a mixture of 50/50 (v/v) methanol/acetonitrile and 50 mM formic acid as well as 25 mM diethylamine).

3. RESULTS AND DISCUSSIONS

3.1 The electrodeposition of mesoporous platinum films and the control of the mesoporous structure by lyotropic liquid crystal templating

Liquid crystals (LCs) exhibit the combined properties of the order of a crystalline solid and the mobility of a liquid phase. Liquid crystalline materials are important candidates for the synthesis of nanostructured materials, which have been widely used in the potential applications such as sensors, displays, drug delivery and optical instruments[200-201]. Owing to the behavior of LCs like a liquid phase but orientation of molecules like in a solid phase, there are many shapes of LCs depending on the orientation of molecules in LCs. Generally, LCs are divided into two types: there are thermotropic and lyotropic LC phases. Thermotropic LC phases, mostly composed of non-amphiphilic anisomeric compounds, are sensitive to temperature changes and do not need solvent to form LCs structures, whereas lyotropic LC phases are based on amphiphilic compounds which form the LC phase in solution and show a phase transition controlled by temperature and concentration [202,203].

Lyotropic LC phase formation is taking place by the self-assembly of hydrophobic or hydrophilic parts of surfactant and solvent. The surfactant can form various types of lyotropic LC phases, depending on temperature and concentration as shown in Scheme 7. In the case of an aqueous medium, the polar part of the surfactant is dissolved in the solvent, while the non-polar part of the surfactant is segregated in order to form a micellar structure when the concentration reaches the critical micelle concentration (L_1 phase). Increasing the concentration of surfactant molecules results in the transformation of lyotropic LC phases from micellar (L_1) to hexagonal (H_1). The further increase of surfactant concentration causes to formation of interwoven networks (V_1). These networks transform into a lamellar phase (L_α) at higher concentrations[200,203].

Because lyotropic LC phases can be organized in various structures and easily transformed form one into another structure, many different mesoporous materials have been successfully prepared using lyotropic LC phases as mesopore-template to control the structure of mesoporous silica[190], mesoporous carbon[189] and mesoporous metals[199] for which mesoporous structures have been observed after removable of the lyotropic LC phase.

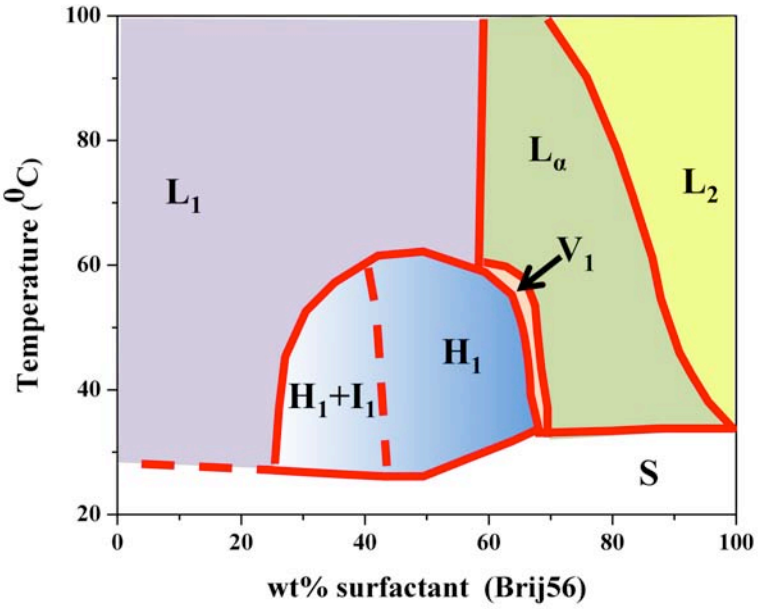

Scheme 7. Phase diagram of lyotropic liquid crystal structures for the nonionic surfactant (Brij56): L_1 = micellar phase, I_1 = micellar cubic phase, H_1 = hexagonal phase, V_1 = cubic phase, L_α = lamellar phase and L_2 = inverse micellar phase and S = solid phase. Reproduced from Ref. [204].

There are many mesoporous metals that have been fabricated by using lyotropic LC phases such as Pt, Ni, Cu, Pd and Ag. Several reports have focused on the fabrication of ordered-mesoporous metals. There are two parameters that strongly affect the degree of order of mesoporous metals: (1) the stability of the lyotropic LC phase in the presence of metal ions and (2) the reduction of metal salts around the lyotropic LC phase[191]. As for the stability of the lyotropic LC phase, a stabilization of metal ion complexes in lyotropic LC phases is observed because the aqueous metal complex is formed by the coordination of metal ions and water molecules, resulting in hydrogen bond formation between aqueous metal complex and the ethylene glycol group of the surfactant[191,205]. However, changing the mole ratio of surfactant and metal ions results in the phase transformation of lyotropic LC phases. Therefore, optimization of the concentration of surfactant and metal ions is necessary to reach a high degree of order of mesoporous metal[191].

In addition to the stability of lyotropic LC phases in the presence of metal ions, the reduction rate also plays an important role for the formation of mesoporous order. The reduction process has been successfully carried out by either electroless or

electrodeposition approaches [192,199]. As for the electroless method, the deposition rate can be controlled by the nature of the reducing agent. For example, Yamauchi and coworkers reported that highly ordered mesoporous Ni was obtained by the electroless procedure when the deposition speed was low, for example when using dimethylaminoborane (DMAB) as reducing agent, whereas disordered mesoporous Ni was observed at high deposition rate using sodium borohydride-SBH as reducing agent [192]. Because high deposition rate results in the formation of a high number of nuclei, the rapid growth of these nuclei leads to disordered mesoporous structures. Similarly, the order of the structure of mesoporous metal films obtained by the electrodeposition method was controlled by the deposition rate, related to the electrodeposition potential. Mesoporous platinum has been first obtained by the electrodepositon method in the presence of a lyotropic liquid crystal phase[199]. Attard and coworkers reported not only a high active surface area of mesoporous platinum, but also a highly ordered structure. Currently, many mesoporous metallic structures such as from Co, Ni, Pd, Rh, Ru, Ag, Cd, Sn and alloys of these metals have been widely reported[191,206]. However, some metals can be easily oxidized by air such as Ni, resulting in the collapse of the mesoporous structure[191]. In addition, the properties of magnetic mesoporous metal films obtained by electrodeposition from lyotropic liquid crystalline phases were studied. Compared to nonporous polycrystalline films, the magnetic measurements of mesoporous Ni and Co show higher coercivity (Hc)[207]. It therefore clearly shows that mesoporous metals obtained by the electrodeposition method from lyotropic liquid crystalline phases have been attracted much attention and these materials seem to be promising candidates for a wide range of applications.

There are many mesoporous metals that have been successfully prepared by several nonionic surfactants. For example, the average pore diameter of mesoporous platinum obtained by an electrochemical method using $C_{12}EO_8$ was 17.5 Å, whereas the average pore diameter of mesoporous platinum using quaternary mixture of $C_{16}EO_8$ and *n*-heptane ($C_{16}EO_8$:*n*-heptane= 2:1) was 35 Å. This result indicates that the mesopore size directly depends on the chain length of the surfactants or using a hydrophobic additive to form larger structures of LLC[199]. In addition, the bigger surfactants such as $C_{16}EO_{10}$ (Brij® 56) and $C_{18}EO_{10}$ (Brij® 76) were used as the template for mesoporous metals[194,208]. A 2D hexagonal mesoporous platinum film has been successfully prepared by the electrodeposition method in the presence of $C_{16}EO_{10}$ (Brij® 56) as lyotropic liquid

crystal phase[208,209]. It has been also demonstrated that in-plane pore alignment of 2D hexagonal meoporous structures can be easily controlled by using shear force[208].

As for the electrodeposition process of platinum, it has been proposed that the electroreduction of platinum cation may involve two steps processes as following:

1. $[Pt(Cl)_6]^{2-} + 2e^- \rightarrow [Pt(Cl)_4]^{2-} + 2Cl^-$
2. $[Pt(Cl)_4]^{2-} + 2e^- \rightarrow Pt + 2Cl^-$

Elliott and coworkers reported that the current potential curve of electroreduction of platinum cation in the presence of lyotropic LC phase shows two characteristic peaks, corresponding to the participation of $[Pt(Cl)_4]^{2-}$ during the electrodeposition process (see Figure 2b in ref [210]). Furthermore, they suggested that the highly ordered well-controlled porosity of mesoporous Pt can be observed only when the electrodeposition condition (e.g. the electrodeposition potential and temperatures) are controlled in order to avoid side reactions and the optimum condition of electrodepositon process should be controlled in the range of -0.1 to -0.2 V vs SCE at 25°C in order to gain both high surface area and ordered nanostructure [210].

In this work, a nonionic surfactant of polyoxyethylene (10) cetyl ether $C_{16}EO_{10}$ or (Brij® 56) was used to form a lyotropic liquid crystal phase in aqueous solution. The chiral imprinted mesoporous platinum films have been successfully made by an electrodeposition method in the simultaneous presence of a lyotropic liquid crystal phase and chiral molecules, which serve as a template to generate the mesopores, and as a template to create a chiral cavity in the walls of the mesopores, respectively. The final mesopores of mesoporous platinum are aligned in a hexagonal lattice[199,208]. The electrochemical reduction of metal salt occurs around the lyotropic crystal phase and the chiral molecules, resulting in the formation of mesoporous channels and chiral cavities at their inner surface after the removal of these templates as shown in Scheme 8 for preparation process.

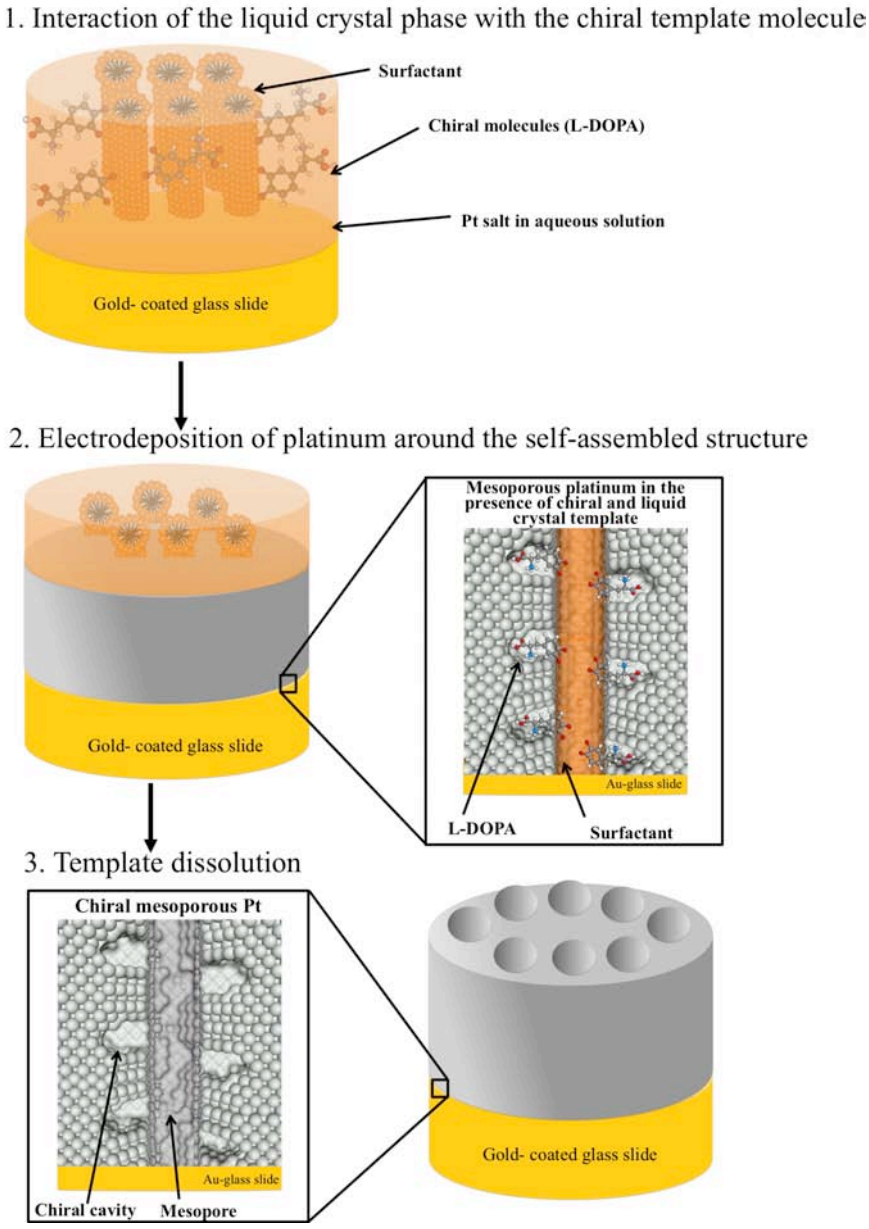

Scheme 8. Illustration of the fabrication process of chiral imprinted mesoporous platinum films on gold-coated glass electrodes.

In this work, $C_{16}EO_{10}$ and DOPA enantiomers have been chosen as lyotropic liquid crystalline template and chiral template, respectively (Figures 36a and 36b). DOPA enantiomers were used as chiral templates because L-DOPA plays for example a key role in pharmaceutics and neurochemistry[211]. The two enantiomers of 3,4-dihydroxyphenylalanine (DOPA) are chiral drugs and exhibit different pharmacological and pharmacokinetic activities. L-DOPA is efficient for the treatment of Parkinson

disease, because the correct chiral enantiomer structure binds with enzymes and receptors consisting of amino acids and other chiral biomolecules, while D-DOPA is not only inactive but also strongly toxic, leading to agranulocytosis[212]. In addition, DOPA and other catechol compounds have also been employed as reactants to modify not only inorganic but also biological materials[213-215]. Therefore, the transfer of the chiral features from a DOPA enantiomer to the internal pore walls of mesoporous platinum via imprinting is an interesting choice for this first proof-of-principle study. An additional reason for using DOPA molecules as chiral templates is that its electroactivity is compatible with the potential window where platinum is subject to neither oxidation nor hydrogen adsorption or evolution. Therefore when it is used as a probe molecule after the imprinting, its reaction on the platinum electrode can be easily monitored without altering the metal structure. It is important to note that the mixture of surfactant and DOPA contains also $PtCl_6^{2-}$ as platinum precursor which can undergo a chemical redox reaction with DOPA molecules before the electrodeposition process. This is confirmed by the color of $PtCl_6^{2-}$ turning to brown after adding DOPA (Figure 35). Due to the strong oxidizing character of the platinum salt[216], the two hydroxyl groups that are located on the aromatic ring of DOPA will be transformed into their quinoic form (Figure 36c). In addition, DOPA molecules are also pH-sensitive (Figure 37), and the electrodeposition is carried out in a mixture which has a pH=2, therefore the fully protonated form of quinoic DOPA is expected to act as the chiral template of this imprinted material.

Figure 35. Optical photograph of 60 mM H_2PtCl_6 (right) before adding L-DOPA and (left) after adding L-DOPA.

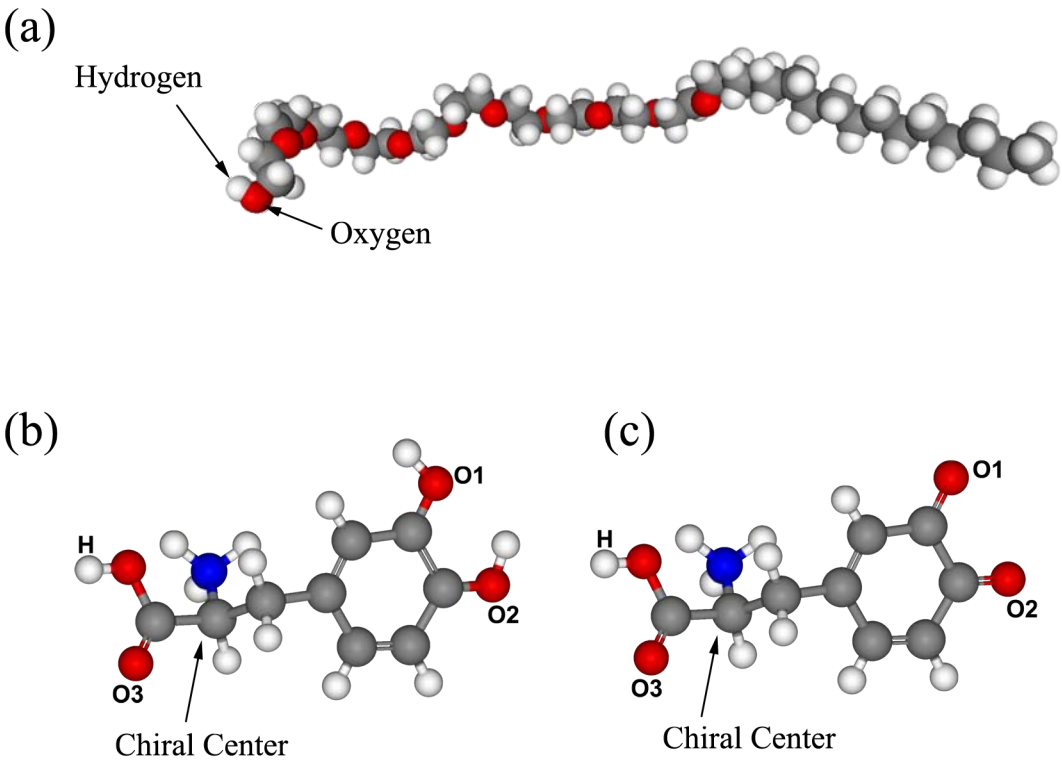

Figure 36. Illustration of structures of (a) $C_{16}EO_{10}$ (Brij®56) (b) 3,4-L-dihydroxyphenylalanine (L-DOPA) and (c), oxidized form of L-DOPA (quinoic form).

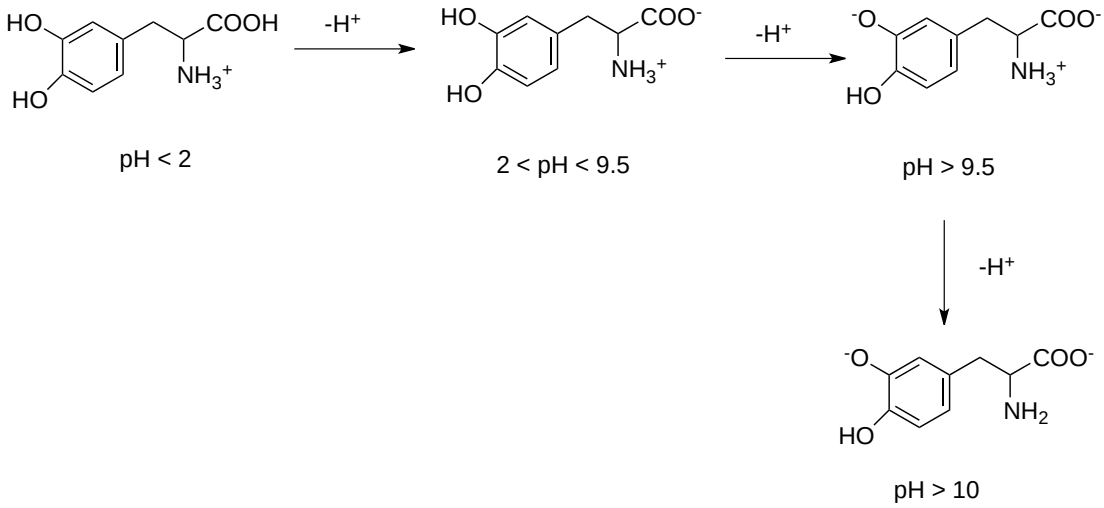

Figure 37. The effect of pH on DOPA structure

3.2 Surface area measurements of platinum electrodes obtained by cyclic voltammetry (CV)

To calculate the active surface area of platinum and gold electrodes, cyclic voltammetry was carried out in 0.5 M H_2SO_4 at a scan rate of 100 mV/s in the potential window from -2.5 to +1.25 V. In the case of gold coated-glass slide electrodes, the oxide formation region and oxide reduction appear at +0.6 and +0.5 V vs Ag/AgCl, respectively, as shown in Figure 38. Oxygen evolution from water oxidation was observed at a potential above +1.1 V. However, after the electrodeposition of mesoporous platinum on the gold electrode, the cyclic voltammogram was completely changed as shown in Figure 39. The different amplitudes of redox currents of deposited mesoporous platinum and of gold were clearly observed, confirming that the deposit of polycrystalline Pt covered the gold electrode. The voltammogram of mesoporous platinum exhibited the characteristic features of polycrystalline platinum, composed of the oxidation and reduction of Pt and PtO_n, respectively. In addition, on the mesoporous platinum electrode two cathodic (H_a) and anodic peaks (H_d) are clearly visible while these features don't exist on a gold electrode. This behavior is explained by the fact that hydrogen chemisorption takes place on mesoporous Pt, whereas hydrogen cannot chemisorb on gold[217]. However, at high cathodic potential the hydrogen evolution occurred on both mesoporous Pt and gold.

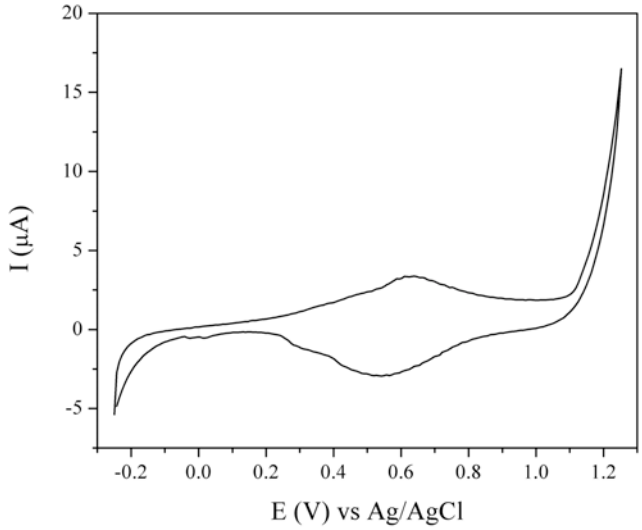

Figure 38. Cyclic Voltammograms of bare gold-coated glass electrode recorded in 0.5 M H_2SO_4 at 100 mV/s between -0.25 to +1.25 V.

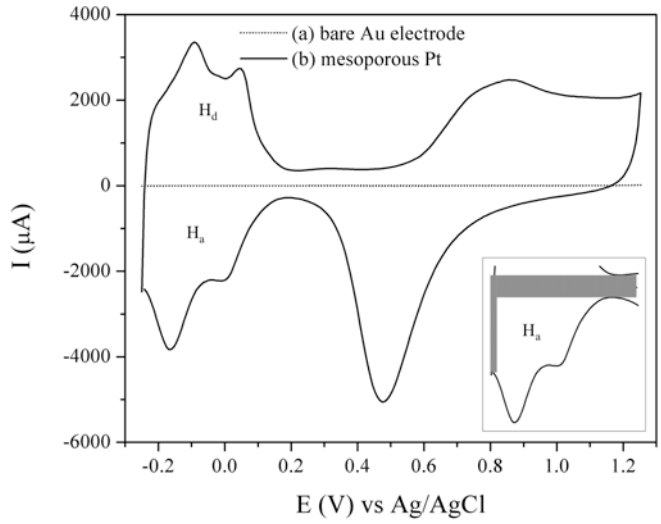

Figure 39. Cyclic Voltammograms of (a) bare gold-coated glass electrode (before mesoporous Pt film deposition) and (b) mesoporous platinum electrode deposited on a gold-coated glass electrode with an injected charge density of 2 C/cm^2 recorded in 0.5 M H_2SO_4 at 100 mV/s between -0.25 to +1.25 V.

The active surface area of polycrystalline Pt can be calculated from the hydrogen chemisorption peaks in the potential range of -0.2 to +0.1 V vs Ag/AgCl as reference electrode. The hydrogen sorption region is divided into hydrogen adsorption charge (H_a) and hydrogen desorption charge (H_d) regions after subtraction of the capacitive current.

Because the peak areas of hydrogen adsorption/desorption charge regions directly relate to a monolayer coverage of hydrogen on the Pt surface, the amount of hydrogen adsorbed in the monolayer (n_a) can be calculated ($n_a=Q_m/F$, where F is the Faraday constant and Q_m represents the charge of the hydrogen adsorption monolayer formation). Subsequently, the real surface area of Pt electrodes can be investigated by the following equation[218].

$$S_r = \frac{Q_m}{ed_m}$$

Where S_r is the real surface area of electrode, e is an electron charge (1.602×10^{-19} C) and d_m is the surface metal atom density. In the case of polycrystalline Pt, the d_m value equals to 1.3×10^{15} cm^{-2}. Therefore, using cyclic voltammetry (CV) in sulfuric acid is very useful to investigate the real surface area of a platinum electrode.

In order to compare the real surface area of chiral imprinted mesoporous platinum electrodes and a polished flat platinum electrode, the cyclic voltammograms of both electrodes are superposed in Figure 40. The real active surface area is calculated from the charge associated with the hydrogen adsorption (H_a, see inset)[219]. Compared to a polished flat platinum electrode, the chiral imprinted mesoporous platinum films show a strong increase in surface area. The roughness factor is an important parameter for the efficiency of the electrode[220]. The calculated surface area is used to estimate a roughness factor, which is defined as the ratio between the active surface area and the geometric surface area of an electrode. Compared to polished flat platinum, the roughness of chiral imprinted mesoporous Pt is increased by a factor of 80. This result suggests that a mesoporous network has been successfully generated.

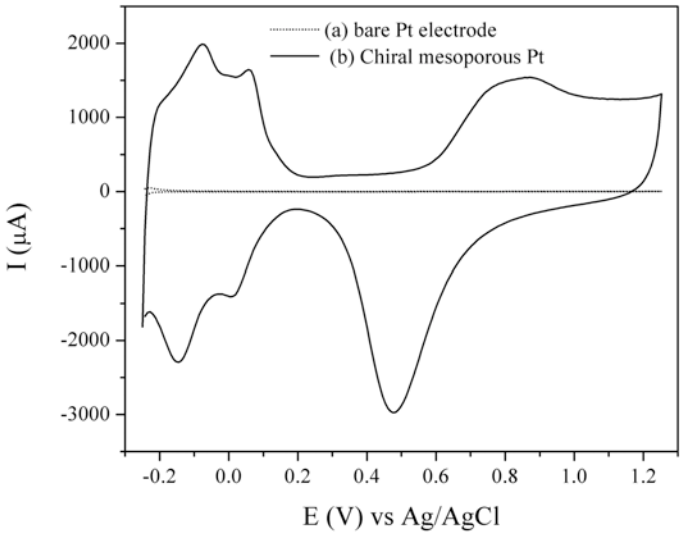

Figure 40. Cyclic Voltammograms of (a) a polished flat platinum electrode and (b) a chiral imprinted mesoporous platinum film deposited on a gold coated glass electrode with a charge density of 2 C/cm^2 recording in 0.5 M H_2SO_4 at 100 mV/s between -0.25 to +1.25 V.

3.3 The morphologies of chiral imprinted mesoporous platinum films

The thickness of chiral mesoporous platinum films obtained at different injected charge densities was observed by SEM images of cross sections of the films as shown in Figure 41. SEM images of all resulting films show that the thickness of chiral imprinted mesoporous platinum films is very uniform over the entire area and the surfaces are very rough. As expected, the thickness of metal films strongly depends on the injected charge density during the electrodeposition process. The thickness of metal films increases linearly with the injected charge density (Figure 42).

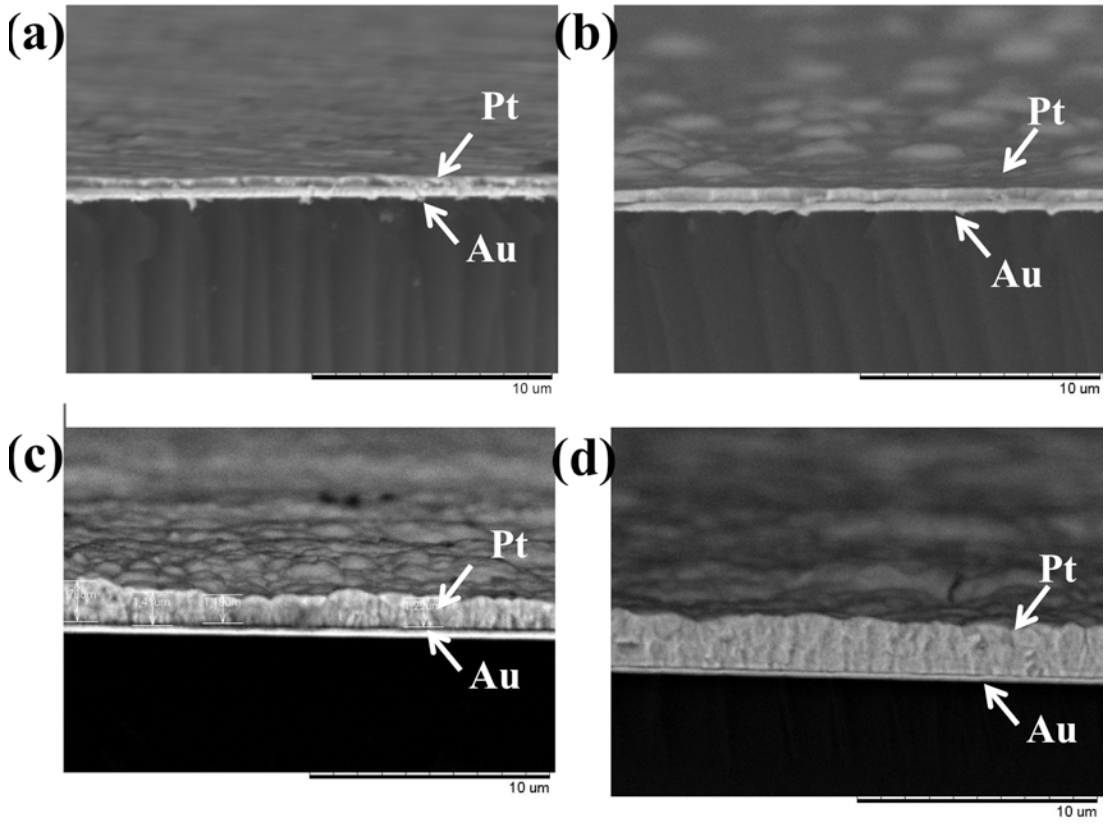

Figure 41. Scanning electron microscopy images of typical cross sections of metal films obtained at different injected charge densities of (a) 2, (b) 4, (c) 8 and (d) 12 C/cm^2, respectively.

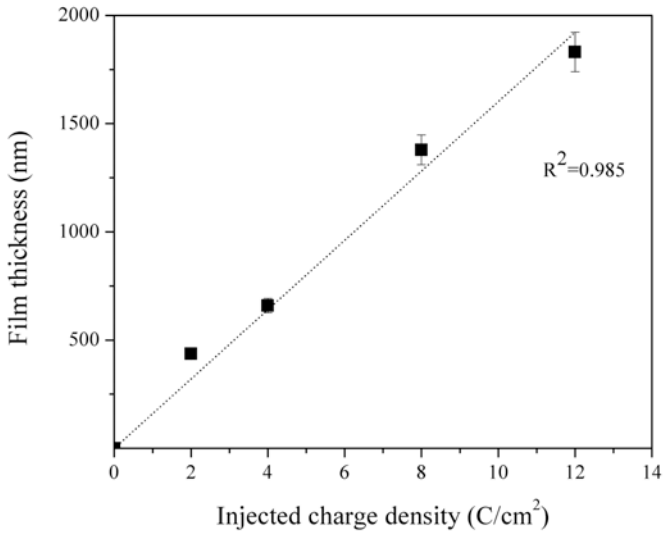

Figure 42. The layer thickness as a function of the injected charge densities for chiral imprinted mesoporous platinum films deposited on gold-coated glass slides.

Because the bright area inside the crystalline structure in TEM images is representative of porous cavities[62], it reveals that the chiral mesoporous Pt film is composed of mesoporous cavities inside the polycrystalline Pt with pores of 5 nm in diameter as shown in Figure 43. It is noted that TEM images of mesoporous structures cannot be observed on the metal film with a high thickness. In this case, the electrodeposition of chiral mesoporous platinum film has been performed using an injected charge density of 0.6 C/cm^2. It should be mentioned that the ordered mesoporous structure is easily damaged during the TEM measurement when the samples are exposed to electron beams over 10 min due to the growth of Pt crystals[191].

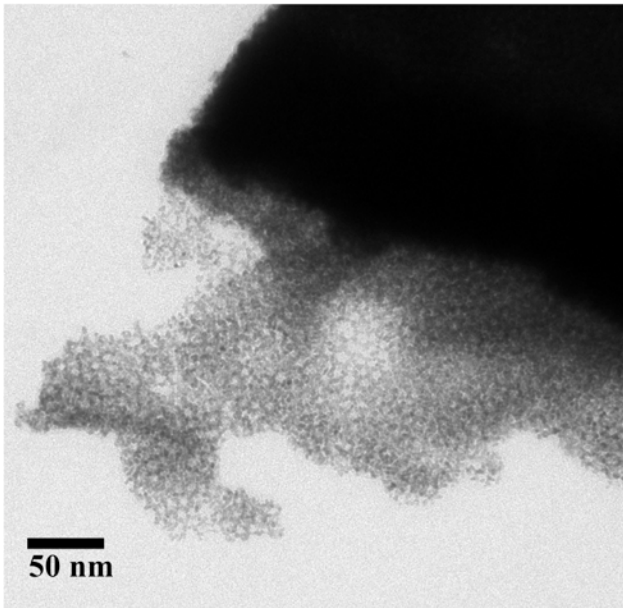

Figure 43. Transmission electron microscope image of a planar chiral mesoporous Pt film obtained by electrodepostion at -0.1 V and with an injected charge density of 0.6 C/cm^2 (imprinted by L-DOPA, L-DOPA/Pt = 1/25).

3.4 Enantioselective recognition study of DOPA enantiomers on chiral imprinted mesoporous platinum electrodes by cyclic voltammetry (CV)

Enantioselective recognition plays an important role in several potential applications[221], including the development of chiral separation process, chiral sensing and asymmetric catalysis. Enantioselective electrochemical reactions can be performed in chiral solvents, chiral supporting electrolytes or on the chiral surface of electrodes[222]. In this part, we report that enantioselective properties have been observed by the

electrochemical reaction on the chiral surface of imprinted mesoporous platinum electrode. The transfer of chiral features from a DOPA enantiomer to the internal pore walls of mesoporous platinum is obtained by the electrodepositon of Pt in the presence of a lyotropic crystalline phase and chiral molecules.

In order to demonstrate the enantioselective properties of such chiral imprinted mesoporous platinum films, the first experiment was performed by cyclic voltammetry. As stated above, several electrochemical processes, including hydrogen sorption and oxidation of platinum, were observed during the electrochemical measurement (Figure 39). To avoid interference of these effects with the enantioselective recognition, the electrochemical activity of the probe molecule should be located in a potential range where no such faradaic processes occur (typically in the range between 0.2 and 0.7 V). It is important to indicate that DOPA undergoes an electrooxidation in a potential window between 0.2 and 0.8 V. It is therefore reasonable to state that the electrochemical behavior of DOPA is compatible with the potential window where the side reactions on platinum electrodes are excluded. Therefore, the electro-reaction of chiral probe molecules on platinum electrodes could be easily observed without changing of the metal structure.

From cyclic voltammetry, as expected the electrochemical behavior of L-DOPA and D-DOPA on non-imprinted flat platinum electrodes is identical within the limits of experimental error bars as shown in Figure 44. The electrooxidation and reduction of DOPA appears with E_{pc}= 0.439 V and E_{pa} = 0.589 V (ΔE_p= 0.150 V) in 50 mM HCl as supporting electrolyte, respectively. The mechanism reaction of this electro-reaction is illustrated in Figure 45, corresponding to a 2-electron-2proton oxidation and reduction of DOPA and the quinoic form of DOPA[223]. It is important to note that the electrochemical behavior of DOPA strongly depends on the pH of the solution, because its structure is sensitive to the pH of the electrolyte. For example, at neutral pH two reaction steps can be observed as shown in Figure 46, leading to side reactions. Under such conditions, the quinoic form of the DOPA molecules are deprotonated due to insufficient acidity in solution, leading to further cyclization to produce cyclodopa, which simultaneously undergoes an electrooxidation to form dopachrome as side reaction[224]. In addition, DOPA is very unstable in basic solutions because it is easily oxidized in air. To avoid such a behavior, the electrochemical study of DOPA molecules should be carried out in acid solutions (see Figure 45 for the mechanism in acidic media).

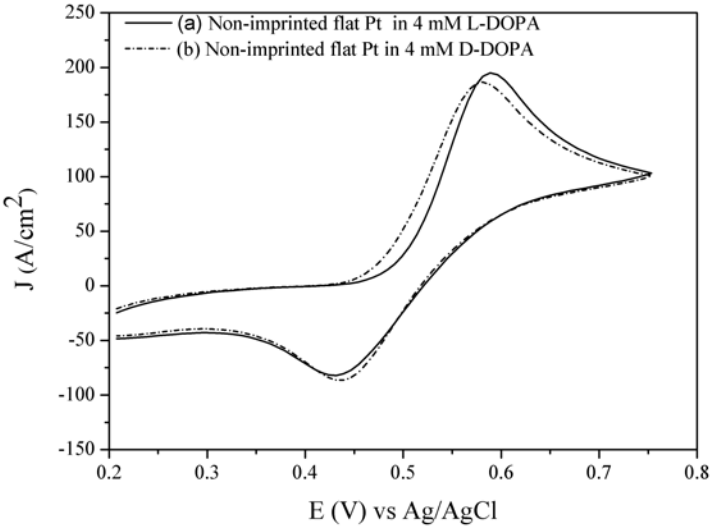

Figure 44. Cyclic voltammograms recorded in 4 mM of (a) L-DOPA and (b) D-DOPA using 50 mM HCl as supporting electrolyte at a scan rate of 10 mVs^{-1} on non-imprinted flat platinum electrodes ($J=I/S_g$, I and S_g are current and geometric surface area, respectively).

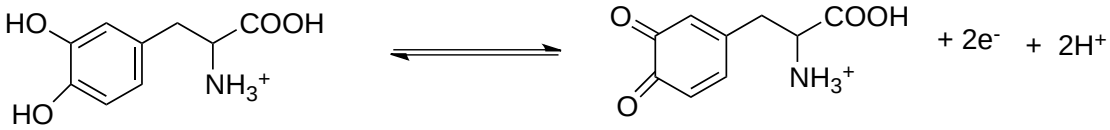

Figure 45. The mechanism of DOPA electro-oxidation/reduction in acidic media

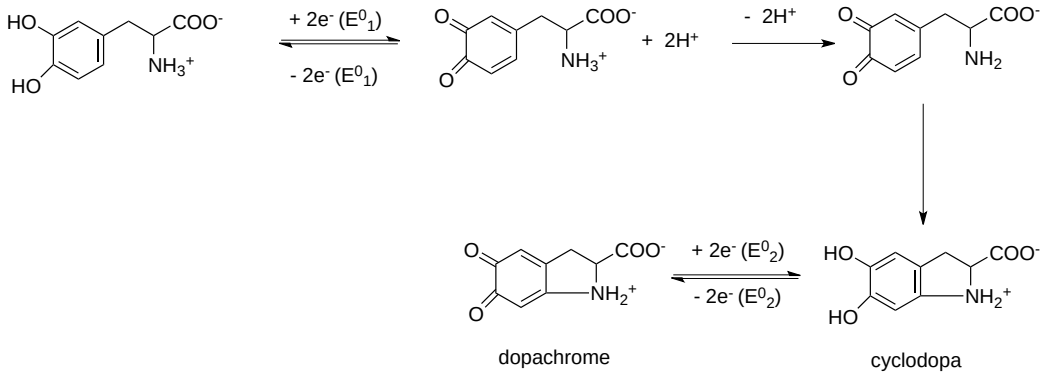

Figure 46. The mechanism of DOPA electro-oxidation/reduction in neutral media, Reproduced from Ref. [224].

The oxidation and reduction peaks of DOPA on non-imprinted mesoporous platinum appear at anodic and cathodic potentials of 0.559 V and 0.499 V (Figure 47, (a) and (b)), respectively, whereas this behavior cannot be observed in supporting electrolyte without adding DOPA molecules as chiral probes (Figure 47, (c)). Compared to non-imprinted flat platinum electrodes, ΔE_p is decreased by 90 mV, which indicates easier oxidation and reduction of the molecules at a mesoporous surface. This behavior might be explained by the fast kinetics of electrons transfer at mesoporous platinum electrodes with respect to a flat electrode[225].

The enantioselective properties of non-imprinted mesoporous platinum have also been studied in order to exclude parasitic effects. Again there is no discrimination between L-DOPA and D-DOPA. These observations on both non-imprinted flat platinum and non-imprinted mesoporous platinum clearly confirm that two the enantiomers of DOPA cannot be distinguished on non-imprinted electrodes.

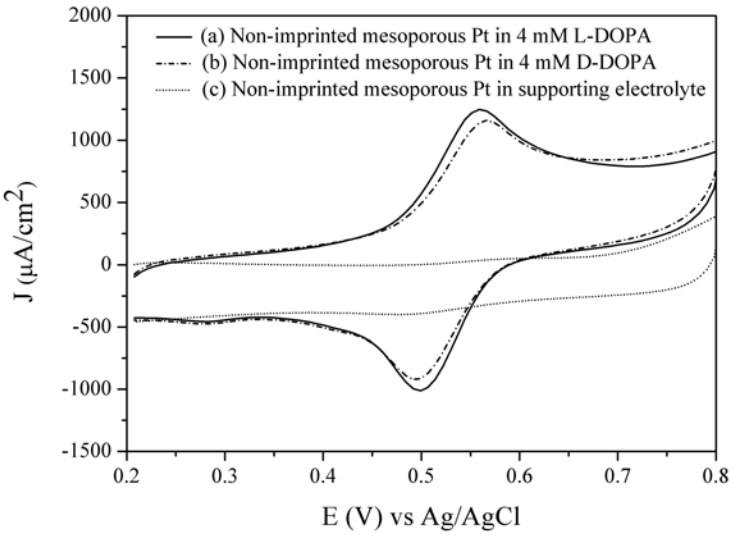

Figure 47. Cyclic voltammograms recorded in 4 mM of (a) L-DOPA (b) D-DOPA using 50 mM HCl as supporting electrolyte and (c) pure 50 mM HCl at a scan rate of 10 mVs^{-1} with the non-imprinted mesoporous platinum electrodes obtained by injecting a charge density of 2 C/cm^2 ($J=I/S_g$, I and S_g are current and geometric surface area, respectively).

In contrast to non-imprinted electrodes, the chiral imprinted mesoporous platinum exhibits slight differences in current densities for L-DOPA and D-DOPA. For mesoporous platinum that was imprinted by L-DOPA it was found that this kind of electrode was more active for oxidation/reduction of L-DOPA compared to that of D-DOPA as shown in Figure 48. The voltammogram of the electrode recording in supporting electrolyte shows only capacitive current without faradaic current. Scanning the potential of the electrode in pure supporting electrolyte confirms that no DOPA is left inside the mesoporous structure before using it for the recognition study. Therefore, the currents are solely due to the faradaic process involving the reaction of the chiral probe at the metal surface.

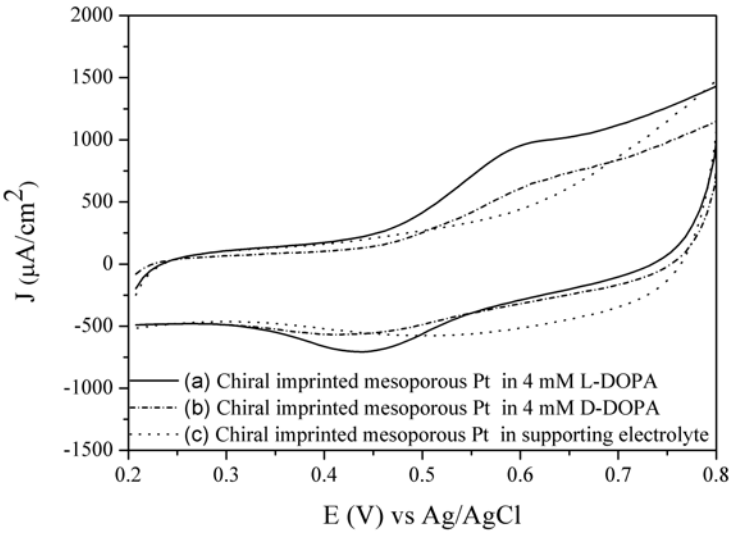

Figure 48. Cyclic voltammograms recorded in 4 mM of (a) L-DOPA (b) D-DOPA using 50 mM HCl as supporting electrolyte and (c) 50 mM HCl at scan rate of 10 mVs^{-1} on the chiral mesoporous platinum electrodes imprinted with L-DOPA using a L-DOPA/ $PtCl_6^{2-}$ ratio of 1/25 and injecting a charge density of 2 C/cm^2 ($J=I/S_g$, I and S_g are current and geometric surface area, respectively).

Although promising results were observed for the chiral imprinted mesoporous platinum compared to the non-imprinted one, only a small difference was detectable by cyclic voltammetry (CV) because the signal is dominated by the large capacitive current. In order to observe more clearly the faradaic process (the current generated by the redox reaction of the chiral probes at the electrode surface), differential pulse voltammetry

(DPV) was perform instead of CV because with this technique non-faradaic currents are largely removed.

3.5 Enantioselective recognition study of DOPA enantiomers on chiral imprinted mesoporous platinum electrodes by Differential Pulse Voltammetry (DPV)

As already stated, many electrochemical processes, including hydrogen sorption and oxidation of platinum, can be observed during the electrochemical measurement. To avoid interference of these reactions with the enantioselective recognition, the differential pulse voltammetry (DPV) of the chiral probes was performed in a potential range from 0.2 to 0.7 V where no such interference appears. The electrooxidation behavior of the two DOPA enantiomers on non-imprinted flat platinum electrodes is identical and this result is similar to what has been observed by cyclic voltammetry (Figure 49). In order to characterize the activity of mesoporous platinum, the voltammograms of non-imprinted flat platinum and non-imprinted mesoporous platinum were compared (Figure 50). The current density of DOPA electrooxidation on non-imprinted mesoporous platinum is dramatically increased compared to a non-imprinted flat platinum electrode. In addition, it clearly shows again that the electrooxidation potential of L-DOPA on non-imprinted mesoporous platinum electrodes is significantly lower than that on non-imprinted flat platinum due to fast electron transfer kinetics at mesoporous surfaces compared to flat surfaces[225]. In addition, the electrooxidation of the two enantiomers is also undistinguishable on non-imprinted mesoporus platinum in the limit of experimental error (Figure 51). From these observations, it is concluded that, as expected, non-imprinted platinum cannot distinguish the stereospecific behavior of two enantiomers of DOPA molecules.

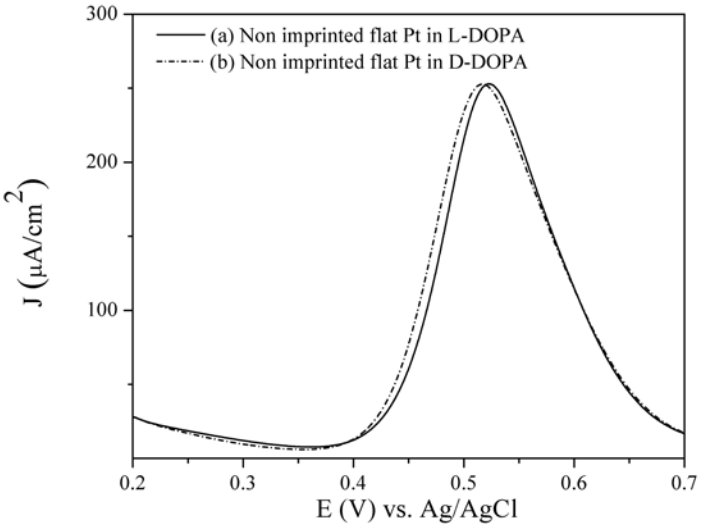

Figure 49. Differential pulse voltammograms recorded in 4 mM of (a) L-DOPA and (b) D- DOPA using 50 mM HCl as supporting electrolyte on non-imprinted flat platinum electrodes.

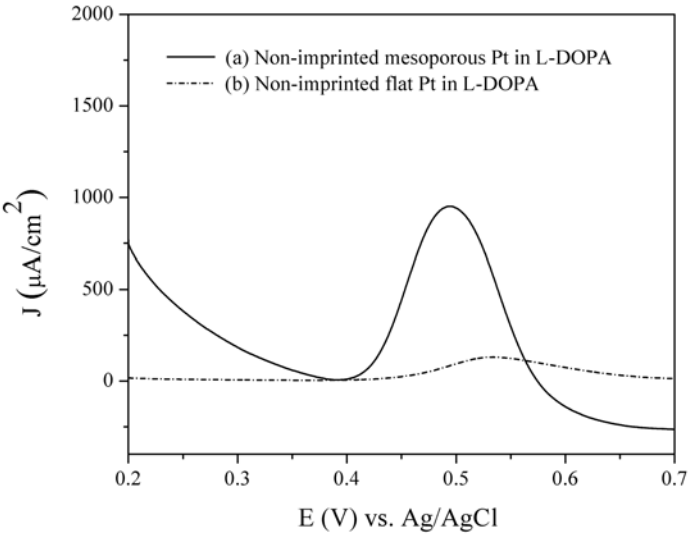

Figure 50. Differential pulse voltammograms recorded in 4 mM DOPA using 50 mM HCl as supporting electrolyte on (a) non-imprinted mesoporous Pt obtained by injecting a charge density of 2 C/cm and (b) non-imprinted flat Pt ($J=I/S_g$, I and S_g are current and geometric surface area, respectively).

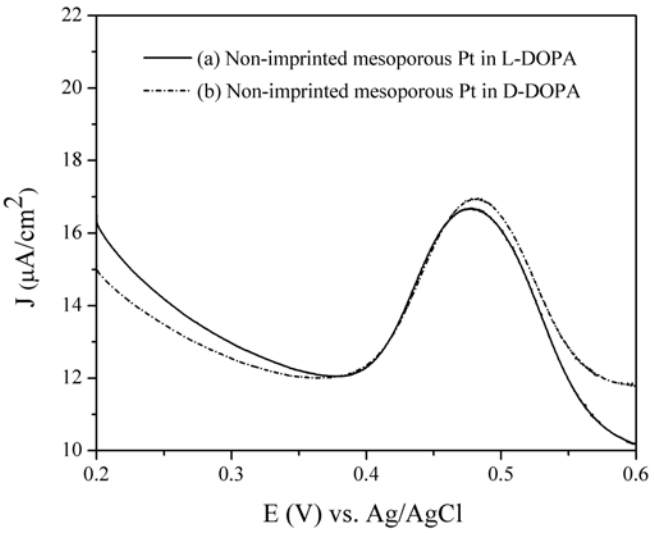

Figure 51. Differential pulse voltammograms recorded in 4 mM of (a) L-DOPA and (b) D-DOPA using 50 mM HCl as supporting electrolyte on non-imprinted mesoporous platinum electrodes obtained by injecting a charge density of 2 C/cm^2 ($J=I/S_r$, I and S_r are current and real surface area, respectively).

After the electrodeposition process, the electrochemical behavior of chiral imprinted mesoporous platinum was observed by DPV in 50 mM HCl as supporting electrolyte in the potential range of +0.2 to +0.6 V before removal of both surfactant and chiral templates as illustrated in Figure 52. It shows that the electrooxidation current of the DOPA molecules left inside the porous Pt appears at a potential around +0.55 V. This feature completely disappears after removal of all templates by washing in a large amount of water for 24 hours (Figure 53). This indicates that all DOPA molecules as chiral template were completely removed during the washing process.

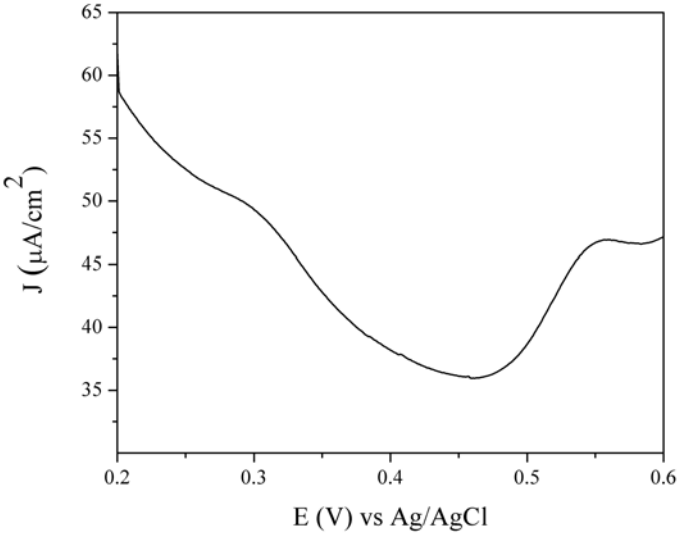

Figure 52. Differential pulse voltammogram recorded in 50 mM HCl of a chiral mesoporous platinum electrode imprinted with L-DOPA using a L-DOPA/ $PtCl_6^{2-}$ ratio of 1/25 and the injected charge density of 2 C/cm^2 before removable of the chiral template ($J=I/S_r$, I and S_r are current and real surface area, respectively).

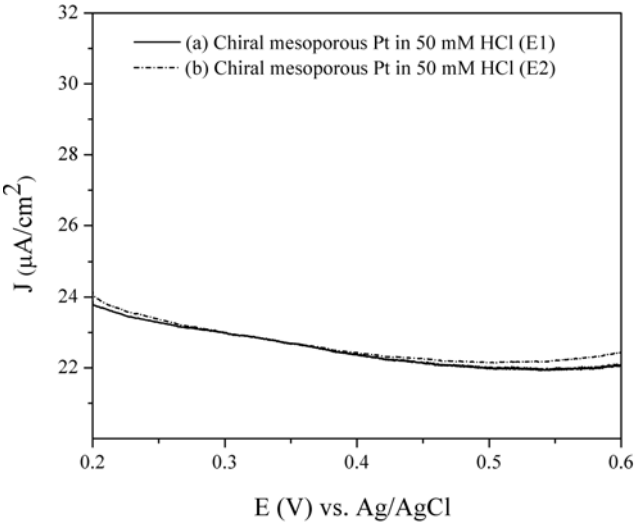

Figure 53. Differential pulse voltammogram recorded in 50 mM HCl of the chiral mesoporous platinum electrodes imprinted with L-DOPA using a L-DOPA/ $PtCl_6^{2-}$ ratio of 1/25 and an injected charge density of 2 C/cm^2 after removable of chiral template (a) the electrode 1 (E1, used for L-DOPA recognition) and (b) the electrode 2 (E2, used for D-DOPA recognition) ($J=I/S_r$, I and S_r are current and real surface area, respectively).

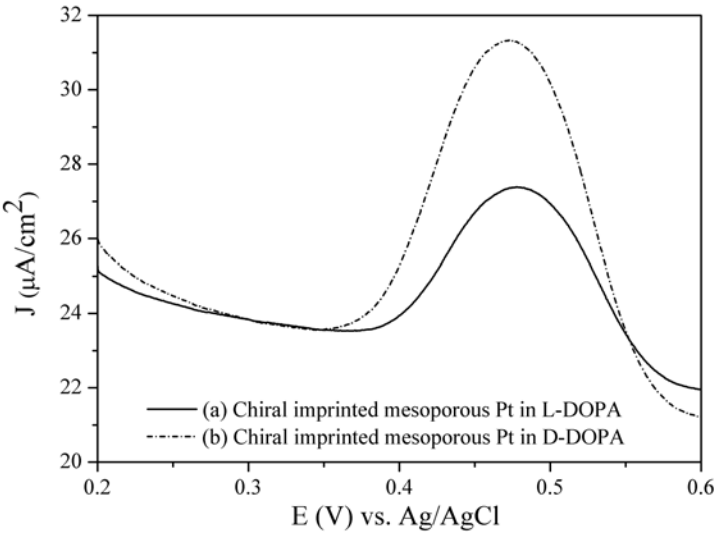

Figure 54. Differential pulse voltammogram recorded in 4 mM of (a) L-DOPA and (b) D-DOPA using 50 mM HCl as supporting electrolyte with a chiral mesoporous platinum electrode imprinted with D-DOPA using a D-DOPA/ $PtCl_6^{2-}$ ratio of 1/25 and injecting a charge density of 2 C/cm^2 ($J=I/S_r$, I and S_r are current and real surface area, respectively).

The surface area is an important factor, which strongly influences the current intensity. In order to compare different samples we therefore normalized the current by the real active surface area (current density, J). Thus, the enantioselective properties of all electrodes were compared at the level of normalized current density. In order to observe the enantioselective properties, two types of chiral imprinted mesoporous platinum electrodes were studied by DPV. The first one is the chiral mesoporous electrode imprinted with D-DOPA using a D-DOPA/ $PtCl_6^{2-}$ ratio of 1/25 and the second one is the electrode imprinted with L-DOPA. In the first case, it is very clear that the chiral imprinted mesoporous platinum shows significant differences in the electrooxidation current densities for L-DOPA and D-DOPA. For the chiral mesoporous platinum electrodes imprinted by D-DOPA, the electrooxidation signal of D-DOPA is much more pronounced compared to the one of L-DOPA (Figure 54).

A control experiment was performed in order to verify that no artifacts, such as a change in active surface area, leads to the difference in the enantioselective recognition of the two enantiomers. The electrodes were oxidized and reduced in sulfuric acid by cyclic

voltammetry in the potential window from -0.25 to +1.25V (Figure 55). As mentioned above, the surface starts to become oxidized to form platinum oxide at potentials more positive than +0.6 V and the reduction of the formed platinum oxide was observed in the backscan. Therefore, the platinum atoms at the surface of the mesopore walls, that initially encode the chiral information, will change position and reorganize after oxidation/backreduction. This should erase the chiral surface imprints. In order to examine this hypothesis, the enantioselective recognition on all oxidized electrodes was reinvestigated by the electrooxidation of L-DOPA and D-DOPA enantiomers as shown in Figure 56. In this experiment, no enantioselective recognition of the two enantiomers was observed, confirming that the electrooxidation/backreduction of the chiral imprinted mesoporous platinum electrode destroyed the chirality of the metal surface. The hydrogen sorption on these electrodes was also obtained from these cyclic voltammograms, thus allowing calculation of real surface areas and renormalization of the current densities, facilitating the comparison of all electrodes with each other. It is reasonable to conclude that the significant difference in the current densities of L-DOPA and D-DOPA before the oxidation of the different electrodes originates from the chiral "footprint" rather than any artifacts.

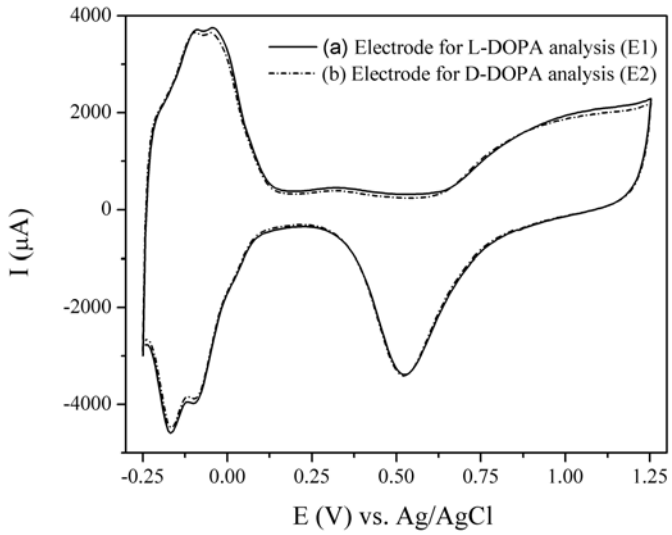

Figure 55. Cyclic voltammogram recorded in 0.5 M H_2SO_4 with the chiral imprinted mesoporous platinum electrodes imprinted with D-DOPA using a D-DOPA/ $PtCl_6^{2-}$ ratio of 1/25 and an injected charge density of 2 C/cm^2 (a) the electrode1 (E1, using for L-DOPA recognition) and (b) the electrode2 (E2, using for D-DOPA recognition).

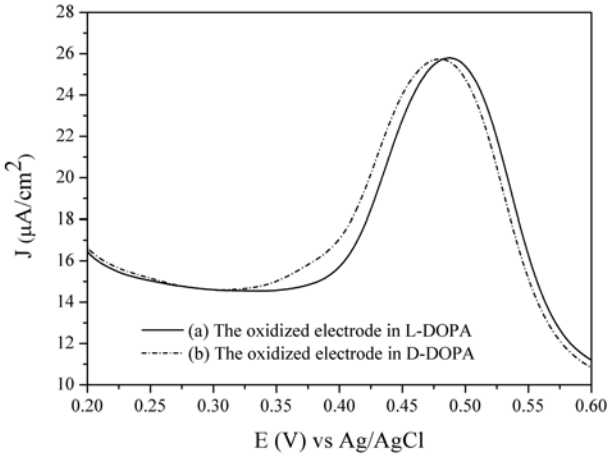

Figure 56. Differential pulse voltammogram recorded in 4 mM of (a) L-DOPA and (b) D-DOPA using 50 mM HCl as supporting electrolyte with chiral mesoporous platinum electrodes initially imprinted with D-DOPA using a D-DOPA/ $PtCl_6^{2-}$ ratio of 1/25 and an injected charge density of 2 C/cm^2, but measured after destroying on purpose the chiral information by scanning in the potential between -0.25 V and +1.25 V in 0.5 M H_2SO_4 ($J=I/S_r$, I and S_r are current and real surface area, respectively).

In a second control experiment, the chiral mesoporous platinum electrodes imprinted by L-DOPA were also examined with respect to their activities for electrooxidation of the two DOPA enantiomers by DPV. In this case, the electrodes are much more active for the oxidation of L-DOPA compared to D-DOPA (Figure 57). Subsequently, these electrodes were also oxidized by cyclic voltammetry as stated above and the enantioselective recognition was reinvestigated electrodes after one oxidation/reduction cycle (Figure 58). As in the previous case of D-DOPA imprinted electrodes, no enantioselective recognition of the two enantiomers could be observed after erasing the chiral information. These observations again confirm that the difference in activity of the two enantiomers can be attributed to the chiral “footprints” that have been generated due to an encoding of chiral information in the mesopore walls during the imprinting process.

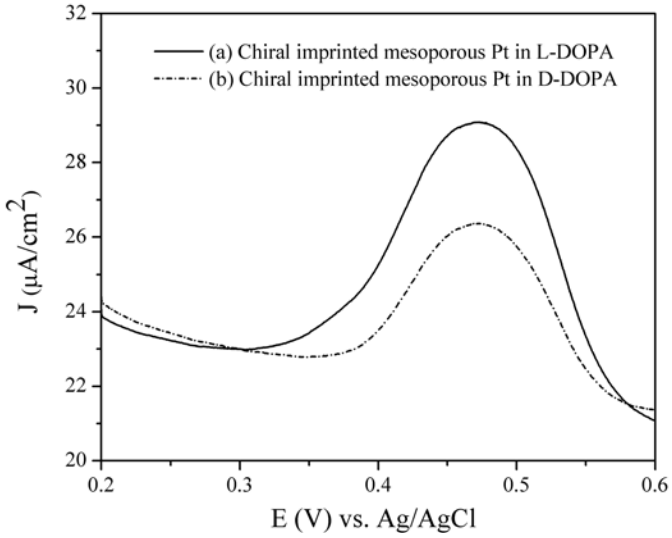

Figure 57. Differential pulse voltammogram recorded in 4 mM of (a) L-DOPA and (b) D-DOPA using 50 mM HCl as supporting electrolyte with chiral mesoporous platinum electrodes imprinted with L-DOPA using a L-DOPA/ $PtCl_6^{2-}$ ratio of 1/25 and an injected charge density of 2 C/cm^2 ($J=I/S_r$, I and S_r are current and real surface area, respectively).

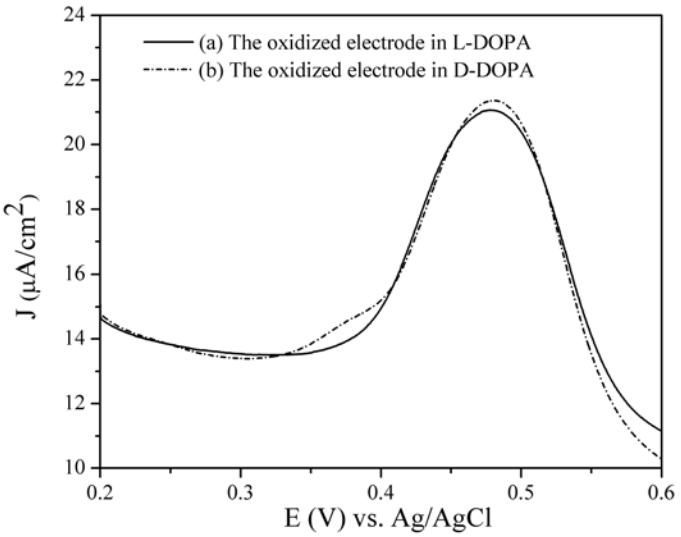

Figure 58. Differential pulse voltammogram recorded in 4 mM of (a) L-DOPA and (b) D-DOPA using 50 mM HCl as supporting electrolyte with chiral mesoporous platinum electrodes initially imprinted with L-DOPA using a L-DOPA/ $PtCl_6^{2-}$ ratio of 1/25 and an injected charge density of 2 C/cm^2, but measured after destroying on purpose the chiral information by scanning the potential between -0.25 V and +1.25 V in 0.5 M H_2SO_4 ($J=I/S_r$, I and S_r are current and real surface area, respectively).

We carried out several experiments with varying amounts of L-DOPA in the electroplating mixture in order to investigate the effect of the content of chiral template on the enantioselectivity. The amount of imprinted recognition sites, related to the amount of chiral template during imprinting step, should influence the enantioselective recognition properties. The relationship between the enantioselectivity and the content of chiral template is shown in Figure 59. The enantioselectivity was calculated by the ratio of electrooxidation current densities of L-DOPA and D-DOPA ($J_{L\text{-}dopa}/J_{D\text{-}dopa}$). It clearly demonstrates that the enantioselectivity significantly increases with the content of chiral template. As shown in Figure 59, the $J_{L\text{-}dopa}/J_{D\text{-}dopa}$ ratio increase from 1.2 to 2 for chiral imprinted mesoporous platinum obtained with L-DOPA/$PtCl_6^{2-}$ molar ratios from 1/50 to 1/17. However, when the chiral template content is increased further (DOPA/$PtCl_6^{2-}$ molar ratios of 1/12), the efficiency of enantioselective recognition starts to decrease. The reason for this decrease might be a destabilization of the lyotropic liquid crystal phase of the surfactant when adding too much DOPA. This is in agreement with the observed destabilization of the platinum film. Indeed the final metal layer obtained by using high ratios of L-DOPA/surfactant is much more fragile and tends to detach from the electrode surface, whereas the metal layer obtained by using a moderate ratio of L-DOPA/surfactant was mechanically very stable even when the electrodes were oxidized in sulfuric acid several times.

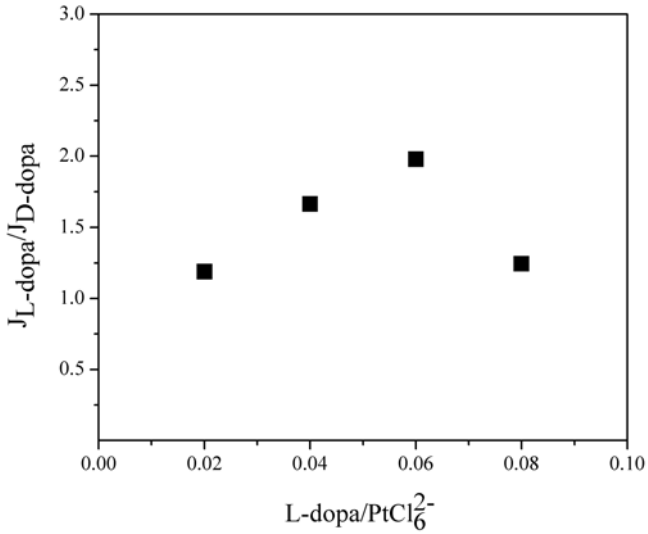

Figure 59. The effect of the chiral template content on the enantioselectivity. The different chiral mesoporous platinum electrodes were obtained by imprinting with various amounts of L-DOPA.

In order to estimate the impact of mesoporosity on the efficiency of enantioselectivity, the enantioselective recognition was also tested with imprinted non-mesoporous platinum electrodes (Figure 60). Chiral imprinted non-mesoporous platinum, was prepared by electrodeposition at a potential of -0.1 V in a solution containing 60 mM hexachloroplatinic acid and L-DOPA as chiral template (L-DOPA/ $PtCl_6^{2-}$ molar ratios of 1/25) without addition of surfactant. Interestingly, only a slight difference in the electrooxidation signal of the two enantiomers was observed on such electrodes. This implies that almost no chiral cavities seem to be generated in the absence of surfactant. Thus mesoporosity is an important feature enhancing the efficiency of enantioselective recognition properties. In addition, we also found that the mechanical stability of chiral imprinted compact platinum films is very low. The final metal layer are easily destroyed during oxidation by cyclic voltammetry in sulfuric acid, whereas the metal films of chiral mesoporous platinum obtained from the lyotropic liquid crystalline phase are stable, even when the electrode is oxidized and reduced several times. It should be noted that values of real surface area could not be calculated on chiral imprinted non-mesoporous platinum due to detachment of the platinum film during the CV measurements. To compare the enantioselectivity on such chiral electrodes, the normalized current density of the electrooxidation of DOPA was obtained using the geometric surface area.

The exact reason for the significant enantioselectivity of chiral imprinted mesoporous platinum remains to be discussed. One of our assumptions is that the chiral cavities at the mesopore walls might be generated due to the interaction between the DOPA molecules and the lyotropic liquid crystalline surfactant, which entraps DOPA at the surface of the pillars of the lyotropic liquid crystal phase. The chiral templates seem to be maintained in this position during the electroreduction of the platinum salt around the assembly of DOPA and lyotropic liquid crystalline surfactants, resulting in the transfer of a chiral “footprint” into mesoporous platinum walls. In contrast, in the system without surfactant only a few chiral recognition sites are imprinted into the outermost surface of the platinum layer. As a result, a significant discrimination between the two enantiomers of L- and D-DOPA is observed with the chiral mesoporous structure, whereas the compact platinum deposit shows only very modest selectivity. In order to study in more detail this assumption molecular dynamics simulations might be an alternative way to gain additional information about these interactions.

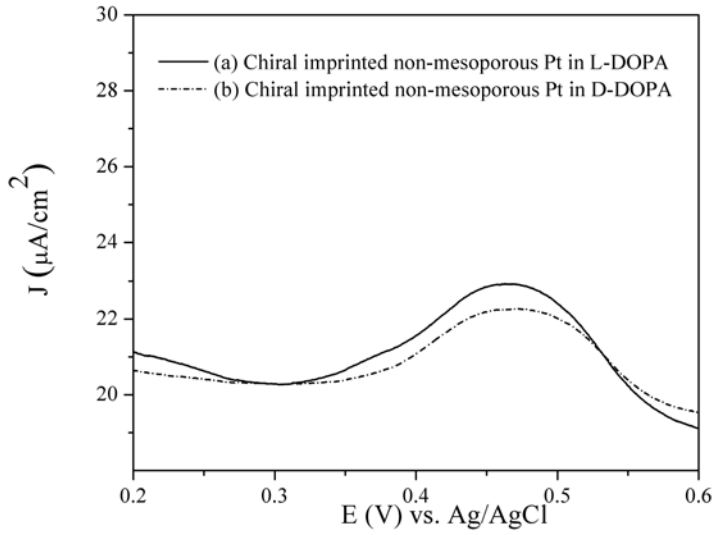

Figure 60. Differential pulse voltammogram recorded in 4 mM of (a) L-DOPA and (b) D-DOPA using 50 mM HCl as supporting electrolyte with chiral non-mesoporous platinum electrodes imprinted with L-DOPA using a L-DOPA/ $PtCl_6^{2-}$ ratio of 1/25 and an injected charge density of 2 C/cm^2 ($J=I/S_r$, I and S_r are current and real surface area, respectively).

3.6 The enantioselectivity at chiral imprinted mesoporous platinum surfaces with respect to the relevant literature

There are many relevant literature studies that have reported the generation of chirality at metal surfaces. Chiral metal surfaces can be obtained in many different ways[179] like through the helicity of metal nanowires[226], the adsorption of chiral molecules at metal surfaces[227-229], the entrapment of chiral molecules inside the metal structure[179] and the formation of intrinsic metal interfaces with a high Miller index by cutting a bulk metal crystal along a low symmetry plane[174,228]. Chiral metal surfaces obtained by adsorption of chiral molecules is a popular method because it is simple to retain the chirality of chiral probes after their adsorption on metal surfaces. However, this approach often suffers from the desorption of the chiral molecule due to its water-solubility. Two alternative ways are the entrapment of chiral molecules within the metal and the design of intrinsic chiral metal surfaces by cutting metal crystals. The first approach can retain the chirality at metal surfaces because the chiral molecules are embedded between the aggregated metal nano-domains [179]. However, an intrinsic chiral metal surface could not be generated because after extraction of the entrapped chiral molecules no more chiral

features remain. For example, Pachón and coworker reported the entrapment of alkaloid within Pd that was supposed to lead to the stereoselective hydrogenation of isophorone and acetophenone but after extraction of the dopant no enantiomeric excess (e.e) could be observed in the products[178].

The second approach is based on the fact that a chiral surface can be generated by a well chosen cutting of a metal crystal. Typically, the bulk structure of transition metals such as Cu, Pt and Ni is face centered cubic (fcc) with a high symmetry. Therefore, such metal structures are not considered to show enantiomorphism. However, by the cutting in the right way a bulk metal plan of high symmetry, a chiral metal structure with high Miller index can be produced due to a lack of symmetry. For example the structures of (643) and ($\bar{6}\bar{4}\bar{3}$) faces of Pt are enantiomoph as shown in Figure 61[174]. The chiral surfaces are due to flat (fcc) terraces separated by monoatomic steps.

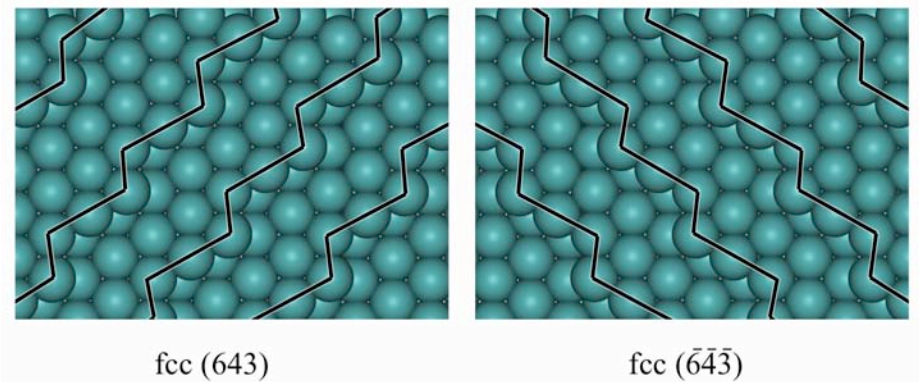

Figure 61. Intrinsically chiral surfaces on metals. Reproduced from ref. [174].

On such surfaces, Attard studied the enantioselective behavior of chiral probes by an electrochemical method[173]. In terms of voltammetric profiles, the electrooxidation behavior of D-glucose and L-glucose was different at the chiral metal surface Pt(643). It was also demonstrated that the behavior of D-glucose on (R)-Pt(643) and L-glucose on (S)-Pt(643) were equivalent. This clearly shows that the existence of intrinsic surface chirality results in the enantioselectivity with respect to the reactivity of various sugar molecules on such interfaces. Furthermore, a small difference in adsorption energy between two enantiomers on chiral metal surfaces has been reported[170,173,230,231]. For example, Attard and coworkers reported that the activation energies for glucose electro-

oxidation on R-Pt(643) and S-Pt(643) differed by about 1-2 kJ/mol[173]. In addition, Gellman and coworkers also studied the different desorption energies between two enantiomers on chiral single crystal surfaces. They found a small difference in desorption energy of R-3-methyl-cyclohexanone on R-Cu(643) and on S-Cu(643) and they also observed differences in the orientation of R- and S-2-butanoxy on R-Ag(643), indicating the enantioselectivity of such surfaces[232].

It is therefore reasonable to suppose that in our case of chiral mesoporous metal surfaces it is also possible to introduce a chiral feature in the metal structure by the imprinting approach. The enantioselective properties of such materials might be explained by the differences in the adsorption enthalpies for the two enantiomers. Macroscopically this should lead to a difference in partition coefficient between the outer solution phase and the inside of the porous structure when comparing the two enantiomers.

Furthermore, we have also undertaken other independent experiments in order to further confirm the chirality of the resulting chiral mesoporous metal. One alternative experiment was based on the Secondary Harmonic Generation (SHG) technique.

3.7 The characterisation of chirality at mesoporous metal surfaces by Secondary Harmonic Generation (SHG)

The fundamentals of Secondary Harmonic Generation (SHG) is based on the fact that a monochromatic coherent optical wave with energy E is converted into a new single photon of energy 2E after it interacts with a second-order nonlinear media such as non-centrosymmetric material, which should have no inversion symmetry within the crystalline structure[233]. Based on the second-order nonlinear polarization, the nonlinear response at the secondary harmonic frequency is described by the following equation:

$$P_i(2\omega) = \sum_{j,k} \chi_{ijk}^{eee} \, E_j(\omega) \, E_k(\omega)$$

where P_i is the nonlinear polarization, χ_{ijk}^{eee} is the electric-dipole allowed second- order susceptibility tensor, $E_j(\omega)$ the incident light field and the indices ijk are the Cartesian coordinates[197].

In a chiral system, each enantiomer of chiral molecules shows different responses to left and right-hand circularly polarized light in terms of optical properties with respect to linear optics as well as nonlinear optical systems. The interaction between a chiral film and circularly-polarized light produces different intensities of generated second-harmonic light by left- and right-hand circularly-polarized excitation[197,234]. Therefore, it is possible to use the secondary harmonic generation to monitor the chirality at surfaces.

In order to observe the chirality at mesoporous metal surfaces, the SHG experiment was carried out by continuous polarization scans of an incident beam at fixed incident angle. Scheme 8 shows the different polarization states depending on the rotating angle of the half-waveplate. In the first step, a starting beam is polarized through the combination of a rotating half-waveplate (λ/2) and fixed quarter-waveplate (λ/4) to produce out of the plane incidence (s). By rotating a half waveplate (λ/2), it is possible to change the polarizations from linear to elliptical and circular polarization. For example, changing of the rotating angle from 0° to 22.5° results in the transformation of polarization states from linear to left-hand circular polarization. Subsequently, the further changing of rotating angle from 22.5° to 67.5° leads to converting the left-hand circular polarization to right-hand circular polarization. Therefore, the generated secondary harmonic intensity is recorded versus the rotation angle of half-waveplate (Ψ). In the case of a chiral surface system, the different intensity at left- and right-hand circular polarized states is expected to be observed by this technique. As for a SHG experimental setup, the SHG response was measured either in transmission and reflection mode with two components: polarized parallel (p) and perpendicular (s) to the plane of incidence as shown in Scheme 9[197,235].

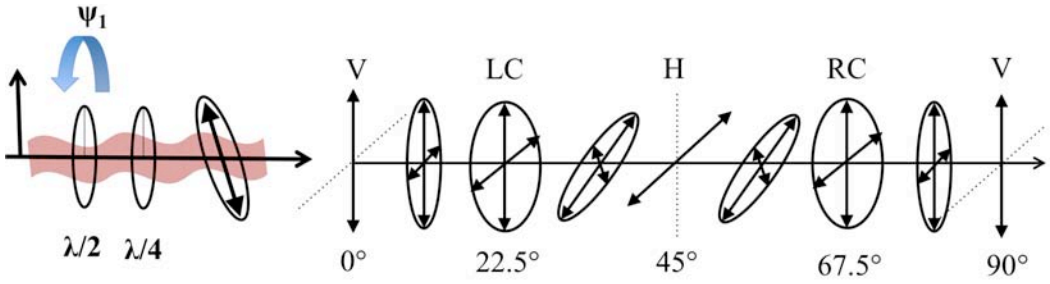

Scheme 8. The transformation of polarization states by changing rotating angle (Ψ_1) of a half-waveplate ($\lambda/2$) and fixing rotating angle (Ψ_2) of a quarter-waveplate ($\lambda/4$): V, H, LC and RC are linear vertical, linear horizontal, left-hand circular and right-hand circular, respectively. Reproduced from Ref. [198].

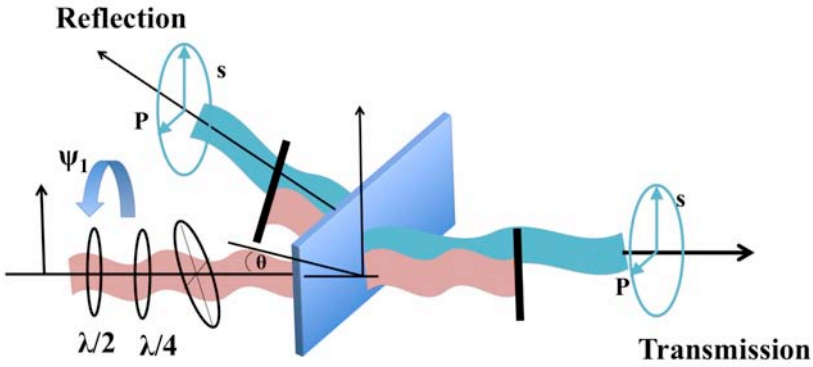

Scheme 9. Illustration of a secondary harmonic generation (SHG) setup, Reproduced from ref. [197].

The first SHG experiment was carried out with a chiral imprinted mesoporous platinum film deposited on a gold-coated glass slide. Because the platinum film was deposited on a gold electrode, which is not transparent, the generated secondary harmonic response was measured in the reflection mode. In this experimental setup, the sample was fixed at a position of 45° with respect to the incident beam. Unfortunately, the SHG intensity was not stable as a function of time. It was found that the SHG intensity measured in the reflection mode exponentially decayed versus time when the sample was exposed to left- or right-hand circular polarized light as shown in Figure 62. Therefore, it is not possible to monitor the changes in SHG intensity as a function of the rotating angle of the waveplate.

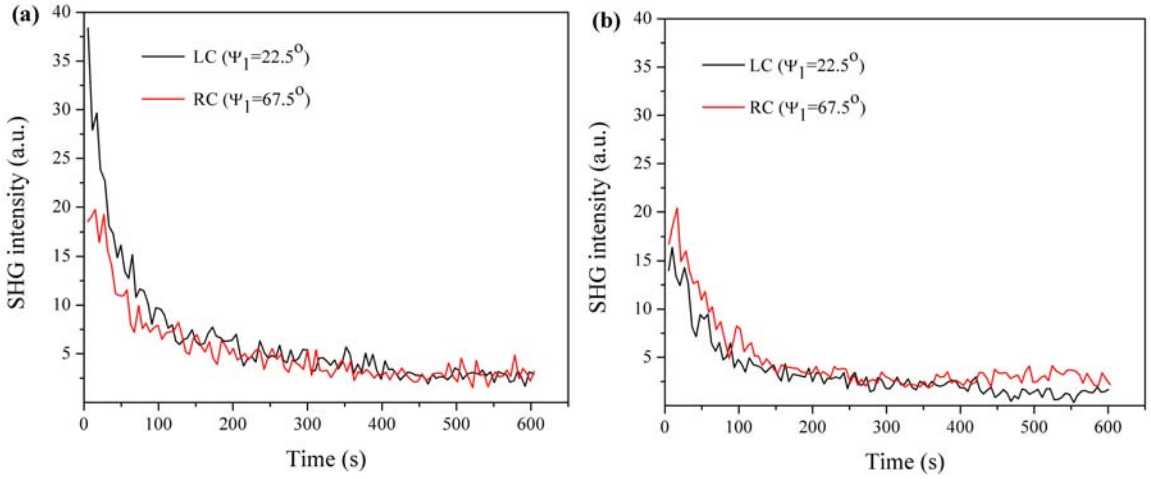

Figure 62. The SHG intensity as a function of time using left-circular polarized (LC, Ψ_1 = 22.5°) and right-circular polarized (RC, Ψ_1 = 67.5°) excitations on chiral imprinted mesoporous Pt deposited on a gold coated glass slide (a) imprinted with L-DOPA (b) imprinted with D-DOPA using a DOPA/ $PtCl_6^{2-}$ molar ratio of 1/17.

In order to avoid the SHG intensity decay during the measurement, the experiment should be performed by using the transmission mode monitoring the transmitted SHG response. The chiral mesoporous Pt films were deposited on ITO instead of gold-coated glass slides because the incident laser beam could not go through the chiral imprinted mesoporous platinum film deposited on gold electrodes. In this case, the chiral imprinted mesoporous platinum was deposited on ITO by the same procedure as stated in the experimental section. It is noted that the conductivity of ITO is much lower than that of gold electrodes. To increase the conductivity of ITO, the ITO was coated by the evaporating a very thin gold layer (ITO-Au) before using it for electrodeposition of the Pt film. After the electrodeposition process, lyotropic liquid crystalline surfactant and chiral template were carefully removed by washing in DI water for 24 hours and the electrodes were dried at room temperature. As for the SHG experiment, the sample holder was rotated at different angles between -80 and +80° in order to observe the optimum sample position using a fixed input beam initially with in-plane (p) or out-of-plane (s) incidence. The in-plane transmitted SHG intensity (p) was monitored as a function of the sample rotating angle as shown in Figure 63. The notation of p-p represents the in-plane incidence (p) and monitoring the in-plane transmitted SHG response (p), and s-p corresponds to the out-of-plane incidence (s)/in-plane of transmitted SHG response (p).

This result shows that a sample rotation angle of approximately 56° corresponds the maximum SHG intensity.

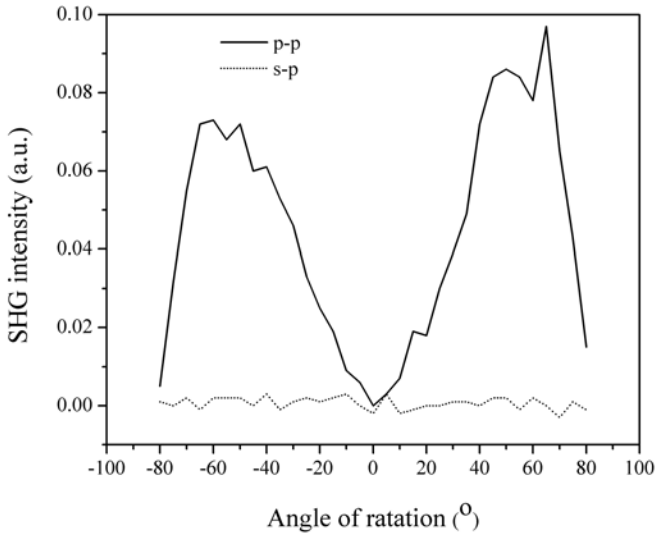

Figure 63. The SHG response as a function of the sample rotation angle of chiral imprinted mesoporous Pt deposited on ITO-Au, obtained in the transmission mode. The solid line represents the intensity monitoring by using a fixed angle of the in-plane polarized incident beam (p) and analyzing the p-polarized component (p) of the SHG signal (p-p). The dotted line shows the intensity using a fixed angle of out-of-plane polarized incident beam (s) and analyzing the p-polarized component (p) of the SHG signal (s-p).

In order to observe the SHG response at different polarization states, the sample was fixed at 56° with respect to the incident beam. The polarization patterns of the SHG intensity obtained by the transmitted response of p- and s-polarized second harmonic components are shown in Figure 64 and 66. The SHG intensity was monitored by changing the rotating angle of the half-waveplate (Ψ_1). As mentioned above, the SHG intensity was not stable during the reflection mode measurement, but in this case the signal remained stable as shown by the symmetric feature of the polarization patterns of the SHG intensity in a range from 0 to 90° and the pattern between 90 and 180°, confirming that the stability of the SHG response has been achieved by measuring in transmission mode.

In the case of non-imprinted mesoporous platinum the SHG intensities of the p-polarized component using left-hand circular excitation (Ψ_1=22.5°) and right-hand circular excitation (Ψ_1=67.5°) varied by approximately 0.02 (arb. units). Similarly, the SHG intensities of the s-polarized component using left-hand circular excitation (Ψ_1=22.5°) and right-hand circular excitation (Ψ_1=67.5°) were insignificantly different. This result shows no chirality at the surface of non-imprinted mesoporous platinum films.

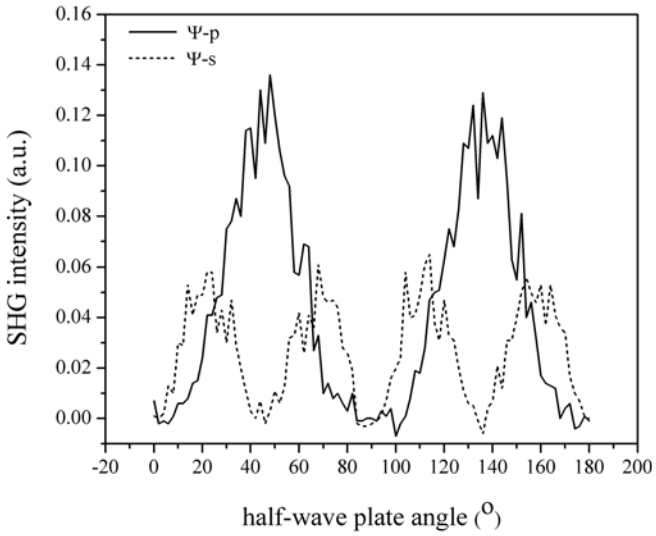

Figure 64. The SHG response as a function of the rotation angle of the half-waveplate (Ψ_1) for a non-imprinted mesoporous Pt film deposited on ITO-Au obtained in the transmission mode. The solid line represents the transmitted SHG intensity of the p-polarized component (Ψ-p). The dashed line shows the transmitted SHG intensity of the s-polarized component (Ψ-s).

For chiral imprinted mesoporous platinum, we observed the SHG intensities of the s-polarized component for left-hand circular excitation (Ψ_1=22.5°) and right-hand circular excitation (Ψ_1=67.5°). There was a slight difference in the SHG intensities between left- and right-hand circular excitations. Although, a difference in the SHG intensity for both excitations was observed, this behavior was not very pronounced. As it is well known, there are other possibilities to observe a change in intensity between left and right-hand circular polarized excitations, such as in the nonhomogeneous or anisotropic media in which the properties depend on the orientation of sample. Particularly, the anisotropic response for metals is strongly influenced due to details of their structure[233,236].

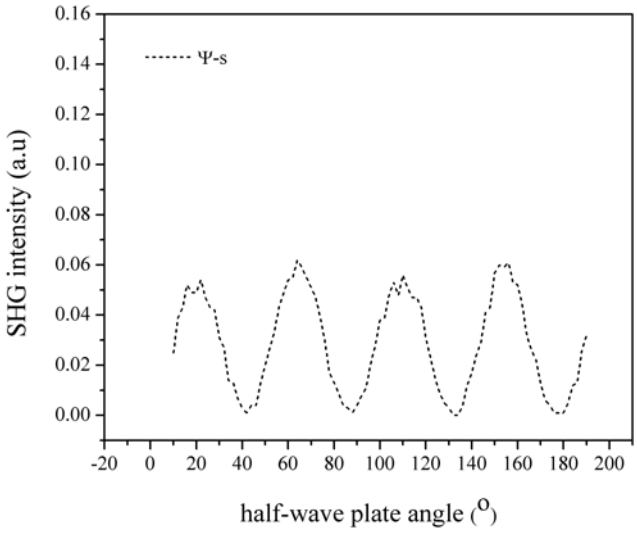

Figure 65. The SHG response as a function of the rotating angle of the half waveplate (Ψ_1) for a chiral imprinted mesoporous Pt film deposited on ITO-Au (imprinted by D-DOPA, D-DOPA/Pt=1/25) obtained in the transmission mode. The dashed line shows the transmitted SHG intensity of the s-polarized component (Ψ-s).

In addition, a control experiment was performed in order to make sure that the different SHG intensities obtained with left- and right-hand circular excitation don't come from other artifacts but originate from the chirality of the surfaces. The SHG response was measured with L-DOPA molecules on ITO-Au, prepared by drying of L-DOPA solution on ITO-Au. Because this electrode was prepared with real chiral molecules, a chiral response could be measured. In this experiment, different SHG intensities with left-hand circular excitation (Ψ_1=22.5°) and right-hand circular excitation (Ψ_1=67.5°) when the sample was fixed at 56° with respect to incident beam were clearly observed (Figures 66a and 66b), especially when monitoring the s-polarized component as shown in Figure 66b. As stated above, anisotropy strongly influences SHG signals. To investigate this effect, the SHG intensity was measured by rotating the sample holder from 56 to 236°. The SHG response of the s-polarized component obtained at a sample angle of 236° is shown in Figure 66c. It clearly reveals the different signals for left-hand circular excitation (Ψ_1=22.5°) and right-hand circular excitation (Ψ_1=67.5°). In contrast to the fixed sample at 56°, the opposite trend after rotating the sample for 180° was observed. In

other words, the SHG intensity of right-hand circular excitation was lower than that of left-hand circular excitation in the case of the fixing sample holder at 236°, whereas the response of right circular polarization was higher than that of left one for fixing sample holder at 56°. This behavior can be explained by the fact that in anisotropic medium the properties become directionally dependent, resulting in the change in the SHG pattern when the sample is rotated by 180°. In contrast, in the isotropic medium composing of only chirality at surface do not affect such pattern change. This result clearly demonstrates that anisotropic response is sufficiently strong to be detected in this system.

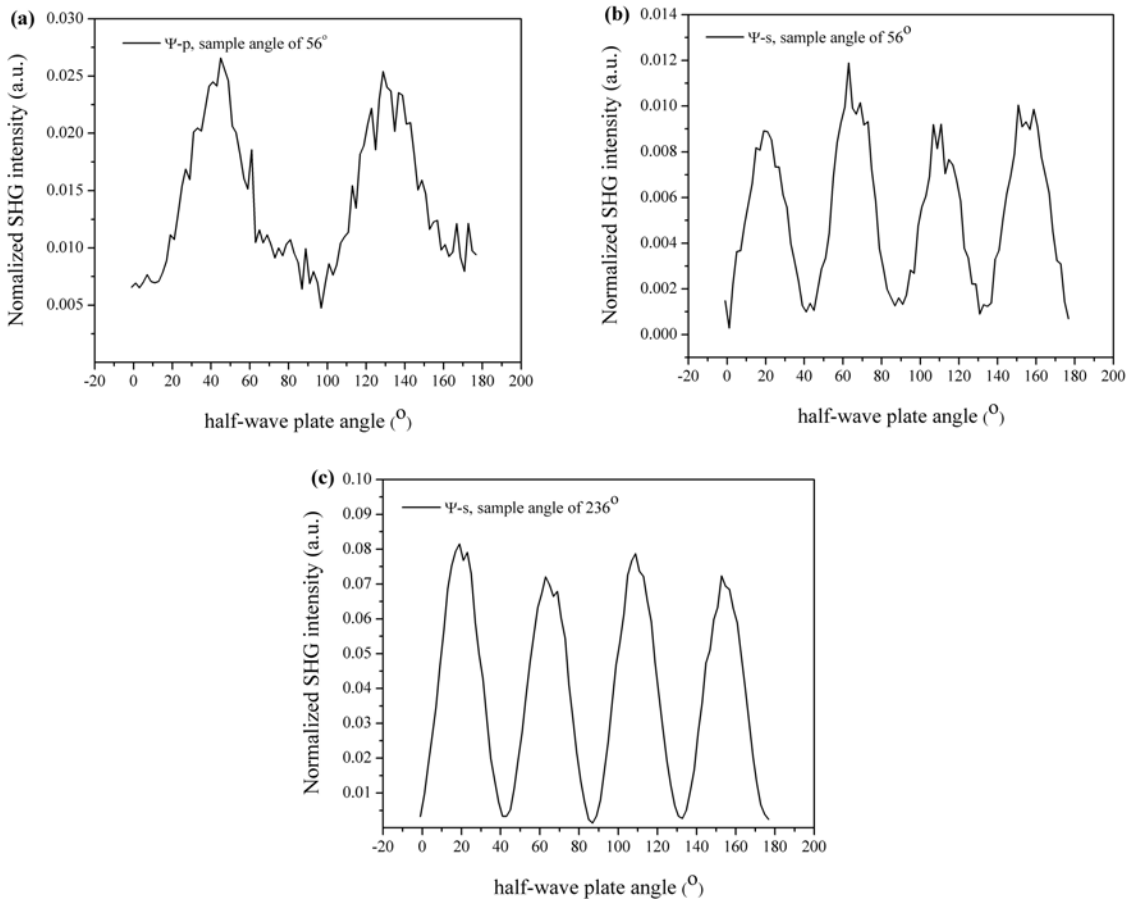

Figure 66. The SHG response as a function of the rotation angle of the half-waveplate (Ψ_1) for the L-dopa dried on ITO-Au obtained in the transmission mode: (a) the SHG intensity of the p-polarized component when the sample was fixed at 56°, (b) s-polarized component when the sample was fixed at 56°and (c) s-polarized component when the sample was fixed at 236°.

Because an anisotropic response strongly affects the SHG intensity in our experiment, this effect should be eliminated to verify the chirality of a mesoporous platinum surface. As it is well known, an anisotropic response can be reduced by rotation of the sample, whereas the chirality signal should be unaffected[237]. Therefore, it is not sufficient to perform the SHG experiment with a statically oriented sample angle, but more data from SHG experiments in which the anisotropic effect is eliminated are needed to confirm the chiral character of these metal surfaces.

3.8 Enantioselective adsorption of DOPA enantiomers on chiral imprinted mesoporous platinum

In order to further verify the chiral properties of the mesoporous metal surfaces, other independent experiments were performed based on the enantioselective adsorption of chiral probes on the chiral imprinted mesoporous platinum. The selective adsorption experiments were carried out by exposing the chiral mesoporous platinum films to racemic mixtures of L-DOPA and D-DOPA and subsequently monitoring by HPLC the composition of the supernatant solution. The supernatant solution was collected at different times and analyzed by HPLC equipped with a capillary column with a chiral stationary phase. Because a UV detector was used in this study, the wavelength of maximum absorbance (λ_{max}) of DOPA molecules was investigated by UV/vis spectroscopy. As shown in Figure 67, the UV/vis absorption spectrum was continuously scanned in a range from 200 to 800 nm. It shows two strong absorption peaks at around 230 and 285 nm, related to the π-π^* transition of the benzene ring and the L_a-L_b transition, respectively[238]. Typically, in the benzene molecule the first peak is strong, whereas the second band is not significant due to the weak symmetry-forbidden transition. However, in substituted benzene the symmetry is broken and the symmetry-forbidden transitions (L_a-L_b transition) is allowed, resulting in an enhancement of the second peak. In the case of DOPA (two hydroxyl and one aliphatic substituents on the benzene ring), the first peak is more pronounced with respect to the second one, thus the wavelength of maximum absorption (λ_{max}) of the first peak (230 nm) was used for monitoring all samples by HPLC.

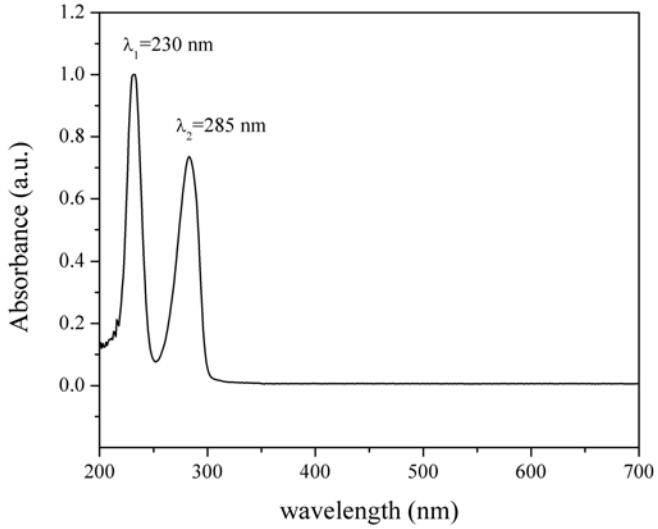

Figure 67. The absorption spectrum of a racemic mixture of L-DOPA and D-DOPA in a mixture of 50/50 (v/v) methanol/acetonitrile, 50 mM formic acid and 25 mM diethylamine.

For the HPLC measurement the separation of the constituents of the supernatant solution was first carried out at 22°C using a mixture of 50/50 (v/v) methanol/acetonitrile, 50 mM formic acid and 25 mM diethylamine as mobile phase. The chromatogram of L-DOPA and D-DOPA separation is shown in Figure 68a. It shows that parts of the L-DOPA and D-DOPA peaks are overlapping. In order to quantify the peak separation, the resolution factor (R_s) is calculated by the following equation:

$$R_s = \frac{1.18(t_{R2}-t_{R1})}{(W_{b1}+W_{b2})}$$

where t_{R2} and t_{R1} are the retention times of components 2 and 1, respectively. W_{b1} and W_{b2} represent the peak widths determined at half peak height for components 1 and 2, respectively [239]. Typically, the value of R_s should be at least 1.5. However, in our case the separation ability of the two enantiomers is characterized by a R_s of 0.8.

Enantioselective separation ability at different temperatures by chromatography can be explained by thermodynamic aspects. The Gibbs-Helmholz equation is applied to explain the effect of temperature on enantioselective separation.

$$\ln\alpha = -\frac{\Delta\Delta H^0}{RT} + \frac{\Delta\Delta S^0}{R}$$

α is the enantiomer separation factor. $\Delta\Delta H^0$ and $\Delta\Delta S^0$ are the enthalpy and entropy differences between the two enantiomers when they interact with the stationary phase. T and R are the absolute temperature and the universal gas constant, respectively [240]. In fact, at low temperature the separation is enthalpy controlled. The enantiomer separation decreases with temperature until the enantiomer separation is suppressed when the first term and second term of this equation are equal ($\ln \alpha = 0$). This temperature is called the isoenantioselective temperature where $T_{iso} = \Delta\Delta H^0/\Delta\Delta S^0$. Above T_{iso}, the enantioselective separation is dominated by the entropy control and the reverse order of elution is observed [241].

Almost all enantiomer separations are better at lower temperature. Therefore we also investigated the enantiomer separation by HPLC at 2°C. As shown in the chromatogram of Figure 68b, at lower temperature the separation of D-DOPA and L-DOPA is better compared to their separation at 22°C. Furthermore, an improved resolution factor (Rs) of approximately 1.5 was also observed. Therefore, this condition was used to monitor the ratio between D-DOPA and L-DOPA in the supernatant solution after being in contact with the platinum films.

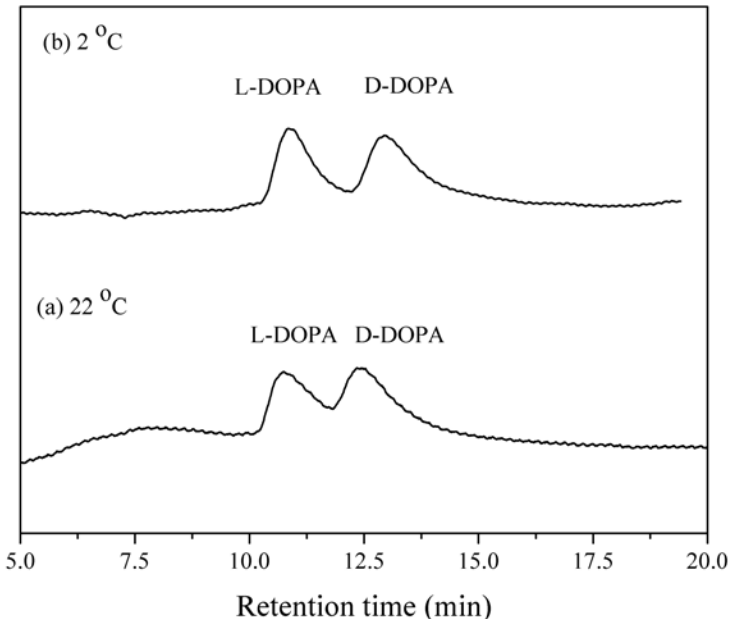

Figure 68. HPLC chromatograms of 100 µM D-DOPA/L-DOPA separation monitored by a UV detector at 230 nm and using a CHIRALPAK ZWIX (+) chiral column with a mixture of 50/50 (v/v) methanol/acetonitrile, 50 mM formic acid and 25 mM diethylamine as mobile phase at (a) 22° and (b) 2°.

In this work, the enantioselective adsorption was characterised by the enantiomeric separation factor ($\alpha_{D/L}$), derived from the quotient of the ratios of D-DOPA to L-DOPA concentrations in the solution, after and before being in contact with the platinum films. The ($\alpha_{D/L}$) is described by the following equation.

$$\alpha_{D/L} = \frac{\left([D-DOPA]/[L-DOPA]\right)_{before}}{\left([D-DOPA]/[L-DOPA]\right)_{after}}$$

$[D\text{-}DOPA]_{before}$ and $[L\text{-}DOPA]_{before}$ are the concentration of D- and L-DOPA enantiomers in solution, respectively, before being in contact with the platinum films. $[D\text{-}DOPA]_{after}$ and $[L\text{-}DOPA]_{after}$ represent their concentration terms after exposing with such films. Table 17 shows the D/L DOPA separation factors ($\alpha_{D/L}$) for a certain time (1, 3 and 5 hours) at various temperatures and thicknesses of the platinum films. The control experiment was performed at 22°C on a non-imprinted mesporous platinum film obtained by injecting a charge density of 4C/cm^2 (NIM-Pt 4C/cm^2). As expected, the $\alpha_{D/L}$ of this film was close to one within the experimental error after an adsorption time of 1 hour (Entry 1). At longer adsorption times, the $\alpha_{D/L}$ remained steady with a value of 0.98±0.05 after 5 hours. This result indicates that there is, as expected, no enantioselective adsorption on such materials. The chiral mesoporous platinum film obtained with L-DOPA as chiral template (CIM-Pt-L 4C/cm^2) shows insignificant enantioselectivity for an adsorption time of 1 hour at 22°C, but the enantioselectivity is more pronounced for longer exposure times (1.29 ±0.05 after five hours). It is important to note that this characteristic adsorption time is much longer compared to the duration of the electrochemical experiments. This behavior is explained by the fact that dry platinum films were used for the enantioselective adsorption experiments, while the electrochemical experiments were carried out with already wet electrodes. Therefore, the diffusion of DOPA into the mesoporous channels needs more time in the case of an initially dry electrode, because the wetting of mesopores can be more or less time consuming, depending on the hydrophilicity of the matrix.

The $\alpha_{D/L}$ was compared for platinum films with different thicknesses. By increasing the thickness of the platinum film, which is proportional to the injected charge density, the enantioselective adsorption doesn't change very much at room temperature (22°C) (Entries 2 and 3). The $\alpha_{D/L}$ values of the chiral platinum films obtained for injected charge densities of 4 and 8 C/cm^2 was 1.29±0.05 and 1.32±0.05 at the exposure

time of 5 hours, respectively. As stated above, the enantiomeric separation is strongly depended on temperature. From a thermodynamic point of view, almost all enantiomers shows higher separation when the temperature is reduced[242]. In order to optimize the enantioselectivity of the meosporous surfaces, the adsorption has been also studied at lower temperature. The enantioselective separation factor ($\alpha_{D/L}$) was significantly increased at low temperature, as expected, the $\alpha_{D/L}$ of chiral mesoporous platinum imprinted by L-DOPA with an injected charge density of 8 C/cm^2 at 22 and 2 °C was 0.96±0.05 and 1.18±0.05 for the exposure time of 1 hour, respectively. The value at longer adsorption time was 1.32±0.05 and 1.52±0.05 at 22 and 2 °C, respectively (Entries 3 and 4). This result indicates that L-DOPA is preferentially adsorbed in the metal matrix, imprinted by L-DOPA as chiral template, leaving an excess of D-DOPA in the supernatant phase.

The opposite tendency was observed when the chiral mesoporous platinum imprinted by D-DOPA was exposed to the racemic mixture of D-DOPA/L-DOPA. The $\alpha_{D/L}$ becomes smaller than 1, suggesting that the adsorption of D-DOPA is favored on these materials (Entries 5 and 6). This enantioselectivity was more pronounced for thicker films. The observed differences are in agreement with an energetic stabilization of the preferred adsorption state in such chiral materials [173,232].

Table 17. Enantioselective adsorption of a racemic DOPA solution on chiral mesoporous platinum films (CIM-Pt) under different conditions.

Entry		Temp. (°C)	Time (h)	$\alpha_{D/L}$ [a]
1	NIM-Pt 4C/cm^2 [b]	22	1	0.99±0.05
			5	0.98±0.05
2	CIM-Pt-L 4C/cm^2 [c]	22	1	1.02±0.05
			5	1.29±0.05
3	CIM-Pt-L 8C/cm^2 [d]	22	1	0.96±0.05
			5	1.32±0.05
4	CIM-Pt-L 8C/cm^2 [d]	2	1	1.18±0.05
			3	1.52±0.05
5	CIM-Pt-D 4C/cm^2 [e]	2	1	0.98±0.05
			5	0.93±0.05
6	CIM-Pt-D 8C/cm^2 [f]	2	1	0.91±0.05
			3	0.85±0.05

[a]The D/L DOPA separation factor ($\alpha_{D/L}$) was calculated as the quotient of the ratios of D-DOPA to L-DOPA concentrations in the solution, after and before being in contact with the platinum films for a certain time (1, 3 and 5 hours).

[b]Non-imprinted mesoporous platinum using a deposition charge density of *4 C/cm^2*.

[c]Chiral imprinted mesoporous platinum obtained using *L-DOPA (L-DOPA/ $PtCl_6^{2-}$ = 1/17)* as template, and a deposition charge density of *4 C/cm^2*.

[d]Chiral imprinted mesoporous platinum obtained using *L-DOPA (L-DOPA/ $PtCl_6^{2-}$ = 1/17)* as template, and a deposition charge density of *8 C/cm^2*.

[e]Chiral imprinted mesoporous platinum obtained using *D-DOPA (D-DOPA/ $PtCl_6^{2-}$ = 1/17)* as template, and a deposition charge density of *4 C/cm^2*.

[f]Chiral imprinted mesoporous platinum obtained using *D-DOPA (D-DOPA/ $PtCl_6^{2-}$ = 1/17)* as template, and a deposition charge density of *8 C/cm^2*.

4. CONCLUSION

In conclusion, this chapter demonstrates that chiral imprinted mesoporous platinum has been successfully obtained by the electrodeposition of platinum in the simultaneous presence of surfactant, forming a lyotropic crystal phase, and a chiral template molecule. The results suggest that due to interactions between the surfactant and the chiral template, it was possible to generate chiral “footprints” on the walls of the mesopores. The generated material exhibits not only a dramatic increase in active surface area due to the mesoporosity, but also a significant discrimination between two enantiomers of a chiral probe, confirmed by both electrochemical and enantioselective adsorption experiments. In addition, the chiral properties of the mesoporous metal matrix strongly increase with the amount of chiral template used in the electrodeposition step, and with the thickness of the film, which can be controlled by the charge injected during the deposition.

Although the chirality of the metal surfaces measured by SHG experiments still needs further confirmation the results from the electrochemical and selective adsorption measurements strongly support the presence of chirality in the bulk of the mesoporous metal layer. Interestingly, the mesoporous feature amplifies the chirality of the metal phase. This behavior might be explained by a chirality transfer from the molecular species to the inner walls of the mesopores, maintaining at the same time a very good accessibility of the chiral cavities by the chiral probes, compared to nonporous metal phase. This work illustrates the first example of a chiral imprinted metal that retains its chirality even after removal of the template, and thus is very complementary to the class of molecular imprinted polymers. Our findings could lead to the development of new materials, which are of potential interest for applications in areas such as chiral synthesis, sensors, separation, purification and drug development.

4 CONCLUSIONS AND PERSPECTIVES

This thesis presented several aspects concerning the elaboration, characterisation and application of various porous materials. Three main points were studied, namely the synthesis of the hierarchical micro/mesoporous zeolite and their applications for petrochemical processes as demonstrated in Chapter 1, the theoretical study of the reaction mechanism at microporous zeolite for Chapter 2 and the design of mesoporous metals with intrinsic chirality in Chapter 3.

Chapter 1: Synthesis of the hierarchical micro/mesoporous zeolite and its applications in petrochemical industry as catalyst for hydrocarbon transformations

In the first part of the thesis, we demonstrated the fabrication and application of the hierarchical micro/mesoprorous zeolite. The motivation of this work is based on the disadvantages of conventional microporous zeolite. Although usual zeolites have been widely used in petrochemical industry, they often suffer from the disadvantages of microporous features such as the restriction of diffusion of molecules in the matrix. Therefore, an introduction of mesoporous cavities into a part of the microporous crystal is one of alternative ways to overcome such problems. In this work, we reported that the hierarchical micro/mesoporous zeolites, combining microporous and mesoporous features, have been successfully prepared using carbon-silica (C/SiO_2) composites, derived from a pyrolysis of hydrocarbon gas on silica gel. The C/SiO_2 composites act as a bifunctional material in which carbon residues and SiO_2 act as mesoporous template and a silica source for the zeolite synthesis, respectively. The mesoporosity of zeolite is clearly obtained when carbon residues are incorporated during zeolite synthesis and it can be easily controlled by varying the carbon content in the C/SiO_2 composites. Increasing the carbon content in such composites results in a significant increase in surface area and total pore volume, which reflects a rise of the mesopore volume whereas the micropore volume of the sample is not significantly altered. These observations are promising and confirm the existence of hierarchical zeolite combining microporous and mesoporous

features obtained by using carbon templates derived from a pyrolysis of hydrocarbon gas on silica gel. Their catalytic performance for different reactions, including *n*-butene isomerization, and catalytic cracking of hexane, methylpentane and *n*-hexadecane, were also investigated. It clearly demonstrated that the catalytic efficiency of the reactions with respect to large molecules such as *n*-butene isomerization and catalytic cracking of *n*-hexadecane, could be improved by the mesoporosity, whereas the performances of catalytic cracking of C6 molecules could not be enhanced by the mesoporous material. In addition, the catalytic activities of bifunctional zeolites, which are obtained by the incorporation of active metallic sites (Pt) into H^+ type zeolite, are investigated on both, the conventional and the hierarchical micro/mesoporous zeolite. It is found that the hierarchical micro/mesoporous Pt/HZSM-5 not only improved the degree of metal nanoparticle dispersion into secondary zeolite voids, but importantly also enhanced the catalytic reaction of *n*-hexadecane hydrocracking. Our findings confirm that the hierarchical zeolite with a bimodal porous system of microporous and mesoporous cavities can be generated by using carbon residues as mesopore-templates derived from pyrolysis of hydrocarbon gases and these catalysts show promising results, especially when the reaction involves large molecules in the catalytic processes. We strongly believe that this synthesis method of the hierarchical microporous/mesoporous zeolites can be used to produce any types of hierarchical zeolite, which might be useful for many potential reactions in petrochemical industry.

Chapter 2: A Quantum chemical analysis of structures and reaction mechanisms of *1*-butene skeletal isomerization over ferrierite zeolite

Based on previous reports in the literature, the skeletal isomerization of *1*-butene over zeolite is one of the most interesting topics in both the academic and industrial context. However, the mechanism of this reaction and the existence of intermediates are still debated. In this chapter the complete mechanism of skeletal isomerization of *1*-butene over ferrierite zeolite was theoretically studied by means of quantum calculation methods. The reaction mechanisms are proposed to occur via a monomolecular reaction, involving the transformation of adsorbed *1*-butene through *2*-butoxide, isobutoxide, and *tert*-butyl cation intermediates. Two different mechanisms are found depending on the size of the framework model. In the case of a large model (37T cluster) including the effect of the zeolite framework, the monomolecular reaction mechanism proceeds through four transition state structures, namely, the protonation of *1*-butene TS1(**II**), the cyclic

transition state TS2(**IV**), the conversion of isobutoxide to *tert*-butyl cation by the 1,2 hydride shift transition state (**VI**) and the deprotonation of *tert*-butyl cation (**VIII**), with the corresponding intermediates, *2*-butoxide, isobutoxide and *tert*-butyl carbenium ion. In contrast, the mechanism in a small model (5T) excluding the framework effect is leading to three transition state structures and two alkoxide species. The difference in mechanism for the 5T model compared to 37T is that the isobutoxide (**V**) intermediate can be directly decomposed to form the isobutene adsorption complex, whereas this is prohibited in the case of 37T. Moreover, different rate-determining steps were observed in the 5T and 37T model. The rate-determining step for the 37T model is found to be the decomposition of the surface isobutoxide intermediate through a highly unstable primary isobutyl carbenium ion transition state via the intramolecular 1,2-hydride shift of the *tert*-butyl cation as reactive intermediate, whereas the rate-determining step for the 5T model is the branching step in which *2*-butoxide transforms into isobutoxide. In addition, these observations demonstrated that using medium-pore size ferrierite zeolite (H-FER), presented by the 37T model, suggests the *tert*-butyl carbenium cation as a true intermediate, whereas this species cannot be found when the effects of the zeolite framework were neglected. Our findings support the idea that the shape selectivity due to the "nano-confinement" effect of the zeolite framework strongly affects not only the adsorption, the stability of reaction intermediates and transition states, but also the mechanisms of the reaction. We also made evident here that the choice of methods, models used and model constrains must be carefully considered in order to get correct results.

Chapter III: Enantioselective recognition at metallic mesoporous surfaces

Apart from porous zeolite, we also investigated the generation of chiral mesoporous metal and its enantioselective recognition properties by a molecular imprinting (MI) approach. MI method is a major approach for generating materials with enantioselective properties, however, this technique has been restricted so far mostly to soft matrices such as polymers, leading to molecularly imprinted polymers (MIPs). They often suffers from some disadvantages, such as difficult template removal, slow binding kinetics and high flexibility of the polymer, which results in destruction of the chiral structure of the cavity after removal of the template. Introduction of chiral features at metal surfaces has been reported in many literature reports. However, so far no study achieved the design of chiral metallic surfaces by molecular imprinting in which the

chiral footprint could be retained even after removal of the chiral template. The reason might be the low surface area of flat metallic surfaces. This has motivated us to design a matrix bearing mesoporous features and chiral cavities at the internal metallic surface. In this work, chiral imprinted mesoporous platinum has been successfully elaborated by the electrodeposition of platinum in the simultaneous presence of surfactant, forming a lyotropic crystal phase, and a chiral template molecule. This material exhibits not only a dramatic increase in active surface area due to the mesoporosity, but also a significant discrimination between two enantiomers of a chiral probe, confirmed by both electrochemical and enantioselective adsorption experiments. This preliminary work shows very promising results with respect to a chiral imprinted metal that retains its chirality even after removal of the template, and is therefore very complementary to the class of molecular imprinted polymers. Our findings could lead to the development of new materials, which are of potential interest for applications in areas such as chiral synthesis, sensors, separation, purification and drug development.

In summary, this thesis demonstrated that porous materials are very useful for various potential applications such as catalysis, separation and chiral technologies. The design of porous features can be efficiently controlled by the presence of both, hard and soft templates. The well-organized porous structure results in unique properties of the materials. The materials, composed of only small porous cavities (microporous materials), exhibit a shape selectivity for molecules that are comparable with the porous features. However, microporous materials are not efficient for some applications due to eventual difficulties to access the active sites. In order to improve these weaknesses of such materials, the design of materials with larger porous cavities might be an alternative way. Introducing mesoporous cavities into the materials not only enhances the surface area due to mesoporosity, but also increases the possibility of molecules to access the specific sites. Furthermore, in this thesis we also demonstrated that materials bearing mesoporous features and chiral cavities at the inner pore surface allow the discrimination between two enantiomers of a chiral probe compared to nonporous materials. Our findings verified that many types of porous materials can be designed in a controllable way in order to improve their efficiency, and make them suitable for desired applications such as petrochemical catalysis, chiral synthesis, sensors, separation and drug development.

5 REFERENCES

1. Kung, H. H.; Williams, B. A.; Babitz, S. M.; Miller, J. T.; Haag, W. O.; Snurr, R. Q., Enhanced hydrocarbon cracking activity of Y zeolites. *Topics in Catalysis* **2000,** *10* (1), 59-64.

2. Houžvička, J.; Diefenbach, O.; Ponec, V., The Role of Bimolecular Mechanism in the Skeletal Isomerisation ofn-Butene to Isobutene. *Journal of Catalysis* **1996,** *164* (2), 288-300.

3. Choudhary, V. R.; Kinage, A. K.; Choudhary, T. V., Simultaneous aromatization of propane and higher alkanes or alkenes over H-GaAlMFI zeolite. *Chemical Communications* **1996,** (22), 2545-2546.

4. Maxwell, I. E., Zeolite catalysis in hydroprocessing technology. *Catalysis Today* **1987,** *1* (4), 385-413.

5. van Santen, R. A.; Niemantsverdriet, J. W., *Chemical Kinetics and Catalysis*. Plenum: New York, 1995; p 275.

6. Chang, C. D., *Hydrocarbons from Methanol*. Marcel Dekker, Inc.: New York, 1983.

7. Tosheva, L.; Valtchev, V. P., Nanozeolites: Synthesis, Crystallization Mechanism, and Applications. *Chemistry of Materials* **2005,** *17* (10), 2494-2513.

8. Van Grieken, R.; Sotelo, J. L.; Menéndez, J. M.; Melero, J. A., Anomalous crystallization mechanism in the synthesis of nanocrystalline ZSM-5. *Microporous and Mesoporous Materials* **2000,** *39* (1–2), 135-147.

9. Zhan, B.-Z.; White, M. A.; Lumsden, M.; Mueller-Neuhaus, J.; Robertson, K. N.; Cameron, T. S.; Gharghouri, M., Control of Particle Size and Surface Properties of Crystals of NaX Zeolite. *Chemistry of Materials* **2002,** *14* (9), 3636-3642.

10. Song, W.; Grassian, V. H.; Larsen, S. C., High yield method for nanocrystalline zeolite synthesis. *Chemical Communications* **2005,** (23), 2951-2953.

11. Valtchev, V. P.; Bozhilov, K. N., Evidences for Zeolite Nucleation at the Solid−Liquid Interface of Gel Cavities. *Journal of the American Chemical Society* **2005,** *127* (46), 16171-16177.

12. Jacobsen, C. J. H.; Madsen, C.; Houzvicka, J.; Schmidt, I.; Carlsson, A., Mesoporous Zeolite Single Crystals. *Journal of the American Chemical Society* **2000,** *122* (29), 7116-7117.

13. Schmidt, I.; Madsen, C.; Jacobsen, C. J. H., Confined Space Synthesis. A Novel Route to Nanosized Zeolites. *Inorganic Chemistry* **2000,** *39* (11), 2279-2283.

14. Jacobsen, C. J. H.; Madsen, C.; Janssens, T. V. W.; Jakobsen, H. J.; Skibsted, J., Zeolites by confined space synthesis – characterization of the acid sites in nanosized ZSM-5 by ammonia desorption and 27Al/29Si-MAS NMR spectroscopy. *Microporous and Mesoporous Materials* **2000,** *39* (1–2), 393-401.

15. Janssen, A. H.; Koster, A. J.; de Jong, K. P., On the Shape of the Mesopores in Zeolite Y: A Three-Dimensional Transmission Electron Microscopy Study Combined with Texture Analysis. *Journal of Physical Chemistry B* **2002,** *106* (46), 11905-11909.

16. Groen, J. C.; Moulijn, J. A.; Perez-Ramirez, J., Desilication: on the controlled generation of mesoporosity in MFI zeolites. *Journal of Materials Chemistry* **2006,** *16* (22), 2121-2131.

17. Egeblad, K.; Christensen, C. H.; Kustova, M.; Christensen, C. H., Templating Mesoporous Zeolites†. *Chemistry of Materials* **2007,** *20* (3), 946-960.

18. Zhu, K.; Sun, J.; Liu, J.; Wang, L.; Wan, H.; Hu, J.; Wang, Y.; Peden, C. H. F.; Nie, Z., Solvent Evaporation Assisted Preparation of Oriented Nanocrystalline Mesoporous MFI Zeolites. *ACS Catalysis* **2011,** *1* (7), 682-690.

19. Yang, X.-Y.; Tian, G.; Chen, L.-H.; Li , Y.; Rooke, J. C.; Wei, Y.-X.; Liu, Z.-M.; Deng, Z.; Van Tendeloo, G.; Su , B.-L., Well-Organized Zeolite Nanocrystal Aggregates with Interconnected Hierarchically Micro–Meso–Macropore Systems Showing Enhanced Catalytic Performance. *Chemistry – A European Journal* **2011,** *17* (52), 14987-14995.

20. Tao, Y.; Kanoh, H.; Abrams, L.; and Kaneko, K., Mesopore-modified zeolites : Preparation, characterization, and applications. *Chemical Reviews* **2006,** *106* (3), 896-910.

21. Kim, S.-S.; Shah, J.; Pinnavaia, T. J., Colloid-Imprinted Carbons as Templates for the Nanocasting Synthesis of Mesoporous ZSM-5 Zeolite. *Chemistry of Materials* **2003,** *15* (8), 1664-1668.

22. Perez-Ramirez, J.; Christensen, C. H.; Egeblad, K.; Christensen, C. H.; Groen, J. C., Hierarchical zeolites: enhanced utilisation of microporous crystals in catalysis by advances in materials design. *Chemical Society Reviews* **2008,** *37* (11), 2530-2542.

23. Xiao, F.-S.; Wang, L.; Yin, C.; Lin, K.; Di, Y.; Li, J.; Xu, R.; Su, D. S.; Schlögl, R.; Yokoi, T.; Tatsumi, T., Catalytic Properties of Hierarchical Mesoporous Zeolites Templated with a Mixture of Small Organic Ammonium Salts and Mesoscale Cationic Polymers. *Angewandte Chemie* **2006,** *118* (19), 3162-3165.

24. Pérez-Ramírez, J.; Abelló, S.; Bonilla, A.; Groen, J. C., Tailored Mesoporosity Development in Zeolite Crystals by Partial Detemplation and Desilication. *Advanced Functional Materials* **2009,** *19* (1), 164-172.

25. Groen, J. C.; Jansen, J. C.; Moulijn, J. A.; Pérez-Ramírez, J., Optimal Aluminum-Assisted Mesoporosity Development in MFI Zeolites by Desilication. *The Journal of Physical Chemistry B* **2004,** *108* (35), 13062-13065.

26. Kortunov, P.; Vasenkov, S.; Kärger, J.; Valiullin, R.; Gottschalk, P.; Fé Elía, M.; Perez, M.; Stöcker, M.; Drescher, B.; McElhiney, G.; Berger, C.; Gläser, R.; Weitkamp, J., The Role of Mesopores in Intracrystalline Transport in USY Zeolite: PFG NMR Diffusion Study on Various Length Scales. *Journal of the American Chemical Society* **2005,** *127* (37), 13055-13059.

27. Wang, L.; Zhang, Z.; Yin, C.; Shan, Z.; Xiao, F.-S., Hierarchical mesoporous zeolites with controllable mesoporosity templated from cationic polymers. *Microporous and Mesoporous Materials In Press, Corrected Proof*.

28. Xiao, F.-S.; Wang, L.; Yin, C.; Lin, K.; Di, Y.; Li, J.; Xu, R.; Su, D. S.; Schlögl, R.; Yokoi, T.; Tatsumi, T., Catalytic Properties of Hierarchical Mesoporous Zeolites Templated with a Mixture of Small Organic Ammonium Salts and Mesoscale Cationic Polymers13. *Angewandte Chemie International Edition* **2006,** *45* (19), 3090-3093.

29. Choi, M.; Cho Hae, S.; Srivastava, R.; Venkatesan, C.; Choi, D.-H.; Ryoo, R., Amphiphilic Organosilane-Directed Synthesis of Crystalline Zeolite with Tunable Mesoporosity. *Nature Materials* **2006,** *5* (9), 718-723.

30. Tao, Y.; Hattori, Y.; Matumoto, A.; Kanoh, H.; Kaneko, K., Comparative Study on Pore Structures of Mesoporous ZSM-5 from Resorcinol-Formaldehyde Aerogel and Carbon Aerogel Templating. *Journal of Physical Chemistry B* **2005,** *109* (1), 194-199.

31. Zhao, J.; Hua, Z.; Liu, Z.; Li, Y.; Guo, L.; Bu, W.; Cui, X.; Ruan, M.; Chen, H.; Shi, J., Direct fabrication of mesoporous zeolite with a hollow capsular structure. *Chemical Communications* **2009,** *0* (48), 7578-7580.

32. Schmidt, I.; Boisen, A.; Gustavsson, E.; Ståhl, K.; Pehrson, S.; Dahl, S.; Carlsson, A.; Jacobsen, C. J. H., Carbon Nanotube Templated Growth of Mesoporous Zeolite Single Crystals. *Chemistry of Materials* **2001,** *13* (12), 4416-4418.

33. Tosheva, L.; Valtchev, V.; Sterte, J., Silicalite-1 containing microspheres prepared using shape-directing macro-templates. *Microporous and Mesoporous Materials* **2000,** *35–36* (0), 621-629.

34. Verhoef, M. J.; Kooyman, P. J.; van der Waal, J. C.; Rigutto, M. S.; Peters, J. A.; van Bekkum, H., Partial Transformation of MCM-41 Material into Zeolites: Formation of Nanosized MFI Type Crystallites. *Chemistry of Materials* **2001,** *13* (2), 683-687.

35. Janssen, A. H.; Schmidt, I.; Jacobsen, C. J. H.; Koster, A. J.; de Jong, K. P., Exploratory study of mesopore templating with carbon during zeolite synthesis. *Microporous and Mesoporous Materials* **2003,** *65* (1), 59-75.

36. Kustova, M.; Egeblad, K.; Zhu, K.; Christensen, C. H., Versatile Route to Zeolite Single Crystals with Controlled Mesoporosity: in situ Sugar Decomposition for Templating of Hierarchical Zeolites. *Chemistry of Materials* **2007,** *19* (12), 2915-2917.

37. Butler, A. C.; Nicolaides, C. P., Catalytic skeletal isomerization of linear butenes to isobutene. *Catalysis Today* **1993,** *18* (4), 443-471.

38. Collignon, F.; Mariani, M.; Moreno, S.; Remy, M.; Poncelet, G., Gas Phase Synthesis of MTBE from Methanol and Isobutene over Dealuminated Zeolites. *Journal of Catalysis* **1997,** *166* (1), 53-66.

39. Seddon, D., Reformulated gasoline, opportunities for new catalyst technology. *Catalysis Today* **1992,** *15* (1), 1-21.

40. Mooiweer, H. H.; de Jong, K. P.; Kraushaar-Czarnetzki, B.; Stork, W. H. J.; Krutzen, B. C. H., Skeletal isomerisation of olefins with the zeolite Ferrierite as catalyst. In *Studies in Surface Science and Catalysis*, J. Weitkamp, H. G. K. H. P.; Hölderich, W., Eds. Elsevier: 1994; Vol. Volume 84, pp 2327-2334.

41. Houžvička, J.; Hansildaar, S.; Ponec, V., The Shape Selectivity in the Skeletal Isomerisation ofn-Butene to Isobutene. *Journal of Catalysis* **1997,** *167* (1), 273-278.

42. Oyoung, C. L.; Pellet, R. J.; Casey, D. G.; Ugolini, J. R.; Sawicki, R. A., Skeletal Isomerization of 1-Butene on 10-Member Ring Zeolite Catalysts. *Journal of Catalysis* **1995,** *151* (2), 467-469.

43. Xu, W. Q.; Yin, Y. G.; Suib, S. L.; Oyoung, C. L., Selective Conversion of n-Butene to Isobutylene at Extremely High Space Velocities on ZSM-23 Zeolites. *Journal of Catalysis* **1994,** *150* (1), 34-45.

44. Simon, M. W.; Suib, S. L.; Oyoung, C. L., Synthesis and Characterization of ZSM-22 Zeolites and Their Catalytic Behavior in 1-Butene Isomerization Reactions. *Journal of Catalysis* **1994,** *147* (2), 484-493.

45. Klepel, O.; Loubentsov, A.; Böhlmann, W.; Papp, H., Oligomerization as an important step and side reaction for skeletal isomerization of linear butenes on H-ZSM-5. *Applied Catalysis A: General* **2003,** *255* (2), 349-354.

46. de Ménorval, B.; Ayrault, P.; Gnep, N. S.; Guisnet, M., Mechanism of n-butene skeletal isomerization over HFER zeolites: a new proposal. *Journal of Catalysis* **2005,** *230* (1), 38-51.

47. Grandvallet, P.; de Jong, K. P.; Mooiweer, H. H.; Kortbeek, A. G. T. G.; Kraushaar-Czarnetzki, B. Process for the conversion of a feedstock comprising linear olefins. European Patent, EP0501577, 1992.

48. Rutenbeck, D.; Papp, H.; Freude, D.; Schwieger, W., Investigations on the reaction mechanism of the skeletal isomerization of n-butenes to isobutene: Part I. Reaction mechanism on H-ZSM-5 zeolites. *Applied Catalysis A: General* **2001,** *206* (1), 57-66.

49. van Donk, S.; Bitter, J. H.; de Jong, K. P., Deactivation of solid acid catalysts for butene skeletal isomerisation: on the beneficial and harmful effects of carbonaceous deposits. *Applied Catalysis A: General* **2001,** *212* (1–2), 97-116.

50. Houžvička, J.; Klik, R.; Kubelková, L.; Ponec, V., The role of the density of active sites in skeletal isomerisation of n-butene. *Applied Catalysis A: General* **1997,** *150* (1), 101-114.

51. den Hollander, M. A.; Wissink, M.; Makkee, M.; Moulijn, J. A., Synergy effects of ZSM-5 addition in fluid catalytic cracking of hydrotreated flashed distillate. *Applied Catalysis A: General* **2002,** *223* (1–2), 103-119.

52. Ancheyta, J.; Sánchez, S.; Rodríguez, M. A., Kinetic modeling of hydrocracking of heavy oil fractions: A review. *Catalysis Today* **2005,** *109* (1–4), 76-92.

53. Burton, A. W.; Ong, K.; Rea, T.; Chan, I. Y., On the estimation of average crystallite size of zeolites from the Scherrer equation: A critical evaluation of its application to zeolites with one-dimensional pore systems. *Microporous and Mesoporous Materials* **2009,** *117* (1–2), 75-90.

54. Silva, B.; Figueiredo, H.; Soares, O. S. G. P.; Pereira, M. F. R.; Figueiredo, J. L.; Lewandowska, A. E.; Bañares, M. A.; Neves, I. C.; Tavares, T., Evaluation of ion exchange-modified Y and ZSM5 zeolites in Cr(VI) biosorption and catalytic oxidation of ethyl acetate. *Applied Catalysis B: Environmental* **2012,** *117–118* (0), 406-413.

55. Lippens, B. C.; de Boer, J. H., Studies on pore systems in catalysts: V. The t method. *Journal of Catalysis* **1965,** *4* (3), 319-323.

56. Barrett, E. P.; Joyner, L. G.; Halenda, P. P., The Determination of Pore Volume and Area Distributions in Porous Substances. I. Computations from Nitrogen Isotherms. *Journal of the American Chemical Society* **1951,** *73* (1), 373-380.

57. Alberty, R. A.; Burmenko, E., Standard Chemical Thermodynamic Properties of Alkyne Isomer Groups. *Journal of Physical and Chemical Reference Data* **1986,** *15* (4), 1339-1349.

58. Chao, J.; Wilhoit, R. C.; Zwolinski, B. J., Ideal Gas Thermodynamic Properties of Ethane and Propane. *Journal of Physical and Chemical Reference Data* **1973,** *2* (2), 427-438.

59. Do Duong, D., *Absorption Analysis: Equilibria and Kinetics*. Imperial College Press: 1998.

60. van Koningsveld, H.; Jansen, J. C.; van Bekkum, H., The monoclinic framework structure of zeolite H-ZSM-5. Comparison with the orthorhombic framework of as-synthesized ZSM-5. *Zeolites* **1990,** *10* (4), 235-242.

61. Cubillas, P.; Anderson, M. W., Synthesis Mechanism: Crystal Growth and Nucleation. In *Zeolites and Catalysis*, Wiley-VCH Verlag GmbH & Co. KGaA: 2010; pp 1-55.

62. Janssen, A. H.; Koster, A. J.; de Jong, K. P., Three-Dimensional Transmission Electron Microscopic Observations of Mesopores in Dealuminated Zeolite Y. *Angewandte Chemie International Edition* **2001,** *40* (6), 1102-1104.

63. Zhu, H.; Liu, Z.; Kong, D.; Wang, Y.; Xie, Z., Synthesis and Catalytic Performances of Mesoporous Zeolites Templated by Polyvinyl Butyral Gel as the Mesopore Directing Agent. *The Journal of Physical Chemistry C* **2008,** *112* (44), 17257-17264.

64. Lowell, S.; Shields, J. E.; Thomas, M. A.; Thommes, M., *Characterization of Porous Solids and Powders: Surface Area, Pore Size and Density*. 1st ed.; Kluwer Academic Publishers: 2004; p 350.

65. Sing, K. S. W.; Everett, D. H.; Haul, R. A. W.; Moscou, L.; Pierotti, R. A.; Rouquerol, J.; Siemieniewska, T., Reporting physisorption data for gas/solid systems with special reference to the determination of surface area and porosity (Recommendations 1984). *Pure and Applied Chemistry* **1985,** *57* (4), 603-619.

66. Hou, L.-Y.; Sand, L. B.; Thompson, R. W., Nucleation and Growth of NH4-ZSM-5 Zeolites. In *Studies in Surface Science and Catalysis*, Y. Murakami, A. I.; Ward, J. W., Eds. Elsevier: 1986; Vol. Volume 28, pp 239-246.

67. Armaroli, T.; Simon, L. J.; Digne, M.; Montanari, T.; Bevilacqua, M.; Valtchev, V.; Patarin, J.; Busca, G., Effects of crystal size and Si/Al ratio on the surface properties of H-ZSM-5 zeolites. *Applied Catalysis A: General* **2006,** *306* (0), 78-84.

68. Christensen, C. H.; Schmidt, I.; Carlsson, A.; Johannsen, K.; Herbst, K., Crystals in CrystalsNanocrystals within Mesoporous Zeolite Single Crystals. *Journal of the American Chemical Society* **2005,** *127* (22), 8098-8102.

69. Guisnet, M.; Andy, P.; Boucheffa, Y.; Gnep, N. S.; Travers, C.; Benazzi, E., Selective isomerization of n-butenes into isobutene over aged H-ferrierite catalyst: Nature of the active species. *Catalysis Letters* **1998,** *50* (3-4), 159-164.

70. Seo, G.; Jeong, H.; Hong, S.; Uh, Y., Skeletal isomerization of 1-butene over ferrierite and ZSM-5 zeolites: influence of zeolite acidity. *Catalysis Letters* **1996,** *36* (3-4), 249-253.

71. Rutenbeck, D.; Papp, H.; Ernst, H.; Schwieger, W., Investigations on the reaction mechanism of the skeletal isomerization of n-butenes to isobutene: Part II. Reaction mechanism on ferrierites. *Applied Catalysis A: General* **2001,** *208* (1–2), 153-161.

72. Kangas, M.; Kumar, N.; Harlin, E.; Salmi, T.; Murzin, D. Y., Skeletal Isomerization of Butene in Fixed Beds. 1. Experimental Investigation and Structure−Performance Effects. *Industrial & Engineering Chemistry Research* **2008,** *47* (15), 5402-5412.

73. Dietz, W. A., Response factors for gas chromatographic analyses. *J. Gas Chromatogr.* **1967,** *5* (Copyright (C) 2013 American Chemical Society (ACS). All Rights Reserved.), 68-71.

74. Basu, B.; Kunzru, D., Catalytic pyrolysis of naphtha. *Industrial & Engineering Chemistry Research* **1992,** *31* (1), 146-155.

75. Jung, J. S.; Park, J. W.; Seo, G., Catalytic cracking of n-octane over alkali-treated MFI zeolites. *Applied Catalysis A: General* **2005,** *288* (1–2), 149-157.

76. Corma, A.; Orchillés, A. V., Current views on the mechanism of catalytic cracking. *Microporous and Mesoporous Materials* **2000,** *35–36* (0), 21-30.

77. Joyner, R. W.; van Santen, R. A., *Elementary reaction steps in heterogeneous catalysis*. Kluwer Academic Publishers: 1993.

78. Kotrel, S.; Knözinger, H.; Gates, B. C., The Haag–Dessau mechanism of protolytic cracking of alkanes. *Microporous and Mesoporous Materials* **2000,** *35–36* (0), 11-20.

79. Maloncy, M. L.; Gora, L.; Jansen, J. C.; Maschmeyer, T., Conceptual Processes for Zeolite Membrane Based Hydroisomerization of Light Alkanes *Ars Separatoria Acta* **2003,** *2*, 18.

80. Lai, Z.; Tsapatsis, M.; Nicolich, J. P., Siliceous ZSM-5 Membranes by Secondary Growth of b-Oriented Seed Layers. *Advanced Functional Materials* **2004,** *14* (7), 716-729.

81. Jolly, S.; Saussey, J.; Bettahar, M. M.; Lavalley, J. C.; Benazzi, E., Reaction mechanisms and kinetics in the n-hexane cracking over zeolites. *Applied Catalysis A: General* **1997,** *156* (1), 71-96.

82. Xu, B.; Sievers, C.; Hong, S. B.; Prins, R.; van Bokhoven, J. A., Catalytic activity of Brønsted acid sites in zeolites: Intrinsic activity, rate-limiting step, and influence of the local structure of the acid sites. *Journal of Catalysis* **2006,** *244* (2), 163-168.

83. Frillette, V. J.; Haag, W. O.; Lago, R. M., Catalysis by crystalline aluminosilicates: Characterization of intermediate pore-size zeolites by the "Constraint Index". *Journal of Catalysis* **1981,** *67* (1), 218-222.

84. Carpenter, J. R.; Yeh, S.; Zones, S. I.; Davis, M. E., Further investigations on Constraint Index testing of zeolites that contain cages. *Journal of Catalysis* **2010,** *269* (1), 64-70.

85. Jacobs, P. A.; Martens, J. A., Exploration of the Void Size and Structure of Zeolites and Molecular Sieves Using Chemical Reactions. In *Studies in Surface Science and Catalysis*, Y. Murakami, A. I.; Ward, J. W., Eds. Elsevier: 1986; Vol. Volume 28, pp 23-32.

86. Park, K.-C.; Ihm, S.-K., Comparison of Pt/zeolite catalysts for n-hexadecane hydroisomerization. *Applied Catalysis A: General* **2000,** *203* (2), 201-209.

87. Christensen, C. H.; Schmidt, I.; Christensen, C. H., Improved performance of mesoporous zeolite single crystals in catalytic cracking and isomerization of n-hexadecane. *Catalysis Communications* **2004,** *5* (9), 543-546.

88. Park, K. C.; Ihm, S. K., Comparison of Pt/zeolite catalysts for n-hexadecane hydroisomerization. *Applied Catalysis A: General* **2000,** *203* (2), 201-209.

89. Almutairi, S. M. T.; Mezari, B.; Filonenko, G. A.; Magusin, P. C. M. M.; Rigutto, M. S.; Pidko, E. A.; Hensen, E. J. M., Influence of Extraframework Aluminum on the Brønsted Acidity and Catalytic Reactivity of Faujasite Zeolite. *ChemCatChem* **2013,** *5* (2), 452-466.

90. Čejka, J.; Ílková, N.; Nachtigall, P., Preface. In *Studies in Surface Science and Catalysis*, J. Čejka, N. Ž.; Nachtigall, P., Eds. Elsevier: 2005; Vol. Volume 158, Part A, p v.

91. Corma, A., Inorganic Solid Acids and Their Use in Acid-Catalyzed Hydrocarbon Reactions. *Chemical Reviews* **1995,** *95* (3), 559-614.

92. Cundy, C. S.; Cox, P. A., The Hydrothermal Synthesis of Zeolites: History and Development from the Earliest Days to the Present Time. *Chemical Reviews* **2003,** *103* (3), 663-702.

93. Butler, A. C.; Nicolaides, C. P., Catalytic skeletal isomerization of linear butenes to isobutene. *Catalysis Today* **1994,** *18* (4), 443-471.

94. Juguin, B.; Torck, B.; Martino, G., Upgrading of C4 cracking cuts with acid catalysts. *Studies in Surface Science and Catalysis* **1985,** *20* (Catal. Acids Bases), 253-264.

95. Maxwell, I. E.; Naber, J. E.; de Jong, K. P., The pivotal role of catalysis in energy related environmental technology. *Applied Catalysis A* **1994,** *113* (2), 153-173.

96. Corma, A.; Martinez, A., Chemistry, catalysts, and processes for isoparaffin-olefin alkylation: actual situation and future trends. *Catalysis Reviews: Science and Engineering* **1993,** *35* (4), 483-570.

97. Haw, J. F.; Nicholas, J. B.; Xu, T.; Beck, L. W.; Ferguson, D. B., Physical Organic Chemistry of Solid Acids: Lessons From in Situ NMR and Theoretical Chemistry. *Accounts of Chemical Research* **1996,** *29* (6), 259-267.

98. Nivarthy, G. S.; Feller, A.; Seshan, K.; Lercher, J. A., Alkylation of isobutane with light olefins catalyzed by zeolite beta. *Microporous and Mesoporous Materials* **2000,** *35-36*, 75-87.

99. Mooiweer, H. H.; Jong, K. P. d.; Kraushaar-Czarnetzki, B.; Stork, W. H. J.; Krutzen, B. C. H., Skeletal isomerization of olefins with the zeolite Ferrierite as catalyst. *Studies in Surface Science and Catalysis* **1994,** *84* (ZEOLITES AND RELATED MICROPOROUS MATERIALS, PT. C), 2327-2334.

100. Petkovic, L. M.; Larsen, G., Linear Butenes from Isobutene over H-Ferrierite: In Situ Studies Using an Oscillating Balance Reactor. *Journal of Catalysis* **2000,** *191* (1), 1-11.

101. Houzvicka, J.; Hansildaar, S.; Ponec, V., The shape selectivity in the skeletal isomerization of n-Butene to isobutene. *Journal of Catalysis* **1997,** *167* (1), 273-278.

102. Domokos, L.; Lefferts, L.; Seshan, K.; Lercher, J. A., Isomerization of Linear Butenes to iso-Butene over Medium Pore Zeolites: I. Kinetic Aspects of the Reaction over H-FER. *Journal of Catalysis* **2001,** *197* (1), 68-80.

103. Seo, G., Skeletal Isomerization of n-butenes over Solid Acid Catalysts. *Catalysis Surveys from Asia* **2005,** *9* (3), 139-146.

104. Meriaudeau, P.; Bacaud, R.; Hung, L. N.; Vu, A. T., Isomerisation of butene in isobutene on ferrierite catalyst: A mono- or a bimolecular process? *Journal of Molecular Catalysis A: Chemical* **1996,** *110* (3), L177-L179.

105. Houžvička, J.; Ponec, V., Skeletal Isomerization of Butene: On the Role of the Bimolecular Mechanism. *Industrial & Engineering Chemistry Research* **1997,** *36* (5), 1424-1430.

106. Kangas, M.; Salmi, T.; Murzin, D. Y., Skeletal Isomerization of Butene in Fixed Beds. Part 2. Kinetic and Flow Modeling. *Industrial & Engineering Chemistry Research* **2008,** *47* (15), 5413-5426.

107. Seo, G.; Park, S.-H.; Kim, J.-H., The reversible skeletal isomerization between n-butenes and isobutene over solid acid catalysts. *Catalysis Today* **1998,** *44* (1-4), 215-222.

108. Cheng, Z.; Ponec, V., Fluorinated alumina as a catalyst for skeletal isomerization of n-butene. *Applied Catalysis A: General* **1994,** *118* (2), 127-138.

109. Rigby, A. M.; Frash, M. V., Ab initio calculations on the mechanisms of hydrocarbon conversion in zeolites: Skeletal isomerisation and olefin chemisorption. *Journal of Molecular Catalysis A: Chemical* **1997,** *126* (1), 61-72.

110. Rigby, A. M.; Kramer, G. J.; Van Santen, R. A., Mechanisms of hydrocarbon conversion in zeolites: a quantum mechanical study. *Journal of Catalysis* **1997,** *170* (1), 1-10.

111. Boronat, M.; Viruela, P.; Corma, A., Theoretical Study of the Mechanism of Zeolite-Catalyzed Isomerization Reactions of Linear Butenes. *Journal of Physical Chemistry A* **1998,** *102* (6), 982-989.

112. Boronat, M.; Viruela, P.; Corma, A., The skeletal isomerization of but-1-ene catalyzed by theta-1 zeolite. *Physical Chemistry Chemical Physics* **2001,** *3* (15), 3235-3239.

113. Boronat, M.; Zicovich-Wilson, C. M.; Viruela, P.; Corma, A., Influence of the Local Geometry of Zeolite Active Sites and Olefin Size on the Stability of Alkoxide Intermediates. *Journal of Physical Chemistry B* **2001,** *105* (45), 11169-11177.

114. Boronat, M.; Viruela, P. M.; Corma, A., Reaction intermediates in acid catalysis by zeolites: prediction of the relative tendency to form alkoxides or carbocations as a function of hydrocarbon nature and active site structure. *Journal of the American Chemical Society* **2004,** *126* (10), 3300-3309.

115. Nieminen, V.; Sierka, M.; Murzin, D. Y.; Sauer, J., Stabilities of C3-C5 alkoxide species inside H-FER zeolite: a hybrid QM/MM study. *Journal of Catalysis* **2005,** *231* (2), 393-404.

116. Boronat, M.; Corma, A., Are carbenium and carbonium ions reaction intermediates in zeolite-catalyzed reactions? *Applied Catalysis A* **2008,** *336* (1-2), 2-10.

117. Brouwer, D. M.; Oelderik, J. M., Hydrogen Fluoride-antimony pentafluoride catalyzed isomerization of 2-methylpentane. Kinetics and mechanism of rearrangement and hydride-ion transfer steps in alkylcarbonium ion reactions. *Recueil des Travaux Chimiques des Pays-Bas* **1968,** *87* (8), 721-736.

118. Brouwer, D. M.; Hogeveen, H., Electrophilic substitutions at alkanes and in alkylcarbonium ions. *Progress in Physical Organic Chemistry* **1972,** *9*, 179-240.

119. Guisnet, M.; Andy, P.; Gnep, N. S.; Benazzi, E.; Travers, C., Skeletal isomerization of n-butenes. I. Mechanism of n-butene transformation on a nondeactivated H-ferrierite catalyst. *Journal of Catalysis* **1996,** *158* (2), 551-560.

120. Xu, W.-Q.; Yin, Y.-G.; Suib, S. L.; O'Young, C.-L., Selective conversion of n-butene to isobutylene at extremely high space velocities on ZSM-23 zeolites. *Journal of Catalysis* **1994,** *150* (1), 34-45.

121. Asensi, M. A.; Corma, A.; Martinez, A., Skeletal isomerization of 1-butene on MCM-22 zeolite catalyst. *Journal of Catalysis* **1996,** *158* (2), 561-569.

122. Seo, G.; Jeong, H. S.; Hong, S. B.; Uh, Y. S., Skeletal isomerization of 1-butene over ferrierite and ZSM-5 zeolites: influence of zeolite acidity. *Catalysis Letters* **1996,** *36* (3,4), 249-253.

123. Houzvicka, J.; Ponec, V., Skeletal isomerization of n-butene. *Catalysis Reviews: Science and Engineering* **1997,** *39* (4), 319-344.

124. Seo, G.; Kim, N.-H.; Lee, Y.-H.; Kim, J.-H., Skeletal isomerization of 1-butene over mesoporous materials. *Catalysis Letters* **1999,** *57* (4), 209-215.

125. Farneth, W. E.; Gorte, R. J., Methods for Characterizing Zeolite Acidity. *Chemical Reviews* **1995,** *95* (3), 615-635.

126. Haw, J. F., Zeolite acid strength and reaction mechanisms in catalysis. *Physical Chemistry Chemical Physics* **2002,** *4* (22), 5431-5441.

127. Rozanska, X.; van Santen, R. A.; Demuth, T.; Hutschka, F.; Hafner, J., A Periodic DFT Study of Isobutene Chemisorption in Proton-Exchanged Zeolites: Dependence of Reactivity on the Zeolite Framework Structure. *Journal of Physical Chemistry B* **2003,** *107* (6), 1309-1315.

128. Sinclair, P. E.; de Vries, A.; Sherwood, P.; Catlow, C. R. A.; van Santen, R. A., Quantum-chemical studies of alkene chemisorption in chabazite: A comparison of cluster and embedded-cluster models. *Journal of the Chemical Society, Faraday Transactions* **1998,** *94* (22), 3401-3408.

129. Tuma, C.; Sauer, J., Protonated isobutene in zeolites: Tert-butyl cation or alkoxide? *Angewandte Chemie International Edition* **2005,** *44* (30), 4769-4771.

130. Tuma, C.; Sauer, J., Treating dispersion effects in extended systems by hybrid MP2:DFT calculations-protonation of isobutene in zeolite ferrierite. *Physical Chemistry Chemical Physics* **2006,** *8* (34), 3955-3965.

131. Haw, J. F.; Nicholas, J. B.; Xu, T.; Beck, L. W.; Ferguson, D. B., Physical Organic Chemistry of Solid Acids: Lessons from in Situ NMR and Theoretical Chemistry. *Accounts of Chemical Research* **1996,** *29* (6), 259-267.

132. Boronat, M.; Viruela, P.; Corma, A., The skeletal isomerization of but-1-ene catalyzed by theta-1 zeolite. *Physical Chemistry Chemical Physics* **2001,** *3* (15), 3235-3239.

133. Rosenbach, N.; dos Santos, A. P. A.; Franco, M.; Mota, C. J. A., The tert-butyl cation on zeolite Y: A theoretical and experimental study. *Chemical Physics Letters* **2010,** *485* (1-3), 124-128.

134. Tuma, C.; Kerber, T.; Sauer, J., The *tert*-Butyl Cation in H-Zeolites: Deprotonation to Isobutene and Conversion into Surface Alkoxides. *Angewandte Chemie International Edition* **2010**, DOI: 10.1002/anie.200907015.

135. Xu, W.-Q.; Yin, Y.-G.; Suib, S. L.; Edwards, J. C.; Oyoung, C.-L., n-Butene Skeletal Isomerization to Isobutylene on Shape Selective Catalysts: Ferrierite/ZSM-35. *Journal of Physical Chemistry* **1995,** *99* (23), 9443-9451.

136. Guisnet, M.; Andy, P.; Gnep, N. S.; Travers, C.; Benazzi, E., Origin of the positive effect of coke deposits on the skeletal isomerization of n-butenes over a H-FER zeolite. *Journal of the Chemical Society, Chemical Communications* **1995,** (16), 1685-1686.

137. Vaughan, P. A., Crystal structure of the zeolite ferrierite. *Acta Crystallogr.* **1966,** *21* (6), 983-990.

138. Namuangruk, S.; Tantanak, D.; Limtrakul, J., Application of ONIOM calculations in the study of the effect of the zeolite framework on the adsorption of alkenes to ZSM-5. *Journal of Molecular Catalysis A: Chemical* **2006,** *256* (1-2), 113-121.

139. Namuangruk, S.; Khongpracha, P.; Pantu, P.; Limtrakul, J., Structures and Reaction Mechanisms of Propene Oxide Isomerization on H-ZSM-5: An ONIOM Study. *Journal of Physical Chemistry B* **2006,** *110* (51), 25950-25957.

140. Jansang, B.; Nanok, T.; Limtrakul, J., Interaction of mordenite with an aromatic hydrocarbon: An embedded ONIOM study. *Journal of Molecular Catalysis A: Chemical* **2007,** *264* (1-2), 33-39.

141. Maihom, T.; Namuangruk, S.; Nanok, T.; Limtrakul, J., Theoretical Study on Structures and Reaction Mechanisms of Ethylene Oxide Hydration over H-ZSM-5: Ethylene Glycol Formation. *Journal of Physical Chemistry C* **2008,** *112* (33), 12914-12920.

142. Jansang, B.; Nanok, T.; Limtrakul, J., Structure and reaction mechanism of alkylation of phenol with methanol over H-FAU zeolite: an ONIOM study. *Journal of Physical Chemistry C* **2008,** *112* (2), 540-547.

143. Boekfa, B.; Choomwattana, S.; Khongpracha, P.; Limtrakul, J., Effects of the Zeolite Framework on the Adsorptions and Hydrogen-Exchange Reactions of Unsaturated Aliphatic, Aromatic, and Heterocyclic Compounds in ZSM-5 Zeolite: A Combination of Perturbation Theory (MP2) and a Newly Developed Density Functional Theory (M06-2X) in ONIOM Scheme. *Langmuir* **2009,** *25* (22), 12990-12999.

144. Maihom, T.; Boekfa, B.; Sirijaraensre, J.; Nanok, T.; Probst, M.; Limtrakul, J., Reaction Mechanisms of the Methylation of Ethene with Methanol and Dimethyl Ether over H-ZSM-5: An ONIOM Study. *Journal of Physical Chemistry C* **2009,** *113* (16), 6654-6662.

145. Sirijaraensre, J.; Limtrakul, J., Effect of the acidic strength on the vapor phase Beckmann rearrangement of cyclohexanone oxime over the MFI zeolite: an embedded ONIOM study. *Physical Chemistry Chemical Physics* **2009,** *11* (3), 578-585.

146. Jousse, F.; Leherte, L.; Vercauteren, D. P., Molecular mechanical investigation of the energetics of butene sorbed in H-ferrierite. *Molecular Simulation* **1996,** *17* (3), 175-196.

147. Blanco, F.; Urbina-Villalba, G.; Agudelo, M. M. R. D., Theoretical calculations on zeolites: The aluminum substitution in mordenite, ferrierite and ZSM-5. *Molecular Simulation* **1995,** *14* (3), 165-176.

148. Frisch, M. J.; Trucks, G. W.; Schlegel, H. B.; Scuseria, G. E.; Robb, M. A.; Cheeseman, J. R.; Montgomery, J. A., Jr.; Vreven, T.; Kudin, K. N.; Burant, J. C.; Millam, J. M.; Iyengar, S. S.; Tomasi, J.; Barone, V.; Mennucci, B.; Cossi, M.; Scalmani, G.; Rega, N.; Petersson, G. A.; Nakatsuji, H.; Hada, M.; Ehara, M.; Toyota, K.; Fukuda, R.; Hasegawa, J.; Ishida, M.; Nakajima, T.; Honda, Y.; Kitao, O.; Nakai, H.; Klene, M.; Li, X.; Knox, J. E.; Hratchian, H. P.; Cross, J. B.; Adamo, C.; Jaramillo, J.; Gomperts, R.; Stratmann, R. E.; Yazyev, O.; Austin, A. J.; Cammi, R.; Pomelli, C.; Ochterski, J. W.; Ayala, P. Y.; Morokuma, K.; Voth, G. A.; Salvador, P.; Dannenberg, J. J.; Zakrzewski, V. G.; Dapprich, S.; Daniels, A. D.; Strain, M. C.; Farkas, O.; Malick, D. K.; Rabuck, A. D.; Raghavachari, K.; Foresman, J. B.; Ortiz, J. V.; Cui, Q.; Baboul, A. G.; Clifford, S.; Cioslowski, J.; Stefanov, B. B.; Liu, G.; Liashenko, A.; Piskorz, P.; Komaromi, I.; Martin, R. L.; Fox, D. J.; Keith, T.; Al-Laham, M. A.; Peng, C. Y.; Nanayakkara, A.; Challacombe, M.; Gill, P. M. W.; Johnson, B.; Chen, W.; Wong, M. W.; Gonzalez, C.; Pople, J. A., *Gaussian 03*. revision B.05 ed.; Gaussian, Inc.: Pittsburgh, PA, 2003.

149. Zhao, Y.; Truhlar, D. G., Exploring the Limit of Accuracy of the Global Hybrid Meta Density Functional for Main-Group Thermochemistry, Kinetics, and Noncovalent Interactions. *Journal of Chemical Theory and Computation* **2008,** *4* (11), 1849-1868.

150. Eder, F.; Lercher, J. A., On the Role of the Pore Size and Tortuosity for Sorption of Alkanes in Molecular Sieves. *Journal of Physical Chemistry B* **1997,** *101* (8), 1273-1278.

151. Yoda, E.; Kondo, J. N.; Domen, K., Detailed process of adsorption of alkanes and alkenes on zeolites. *Journal of Physical Chemistry B* **2005,** *109* (4), 1464-1472.

152. Correa, R. J.; Mota, C. J. A., Theoretical study of protonation of butene isomers on acidic zeolite: the relative stability among primary, secondary and tertiary alkoxy intermediates. *Physical Chemistry Chemical Physics* **2002,** *4* (2), 375-380.

153. Pantu, P.; Boekfa, B.; Limtrakul, J., The adsorption of saturated and unsaturated hydrocarbons on nanostructured zeolites (H-MOR and H-FAU): An ONIOM study. *Journal of Molecular Catalysis A: Chemical* **2007,** *277* (1-2), 171-179.

154. Jousse, F.; Leherte, L.; Vercauteren, D. P., Energetics and diffusion of butene isomers in channel zeolites from molecular dynamics simulations. *Journal of Molecular Catalysis A: Chemical* **1997,** *119* (1-3), 165-176.

155. Andy, P.; Martin, D.; Guisnet, M.; Bell, R. G.; Catlow, C. R. A., Molecular Modeling of Carbonaceous Compounds Formed Inside the Pores of FER Zeolite during Skeletal Isomerization of n-Butene. *Journal of Physical Chemistry B* **2000,** *104* (20), 4827-4834.

156. Zhang, J.; Zhao, Z.; Duan, A.; Jiang, G.; Liu, J.; Zhang, D., Chromatographic Study on the Adsorption and Diffusion of Light Hydrocarbons in ZSM-5 and USY Zeolites. *Energy & Fuels* **2008,** *23* (2), 617-623.

157. Eder, F.; Lercher, J. A., On the Role of the Pore Size and Tortuosity for Sorption of Alkanes in Molecular Sieves. *The Journal of Physical Chemistry B* **1997,** *101* (8), 1273-1278.

158. de Ménorval, B.; Ayrault, P.; Gnep, N. S.; Guisnet, M., n-Butene skeletal isomerization over HFER zeolites: Influence of Si/Al ratio and of carbonaceous deposits. *Applied Catalysis A: General* **2006,** *304*, 1-13.

159. Berthod, A., Chiral Recognition Mechanisms. *Analytical Chemistry* **2006,** *78* (7), 2093-2099.

160. Pernites, R. B.; Venkata, S. K.; Tiu, B. D. B.; Yago, A. C. C.; Advincula, R. C., Nanostructured, Molecularly Imprinted, and Template-Patterned Polythiophenes for Chiral Sensing and Differentiation. *Small* **2012,** *8* (11), 1669-1674.

161. Vlatakis, G.; Andersson, L. I.; Muller, R.; Mosbach, K., Drug assay using antibody mimics made by molecular imprinting. *Nature* **1993,** *361* (6413), 645-647.

162. Ramström, O.; Ansell, R. J., Molecular imprinting technology: Challenges and prospects for the future. *Chirality* **1998,** *10* (3), 195-209.

163. Tada, M.; Iwasawa, Y., Design of molecular-imprinting metal-complex catalysts. *Journal of Molecular Catalysis A: Chemical* **2003,** *199* (1–2), 115-137.

164. Zhang, M.; Qing, G.; Sun, T., Chiral biointerface materials. *Chemical Society Reviews* **2012,** *41* (5), 1972-1984.

165. Wang, H. F.; Zhu, Y. Z.; Yan, X. P.; Gao, R. Y.; Zheng, J. Y., A Room Temperature Ionic Liquid (RTIL)-Mediated, Non-Hydrolytic Sol–Gel Methodology to Prepare Molecularly Imprinted, Silica-Based Hybrid Monoliths for Chiral Separation. *Advanced Materials* **2006,** *18* (24), 3266-3270.

166. Qu, P.; Lei, J.; Ouyang, R.; Ju, H., Enantioseparation and Amperometric Detection of Chiral Compounds by in Situ Molecular Imprinting on the Microchannel Wall. *Analytical Chemistry* **2009,** *81* (23), 9651-9656.

167. Suryanarayanan, V.; Wu, C.-T.; Ho, K.-C., Molecularly Imprinted Electrochemical Sensors. *Electroanalysis* **2010,** *22* (16), 1795-1811.

168. Chen, L.; Xu, S.; Li, J., Recent advances in molecular imprinting technology: current status, challenges and highlighted applications. *Chemical Society Reviews* **2011,** *40* (5).

169. Günter, G. W., Enzyme-like catalysis by molecularly imprinted polymers. *Chemical Reviews* **2002,** *102* (1), 1-27.

170. Baddeley, C. J.; Richardson, N. V., Chirality at Metal Surfaces. In *Scanning Tunneling Microscopy in Surface Science*, Wiley-VCH Verlag GmbH & Co. KGaA: 2010; pp 1-27.

171. Gellman, A. J., Chiral Surfaces: Accomplishments and Challenges. *ACS Nano* **2010,** *4* (1), 5-10.

172. McFadden, C. F.; Cremer, P. S.; Gellman, A. J., Adsorption of Chiral Alcohols on “Chiral” Metal Surfaces. *Langmuir* **1996,** *12* (10), 2483-2487.

173. Attard, G. A., Electrochemical Studies of Enantioselectivity at Chiral Metal Surfaces. *The Journal of Physical Chemistry B* **2001,** *105* (16), 3158-3167.

174. Sholl, D. S.; Asthagiri, A.; Power, T. D., Naturally Chiral Metal Surfaces as Enantiospecific Adsorbents. *The Journal of Physical Chemistry B* **2001,** *105* (21), 4771-4782.

175. Kuhnle, A.; Linderoth, T. R.; Hammer, B.; Besenbacher, F., Chiral recognition in dimerization of adsorbed cysteine observed by scanning tunnelling microscopy. *Nature* **2002,** *415* (6874), 891-893.

176. LeBlond, C.; Wang, J.; Liu, J.; Andrews, A. T.; Sun, Y. K., Highly Enantioselective Heterogeneously Catalyzed Hydrogenation of α-Ketoesters under Mild Conditions. *Journal of the American Chemical Society* **1999,** *121* (20), 4920-4921.

177. Switzer, J. A.; Kothari, H. M.; Poizot, P.; Nakanishi, S.; Bohannan, E. W., Enantiospecific electrodeposition of a chiral catalyst. *Nature* **2003,** *425* (6957), 490-493.

178. Durán Pachón, L.; Yosef, I.; Markus, T. Z.; Naaman, R.; Avnir, D.; Rothenberg, G., Chiral imprinting of palladium with cinchona alkaloids. *Nature Chemistry* **2009,** *1* (2), 160-164.

179. Behar-Levy, H.; Neumann, O.; Naaman, R.; Avnir, D., Chirality Induction in Bulk Gold and Silver. *Advanced Materials* **2007,** *19* (9), 1207-1211.

180. Attard, G.; Casadesús, M.; Macaskie, L. E.; Deplanche, K., Biosynthesis of Platinum Nanoparticles by Escherichia coli MC4100: Can Such Nanoparticles Exhibit Intrinsic Surface Enantioselectivity? *Langmuir* **2012,** *28* (11), 5267-5274.

181. Rouquerol, J.; Avnir, D.; Fairbridge, C. W.; Everett, D. H.; Haynes, J. H.; Pernicone, N.; Ramsay, J. D. F.; Sing, K. S. W.; Unger, K. K., Recommendations for the characterization of porous solids. *Pure and Applied Chemistry* **1994,** *66*, 1739-1758.

182. Corma, A., From microporous to mesoporous molecular sieve materials and their use in catalysis. *Chemical Reviews* **1997,** *97* (6), 2373-2419.

183. Heim, M.; Wattanakit, C.; Reculusa, S.; Warakulwit, C.; Limtrakul, J.; Ravaine, S.; Kuhn, A., Hierarchical Macro-mesoporous Pt Deposits on Gold Microwires for Efficient Methanol Oxidation. *Electroanalysis* **2013,** *25* (4), 888-894.

184. Stein, A., Advances in Microporous and Mesoporous Solids—Highlights of Recent Progress. *Advanced Materials* **2003,** *15* (10), 763-775.

185. Heim, M.; Rousseau, L.; Reculusa, S.; Urbanova, V.; Mazzocco, C.; Joucla, S.; Bouffier, L.; Vytras, K.; Bartlett, P.; Kuhn, A.; Yvert, B., Combined macro/mesoporous microelectrode arrays (MEAs) for low noise extracellular recording of neural networks. *J Neurophysiol* **2012**.

186. Wagner, T.; Haffer, S.; Weinberger, C.; Klaus, D.; Tiemann, M., Mesoporous materials as gas sensors. *Chemical Society Reviews* **2013**.

187. Botella, P.; Corma, A.; Quesada, M., Synthesis of ordered mesoporous silica templated with biocompatible surfactants and applications in controlled release of drugs. *Journal of Materials Chemistry* **2012,** *22* (13), 6394-6401.

188. Kresge, C. T.; Leonowicz, M. E.; Roth, W. J.; Vartuli, J. C.; Beck, J. S., Ordered mesoporous molecular sieves synthesized by a liquid-crystal template mechanism. *Nature* **1992,** *359* (6397), 710-712.

189. Jian, K.; Truong, T. C.; Hoffman, W. P.; Hurt, R. H., Mesoporous carbons with self-assembled surfaces of defined crystal orientation. *Microporous and Mesoporous Materials* **2008,** *108* (1-3), 143-151.

190. Wan, Y.; Zhao, D., On the controllable soft-templating approach to mesoporous silicates. *Chemical Reviews* **2007,** *107* (7), 2821-2860.

191. Yamauchi, Y.; Kuroda, K., Rational Design of Mesoporous Metals and Related Nanomaterials by a Soft-Template Approach. *Chemistry – An Asian Journal* **2008,** *3* (4), 664-676.

192. Yamauchi, Y.; Yokoshima, T.; Mukaibo, H.; Tezuka, M.; Shigeno, T.; Momma, T.; Osaka, T.; Kuroda, K., Highly Ordered Mesoporous Ni Particles Prepared by Electroless Deposition from Lyotropic Liquid Crystals. *Chemistry Letters* **2004,** *33* (5), 542-543.

193. Attard, G. S.; Corker, J. M.; Göltner, C. G.; Henke, S.; Templer, R. H., Liquid-Crystal Templates for Nanostructured Metals. *Angewandte Chemie International Edition in English* **1997,** *36* (12), 1315-1317.

194. Lee, J.; Yoon, S.; Hyeon, T.; M. Oh, S.; Bum Kim, K., Synthesis of a new mesoporous carbon and its application to electrochemical double-layer capacitors. *Chemical Communications* **1999,** *0* (21), 2177-2178.

195. Blanco-López, M. C.; Lobo-Castañón, M. J.; Miranda-Ordieres, A. J.; Tuñón-Blanco, P., Electrochemical sensors based on molecularly imprinted polymers. *TRAC Trends in Analytical Chemistry* **2004,** *23* (1), 36-48.

196. Kang, Y.-J.; Oh, J.-W.; Kim, Y.-R.; Kim, J. S.; Kim, H., Chiral gold nanoparticle-based electrochemical sensor for enantioselective recognition of 3,4-dihydroxyphenylalanine. *Chemical Communications* **2010,** *46* (31), 5665-5667.

197. Rodriguez, V.; Koeckelberghs, G.; Verbiest, T., Second-harmonic generation-circular dichroism in thin films of a chiral poly(3-alkyl)thiophene. *Chemical Physics Letters* **2007,** *450* (1–3), 76-79.

198. Verbiest, T.; Clays, K.; Rodriguez, V., *Second-order Nonlinear Optical Characterization Techniques: An Introduction*. Taylor & Francis: 2009.

199. Attard, G. S.; Bartlett, P. N.; Coleman, N. R. B.; Elliott, J. M.; Owen, J. R.; Wang, J. H., Mesoporous Platinum Films from Lyotropic Liquid Crystalline Phases. *Science* **1997,** *278* (5339), 838-840.

200. Hegmann, T.; Qi, H.; Marx, V., Nanoparticles in Liquid Crystals: Synthesis, Self-Assembly, Defect Formation and Potential Applications. *Journal of Inorganic and Organometallic Polymers and Materials* **2007,** *17* (3), 483-508.

201. Leigh, W. J.; Workentin, M. S.; Demus, D.; Goodby, J.; Gray, G. W.; Spiess, H. W.; Vill, V., Liquid Crystals as Solvents for Spectroscopic, Chemical Reaction, and Gas Chromatographic Applications. In *Handbook of Liquid Crystals Set*, Wiley-VCH Verlag GmbH: 2008; pp 839-895.

202. Tschierske, C., Non-conventional liquid crystals-the importance of micro-segregation for self-organisation. *Journal of Materials Chemistry* **1998,** *8* (7), 1485-1508.

203. Seddon, J. M.; Templer, R. H., Chapter 3 Polymorphism of lipid-water systems. In *Handbook of Biological Physics*, Lipowsky, R.; Sackmann, E., Eds. North-Holland: 1995; Vol. Volume 1, pp 97-160.

204. Coleman, N. R. B.; Attard, G. S., Ordered mesoporous silicas prepared from both micellar solutions and liquid crystal phases. *Microporous and Mesoporous Materials* **2001,** *44–45* (0), 73-80.

205. Çelik, Ö.; Dag, Ö., A New Lyotropic Liquid Crystalline System: Oligo(ethylene oxide) Surfactants with [M(H2O)n]Xm Transition Metal Complexes. *Angewandte Chemie* **2001,** *113* (20), 3915-3919.

206. Attard, G. S.; Leclerc, S. A. A.; Maniguet, S.; Russell, A. E.; Nandhakumar, I.; Bartlett, P. N., Mesoporous Pt/Ru Alloy from the Hexagonal Lyotropic Liquid Crystalline Phase of a Nonionic Surfactant. *Chemistry of Materials* **2001,** *13* (5), 1444-1446.

207. Luo, H.; Sun, L.; Lu, Y.; Yan, Electrodeposition of Mesoporous Semimetal and Magnetic Metal Films from Lyotropic Liquid Crystalline Phases. *Langmuir* **2004,** *20* (23), 10218-10222.

208. Asghar, K. A.; Elliott, J. M.; Squires, A. M., 2D hexagonal mesoporous platinum films exhibiting biaxial, in-plane pore alignment. *Journal of Materials Chemistry* **2012,** *22* (26), 13311-13317.

209. Yamauchi, Y.; Sadasivan Nair, S.; Momma, T.; Ohsuna, T.; Osaka, T.; Kuroda, K., Synthesis and characterization of mesoporous Pt-Ni (HI-Pt/Ni) alloy particles prepared from lyotropic liquid crystalline media. *Journal of Materials Chemistry* **2006,** *16* (23), 2229-2234.

210. Elliott, J. M.; Attard, G. S.; Bartlett, P. N.; Coleman, N. R. B.; Merckel, D. A. S.; Owen, J. R., Nanostructured Platinum (HI-ePt) Films: Effects of Electrodeposition Conditions on Film Properties. *Chemistry of Materials* **1999,** *11* (12), 3602-3609.

211. Sweetman, S. C.; Editor, *Martindale: The Complete Drug Reference*. Pharmaceutical Press: London, 2007.

212. Lien Ai, N.; Hua, H.; Chuong, P.-H., Chiral Drugs. An Overview. *International Journal of Biomedical Science* **2006,** *2* (2), 85-100.

213. Lee, H.; Dellatore, S. M.; Miller, W. M.; Messersmith, P. B., Mussel-Inspired Surface Chemistry for Multifunctional Coatings. *Science* **2007,** *318* (5849), 426-430.

214. Lee, H.; Lee, B. P.; Messersmith, P. B., A reversible wet/dry adhesive inspired by mussels and geckos. *Nature* **2007,** *448* (7151), 338-341.

215. Lee, G.; Lee, H.; Nam, K.; Han, J.-H.; Yang, J.; Lee, S.; Yoon, D.; Eom, K.; Kwon, T., Nanomechanical characterization of chemical interaction between gold nanoparticles and chemical functional groups. *Nanoscale Research Letters* **2012,** *7* (1), 1-11.

216. Rikukawa, M.; Rubner, M. F., Preparation of Multicomponent Langmuir?Blodgett Thin Films Composed of Poly(3-hexylthiophene) and 3-Octadecanoylpyrrole. In *Macromolecular Assemblies in Polymeric Systems*, American Chemical Society: 1992; Vol. 493, pp 64-75.

217. Schwarz, J. A.; Polizzotti, R. S.; Burton, J. J., CHEMISORPTION ON A SURFACE SEGREGATED Pt-Au ALLOY. *J Vac Sci Technol* **1976,** *14* (1), 457-460.

218. Doña Rodríguez, J. M.; Herrera Melián, J. A.; Pérez Peña, J., Determination of the Real Surface Area of Pt Electrodes by Hydrogen Adsorption Using Cyclic Voltammetry. *Journal of Chemical Education* **2000,** *77* (9), 1195.

219. Trasatti, S.; Petrii, O. A., Real surface area measurements in electrochemistry. *Journal of Electroanalytical Chemistry* **1992,** *327* (1–2), 353-376.

220. Shervedani, R. K.; Lasia, A., Evaluation of the surface roughness of microporous Ni–Zn–P electrodes by in situ methods. *Journal of Applied Electrochemistry* **1999,** *29* (8), 979-986.

221. Sellergren, B.; Lepistö, M.; Mosbach, K., Highly enantioselective and substrate-selective polymers obtained by molecular imprinting utilizing noncovalent interactions. NMR and chromatographic studies on the nature of recognition. *Journal of the American Chemical Society* **1988,** *110* (17), 5853-5860.

222. Scholz, F.; Gulaboski, R.; Mirčeski, V.; Langer, P., Quantification of the chiral recognition in electrochemically driven ion transfer across the interface water/chiral liquid. *Electrochemistry Communications* **2002,** *4* (8), 659-662.

223. Han, Q.; Chen, Q.; Wang, Y.; Zhou, J.; Fu, Y., Enantioselective Recognition of Dopa Enantiomers in the Presence of Ascorbic Acid or Tyrosine. *Electroanalysis* **2012,** *24* (2), 332-337.

224. Wang, Q.; Das, M. R.; Li, M.; Boukherroub, R.; Szunerits, S., Voltammetric detection of l-dopa and carbidopa on graphene modified glassy carbon interfaces. *Bioelectrochemistry* (0).

225. Ghanem, M. A., Electrocatalytic activity and simultaneous determination of catechol and hydroquinone at mesoporous platinum electrode. *Electrochemistry Communications* **2007,** *9* (10), 2501-2506.

226. Kondo, Y.; Takayanagi, K., Synthesis and Characterization of Helical Multi-Shell Gold Nanowires. *Science* **2000,** *289* (5479), 606-608.

227. Barlow, S. M.; Raval, R., Complex organic molecules at metal surfaces: bonding, organisation and chirality. *Surface Science Reports* **2003,** *50* (6–8), 201-341.

228. Baiker, A., Reflections on chiral metal surfaces and their potential for catalysis. *Catalysis Today* **2005,** *100* (1–2), 159-170.

229. Shemer, G.; Krichevski, O.; Markovich, G.; Molotsky, T.; Lubitz, I.; Kotlyar, A. B., Chirality of Silver Nanoparticles Synthesized on DNA. *Journal of the American Chemical Society* **2006,** *128* (34), 11006-11007.

230. Han, J. W.; Sholl, D. S., Enantiospecific Adsorption of Amino Acids on Hydroxylated Quartz (0001). *Langmuir* **2009,** *25* (18), 10737-10745.

231. Greber, T.; Šljivančanin, Ž.; Schillinger, R.; Wider, J.; Hammer, B., Chiral Recognition of Organic Molecules by Atomic Kinks on Surfaces. *Physical Review Letters* **2006,** *96* (5), 056103.

232. Gellman, A. J.; Horvath, J. D.; Buelow, M. T., Chiral single crystal surface chemistry. *Journal of Molecular Catalysis A: Chemical* **2001,** *167* (1–2), 3-11.

233. He, G. S.; Liu, S. H., *Physics of Nonlinear Optics*. World Scientific: 1999.

234. Petralli-Mallow, T.; Wong, T. M.; Byers, J. D.; Yee, H. I.; Hicks, J. M., Circular dichroism spectroscopy at interfaces: a surface second harmonic generation study. *The Journal of Physical Chemistry* **1993,** *97* (7), 1383-1388.

235. Belsley, M., Second-Order Nonlinear Optical Characterization Techniques: An Introduction, by Thierry Verbiest, Koen Clays and Vincent Rodriguez. *Contemporary Physics* **2011,** *52* (5), 484-485.

236. Tom, H. W. K.; Aumiller, G. D., Observation of rotational anisotropy in the second-harmonic generation from a metal surface. *Physical Review B* **1986,** *33* (12), 8818-8821.

237. Valev, V. K.; Silhanek, A. V.; Smisdom, N.; De Clercq, B.; Gillijns, W.; Aktsipetrov, O. A.; Ameloot, M.; Moshchalkov, V. V.; Verbiest, T., Linearly polarized second harmonic generation microscopy reveals chirality. *Optics Express* **2010,** *18* (8), 8286-8293.

238. Barreto, W. J.; Ponzoni, S.; Sassi, P., A Raman and UV-Vis study of catecholamines oxidized with Mn(III). *Spectrochimica Acta Part A: Molecular and Biomolecular Spectroscopy* **1998,** *55* (1), 65-72.

239. Dong, M. W., Basic Terms and Concepts. In *Modern HPLC for Practicing Scientists*, John Wiley & Sons, Inc.: 2006; pp 15-46.

240. Gautam, U. G.; Gautam, M. P.; Sawada, T.; Takafuji, M.; Ihara, H., Thermodynamic investigations on shape selective separation behaviors of poly(4-vinylpyridine)-grafted silica for polycyclic aromatic hydrocarbons in both normal-phase and reversed-phase high-performance liquid chromatography. *Journal of Chromatography A* **2009,** *1216* (16), 3571-3577.

241. Ali, I.; Aboul-Enein, H. Y., The Analysis of Chiral Pollutants by Gas Chromatography. In *Chiral Pollutants: Distribution, Toxicity and Analysis by Chromatography and Capillary Electrophoresis*, John Wiley & Sons, Ltd: 2004; pp 185-228.

242. Kromidas, S., *HPLC made to measure : a practical handbook for optimization*. Wiley-VCH: Weinheim, 2006.

6 APPENDICES

APPENDIX A

BET theory

In this work, the specific surface area (S_{BET}) of zeolite catalyst is derived from Brunauer-Emmett-Teller (BET) theory in which the amount of adsorbed gas on a solid support is explained by an extension of the Langmuir theory[1]. The BET plot shows the linear relationship between $\frac{P}{V(P_0 - P)}$ and $\frac{P}{P_0}$ as shown in figure A1 and the BET equation is expressed by:

$$\frac{P}{V(P_0 - P)} = \frac{1}{V_m C} + \frac{C - 1P}{V_m C P_0}$$

where P and P_0 are the equilibrium and saturated pressure of adsorbates at adsorption temperature, respectively. V and V_m are the amount of adsorbed gas and the monolayer adsorbed gas quantities, respectively. C is BET constant ($c \approx \frac{e^{(E_{ADS} - E_{COND})}}{RT}$) where E_{ADS} and E_{COND} are the heat of adsorption at the first layer and the heat of condensation at multilayer, respectively. R is gas constant. Therefore, the V_m and C can be obtained by the slope and y-intercept. The specific surface area (S_{BET}) corresponds to V_m and is obtained by:

$$S_{BET} = \frac{V_m N s}{m x 22400}$$

where N, s and m are Avogadro's number, adsorption cross section of the adsorbate molecules and mass of adsorbent, respectively.

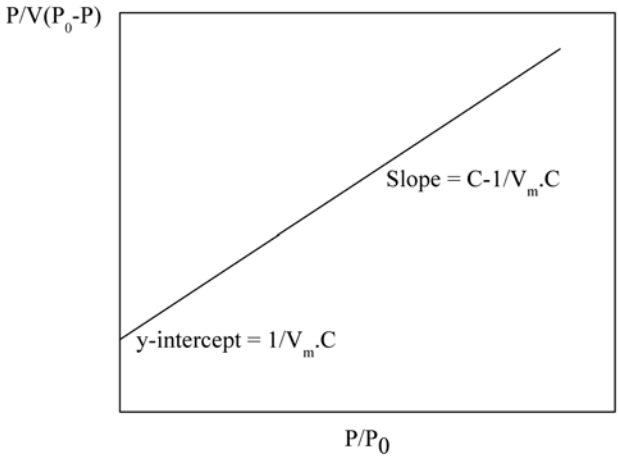

Figure A1. BET plot in the linear range.

t-plot method

The microporous volume (V_{micro}) can be calculated by the t-plot method [2] in which the volume of adsorbed gas is plotted as a function of statistical layer thickness (t) at corresponding P/P_0 as shown in Figure A2. The micropore volume can be estimated by the y-intercept of this graphically curve. The micropore volume (V_{micro}) is derived by:

$$V_{micro} = V_{\text{int}} D$$

where V_{int} is the volume at the y-intercept obtained by the plotting of the adsorbed gas quantity and layer thickness at corresponding P/P_0 and D is density conversion factor.

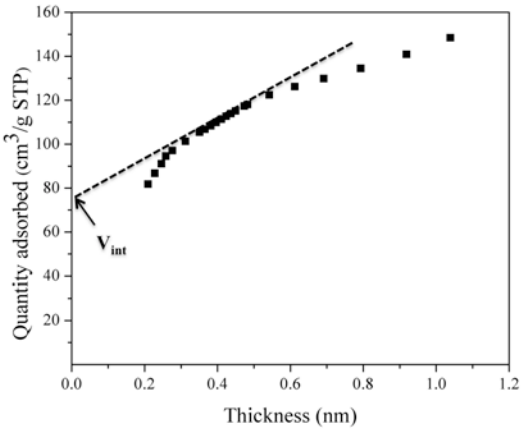

Figure A2. The t-plot curve of selected microporous zeolite sample.

Barret–Jovner–Halenda (BJH) model

In this study, the mesoporous size distribution is explained by BJH theory. The BJH model is based on the assumption that pores are in the cylindrical shape and the pore radius is the summation of the Kelvin radius and the thickness of adsorbed layer on the pore wall[3]. The pore diameter of BJH model is described by the following equation. The first term represents Kelvin radius due to capillary condensation and the second term is the multilayer thickness.

$$d = \frac{2\gamma V_L}{RT \ln\left(\frac{P_0}{P}\right)} + 2t$$

where P and P_0 are the actual and saturated vapor pressure. R is the gas constant, V_L is the molar volume, γ is the surface tension, T is temperature, d is the pore radius and t is the layer thickness.

APPENDIX B

The experimental setup for the catalytic study of *1*-butene isomerization

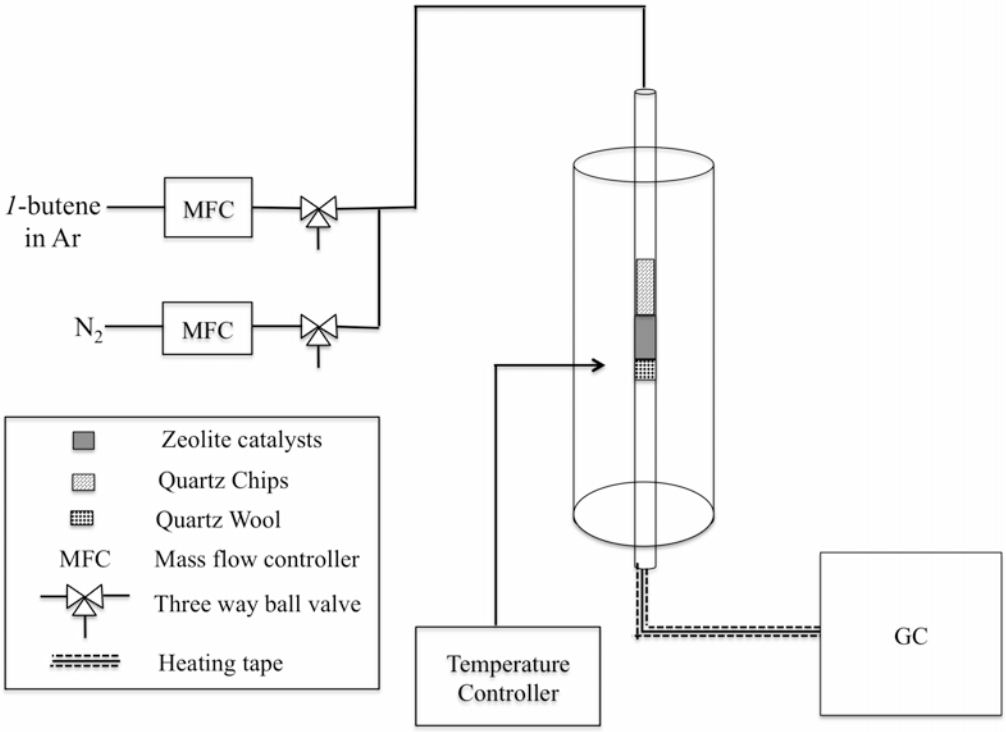

Figure B1. The setup diagram of a fixed-bed tubular reactor for catalytic study of *1*-butene isomerization.

APPENDIX C

The GC condition for the product separation and the example chromatogram of *1*-butene isomerization

As for *1*-butene isomerization, the products were analyzed by an online Agilent 6890N gas chromatograph) equipped with a Flame Ionization Detector (FID) and a capillary column (GS-GasPro, 60 m × 0.32 mm ID). The product separation was carried out by use of the He flow rate of 3.3 cm^3/min as carrier gas and oven temperature program (condition: 80 °C for 0.5 min, 175 °C for 2 min with heating rate of 25 °C/min and 250°C for 15 min with heating rate of 25 °C/min). The example chromatogram of product separation is shown in Figure C1.

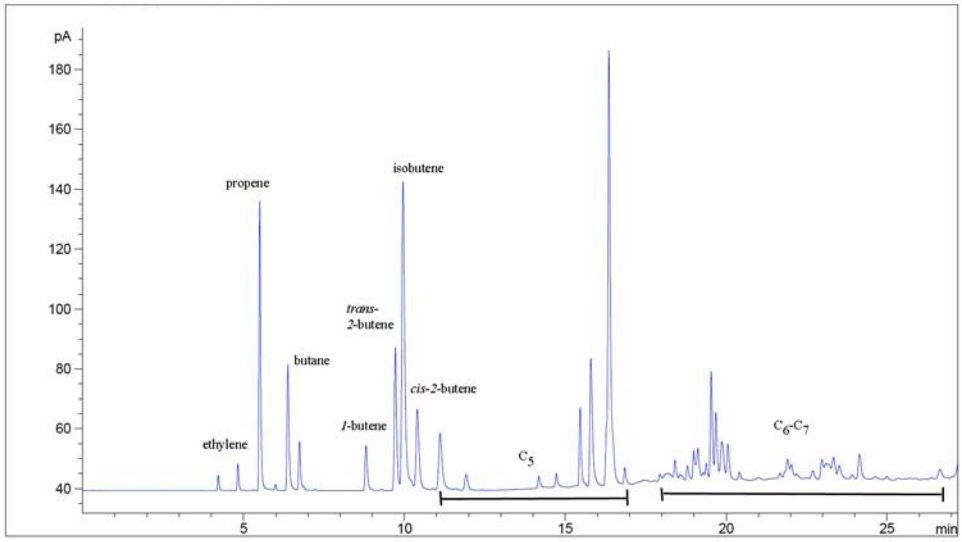

Figure C1. The example chromatogram from gas chromatography technique (GC) of the isomerization of 2 v/v% of *1*-butene in Ar in the total flow of 10 cm^3/min over the hierarchical micro/mesoporous HZSM-5 (Si/Al = 29) obtained by use of the C/SiO_2 composite at 240 °C at 120 min.

The peak at retention time of the 5.5 minute is assigned to be propene. The peak around the 6 minute belonged to butane isomers and the peaks in the range of 8.8 to 10.4 minutes are butene isomers. It is clearly shown that each isomer of butenes can be clearly separated by this GC condition. From this chromatogram, it also shows peaks of *2*-butenes, even we used the *1*-butene as reactant. Because *1*-butene can be easily converted to be *2*-butene over Brønsted zeolite via double bond migration[4] and *1*-butene and *2*-butene can be simultaneously reacted via the same mechanism to convert to isobutene[5], the summation of peaks of *1*-butene and *2*-butene (cis- and trans) are assigned as reactant for calculating of conversion of butenes and product selectivity.

APPENDIX D

The experimental setup for the catalytic study of *n*-hexane and *3*-methylpentane cracking

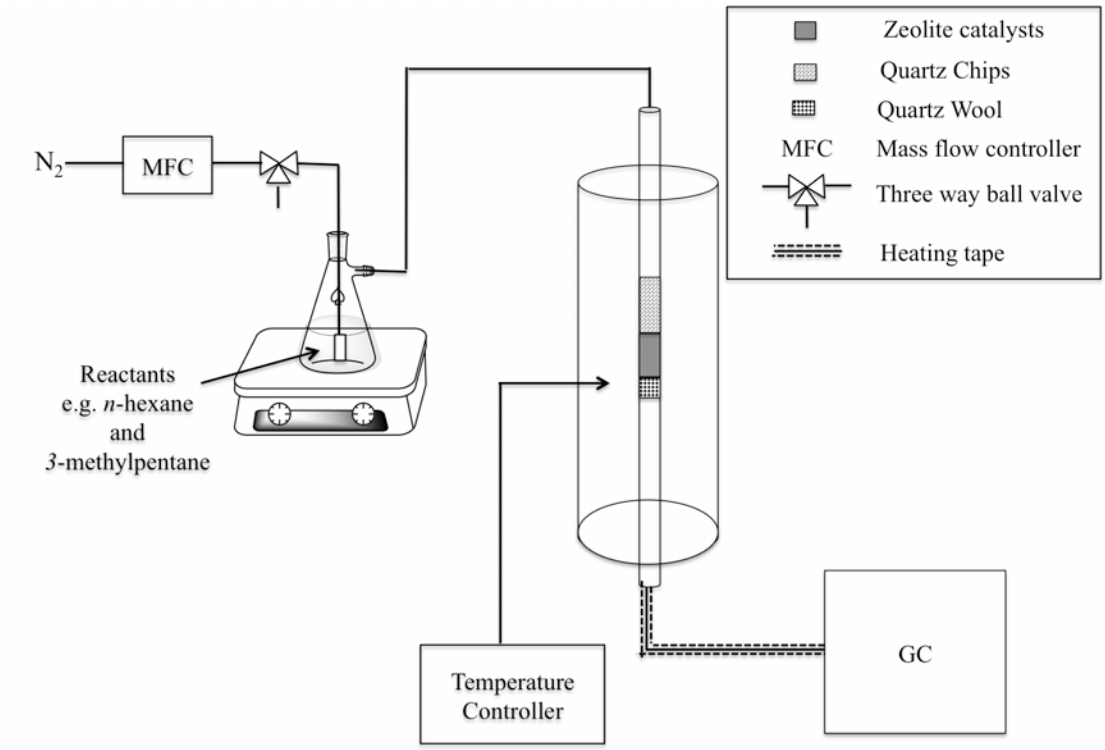

Figure D1. The setup diagram of a fixed-bed tubular reactor for the catalytic study of *n*-hexane and *3*-methylpentane cracking.

APPENDIX E

The GC condition for the product separation and the example chromatogram of *n*-hexane cracking

As for the *n*-hexane cracking, the products were analyzed by an online Agilent 6890N gas chromatograph) equipped with a Flame Ionization Detector (FID) and a capillary column (GS-GasPro, 60 m x 0.32 mm ID). The product separation was carried out by use of the He flow rate of 3.3 cm^3/min as carrier gas and oven temperature program (condition: 80 °C for 0.5 min, 175 °C for 2 min with heating rate of 25 °C/min and 250°C for 15 min with heating rate of 25 °C/min). The example chromatogram of product separation is shown in figure E1.

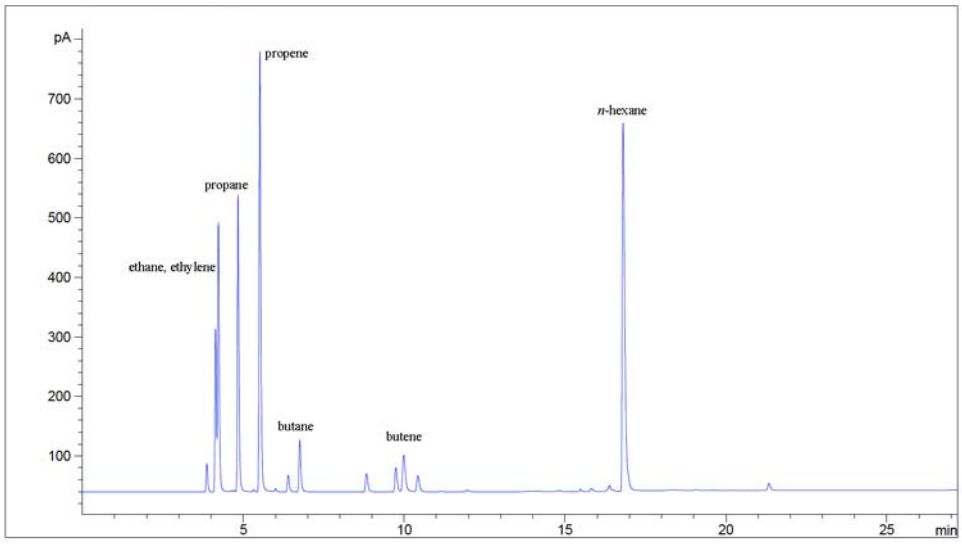

Figure E1. The example chromatogram from gas chromatography technique (GC) of the *n*-hexane cracking over the commercial HZSM-5 (Si/Al = 26) obtained by use of the C/SiO_2 composite at 500 °C.

APPENDIX F

The Antoine equation for the calculation of vapor pressure of reactant feed

The concentrations of vapor pressure of reactant feed of *n*-hexane and *3*-methylpentane in carrier gas are calculated by the Antoine equation, which described the relationship between vapor pressure and temperature as the following equation.

$$\log P = A - \frac{B}{C + T}$$

where P is the vapor pressure, T is temperature and A, B and C are Antoine coefficients that are specific values for each compound. In the case of *n*-hexane and *3*-methypentane, A B and C are shown in Table C1.

Table F1. The Antoine coefficients of *n*-hexane and 3-methylpentane[6].

Compound	T (K)	A	B	C
n-hexane	286.18-342.69	4.00266	1171.53	-48.784
3-methylpentane	288.44-337.23	3.97377	1152.368	-46.021

APPENDIX G

The GC condition for the product separation and the example chromatogram of the *n*-hexadecane cracking and hydrocracking

As for the *n*-hexadecane cracking and hydrocracking, the products are analyzed by an online Agilent 7820A gas chromatograph) equipped with a Flame Ionization Detector (FID) and a capillary column (DB-1, 100 m × 0.25 mm ID × 0.50 μm film thickness). The product separation was carried out by use of the He flow rate of 1.2 cm^3/min as carrier gas and oven temperature program (condition: 80 °C for 1 min and 320 °C for 20 min with heating rate of 10 °C/min). The example chromatogram of the product separation is shown in figure G1.

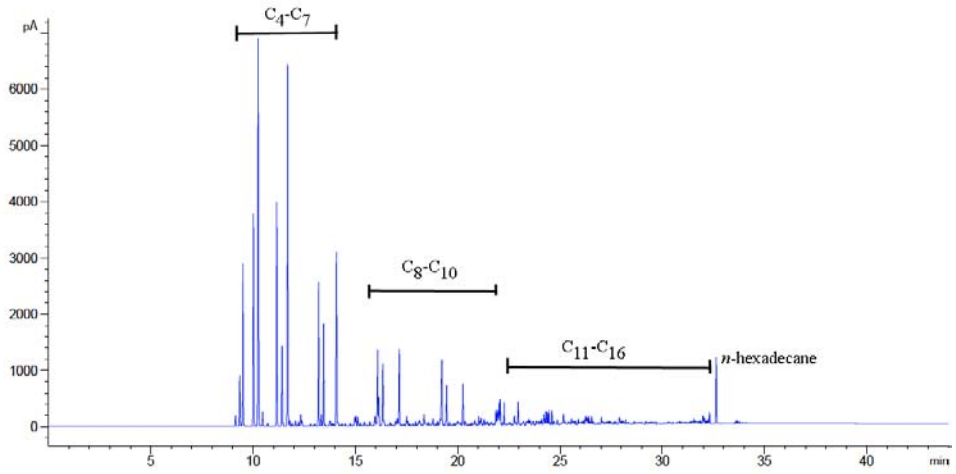

Figure G1. The example chromatogram from gas chromatography technique (GC) of the *n*-hexadecane hydrocracking over the hierarchical micro/mesoporous Pt/HZSM-5 (Si/Al = 29) obtained by use of the C/SiO_2 composite at 600 °C for 6 hours.

APPENDIX H

The ONIOM approach

The ONIOM, which stands for “Our-own-N-layered-Integrated molecular Orbital and molecular Mechanics”, is a multi-layered hybrid approach, which combines between the desired high accuracy and suitable computing resources[7].

The fundamental of the ONIOM approach is based on an extrapolation assumption. This method can be used to perform in large system by defining two or three layers within structure, which are treated at different levels of calculation, as known in ONIOM2 and ONIOM3. A molecular system can be divided into onion shell-like layer as shown in figure H1. For ONIOM2 scheme, the real system or whole system contains both model system and outer layer, that are treated by low level method, whereas the high layer, which is called the model system, belongs to the part of interesting system that is treated by high level of accuracy. Therefore, the link atoms (normally hydrogen is used) are used to saturate open valencies of the dangling bond, which is cut due to separation each layer.

An extrapolation assumption scheme is shown in Figure H2. As for the two-layer approach as example, $E_{ONIOM,\ real}$ refers to the target energy of real system at a high level, which can be approximated by the division of system into two layers: model system at low level (E_1) and high level of accuracy (E_2) and real system at low level (E_3) as shown in the following equation[7].

$$E_{ONIOM,\ real} = E_4(high, real) = E_3(low, real) + E_2(high, model) - E_1(low, model)$$

For the three-layer ONIOM approach, the target energy of entire system at high level can be extrapolated by the following equation [7].

$$E_{ONIOM,\ real} = E_9(high, real)$$

$$= E_6(low, real) + E_5(medium, I\text{-}model) + E_4(high, S\text{-}model) -$$

$$E_3(low, I\text{-}model) - E_2(medium, S\text{-}model)$$

Where I-model and S-model denote to intermediate model and small model, respectively. High, medium and low refer to the high, medium and low levels of calculation, respectively.

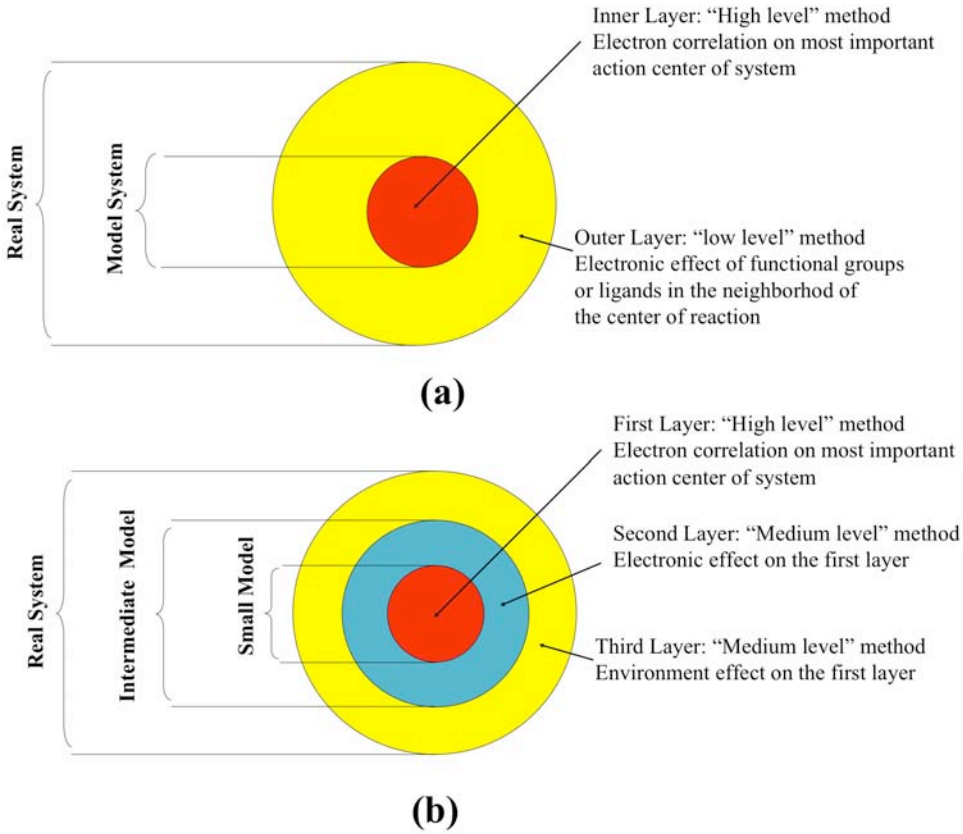

Figure H1. The ONIOM approach scheme: (a) the two-layers ONIOM approach (ONIOM2) and (b) the three-layers ONIOM approach (ONIOM3)[8-9].

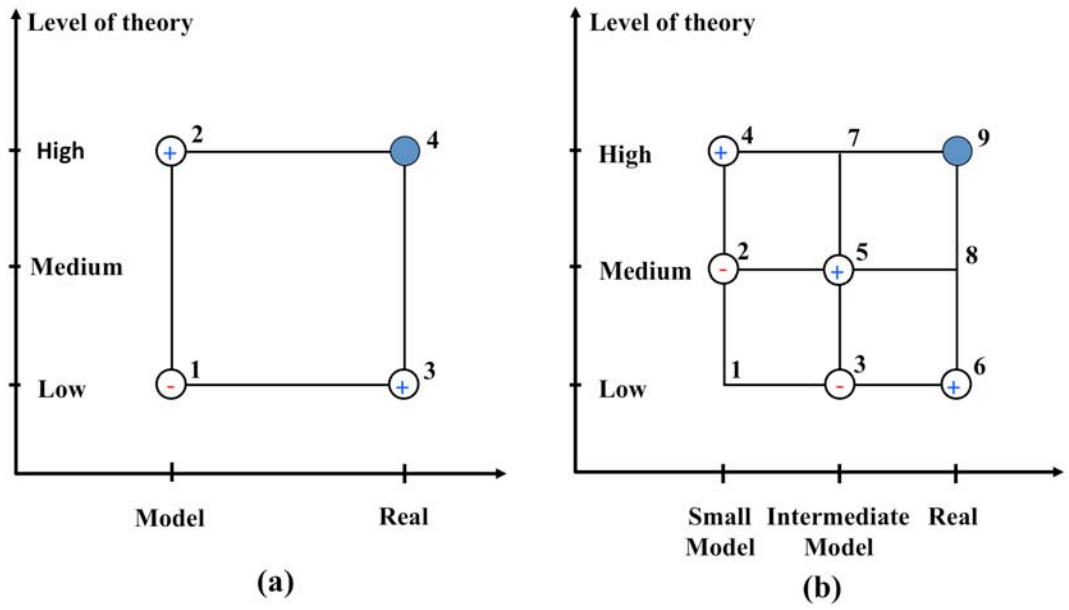

Figure H2. Illustration of the OINIOM extrapolation assumption for (a) the two-layers ONIOM approach (ONIOM2) and (b) the three-layers ONIOM approach (ONIOM3)[8-9].

APPENDIX REFERENCES

1. Brunauer, S.; Emmett, P. H.; Teller, E., Adsorption of Gases in Multimolecular Layers. *Journal of the American Chemical Society* **1938,** *60* (2), 309-319.
2. Lippens, B. C.; de Boer, J. H., Studies on pore systems in catalysts: V. The t method. *Journal of Catalysis* **1965,** *4* (3), 319-323.
3. Barrett, E. P.; Joyner, L. G.; Halenda, P. P., The Determination of Pore Volume and Area Distributions in Porous Substances. I. Computations from Nitrogen Isotherms. *Journal of the American Chemical Society* **1951,** *73* (1), 373-380.
4. Kangas, M.; Salmi, T.; Murzin, D. Y., Skeletal Isomerization of Butene in Fixed Beds. Part 2. Kinetic and Flow Modeling. *Industrial & Engineering Chemistry Research* **2008,** *47* (15), 5413-5426.
5. Rutenbeck, D.; Papp, H.; Freude, D.; Schwieger, W., Investigations on the reaction mechanism of the skeletal isomerization of n-butenes to isobutene: Part I. Reaction mechanism on H-ZSM-5 zeolites. *Applied Catalysis A: General* **2001,** *206* (1), 57-66.
6. Willingham, C. B.; Taylor, W. J.; Pignocco, J. M.; Rossini, F. D., Vapor pressures and boiling points of some paraffin, alkylcyclopentane, alkylcyclohexane, and alkylbenzene hydrocarbons. *Journal of Research of the National Bureau of Standards (U. S.)* **1945,** *35* (Copyright (C) 2013 American Chemical Society (ACS). All Rights Reserved.), 219-244.
7. Svensson, M.; Humbel, S.; Froese, R. D. J.; Matsubara, T.; Sieber, S.; Morokuma, K., ONIOM: A Multilayered Integrated MO + MM Method for Geometry Optimizations and Single Point Energy Predictions. A Test for Diels−Alder Reactions and Pt(P(t-Bu)3)2 + H2 Oxidative Addition. *The Journal of Physical Chemistry* **1996,** *100* (50), 19357-19363.
8. Dapprich, S.; Komáromi, I.; Byun, K. S.; Morokuma, K.; Frisch, M. J., A new ONIOM implementation in Gaussian98. Part I. The calculation of energies, gradients, vibrational frequencies and electric field derivatives. *Journal of Molecular Structure: THEOCHEM* **1999,** *461–462* (0), 1-21.
9. Maseras, F.; Morokuma, K., IMOMM: A new integrated ab initio + molecular mechanics geometry optimization scheme of equilibrium structures and transition states. *Journal of Computational Chemistry* **1995,** *16* (9), 1170-1179.

CV CURRICULUM VITAE

NAME: Ms. Chularat Wattanakit

BIRTH DATE: April 03, 1984

BIRTH PLACE: Bangkok, Thailand

EDUCATION:

YEAR	INSTITUTION	DEGREE/DIPLOMA
2006	Kasetsart Univ.	B.Sc. (Chemistry, 1st class honour)

SCHOLARSHIPS

2002-2005: Human Resource Development in Science Project (Science Achievement Scholarship of Thailand, SAST), the scholarship for undergraduate student, from Office of the Higher Education Commission, Ministry of Education, Thailand

2006-2007: Postgraduate Education and Research Program in Petroleum and Petrochemical Technology (MUA-ADB), Thailand

2008-2013: The Royal Golden Jubilee (RGJ) Ph.D. Program, the scholarship for Ph.D student, from the Thailand Research Fund, Thailand

2010: The JENESYS Programme 2010, JASSO Exchange Program for East Asian Postgraduate Students, in October 2010 - March 2011, Japan

2012: French Government's scholarship contribution to the RGJ-Ph. D. program

PUBLICATIONS:

1. Heim, M.; Wattanakit, C.; Reculusa, S.; Warakulwit, C.; Limtrakul, J.; Ravaine, S.; Kuhn, A., Hierarchical Macro-mesoporous Pt Deposits on Gold Microwires for Efficient Methanol Oxidation. *Electroanalysis* **2013**, *25 (4)*, 888-894.

2. Wattanakit, C.; Warakulwit, C.; Pantu, P.; Sunpetch, B.; Charoenpanich, M.; Limtrakul, J., The versatile synthesis method for hierarchical micro- and mesoporous zeolite: An embedded nanocarbon cluster approach. *The Canadian Journal of Chemical Engineering* **2012,** *90* (4), 873-880.

3. Wattanakit, C.; Nokbin, S.; Boekfa, B.; Pantu, P.; Limtrakul, J., Skeletal Isomerization of *1*-Butene over Ferrierite Zeolite: A Quantum Chemical Analysis of Structures and Reaction Mechanisms. *The Journal of Physical Chemistry C* **2012,** *116* (9), 5654-5663.

4. Maity, N.; Wattanakit, C.; Muratsugu, S.; Ishiguro, N.; Yang, Y.; Ohkoshi, S.-i.; Tada, M., Sulfoxidation on a SiO_2-supported Ru complex using O_2/aldehyde system. *Dalton Transactions* **2012,** *41* (15), 4558-4565.

CONFEREENCE PARTICIPATIONS:

1. Chiral Recognition by Molecular Imprinted Metal Electrodes, RGJ-Ph.D. Congress XIV, Pattaya, Chonburi, Thailand, April 5-7, 2013: Wattanakit, C.; Lapeyre, V.; Nokbin, S.; Warakulwit, C.; Limtrakul, J.; Kuhn, A. (Poster presentation)

2. Selective Sulfide Oxidation on a SiO_2-Supported Ru complex catalyst, The Winter School of Sokendai/Asian CORE Program “Frontiers of Molecular Science - Life, Material, Energy, and Space”, Okazaki, Japan, February 19-22, 2011: Wattanakit, C.; Maity, N.; Muratsugu, S.; Ishiguro, N.; Yang, Y.; Ohkoshi, S.-i.; Tada, M. (Oral presentation)

3. Structures and Reaction Mechanisms of Skeletal Isomerization of 1-Butene over Ferrierite Zeolite: An Embeded Nanocluster Approach, Proceedings of the Nano Thailand 2010 conference, Pathumthani, Thailand, October, 2010: Wattanakit, C., Nokbin, S., Boekfa, B. Pantu, P., Limtrakul, J. (Poster presentation)

4. Skeletal isomerization of *1*−butene over ferrierite zeolite: A quantum chemical analysis of structures and reaction mechanisms, The 239th ACS National Meeting & Exposition, San Francisco, CA, March 21-25, 2010: Wattanakit, C., Nokbin, S., Boekfa, B. Pantu, P., Limtrakul, J. (Poster presentation)

5. Theoretical studies of structures and reaction mechanisms of skeletal isomerization of *1*-butene to isobutene over ferrierite zeolite, The 1st National Research Symposium on Petroleum, Petrochemicals, and Advanced Materials and The 16th PPC Symposium on Petroleum, Petrochemicals, and Polymers, Bangkok, Thailand, April 22, 2010: Wattanakit, C., Nokbin, S., Boekfa, B. Pantu, P., Limtrakul, J. (Poster presentation)

RESUMÉ

Dans le présent travail, l'élaboration, la caractérisation et les applications de différents matériaux poreux ont été étudiés. Les matériaux poreux sont divisés en trois catégories en fonction de la taille de la cavité poreuse, à savoir des matériaux microporeux (diamètre des pores <2 nm), des matériaux mésoporeux (2 nm < diamètre des pores <50 nm) et des matériaux macroporeux (diamètre des pores > 50 nm). Le travail de thèse est organisé en trois grandes parties: la synthèse de zéolithes hiérarchiques micro/mésoporeux et leur application potentielle pour l'industrie pétrochimique comme c'est démontré dans le chapitre 1, l'étude théorique des mécanismes de réaction sur zéolithe microporeuse pour le chapitre 2 et la conception des métaux mésoporeux possédant une chiralité intrinsèque à leur surface intérieure, décrit au chapitre 3.

Dans la première partie de la thèse, les zéolithes hiérarchiques, composées d'éléments microporeux et mésoporeux, ont été préparées en utilisant des composites carbone-silice (C/SiO_2) issus d'une pyrolyse de gaz d'hydrocarbures sur gel de silice. Les composites C/SiO_2 agissent comme un matériau bifonctionnel dans lequel le carbone et le SiO_2 agissent comme template mésoporeuse et comme source de silice pour la synthèse de la zéolithe, respectivement. Une mésoporosité de la zéolithe est clairement obtenu lorsque des résidus de carbone sont incorporées en cours de synthèse de zéolithe et elle peut être facilement réglée en faisant varier la teneur en carbone dans les composites de C/SiO_2. L'augmentation de la teneur en carbone dans les composites se traduit par une augmentation significative de la surface et le volume total des pores, ce qui reflète une augmentation du volume mésoporeux alors que le volume des micropores de l'échantillon n'est pas significativement modifiée. Ces observations démontrent que non seulement la présence d'une grande surface et d'une porosité, mais aussi une meilleure efficacité de ces matériaux pour de nombreux procédés pétrochimiques, tels que l'isomérisation de *n*-butène, le craquage catalytique de *n*-hexadécane et l'hydrocraquage. Leur performance catalytique pour des réactions différentes, y compris l'isomérisation de *n*-butène, et le

craquage catalytique d'hexane, methylpentane et *n*-hexadécane, ont également été étudiées. Il était clairement démontré que l'efficacité catalytique des réactions à l'égard de grosses molécules telles que l'isomérisation de *n*-butène et le craquage catalytique du *n*-hexadécane, peut être améliorée par la mésoporosité, alors que les performances de craquage catalytique de molécules C6 ne pouvaient être améliorées par ce matériau mésoporeux. De plus, les activités catalytiques des zéolithes bifonctionnels, qui sont obtenus par l'incorporation de sites actifs métalliques (Pt) dans une zéolithe de type H^+, sont étudiés à la fois pour la zéolithe classique et la zéolithe hiérarchique micro/ mésoporeux. On constate que la zéolithe hiérarchique micro/mésoporeux Pt/HZSM-5 non seulement améliore le degré de dispersion de nanoparticules métalliques dans les canaux de la zéolithe secondaire, mais surtout aussi améliore la réaction catalytique d'hydrocraquage du *n*-hexadécane. Nos résultats confirment que la zéolithe hiérarchique avec un système poreux bimodal de cavités microporeux et mésoporeux peut être générée à l'aide de résidus de carbone comme template mésoporeux issus de la pyrolyse de gaz d'hydrocarbures et ces catalyseurs montrent des résultats prometteurs, en particulier lorsque la réaction implique de grosses molécules dans les procédés catalytiques. On peut envisager de généraliser cette nouvelle méthode de synthèse à d'autres types de zéolithes, pour créer des zéolithes hiérarchiques micro/mésoporeux pour des applications catalytiques, en particulier dans l'industrie pétrochimique.

En plus de l'étude des aspects pratiques de la catalyse, une approche théorique a été utilisé pour étudier les mécanismes de réaction potentiels tels que l'isomérisation sélective du *1*-butène en isobutène, qui est l'un des sujets les plus intéressants à la fois dans le contexte académique et industriel, parce que l'isobutène est un intermédiaire utile conduisant à de nombreux composés, comme des additifs dans l'essence, par exemple l’éthyl tert-butyl éther (ETBE), le polyisobutylène (PIB) et des méthacrylates. Cependant, le mécanisme de cette réaction et l'existence d'intermédiaires sont encore sujet de discussion. Il existe de nombreux mécanismes proposés dans la littérature, y compris les mécanismes monomoléculaires, pseudomoléculaires et l’oligomérisation-craquage. Cependant, la voie monomoléculaire est la voie la plus importante lorsque la réaction a lieu sur zéolithe de type FER. Par conséquent, dans ce chapitre, le mécanisme monomoléculaire complète d'isomérisation du squelette de butène-1 sur ferrierite zéolithe est étudiée au moyen de méthodes de calcul quantique basé sur l'approche ONIOM. Deux mécanismes différents sont trouvés en fonction de la taille du modèle. Dans le cas d'un

grand modèle (37T cluster), y compris l'effet du squelette de la zéolithe, le mécanisme de réaction monomoléculaire passe par quatre structures de l'état de transition, à savoir, la protonation de butène-1 TS1 (II), l'état de transition cyclique TS2 (IV), la conversion de l'isobutoxyde en cation de tert-butyle via l'état de transition de décalage de hydrure 1,2 (VI) et la déprotonation du cation tertiobutyle (VIII), avec les produits intermédiaires correspondants, 2- butoxyde de potassium, isobutylate et l'ion carbénium de tert-butyle. En revanche, le mécanisme dans un petit modèle (5T) sans effet de squelette donne trois structures d'état de transition et deux espèces d'alcoolates. La différence de mécanisme entre le modèle de 5T et 37T est que l' intermédiaire isobutoxyde (V) peut être décomposé directement pour former le complexe d'adsorption d'isobutène , alors que cela est interdit dans le cas de 37T. L'étape limitant de vitesse est la conversion de l'isobutoxyde en isobutene, dans lequel la réaction doit passer par l'état de transition primaire de cations isobutyle. L'étape limitant pour le modèle 37T se trouve être la décomposition de l' isobutoxyde de surface intermédiaire à travers d'un état de transition primaire hautement instable. En outre, ces observations ont démontré que pour l'utilisation de ferrierite zéolithe (H -FER) avec des pores de taille moyenne, présenté par le modèle 37T, le cation tert-butyle est le véritable intermédiaire, alors que cette espèce ne peut être trouvée lorsque les effets de la squelette de la zéolithe ont été négligés. Ce travail démontre clairement que la sélectivité de forme due à un effet de «nano-confinement» de la squelette de la zéolithe affecte fortement l'adsorption, la stabilité des espèces d'alcoxydes et carbocation, ainsi que le mécanisme d' isomérisation de butène-1.

Outre la forme des matériaux non-conducteurs tels que la zéolithe nanoporeux, la génération de métaux mésoporeux chiraux et ses propriétés de reconnaissance énantiosélectifs ont été étudiés. L'empreinte moléculaire (MI) est une approche importante pour générer des matériaux avec des propriétés énantiosélectives, cependant, cette technique a été limité jusqu'ici principalement à des matrices souples tels que les polymères, conduisant à des polymères à empreintes moléculaires (MIP). Cette technique souffre souvent de quelques inconvénients, comme un enlèvement difficile du template, une cinétique de fixation lente et une grande flexibilité du polymère, ce qui entraîne la destruction de la structure chirale de la cavité après le retrait du template. La génération de fonctionnalités chiraux sur des surfaces métalliques a été signalés dans de nombreux rapports de la littérature. Toutefois, jusqu'à présent, aucune étude a pu démontrer la conception des surfaces métalliques chiraux par empreinte moléculaire pour lesquelles

l'empreinte chiral peut être conservée même après le retrait du template chiral. Dans ce travail, du platine mésoporeux imprimé de façon chiral a été obtenue par la réduction électrochimique de sels de platine, en présence simultanée d'une phase de cristal liquide lyotrope et de molécules template chiraux. Les matériaux obtenus présentent non seulement une augmentation spectaculaire de la surface active en raison de leur mésoporosité, mais aussi une discrimination significative entre les deux énantiomères d'une sonde chiral, confirmée par les voie électrochimique et par des expériences d'adsorption énantiosélectifs. Le platine poreux conserve son caractère chiral, même après le retrait du template chiral. Ce travail préliminaire montre des résultats très prometteurs en ce qui concerne la synthèse d'un métal imprimé avec un motif chiral, qui en plus conserve sa chiralité même après le retrait du template. L'approche est donc très complémentaire à celle des polymères à empreintes moléculaires. Nos résultats pourraient mener au développement de nouveaux matériaux, qui présentent un intérêt potentiel pour des applications dans des domaines tels que la synthèse chirale, les capteurs, la séparation, la purification et le développement de médicaments.

Par conséquent, ce travail démontre que plusieurs types de matériaux poreux, allant de composé non conducteur jusqu'aux matériaux conducteurs ont été fabriqués par des méthodes contrôlables. La conception des éléments poreux peut être géré de manière efficace par la présence de templates appropriés soit mous soit durs. La structure poreuses bien organisées résulte en des propriétés uniques des matériaux. Par exemple, les matériaux microporeux, composé seulement de petites cavités poreuses présentent une sélectivité de forme parce que la dimension de leurs cavités est comparable à la dimension moléculaire. Toutefois, des matériaux microporeux ne sont pas efficaces pour certaines applications en raison d'éventuelles difficultés pour accéder aux sites actifs. Afin d'améliorer les faiblesses de ces matériaux, la conception de matériaux avec de plus grandes cavités poreuses pourrait être une alternative. Introduire des cavités mésoporeux dans les matériaux améliore non seulement la surface en raison de la mésoporosité, mais augmente également la possibilité pour les molécules d'accéder à des sites spécifiques. Nos résultats ont confirmé que de nombreux types de matériaux poreux peuvent être conçus d'une manière contrôlable afin d'améliorer leur efficacité et de les rendre aptes pour les applications souhaitées. Ces matériaux poreux sont très utiles pour diverses applications potentielles allant de la catalyse aux technologies de séparation chirale. En

outre, nous avons également intégré des calculs théoriques ensemble avec les aspects expérimentaux, afin d'étudier et mieux comprendre au niveau moléculaire ces sytèmes.

Mots clés: Zéolithes micro- et mesoporeux, isomérisation, catalyseurs, nano-confinement, métaux mesoporeux chiraux, cristaux liquide lyotrope, electrodéposition, électroanalyse, calcul quantique.